

Design, Control and Error Analysis of a Fast Tool  
Positioning System for Ultra-Precision Machining  
of Freeform Surfaces

by

Fei Ding

Submitted to the Department of Design, Manufacturing and  
Engineering Management in partial fulfilment of the requirements for  
the degree of

Doctor of Philosophy in Mechanical Engineering

at the

University of Strathclyde

September 2019

# Declaration Statement

This thesis is the result of the author's original research. It has been composed by the author and has not been previously submitted for examination, which has led to the award of a degree.

The copyright of this thesis belongs to the author under the terms of the United Kingdom Copyright Acts as qualified by University of Strathclyde Regulation 3.50. Due acknowledgement must always be made of the use of any material contained in or derived from this thesis.

Signed: 

Date: 06/11/2019

# Abstract

Freeform surfaces are widely found in advanced imaging and illumination systems, orthopaedic implants, high-power beam shaping applications, and other high-end scientific instruments. They give the designers greater ability to cope with the performance limitations commonly encountered in simple-shape designs. However, the stringent requirements for surface roughness and form accuracy of freeform components pose significant challenges for current machining techniques—especially in the optical and display market where large surfaces with tens of thousands of micro features are to be machined. Such highly wavy surfaces require the machine tool cutter to move rapidly while keeping following errors small. Manufacturing efficiency has been a bottleneck in these applications. The rapidly changing cutting forces and inertial forces also contribute a great deal to the machining errors.

The difficulty in maintaining good surface quality under conditions of high operational frequency suggests the need for an error analysis approach that can predict the dynamic errors. The machining requirements also impose great challenges on machine tool design and the control process. There has been a knowledge gap on how the mechanical structural design affects the achievable positioning stability. The goal of this study was to develop a tool positioning system capable of delivering fast motion with the required positioning accuracy and stiffness for ultra-precision freeform manufacturing. This goal is achieved through deterministic structural design, detailed error analysis, and novel control algorithms.

Firstly, a novel stiff-support design was proposed to eliminate the structural and bearing compliances in the structural loop. To implement the concept, a fast positioning device was developed based on a new-type flat voice coil motor. Flexure bearing, magnet track, and motor coil parameters were designed and calculated in detail. A high-performance digital controller and a power amplifier were also built to meet the servo rate requirement of the closed-loop system. A thorough understanding was established of how signals propagated within the control system, which is fundamentally important in determining the loop performance of high-speed control.

A systematic error analysis approach based on a detailed model of the system was proposed and verified for the first time that could reveal how disturbances contribute to the tool positioning errors. Each source of disturbance was treated as a stochastic process, and these disturbances were synthesised in the frequency domain. The differences between following error and real positioning error were discussed and clarified. The predicted spectrum of following errors agreed with the measured spectrum across the frequency range. It is found that the following errors read from

the control software underestimated the real positioning errors at low frequencies and overestimated them at high frequencies. The error analysis approach thus successfully revealed the real tool positioning errors that are mingled with sensor noise.

Approaches to suppress disturbances were discussed from the perspectives of both system design and control. A deterministic controller design approach was developed to preclude the uncertainty associated with controller tuning, resulting in a control law that can minimize positioning errors. The influences of mechanical parameters such as mass, damping, and stiffness were investigated within the closed-loop framework. Under a given disturbance condition, the optimal bearing stiffness and optimal damping coefficients were found. Experimental positioning tests showed that a larger moving mass helped to combat all disturbances but sensor noise.

Because of power limits, the inertia of the fast tool positioning system could not be high. A control algorithm with an additional acceleration-feedback loop was then studied to enhance the dynamic stiffness of the cutting system without any need for large inertia. An analytical model of the dynamic stiffness of the system with acceleration feedback was established. The dynamic stiffness was tested by frequency response tests as well as by intermittent diamond-turning experiments. The following errors and the form errors of the machined surfaces were compared with the estimates provided by the model. It is found that the dynamic stiffness within the acceleration sensor bandwidth was proportionally improved. The additional acceleration sensor brought a new error source into the loop, and its contribution of errors increased with a larger acceleration gain. At a certain point, the error caused by the increased acceleration gain surpassed other disturbances and started to dominate, representing the practical upper limit of the acceleration gain.

Finally, the developed positioning system was used to cut some typical freeform surfaces. A surface roughness of 1.2 nm (Ra) was achieved on a NiP alloy substrate in flat cutting experiments. Freeform surfaces—including beam integrator surface, sinusoidal surface, and arbitrary freeform surface—were successfully machined with optical-grade quality. Ideas for future improvements were proposed in the end of this thesis.



# Acknowledgements

Firstly, I want to thank my supervisor Professor Xichun Luo for his dedicated supports for my PhD study for the past years. His immense knowledge and rich experiences in academic researches helped me find a way to finish this thesis. Also, thank him for the providing me an opportunity to study in a new country, which has surely changed the course of my life.

I want to thank all the technicians in the M8 workshop, especially Duncan Lindesay and Fuad Warsame for the help of machining many of the parts and the very warm welcomes from Scotland. My dear colleague students in Room 608, Yukui Cai, Yankang Tian, Zhengjian Wang, Song Yang and many others, have gave me tremendous courage and supports in my PhD lifetime. We have enjoyed many happy moments together in the lab and in the daily life as well, led by the “big brother” Wenlong Chang. Special thanks for Wenbin Zhong for introducing me how to build PCB boards and many valuable discussions on the system design.

The knowledge in this thesis covers several disciplines and they are combined in the context of a precision positioning system. I have learned a lot from the books of *Essentials of Robust Control* by Kemin Zhou; *The Design of High Performance Mechatronics* by Robert Munnig Schmidt; and the PhD thesis of *Mechatronic Design of a Magnetically Suspended Rotating Platform* by Leon Jabben and *Electromagnetically Driven Ultra-Fast Tool Servos for Diamond Turning* by Xiaodong Lu.

Sincere thanks to my families for their endless love and supports.

This study is founded by a joint John Anderson PhD studentship provided by DePuy (Ireland) and the University of Strathclyde [S150852]. Chinese Studentship Council provided the living stipends.

# Previously Published Work

## Journal papers:

- [1] **F. Ding**, X. Luo, W. Zhong, W. Chang, Design of a new fast tool positioning system and systematic study on its positioning stability, *Int. J. Mach. Tools Manuf.* 142(2019) 54–65.
- [2] **F. Ding**, X. Luo, Y. Cai, Acceleration feedback control for enhancing dynamic stiffness of fast tool servo system considering the sensor imperfections, *Mech. Syst. Signal Process.* (2019), accepted/in press.
- [3] **F. Ding**, X. Luo, W. Chang, In situ measurement of spindle radial and tilt error motions by complementary multi-probe method, *Nanomanufacturing and Metrology.* (2019), accepted/in press.
- [4] J. Chen, **F. Ding**, X. Luo, X. Rao, J. Sun, Fundamental study of ductile-regime diamond turning of single crystal gallium arsenide, *Precision Engineering* (2019), accepted/in press.
- [5] W. Zhong, X. Luo, W. Chang, **F. Ding**, Y. Cai, A real-time interpolator for parametric curves, *Int. J. Mach. Tools Manuf.* 125 (2018) 133–145.
- [6] X. Rao, F. Zhang, X. Luo, **F. Ding**, Characterization of hardness, elastic modulus and fracture toughness of RB-SiC ceramics at elevated temperature by Vickers test, *Mater. Sci. Eng. A.* 744 (2019) 426–435.
- [7] X. Rao, F. Zhang, X. Luo, **F. Ding**, Y. Cai, J. Sun, H. Liu, Material removal mode and friction behaviour of RB-SiC ceramics during scratching at elevated temperatures, *J. Eur. Ceram. Soc.* 39(2019) 3534–3545.
- [8] Y. Cai, X. Luo, M. MacLean, Y. Qin, M. Duxbury, **F. Ding**, A single-step fabrication approach for development of antimicrobial surfaces, *J. Mater. Process. Technol.* 271 (2019) 249–260.
- [9] X. Rao, F. Zhang, Y. Lu, X. Luo, **F. Ding**, C. Li, Analysis of diamond wheel wear and surface integrity in laser-assisted grinding of RB-SiC ceramics. *Ceramics International*, 16.08.2019 (in press).
- [10] W. Zhong, X. Luo, W. Chang, Y. Cai, **F. Ding**, H. Liu, Y. Sun, Toolpath interpolation and smoothing for computer numerical control machining of freeform surfaces: a review. *International Journal of Automation and Computing*, 12.06.2019 (in press).
- [11] Z. Li, F. Zhang, X. Luo, W. Chang, Y. Cai, W. Zhong, **F. Ding**, Material removal mechanism of laser-assisted grinding of RB-SiC ceramics and process optimization. *Journal of the European Ceramic Society*, Vol. 39, No. 4, 30.04.2019, p. 705-717.

### Conference papers:

- [1] **F. Ding**, X. Luo, Measurement of spindle error motions by an improved multi-probe method, in: 12th Int. Conf. Exhib. Laser Metrol. Mach. Tool, C. Robot. Perform., 2017: pp. 256–262.
- [2] **F. Ding**, X. Luo, Dynamics stiffness enhancement of fast tool servo by acceleration feedback, in: EUSPEN's 19th International Conference & Exhibition. 2019: pp.572–573.
- [3] W. Chang, W. Zhong, **F. Ding**, F. Wardle, X. Luo, Development of a compact ultra-precision six-axis hybrid micro-machine. World Congress on Micro and Nano Manufacturing, Kaohsiung, Taiwan. 2017.

# Table of Contents

Nomenclature .....	XI
List of Abbreviations .....	XIII
List of Tables .....	XV
List of Figures .....	XVI
CHAPTER 1 Introduction .....	1
1.1 Research background.....	1
1.2 Applications of precision freeform surfaces .....	3
1.2.1 Orthopaedic implants for medical applications.....	3
1.2.2 Optical imaging applications.....	3
1.2.3 High-energy laser applications.....	5
1.2.4 EUV and X-ray mirrors.....	5
1.3 Machining challenges .....	8
1.4 Aim and objectives .....	8
1.5 Thesis overview .....	9
CHAPTER 2 Literature review.....	12
2.1 State-of-the-art freeform machining techniques.....	12
2.2 Positioning system design and active control.....	17
2.2.1 Fast tool servo designs .....	17
2.2.2 Active bearing designs .....	18
2.2.3 Active damping designs .....	20
2.3 Error analysis of positioning systems .....	21
2.4 Feedback control strategies.....	21
2.4.1 Position feedback control .....	21
2.4.2 Acceleration feedback control.....	23
2.5 Summary.....	24
CHAPTER 3 A novel-concept stiff-support positioning system design and its prototyping .....	26
3.1 Introduction.....	26
3.2 Basic concepts in precision machine tool design.....	26
3.2.1 Dynamic errors and machining accuracy .....	26
3.2.2 Structural loop stiffness.....	28
3.3 Machine tool configurations .....	30
3.3.1 Cross-slides configuration.....	30
3.3.2 T-based configuration.....	32
3.4 A novel stiff-support design .....	34
3.4.1 Flexure bearing design and stiffness calculation.....	38

3.4.2	Magnet track design and calculation .....	39
3.4.3	Calculation of FVCM parameters .....	42
3.5	Prototype assembling .....	46
3.6	Summary .....	47
CHAPTER 4	Signal chains in digital controller and power amplifier .....	49
4.1	Introduction .....	49
4.2	Overall structure of the electronic system .....	49
4.3	Development of digital controller board .....	51
4.3.1	Function block diagram of the digital controller board .....	51
4.3.2	On-chip hardware resources of the DSP .....	52
4.3.3	Coordination of multi-core tasks .....	54
4.4	Delays in the digital signal chain .....	54
4.4.1	Transmission delay .....	55
4.4.2	Calculation delay .....	60
4.4.3	Sampling delay .....	61
4.4.4	Measured loop frequency response with delays .....	61
4.5	Noise in the digital signal chains .....	62
4.5.1	ADC noise spectrum .....	63
4.5.2	Displacement sensor noise spectrum .....	64
4.5.3	DAC output noise .....	64
4.6	Power amplifier stage design and tests .....	65
4.6.1	High-power driving techniques .....	65
4.6.2	Open-loop characteristics of voltage amplifier and coil .....	67
4.6.3	Closed-loop current control with linear voltage amplifiers .....	68
4.6.4	Experimental tests of the power amplifier stage .....	74
4.7	Summary .....	77
CHAPTER 5	Dynamic error analysis in single feedback control loop .....	79
5.1	Introduction .....	79
5.2	General model of single-feedback control loop .....	80
5.3	Another point of view on the effects of the closed-loop control .....	82
5.4	Modelling of the mechatronic system with error sources .....	83
5.5	Plant parameter identification .....	86
5.5.1	Input excitation sources and signal processing .....	86
5.5.2	Calculation of frequency response functions .....	90
5.5.3	Parameter estimation .....	92
5.6	Calculation of the PID controller gains .....	94
5.7	Error contribution analysis .....	95
5.7.1	Stochastic and non-stochastic errors .....	95
5.7.2	Frequency domain synthesis of stochastic disturbances .....	97

5.7.3	Closed-loop positioning error tests.....	99
5.7.4	Spectrum analysis of measured errors.....	100
5.7.5	Time domain analysis of non-stochastic components.....	104
5.8	Closed-loop dynamic stiffness and controller gains.....	105
5.9	Summary.....	107
CHAPTER 6	Optimisation of control algorithm and study on influences of structural parameters .....	108
6.1	Introduction.....	108
6.2	Optimal control theory.....	109
6.3	Calculation of control algorithm.....	111
6.3.1	State space model of the closed-loop system .....	111
6.3.2	Selection of weighting filters for coloured disturbances.....	114
6.4	Closed-loop positioning test .....	118
6.4.1	Control algorithm deployment in hardware .....	118
6.4.2	Measured closed-loop response with optimal control.....	120
6.5	Study on influences of plant parameters.....	122
6.5.1	Influence of moving mass .....	122
6.5.2	Influence of flexure bearing stiffness and damping .....	125
6.5.3	Influence of motor force constant .....	128
6.6	Summary.....	129
CHAPTER 7	Acceleration feedback control for enhancement of dynamics stiffness .....	130
7.1	Introduction.....	130
7.2	Limitations with feedback control .....	130
7.3	Control schemes with acceleration feedback.....	132
7.3.1	Cascade acceleration feedback loop.....	133
7.3.2	Disturbance observer and compensator.....	133
7.3.3	Comparison of the two feedback configurations.....	134
7.4	Analytical model of acceleration feedback control .....	136
7.4.1	Analysis of dynamic stiffness with acceleration feedback.....	137
7.4.2	Influences of low-pass characteristics within the acceleration loop .....	140
7.4.3	Error contributions of the added acceleration sensor .....	142
7.5	Experimental verification of the acceleration feedback model .....	144
7.5.1	Acceleration sensor characteristics .....	144
7.5.2	Positioning errors introduced by the acceleration sensor.....	147
7.5.3	Dynamic stiffness with acceleration feedback control.....	148
7.6	Intermittent cutting experiments.....	150
7.6.1	Intermitted cutting setup.....	150

7.6.2	Intermitted cutting results.....	152
7.7	Summary.....	155
CHAPTER 8	Geometric error mapping and freeform machining experiments .	157
8.1	Introduction.....	157
8.2	Diamond turning experimental setup.....	157
8.3	Synchronisation of position command to spindle angle.....	159
8.4	Measurement of spindle error motions.....	160
8.4.1	Measurement of radial and tilt error motions.....	160
8.4.2	Measurement of axial error motions.....	162
8.5	Machining trials with the developed system.....	164
8.5.1	Flat surface turning.....	164
8.5.2	Micro-lenslet cutting.....	165
8.5.3	Beam integrator surface cutting.....	167
8.5.4	Sinusoidal grid cutting.....	172
8.5.5	Arbitrary freeform machining.....	175
8.6	Summary.....	179
CHAPTER 9	Conclusions and future work.....	181
9.1	Conclusions.....	181
9.2	Knowledge contributions.....	183
9.3	Limitations and future work.....	183
9.3.1	Aspects for future improvements.....	184
9.3.2	More ideas.....	185
Appendix A	Screen-shots of control software.....	187
Appendix B	AD/DA interface circuits.....	189
B. 1	A/D interface circuits.....	189
B. 2	D/A interface circuits.....	190
Appendix C	Lumped-parameter model.....	191
Appendix D	Spindle error measurement.....	192
D. 1	Method.....	192
D. 2	Error separation algorithm.....	193
D. 3	Measurement setup.....	194
D. 4	Data processing.....	198
Bibliography	201	

# Nomenclature

Symbols	Meaning
$W_s, W_i, W_{fc}$ and $W_g$	Weighting filter for each disturbance source
$H_{acc}$ and $\omega_{acc}$	Transfer function and bandwidth of the acceleration sensor
$H_{capa}$ and $\omega_{capa}$	Transfer function and bandwidth of the capacitive sensor
$CAS_i$	Cumulative amplitude spectrums of each error source
$D_{coil}$	Equivalent loop diameter of the coil
$FRF_i$	Frequency response functions from each disturbance input to tool position
$H_I(s)$	Transfer function of closed current loop
$H_a$	Frequency response of acceleration loop filter
$K_T$	Motor force constant
$K_a$	Acceleration feedback gain
$K_g$	Global gain for PID controller
$K_p, K_i$ and $K_d$	Proportional, integral and derivative gains
$M_s$	Peak response near the cross over frequency
$N_{coil}$	Number of motor coil turns
$PSD_{Fol}$	Power spectral density of following errors
$PSD_{Real}$	Power spectral density of real tool positioning errors
$PSD_i$	Error power contribution from each disturbance to tool position
$P_s, P_i, P_g$ and $P_a$	Power spectral density of displacement sensor, current, ground and acceleration sensor disturbances
$R_{coil}, L_{coil}$	Resistance and inductance of the coil
$T_f$	Time constant of the first-order low-pass action on the derivative term
$W_u$	Weighting function of the control output
$c_1, c_1, \dots$	Damping of mechanical links
$d_{coil}$	Diameter of the motor coil wire
$f_N$	Nyquist frequency
$k_1, k_2, \dots$	Stiffness of mechanical links



---

$m_1, m_2, \dots$	Mass of mechanical bodies
$\mu_0, \mu_r$	Permeability of vacuum and relative permeability
$\omega_l$	Bandwidth of the closed current loop
$\omega_b$	Intended closed-loop bandwidth
$\omega_{bu}$	Control output corner frequency
$D$ or $D(s)$	Input sensitivity function
$Err_{rms}$	Root mean square value of following errors
$G$ or $G(s)$	Transfer function of mechanical plant
$H$ or $H(s)$	Transfer function of feedback sensors
$J(\omega)$	Cost function in optimal control
$K$ or $K(s)$	Transfer function of control action
$R$ or $R(s)$	Transfer function of control efforts
$S$ or $S(s)$	Output sensitivity function
$T$ or $T(s)$	Complementary output sensitivity function
$n_1, n_2$	Noise inputs from sensors
$\varepsilon$	Infinite small numbers
$\zeta$	Damping coefficient of closed current loop

---

# List of Abbreviations

---

Abbreviation	Full Meaning
ADC	Analogue to Digital Convertor
AR	Augmented Reality
CAS	Cumulative Amplitude Spectrum
CNC	Computer Numerical Control
DAC	Digital to Analogue Convertor
DFT	Discrete Fourier Transform
DOB	Disturbance Observer
DOE	Diffractive Optical Element
DoF	Degree of Freedom
DSP	Digital Signal Processor
EMF	Electromagnetic Force
EMIF	External Memory Interface
ERF	Electrorheological Fluid
EUV	Extreme Ultraviolet
FEA	Finite Element Analysis
FFT	Fast Fourier Transform
FIB	Focused Ion Beam
FPGA	Field Programmable Gate Arrays
FTS	Fast Tool Servo
FVCM	Flat Voice Coil Motor
GBP	Gain Bandwidth Product
GPIO	General Purpose Input/Output
HMD	Head-Mounted Display
IIR	Infinite Impulse Response
IPC	Inter-Process Communication
LIDAR	Light Imaging, Detection, And Ranging
McBSP	Multi-channel Buffered Serial Port
MIMO	Multiple-Input and Multiple-Output
MLA	Micro Lens Array

---

---

MRF	Magnetorheological Fluid
MSM	Multi-core Shared Memory
OFC	Oxygen-Free Copper
PD/PI/PID	Proportional-Integral-Derivative
PSD	Power Spectral Density
PSO	Position Synchronized Output
PWM	Pulse Width Modulation
RHP	Right Hand Plane
RMS	Root Mean Square
SISO	Single-Input and Single-Output
SNR	Signal to Noise Ratio
STS	Slow Tool Servo
UART	Universal Asynchronous Receiver/Transmitter
UHV	Ultra-High Vacuum
UPR	Undulations Per Revolution

---

# List of Tables

Table 1-1: Freeform mirrors used in laser beam shaping .....	6
Table 1-2: Applications for ultra-precision freeform surfaces in optical elements .....	7
Table 2-1: Overview of technologies to fabricate freeform and micro-structured surfaces.....	16
Table 4-1: Specifications of the developed controller and amplifier board.....	51
Table 4-2: Time spent on data transferring .....	59
Table 4-3: CPU cycles required to read a single-precision data from different memory locations .....	60
Table 5-1: Characteristics of common excitation signal types .....	89
Table 5-2: Identified parameters of the positioning system.....	94
Table 5-3: Decomposition of disturbance sources .....	96
Table 6-1: CPU cycles required for the optimal and PID control algorithms.....	119
Table 7-1: Equivalent terms of the closed-loop behaviour .....	138
Table 7-2: Specifications of the acceleration sensor.....	145
Table 7-3: Experimental conditions for intermitted cutting tests .....	151
Table 8-1: Specifications of the work spindle .....	159
Table 8-2: Experimental conditions for flat diamond turning .....	164
Table 8-3: Experimental conditions for micro-lenslet cutting .....	166
Table 8-4: Experimental conditions for beam integrator surface.....	169
Table 8-5: Experimental conditions for sinusoidal grid turning .....	173
Table 8-6: Experimental conditions for arbitrary freeform turning .....	178
Table D-1: Designed probe angles .....	194
Table D-2: Actual probe angles after probe mounting .....	198

# List of Figures

Figure 1-1: Evolution of ultra-precision manufacturing technologies.....	2
Figure 1-2: Hip and knee implants with super-smooth freeform surfaces.....	3
Figure 1-3: Micro lens array optics in 3D display applications .....	4
Figure 1-4: SEM images of diffractive elements and the diffraction image.....	5
Figure 1-5: Flowchart of the thesis structure .....	9
Figure 2-1: Different techniques to machine Fresnel lens on various surfaces .....	13
Figure 2-2: Micro structuring techniques by Takeuchi and Brinksmeier .....	14
Figure 2-3: Micro structuring techniques by Huang and To.....	15
Figure 2-4: Machining complexity of freeform surfaces with different functional dimensions .....	16
Figure 2-5: Different designs and working principles of FTS .....	17
Figure 2-6: Actively controlled bearing for straightness correction .....	19
Figure 2-7: Two degree of freedom framework for positioning control.....	22
Figure 3-1: Influencing factors for machining accuracy and corresponding research topics .....	27
Figure 3-2: Illustration of structural loop stiffness .....	29
Figure 3-3: Cross-slides turning configuration with FTS .....	31
Figure 3-4: Z-axis frequency response of a cross-slides configuration .....	31
Figure 3-5: Typical T-based diamond turning machine with FTS.....	33
Figure 3-6: T-based turning machine configuration with minimum angular compliance .....	34
Figure 3-7: Metrology paths and the force paths for different FTS configurations...	35
Figure 3-8: Stiff-support structural design (Parts in red move in the Z direction and parts in blue move in the X direction together with the red parts.).....	36
Figure 3-9: Detailed design of the flexures .....	36
Figure 3-10: Diamond turning configuration with the proposed device.....	37
Figure 3-11: Precision ruling configuration with the proposed device.....	37
Figure 3-12: Double parallel leaf spring bearing .....	38
Figure 3-13: Deformation of the flexure hinge with unit force .....	39
Figure 3-14: Diagram of the magnet track design .....	40
Figure 3-15: Average magnetic field strength changes with different air gap distances .....	41
Figure 3-16: Using iron shoes to smooth the magnetic field and the leakage problem .....	41

Figure 3-17: Average magnetic field strength changes with different iron shoe thicknesses .....	42
Figure 3-18: Cross section of magnetic field distribution with the selected parameters .....	42
Figure 3-19: Model and photo of the multi-layer carbon-fibre coil assembly .....	43
Figure 3-20: Coil winding design with key dimensions .....	44
Figure 3-21: Calculated electrical time constant with different wire diameters .....	45
Figure 3-22: Calculated motor force constant with different wire diameters .....	45
Figure 3-23: Photo of the capacitive sensor and encoder assembly .....	46
Figure 3-24: Photo of the magnet track assembly (Iron shoe strip not fitted) .....	47
Figure 3-25: Finished assembly of the developed motion system .....	47
Figure 4-1: Model of the designed controller and power amplifier stage .....	50
Figure 4-2: Photograph of the built controller and amplifier electronics .....	50
Figure 4-3: System function block diagram and data flow paths .....	52
Figure 4-4: Data flows in the digital control loop .....	55
Figure 4-5: Timing delay diagram of the ADC input .....	56
Figure 4-6: Information flow of read action from the peripheral through the TeraNet bus .....	57
Figure 4-7: Parallel processing to improve the servo update rate .....	58
Figure 4-8: Timing delay diagram of the DAC output .....	59
Figure 4-9: Accurate delay estimation helps improve modelling accuracy .....	62
Figure 4-10: Noise spectrum of ADC with $4 \times$ oversampling without anti-aliasing filter .....	63
Figure 4-11: Measured displacement sensor noise with anti-aliasing filter .....	64
Figure 4-12: DAC Output glitch sampled by ADC when no filter is applied .....	65
Figure 4-13: Comparison of voltage waveforms from linear and PWM power amplifiers .....	66
Figure 4-14: Open-loop gain of voltage amplifier PA04 .....	67
Figure 4-15: High-side and low-side current sensing in current control loop .....	68
Figure 4-16: Two schemes to compensate load poles .....	69
Figure 4-17: Closed-loop responses with different voltage feedback gains .....	70
Figure 4-18: Different analogue compensation circuits for current closed-loop control .....	72
Figure 4-19: Simulated frequency responses with different analogue compensation circuits .....	73
Figure 4-20: Photo of the developed current controller board with cooling block .....	74
Figure 4-21: Frequency responses of the coil with and without core iron (units) .....	75
Figure 4-22: Current closed-loop response with different compensation resistors .....	76
Figure 4-23: Measured current loop response with different proportional gains .....	77

Figure 4-24: Measured current stage noise and corresponding spectrum.....	77
Figure 5-1: Typical single-feedback control loop configuration .....	80
Figure 5-2: State space representation of a simple system under PD control.....	82
Figure 5-3: Closed-loop servo system diagram .....	83
Figure 5-4: Lumped-parameter model of the mechanical system.....	84
Figure 5-5: Flat voice coil motor structure .....	85
Figure 5-6: Typical excitation signals used in frequency response tests .....	88
Figure 5-7: Measured frequency response of the built positioning system .....	91
Figure 5-8: Linear fit results for the motor force constant calibration.....	92
Figure 5-9: Fitted model with grey box model .....	93
Figure 5-10: Fitted model with grey box model and high frequency residue terms..	93
Figure 5-11: Block diagram of PID position loop .....	95
Figure 5-12: Environmental disturbance vibrations.....	96
Figure 5-13: Diagram of stochastic disturbance propagations and measuring noise.	97
Figure 5-14: Comparison between measured following errors and estimated following errors with different moving masses and bandwidths.....	100
Figure 5-15: Spectrum analysis of predicted following errors and real positioning errors in comparison with experimental results .....	102
Figure 5-16: Following errors read from capacitive sensor feedback at 468 Hz bandwidth setting .....	103
Figure 5-17: Error power contribution to the total real positioning error with different bandwidths .....	103
Figure 5-18: Frequency response from cutting force to sensor voltage.....	104
Figure 5-19: Simulated tool deviation with pre-measured force and measured following errors.....	105
Figure 5-20: Stiffness curve with low PID gains .....	106
Figure 5-21: Stiffness curve with high PID gains.....	106
Figure 6-1: Standard representation of H2 optimal control problem.....	109
Figure 6-2: Augmented plant configuration for optimal controller design.....	111
Figure 6-3: H2 optimal control model established in MATLAB for the developed prototype (state space model) .....	112
Figure 6-4: Disturbances measurement and modelling of the disturbance spectrum .....	115
Figure 6-5: Calculated optimal controller and corresponding transfer functions ....	117
Figure 6-6: Calculated controller and transfer functions with PID control .....	117
Figure 6-7: Calculated optimal controller with lower $Wu$ weighting function .....	118
Figure 6-8: Iterative calculation of the optimal control algorithm in hardware.....	119
Figure 6-9: Measured closed-loop response of input sensitivity $D$ .....	120

Figure 6-10: Measured following error with optimal controller at bandwidth of 1.1 kHz	121
Figure 6-11: Measured following error with PID controller	121
Figure 6-12: FFT spectrum of the two error signals with different control algorithms	122
Figure 6-13: Performance with increased moving mass (grey -- before, coloured -- after)	123
Figure 6-14: Achievable minimum positioning error decreases with larger moving masses	124
Figure 6-15: Performance with increased flexure stiffness $k_2$	126
Figure 6-16: Performance with increased flexure damping $c_2$	127
Figure 6-17: Optimal bearing stiffness and damping	128
Figure 6-18: Performance with increased motor force constant $K_T$	129
Figure 7-1: Illustration of the Bode sensitivity integral relationship	131
Figure 7-2: Conventional motion control with position feedback	132
Figure 7-3: Motion control with cascade acceleration feedback	133
Figure 7-4: Motion control with DOB acceleration feedback	134
Figure 7-5: Diagram of the two acceleration feedback structures	135
Figure 7-6: Analytical model of acceleration feedback control along with PID position controller	137
Figure 7-7: Comparison of loop transfer functions with (w) and without (w/o) acceleration feedback	141
Figure 7-8: The transfer functions of the three disturbance sources with increasing acceleration feedback depths	143
Figure 7-9: Typical frequency response of piezo accelerometers	144
Figure 7-10: Measured sensor noise of the acceleration sensor	146
Figure 7-11: Measured frequency responses of the displacement sensor and the acceleration sensor	146
Figure 7-12: Error contributions with different acceleration gains	148
Figure 7-13: Dynamic compliance function with increasing $K_a$ and fixed PID gains	149
Figure 7-14: Dynamic compliance function with increasing $K_a$ and proportionally increased PID gains	150
Figure 7-15: Diagram of the acceleration feedback control experimental setup	150
Figure 7-16: Photo of the acceleration feedback control experimental setup	151
Figure 7-17: Following error caused by cutting force with different acceleration gains	152
Figure 7-18: Measured surface profile with different acceleration gains and the detailed image at the edge	154



Figure 7-19: The averaged cross sectional profile along the cutting path .....	155
Figure 8-1: Photograph of the diamond-turning machine before modification .....	158
Figure 8-2: Machining setup on diamond turning machine with the developed device .....	158
Figure 8-3: Experimental setup for radial and tilt error measurement.....	161
Figure 8-4: Trajectories of spindle rotating centre line with linearly fitted data .....	162
Figure 8-5: Calculated tilt errors about the X and Y axis in one full spindle revolution .....	162
Figure 8-6: Setup for axial error measurement .....	163
Figure 8-7: Measured axial error motions of the spindle.....	163
Figure 8-8: Photo of flat turning sample .....	165
Figure 8-9: Measured flat surface topography on NiP substrate .....	165
Figure 8-10: Diagram of micro-lenslet cutting trajectory .....	166
Figure 8-11: Photo of the micro lens and the micro-lenslet part with different depths .....	167
Figure 8-12: Form error of the machined micro lens.....	167
Figure 8-13: Freeform beam integrator surface .....	168
Figure 8-14: Designed beam integrator surface .....	169
Figure 8-15: Tool trajectory during cutting of beam integrator surface .....	170
Figure 8-16: Machined beam integrator surface .....	171
Figure 8-17: Measured beam integrator shapes and the cross section profile .....	171
Figure 8-18: Form error of the spherical lens element and the cross section profile	171
Figure 8-19: Designed sinusoidal grid surface .....	172
Figure 8-20: Tool trajectory during cutting of sinusoidal grid surface at 200 Hz ...	173
Figure 8-21: Tool trajectory during cutting of sinusoidal grid surface at 20 Hz .....	174
Figure 8-22: Machined sinusoidal grid surface.....	174
Figure 8-23: Measured sinusoidal grid shapes and the cross section profile (edge)	175
Figure 8-24: Measured sinusoidal grid shapes and the cross section profile (centre) .....	175
Figure 8-25: Calculation of tool position in arbitrary freeform machining .....	176
Figure 8-26: Freeform shape derived from sample image .....	177
Figure 8-27: Machined freeform surface from an image .....	179
Figure A-1 Main control user graphical interface.....	187
Figure A-2: Spectrum analysis user graphical interface .....	187
Figure A-3: Frequency response test user graphical interface .....	188
Figure A-4: Controller tuning user graphical interface.....	188
Figure B-1: ADC interface circuits .....	189
Figure B-2: DAC interface circuits .....	190
Figure B-3: PCB layout of the developed controller board .....	190

Figure D-1: Complementary multi-probe error separation method ..... 192  
Figure D-2: Absolute values of  $H(k)$  at different harmonic orders for the designed three sets of angles ..... 194  
Figure D-3: Probe angle arrangement and the axial measurement positions..... 195  
Figure D-4: Sensor readings for the first 200 revolutions after start-up ..... 196  
Figure D-5: Steps for calculation of actual probe angles with an ink mark..... 197  
Figure D-6: Harmonic weighting functions after probe mounting ..... 198  
Figure D-7: Harmonic suppression problem and modified results ..... 200  
Figure D-8: X radial error measured with three angle sets ..... 200

# CHAPTER 1

## Introduction

### 1.1 Research background

Precision machining techniques are necessary to produce parts in applications where both surface roughness and form accuracy are important. Currently, flat and spherical surfaces are dominant in the industry. This is because they are easier to be designed, fabricated and measured. Two typical methods are the three-plate lapping technique and the spherical lapping technique. In these methods, the adaptive material removal mechanism caused by the random movement of the lapping tool and workpiece naturally result in a plane or a sphere. These methods are so simple and effective that they are still used in optical industries. The new standard of international unit of kilogram is fabricated in this way as well [1].

However, these two simple shapes are not enough for the ever-increasing demands from optical, medical and electronics industries. Complex surfaces provide more design freedoms for the designer to cope with some performance limitations encountered in simple-shape designs [2] [3]. In addition, this also helps to make optical assemblies more compact and lighter [4]. One successful example is the wide adoption of aspherical lens elements in consumer camera lens to correct the aberration imperfection [5]. The complexity of freeform parts requires a deterministic manufacturing approach where the relative position of the tool is accurately controlled. The material is only removed at the contact point between the tool and the workpiece. This is where ultra-precision machine tools start to take over the job. In these machine tools, the position of the cutting tool is monitored and actively controlled to follow the position commands. The commands are sent in digital number formats and the movements of different axis are synchronised by the so-called Computer Numerical Control (CNC) technology. The motion trajectory can be programmed arbitrarily by the operator, which greatly increases the machining flexibility. This machining method also improves the machining efficiency of the simple geometries compared with

traditional lapping or polishing approach, although with some limitations on machinable materials [6]. The machined surfaces with diamond tools can reach sub-nanometre surface roughness in a single cut, which is comparable to that of finely polished surfaces [7].

At the beginning, the development of ultra-precision machining was mainly driven by the demands from military and high-energy researches. The advancement of measuring devices and motor techniques has fostered wider commercial applications of ultra-precision manufacturing. More and more complex freeform surfaces can be produced at reasonable costs. Figure 1-1 shows that the achievable machining accuracy keeps improving with the development of new machining and measuring technologies [8].

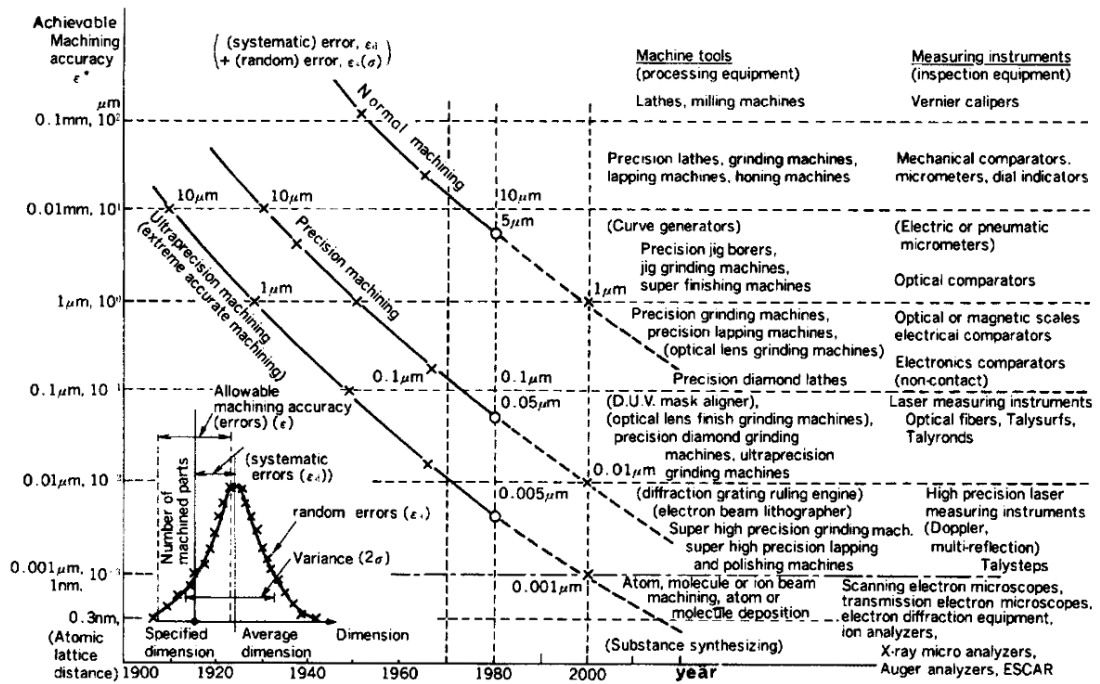


Figure 1-1: Evolution of ultra-precision manufacturing technologies [9]

In this study, ultra-precision freeform machining refers to the manufacturing of arbitrary waveform surfaces or micro-structured surfaces with nanometre-level surface roughness [10]–[12].

## 1.2 Applications of precision freeform surfaces

### 1.2.1 Orthopaedic implants for medical applications

Orthopaedic implants have been used to replace damaged human bones or joints successfully [13]. As shown in Figure 1-2, they are often formed by two or more moving parts and the shape of the part is of spherical or freeform type. During the whole lifetime of the implant, the mating surfaces keep rubbing each other and thus the surface quality and form accuracy are very important. Small scratches on the mating surfaces or uneven load distribution will lead to the generation of micro debris, which is the major cause of early failures of implants [14]. The surface roughness of the contacting surface is required to be less than 20 nm. These medical implants are often made of hard materials like Titanium or Cobalt Chrome (CoCr), which makes it very difficult to fabricate.



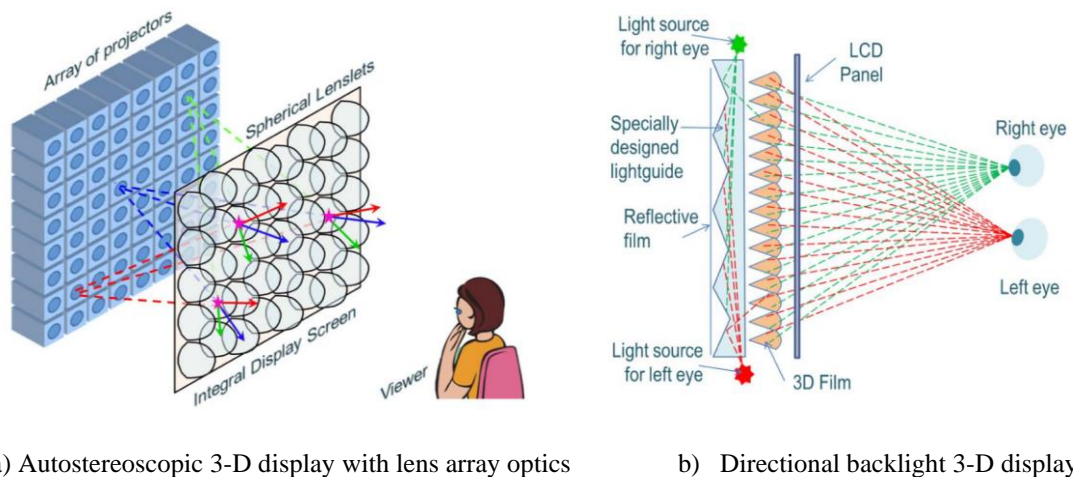
Figure 1-2: Hip and knee implants with super-smooth freeform surfaces (Image courtesy of Depuy)

### 1.2.2 Optical imaging applications

Another important area of applications for ultra-precision machined parts are in the optical industry, such as microscope objectives, next-generation imaging devices, high-end illumination and some other scientific instruments [11]. The precisely defined boundaries of different materials in the machined parts change the behaviour of lights by reflection, refraction or diffractive effects. The shapes of those elements differ a lot based on their working principles. Traditional reflective and refractive elements usually possess slow-varying continuous surface profiles, which can be grouped as rotational symmetric and non-rotational symmetric types. Diffractive

Optical Elements (DOEs) are designed as micro steps with heights that are close to the wavelength of the light [15], [16] [17].

Micro Lens Array (MLA) films are refractive optics with lots of micro-scale lenslets. Different from traditional optics, they may show some discontinuities on the surfaces. MLAs are increasingly found in new designs of 3-D display in Head-Mounted Display (HMD) or Augmented Reality (AR) systems. Such as in Figure 1-3, MLA films combined with LCD technology are used to deliver naked-eye 3-D display [18]. Each lens-let directs the light from the beneath pixel to different directions and thus the two human eyes receive different images and our brain will process these two images as a single 3-D picture. Micro spherical lens array elements are also used in light field microscopes to acquire depth information in a single shot [19]. Some researchers tried to put a freeform lens array film in front of the image sensor to increase the capture field of view [20].



a) Autostereoscopic 3-D display with lens array optics

b) Directional backlight 3-D display

Figure 1-3: Micro lens array optics in 3D display applications [18]

Some other optical elements work under the diffractive principles of light and they possess much smaller structures than MLA parts. A single light beam can be projected into arbitrary shapes after going through a DOE film, as shown in Figure 1-4. They are widely used in structured light applications such as 3-D sensing, Light Imaging, Detection, And Ranging (LIDAR). For those low-power applications, the elements are mostly made from polymer materials such as polycarbonate and PMMA, because they are easier to be produced in large quantity by injection moulding or imprinting techniques.

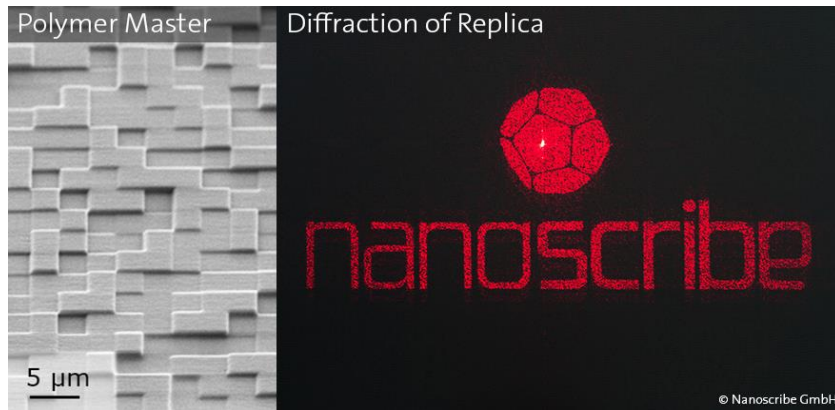


Figure 1-4: SEM images of diffractive elements and the diffraction image (Image courtesy of Nanoscribe GmbH)

DOE is also a critical part in the development of emerging holographic displays. Brian Wowk has composed a futuristic outlook based on the phased array control of light field first published in 1991 [21]. DOEs are also used to correct the chromatic aberrations of refractive lenses [22], [23]. The same principle is used to steer the directions of laser beams in optical tweezers, where controlled laser beams are used to trap and move microscopic objects [24].

### 1.2.3 High-energy laser applications


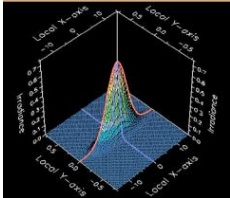
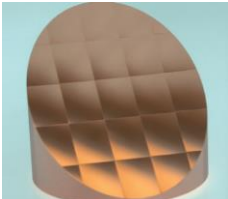
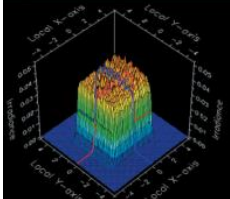

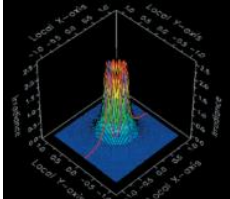
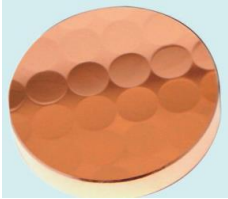
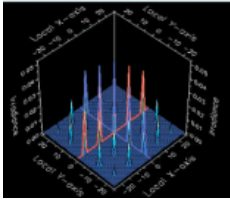
Freeform mirrors are used to shape the infrared laser beams in high-energy laser, medical and aesthetic applications. In each application, the laser beam energy should be uniformly distributed onto a designed area. The direct output laser from the laser source is of Gaussian distribution. Additional infrared optics is used to divert the laser beam to different shapes. The reflective mirrors are often made of copper with water cooling channels as shown in Table 1-1.

### 1.2.4 EUV and X-ray mirrors

In some extreme imaging applications, much shorter light wavelength must be used in order to achieve super high resolution. One typical example is the next generation Extreme Ultraviolet (EUV) lithography machine, which works under a very short wavelength of 13.5 nm. Electromagnetic waves with an even shorter wavelength fall into the X-ray range (10 nm to 10 pm). All the EUV and X-ray lenses are reflective

type and require sub-nanometre surface roughness and sub-micrometre form accuracy, which requires ultra-precision manufacturing technologies to produce.

Table 1-1: Freeform mirrors used in laser beam shaping (Image courtesy of II-VI, Inc.)

Lens type	Lens form	Focused beam shape
Biconic lens		
Beam integrator		
Vortex lens		
Optical array		

As a summary, the optical applications range from the long wavelength end of the electromagnetic spectrum such as infrared and visible radiations up to the X-ray range with very short wavelength. The required dimensional accuracy and surface roughness are proportional to the wavelength of the electromagnetic wave [25]. The typical applications of ultra-precision freeform surfaces are summarised in Table 1-2.



Table 1-2: Applications for ultra-precision freeform surfaces in optical elements

Spectrum (wavelength)	Applications	Working principle	Machining method	Material
X-ray (10 nm to 10 µm)	Telescope mirrors	Reflection	Replicated or Directly machined	Coated Nickel
	Lithography optics	Reflection	Directly machined	Coated Nickel
EUV (13.5 nm)	Aspherical lens	Refraction	Directly machined	Optical glass
	Illumination	Reflection	Replicated	Coated plastics
	Light field imaging (MLA)	Refraction	Replicated	Plastics
	HMD/VR/AR	Refraction	Directly machined	Optical glass
Visible light (380 nm to 760 nm)		Diffraction	Replicated	Plastics
	3-D display (Stereoscopic)	Refraction	Replicated	Plastics
	3-D display (Holographic)	Diffraction	Replicated	Plastics
	LIDAR	Diffraction	Various	Various
	Imaging/Tracking	Refraction	Directly machined	Silicon et al.
Near / Middle Infrared (1 µm to 10 µm)	High-energy laser beam shaping	Reflection	Directly machined	Copper
		Diffraction	Replicated	Fused silica
	Optical tweezers	Diffraction	Various	Various
Terahertz (30 µm to 3 mm)	Security scanning	Reflection	Directly machined	Metal
		Refraction	Directly machined	PTFE, TPX

### **1.3 Machining challenges**

The stringent surface roughness and profile accuracy requirements of the freeform optics design poses significant manufacturing challenges to current freeform diamond turning, grinding and micro structuring techniques. Especially in the optical and display market where large surfaces with tens of thousands micro features are to be manufactured. Such highly wavy surfaces require the machine tool cutter to move rapidly while maintaining small following errors at the same time. The low machining efficiency has been a bottleneck in these applications. The rapidly changing cutting forces and inertial forces also contribute a lot to the machining errors.

Current ultra-precision machine tools tend to adopt large slides to make the most of the averaging effect and to achieve high positioning stability [26]. When the machine slides are minimised in fast positioning applications for high dynamic machining, the environmental disturbances start to affect the positioning accuracy. The challenge in maintaining good surface quality under high operational frequency invokes the need of a systematic error analysis approach to predict the dynamic errors for freeform machining.

The requirements also put great challenges on the machine tool design and control process. Actuation bandwidth and positioning stability are contradictory to each other in the design of motion systems. The designer has to explore the best of the hardware resources with a deterministic approach. Understanding of how the mechanical structural design affects positioning accuracy is also a knowledge gap.

### **1.4 Aim and objectives**

The aim of this study is to establish the knowledge for developing a tool positioning system capable of delivering fast motions (closed-loop bandwidth more than 1 kHz) with required machining surface quality (surface roughness less than 3 nm) for freeform ultra-precision machining. This will be achieved through deterministic structural design, detailed modelling and novel control algorithms. The theoretical limitations will be revealed and considered when designing the system.

The principal objectives are:

- 1) To optimise the structural design of fast tool positioning systems for high precision freeform machining;
- 2) To gain a systematic understanding of how the disturbance error sources originate and affect the tool positioning accuracy;
- 3) To reveal how the structural configuration and parameters affect the achievable positioning stability and stiffness;
- 4) To explore advanced control approaches to increase machine dynamic stiffness with sensing and feedback schemes.

## 1.5 Thesis overview

To address the research challenges listed in Section 1.3, this thesis is organised into nine chapters as below:

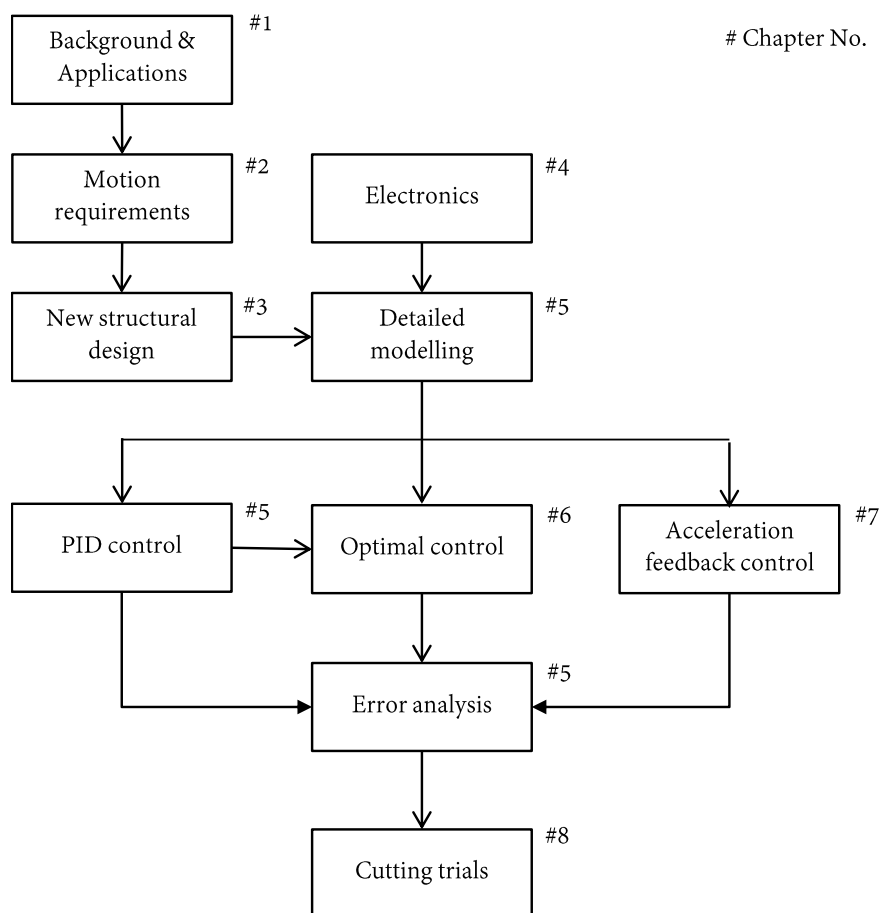


Figure 1-5: Flowchart of the thesis structure

Firstly, the applications of freeform surfaces are summarised and the state-of-the-art machining techniques for freeform surfaces are reviewed in Chapter 2. The current active control method and feedback control algorithms used in precision machine tools are also reviewed. Through this process, the requirements on the machine tool positioning performance and the control algorithm are identified.

In Chapter 3, a novel machine tool positioning concept is proposed for high-speed machining, which features with stiff-loop support and concise dynamic structure. A positioning system prototype is built according to this concept. The detailed design considerations and analysis are presented in this chapter.

In Chapter 4, digital controller and power amplifier boards are designed and built to drive the closed-loop positioning system. The signal chains in the electronics are modelled in details. The time delays and error sources are discussed as well. The finished controller is then tested to verify the design approach. The time delays and errors are used to better model the system performance under closed-loop control.

In Chapter 5, a systematic error-analysis approach is proposed and verified. The mechanical setup and the control electronics are used in the closed-loop position control. Mathematical model is compared against the measured response data of the prototype to ensure accurate modelling. The differences between closed-loop following error and real tool positioning error are identified and the frequency-domain synthesis approach is proposed for characterisation of both errors. Then a series of closed-loop positioning tests are carried out to verify this approach.

In Chapter 6, optimal control theory is applied to optimise the control action. The designed control algorithm is deployed in the developed controller and tested in the closed-loop. The performances are compared with the PID control method. The optimal control algorithm has minimised the positioning errors under the current conditions from the control point of view. Further improvement requires the modification of mechanical parameters. Thus, the influences of the mechanical parameters such as the moving mass, damping and stiffness are quantitatively analysed.

Chapter 7 addresses the low dynamic stiffness issues of fast tool positioning system by additional acceleration feedback. A dynamic stiffness model of the system with acceleration feedback loop is established. The effects of the low-pass characteristics

in the acceleration loop are discussed. The error contribution of the acceleration sensor is analysed and experimentally verified. The dynamic stiffness is tested through both frequency response test and intermittent diamond turning. The results are compared with the estimation from the model.

In Chapter 8, the developed cutting system is used to cut some typical freeform surfaces to verify the performance of developed system. Before the cutting experiment, the geometrical errors of the work spindle are measured and ready for compensation with the fast positioning system. The machined surface roughness is evaluated. Arbitrary image forms are also machined to demonstrate the flexibility of the system.

Lastly, the conclusions are drawn in Chapter 9 and the opportunities for future improvements are discussed.

# CHAPTER 2

## Literature review

### **2.1 State-of-the-art freeform machining techniques**

The complexity of the freeform optics design poses significant manufacturing challenges to current machining technologies. A variety of machining approaches have been developed for different kinds of surface shapes. Each approach features with a designated tool. The size of the tool is selected according to the curvature of the freeform shape and the softness of the tool is closely related to the amount of material to be removed and the hardness of the material [27].

Large scale and relatively flat freeform parts, such as telescope mirrors, are often machined by precision grinding process [28], [29]. Ultra-precision polishing are often used as the last step for freeform machining. New approaches adopt magnetically sensitive fluids to control the viscosity of the abrasive fluid [30]. Very smooth surfaces surface with roughness of 1-2 angstroms can be manufactured in this way [31], [32]. Since the whole process is controlled via the contacting time, the machine tool positioning accuracy is not as critical as in other precision machining processes. The above methods work well for hard or brittle materials. However, they are not good at machining soft metals. Diamond turning is a widely adopted approach to cut super smooth freeform on soft and nonferrous materials, such as contact lens [33], [34]. The diamond tool with a certain radius is controlled to follow a defined trajectory and the contour formed by the cutting edge is the same as the formed part shape.

Currently, Slow Tool Servo (STS) and Fast Tool Servo (FTS) are two major diamond turning techniques for freeform machining [35]–[37]. In STS, the diamond tool is moved by the machine slide in synchronise with the rotation of the spindle. The STS method can machine parts with large deviations in the scale of millimetres. However, it has low machining efficiency with a long cycle time, as the machine can only be operated at a motional frequency lower than 5 Hz [38]. FTS uses piezo or voice

coil motors to actuate the diamond tool with high control bandwidth. Nowadays, very high frequency motion, up to 20 kHz, has been achieved by FTS technique [39]–[41].

In most cases, single diamond cutters with precisely controlled shape are used to cut those small features. For parts that are rotary symmetric such as diffractive Fresnel lens in Figure 2-1 a) and b), turning with a sharp tool is a solution [42]. Different from common diamond turning practices, the sharp diamond tool is rarely used in the contouring mode. This is because the tool radius is so small that the feed rate must be selected unpractically slow in order to get optical grade surface roughness. Instead, the sharp tool is directly used as a mould and the sharp corner is copied to the workpiece. In this way, the surface roughness is only depended on the geometry of the cutting edge.

When the shape of the structure is not rotatory-symmetric, more motion freedoms are required for the tool positioning system and special devices and processes have to be developed. Huang et al. has designed a rotary tool approach to machine Fresnel lens structure onto a roller as shown in Figure 2-1 c) [43]–[45].

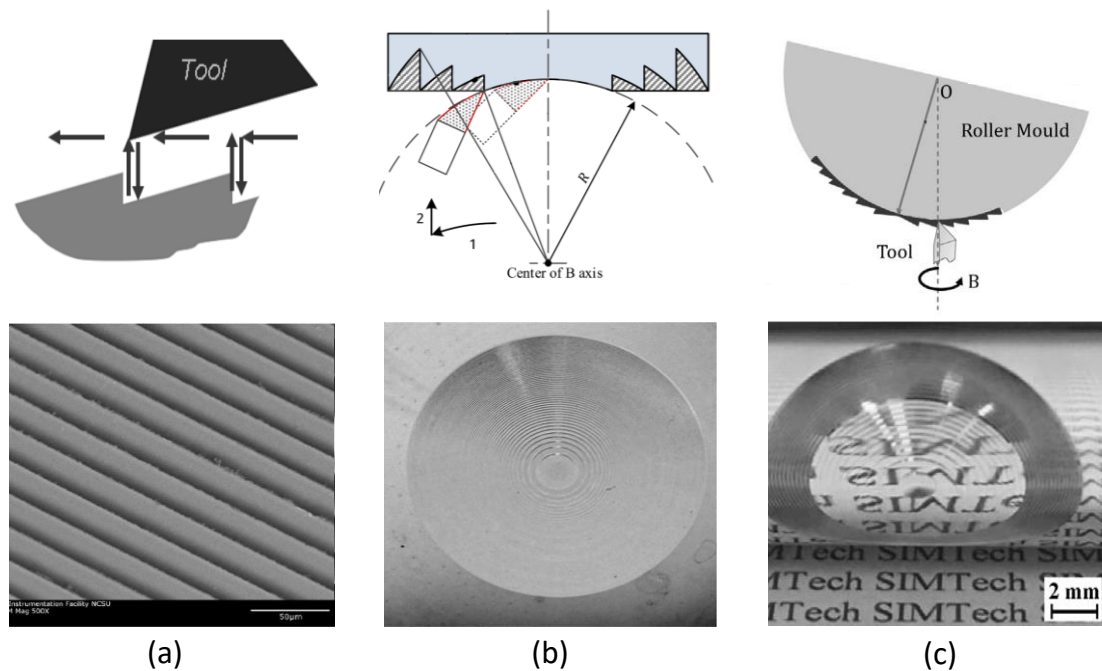


Figure 2-1: Different techniques to machine Fresnel lens on various surfaces [43]–[45]

Takeuchi et al. fabricated a multiple-focus Fresnel lens by non-rotational diamond cutting tool on a 5-axis machine [46]. The cutting trajectory is quite complex and the

cutting speed is low. However, this structure is very difficult to machine by other means. Brinksmeier et al. developed a new Diamond Micro Chiseling (DMC) approach to fabricate discontinuous microstructure array in [47]–[49] and [50], [51]. A diamond sharp tool is used to cut the substrate from different directions and the intersection of each cut will separate the materials from the substrate. Micro cube-corner retroreflector array has been manufactured in this way.

Huang et al. have generated grayscale micro images on metal surfaces by changing the depth of pyramid structures [52]. This is done on a 5-axis machine. To et al. proposed the Virtual Spindle based Tool Servo (VSTS) concept to generate discontinued micro structure array [53]. In this method, the relative rotation axis of the workpiece is programmed to be coaxial with the microstructure cell. Then each structure cell is turned one by one.

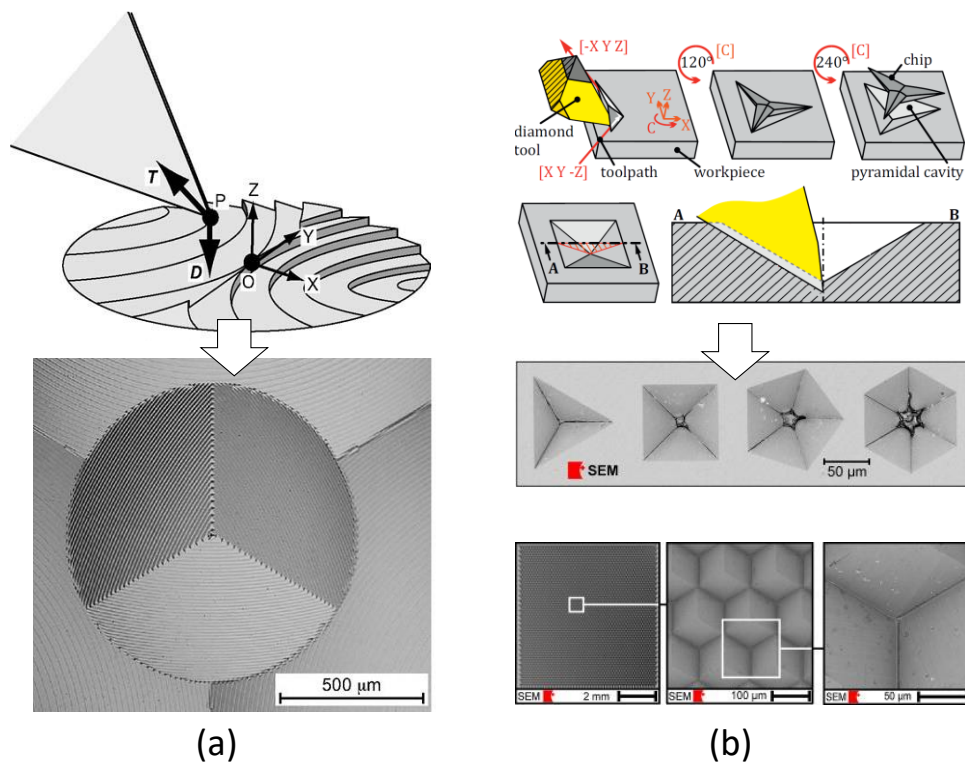


Figure 2-2: Micro structuring techniques by Takeuchi and Brinksmeier [46]–[49]



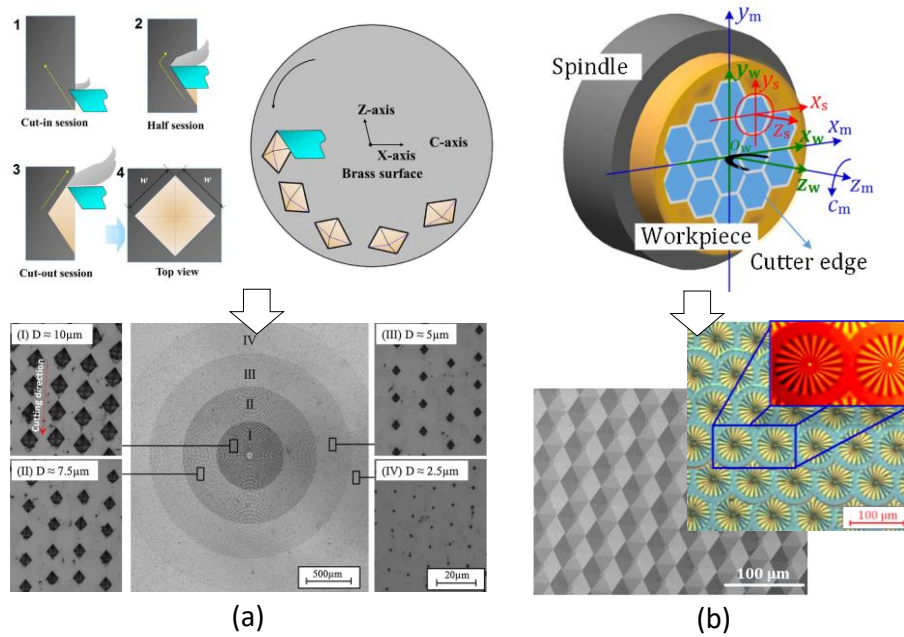


Figure 2-3: Micro structuring techniques by Huang and To [52], [53]

Most of the multi-axis machining techniques rely on the machine tools to provide the required motion degree of freedoms. The sudden stop of the tool path at the corners is very difficult to achieve for commercial machine tools. Therefore, the machining efficiency is very slow.

As shown in Figure 2-4, different machining techniques cover different spatial feature sizes of the freeform parts. As the feature shapes become more and more complicated, the machining setup turns more complex as well. The achievable surface roughness varies from subnanometres to tens of nanometres, as shown in Table 2-1. The form errors of the machined freeform surface depend on lots of factors such as shape, feature depth, rotation speed and diameter of the workpiece etc. It is very difficult to compare different techniques based on the form error value. Motion bandwidth is an alternative indicator of how the positioning system performs at high speeds. The motion frequencies of current techniques are listed in Table 2-1.

From Table 2-1 it can be seen that fast tool servo method is the only way to achieve very high repetitive motion speed. But the resulted surface roughness is usually poorer than the simple diamond turning or slow tool servo method. So it is worthwhile to study how to achieve less than 3 nm surface roughness with fast tool servo method without reducing the motion speed.

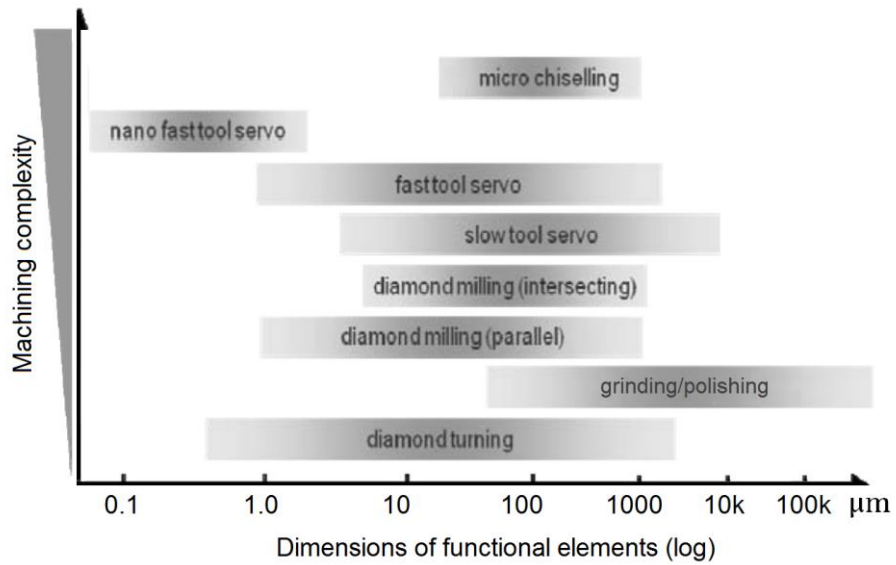


Figure 2-4: Machining complexity of freeform surfaces with different functional dimensions [54]

Table 2-1: Overview of technologies to fabricate freeform and micro-structured surfaces

Method	Surface roughness	Limitations	Motion frequency	Ref
Diamond Turning	< 3 nm	Limited to symmetrical parts	Near zero Hz	[55]
Slow Tool Servo (STS)	< 5 nm	Low efficiency	< 5 Hz	[36], [56]
Fast Tool Servo (FTS)	< 10 nm	Poorer surface roughness	100 Hz – 20 kHz	[57], [58]
Diamond Milling	~ 10 nm	Long machining time & poorer surface	< 2 Hz	[59]
Fly cutting	< 10 nm	For prisms and pyramids	Near zero Hz	[60]
Ultra-precision grinding	< 5 nm	Not suitable as a micro-structuring technique	< 5 Hz	[61]
Polishing	< 1 nm	Limited form accuracy in freeform parts & slow	Near zero Hz	[31], [32]
Micro chiselling/Multi-axis cutting	< 10 nm	Long machining time	< 5 Hz	[51]

## 2.2 Positioning system design and active control

Based on the above review, the precise and fast position control of the tool is a common requirement in various freeform machining techniques. The tool positioning accuracy directly affects the resulted part shapes and the surface quality. The position of the tool in the three-dimensional space is constrained by both passive and active elements in machine tools. Passive elements like bearings are used to limit the motion freedoms to several desired directions and then active elements are used to control the tool motion in those directions [62].

### 2.2.1 Fast tool servo designs

One common way to generate force is the interaction between magnetic fields or current carrying windings. Lorentz force actuator and reluctance actuators are two kinds of actuators used in the positioning systems, as shown in Figure 2-5 a) and c). A hybrid principle of reluctance and magnetic forces has obtained more and more attention recently due to its high energy density [63]–[65].

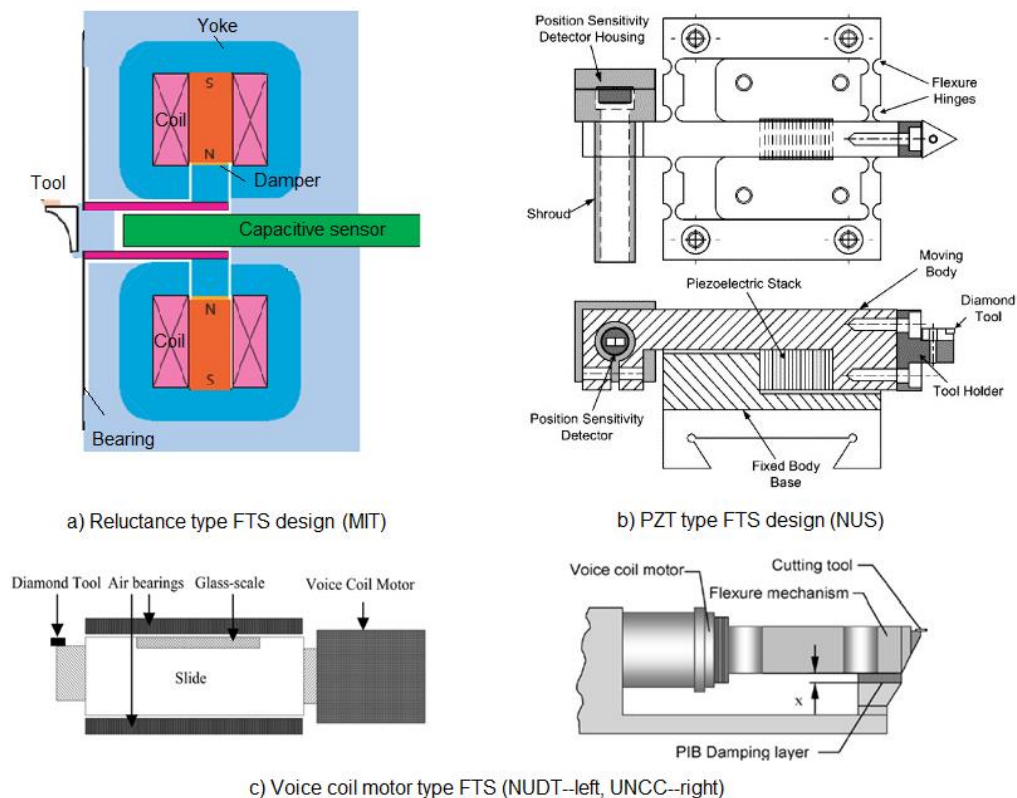


Figure 2-5: Different designs and working principles of FTS [58], [66], [39]

The other ways to generate controlled force or displacement is through the change of material properties under controlled physical fields. Piezo ceramic materials like PZT, whose strain changes under different electrical fields, can be used to locate a tool, as shown in Figure 2-5 b). Those active elements are the essential components in the fast positioning system in a machine tool. PZT-based FTS devices can achieve  $> 1\text{kHz}$  bandwidth but the motion stroke is very limited [67]. PZT actuators also suffer from heating problems during high speed motions [34]. The achieved bandwidth and stroke combinations in the literatures are:  $6.5\ \mu\text{m}$  stroke at  $70\ \text{Hz}$  bandwidth by Kouno [68],  $2.5\ \mu\text{m}$  at  $660\ \text{Hz}$  bandwidth by Patterson [69],  $3.7\ \mu\text{m}$  at  $2\ \text{kHz}$  by Hara [70],  $5\ \mu\text{m}$  at  $1\ \text{kHz}$  by Faulter and Dow [71]. Long-stroke FTS devices ( $> 1\text{mm}$  stroke) are often designed with Lorentz type actuators. Lorentz-based FTS devices are more difficult to achieve  $> 1\ \text{kHz}$  bandwidth. This is because it is open-loop unstable [72] and the position loop bandwidth is limited by the current loop bandwidth.

The accuracy of a positioning system is mostly determined by the metrology reference. The designs in Figure 2-5 a) and c) share the same configuration where the position is measured relative to the FTS frame. This is required by the working principle of the motor and the feedback sensor. The motion of the tool is guided either by flexure structure or air bearings. The design in Figure 2-5 b) adopted a new optical sensor and it has been used to establish an absolute reference to correct the straightness error of other slides. However, the performance is limited by the sensor accuracy [66]. The surface roughness is hardly improved. The metrology frame concept has been adopted in several high-end precision machine tools, like the Large Optics Diamond Turning Machine (LODTM) and the Precision Optical Grinder and Lathe (POGAL) by LLNL [73], Off Axis Generating Machine (OAGM) by Cranfield [74]. The POGAL machine is designed with vertical feed slide, which reduced the length of the structure loop. The metrology frame concept is vital for ultra-precision positioning system. However, it has not been adopted in fast tool servo applications due to structural limitations.

### **2.2.2 Active bearing designs**

Active bearings are bearings whose clearance can be actively controlled. They can also be used to generate small tool motions for cutting purpose [75]. Some researchers

put active elements into the bearing in hope to achieve infinite stiffness and micro motions [62]. The principle of the active bearing is shown in Figure 2-6. Actuator elements are integrated between the bearing and the moving table. Several sensors are used to measure the orientation and position of the table and the deviation errors are fed back to a controller. Then the actuators try to correct this deviation and running accuracy as good as the metrology reference can be achieved.

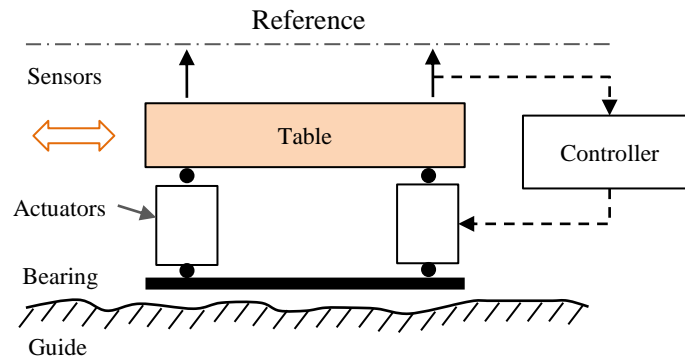


Figure 2-6: Actively controlled bearing for straightness correction

Shimokohbe et al. directly inserted PZT actuators between the air bearing pad and the table. The length change of the elements are equal to table movement [76]–[78]. Lee et al. from South Korea used three PZT actuators and capacitive sensors to compensate for the three-DoF errors of a linear slide and found the method can reduce the geometric errors by more than 90% [79]. Al-Bender et al. adopted a different idea where the PZT elements are used to change the shape of an air-bearing pad. The change of air film shape will affect the pressure distribution within the bearing and thus the floating height can be controlled [80], [81]. This method can achieve larger correction range than the pure PZT method but with more complexity in the feedback loop of the controller. Mizumoto et al. invented an active inherent restrictor (AIR) which is made of PZT material. A small through hole is made in PZT actuator and one end of the actuator functions as an orifice. He has applied this concept in controlling the rotary motions of a spindle [82].

Another idea of controlling the bearing height is to change the preload of the air bearings. Ro et al. designed a variable magnetic preload method by changing the current in an electrical magnet and used it in an air-bearing slide [83]. In this way, the bearing height has been successfully controlled. Slocum et al. from MIT designed a

self-compensation hydrostatic fluid bearing structure to achieve high bearing stiffness [84], [85]. In this fluidic bearing, the gap change caused by larger load forces will change the shape of the fluid passages and then the pressure distributions in the pressured pockets are automatically increased. It can be viewed as a pure analogue version of the active bearing structure with zero reference input and no input energy.

It can be seen that the active bearing technology has been found effective in reducing the geometric errors or increasing the stiffness of the bearing. This concept can also be applied to fast tool servo designs to get better accuracy. The remaining issue is the increased costs of the additional sensors, actuators and controllers. The complexity of the compensating structures also deferred the wide applications of this approach. What's more, whether the active control loop really can compensate for the errors perfectly remains a question.

### **2.2.3 Active damping designs**

The dynamic stiffness is also reflected in the damping of the machine tool. In some applications, more damping is desired to dissipate vibration energies. The damping effects can be achieved by eddy current dampers. Zhang et al. designed a two dimensional eddy current damper for planar motion system [86]. Sze et al. designed a novel damper structure for rotary motions which minimised drag forces along the rotation direction and tested its damping performance [87]. Tan et al. used eddy current braking mechanism to improve the performance of air bearing stage [88]. Other adaptations of eddy current damping in motion systems can be found in [89], [90].

The maximum amount of damping is limited by the strength of the magnetic field and the size of the conductor. In case where more damping effects are required, active power input is necessary. The induced Electromagnetic Force (EMF) are measured, amplified and then returned to the coil as a amplified current. This amplified current can generate more damping force to the stage, similar to a linear motor. In fact, the velocity loop in conventional positioning systems can be viewed as a damping loop and the velocity loop gain, or  $K_d$ , controls the amount of damping.

Although the above techniques deal with different aspects of precision systems, they share one common thing, which is to correct the disturbances by active sensing

and actuating beyond the capabilities of passive elements. The key thing for achieving good performance is to establish a perfect reference and then the position of the end effector should be measured directly against this reference. Even by doing this, the influences of external disturbances on the tool position may not be compensated completely, which deserves further investigations.

## **2.3 Error analysis of positioning systems**

Dynamic errors are the tool positioning errors caused by all kinds of disturbances. Zaeh et al. established a simulation model by finite element method to study the tool-workpiece deviations including disturbance variables [91], and successfully predicted the step response of a feed drive device. Bordatchev et al. used similar approach to study the dynamic behaviours of a machine spindle-bearing system [92]. However, the model is based on time domain analysis and it cannot predict the influences of random disturbances. The random errors can be described by the variance of the signals and there exists a mathematical relationship between the signal variance and the frequency domain [93]. Leon has proposed the Dynamic Error Budgeting (DEB) method based on this frequency domain approach and applied it in the design of a rotary platform with active bearings [94]. Sun et al. also proposed a dynamic error budget approach but it is quite different from the DEB method in that it is focused on spatial frequency errors [95]. Andolfatto et al. measured the errors at the tool tip during high acceleration motions and found that the evolution of the RMS errors with respect to the programmed feed rate can be approximated by a logarithmic law [96]. The quasi-static positioning errors of a multi-axis machine tool can be predicted by geometric configuration of the machine tool [96], [97]. The arrangement of the axes can be described mathematically by homogeneous transform matrix [98].

## **2.4 Feedback control strategies**

### **2.4.1 Position feedback control**

Besides the sensor and the actuator, the control algorithm is the third key part in the actively controlled loop. In the paper by M. Iwasaki [99], he surveyed the state of art

precision motion control techniques in the current publications. The two Degree of Freedom (DoF) framework is a very good summary of all the control structures, as shown in Figure 2-7. The two DoFs refer to the feedback loop and the feedforward path. The ideal feedforward path is an inverse of the feedback system dynamics. In precision motion control scenario, more than 95 percent of control actions come from the feedforward path, according to ASML.

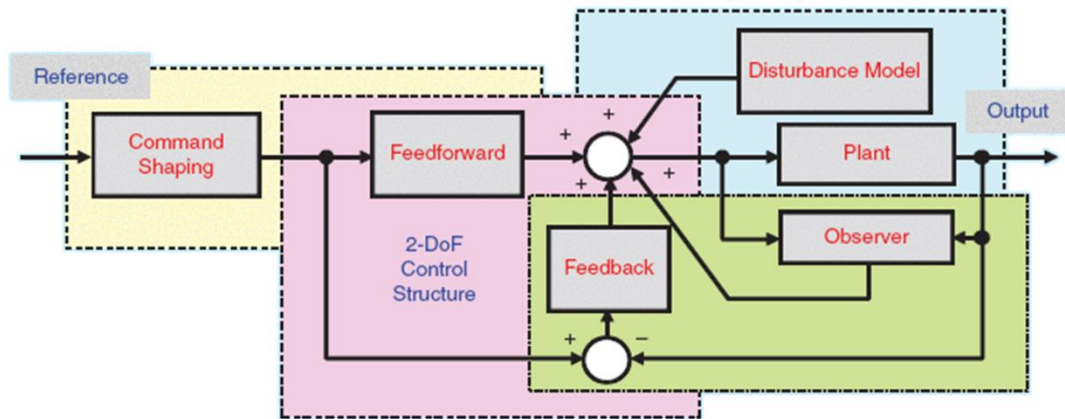


Figure 2-7: Two degree of freedom framework for positioning control [99]

Command shaping technique is one kind of feedforward method and can be found in applications where there exists significant flexible link between the actuator and the end effector. Observers are mostly used in robots with modern state space control. The observer outputs are better estimations of the disturbances and then they are used to generate control output.

In commercial motion controllers, assumptions are made that the system to be controlled can be approximated by a second-order inertia system. The feedback algorithm is thus simplified to PID structure plus a series of notch filters and the feedforward control is designed as velocity and acceleration feedforward gains. Model based disturbance feedforward is not common in commercial controllers.

It will be ideal to use modern control theories, such as state space [100] and optimal control [94], to analyse these errors and optimize control parameters. However, these control theories have seldom been used in fast positioning applications because of the unacceptable computation delay for complex models, which is not acceptable for high rate servo loops. It is therefore necessary to reduce the order of the system model either by approximation of FE model [101] or design a simpler structure.



### 2.4.2 Acceleration feedback control

Additional feedback sensors can be used to improve the closed-loop performance, one of which is the acceleration sensor. The idea of using acceleration information to enhance dynamic performance is first proposed by Hori [102] and Lorentz [103], [104]. According to control theories, an optimal control algorithm requires the full information of position, velocity and acceleration of every moving body instantaneously. When only displacement sensor is used as the feedback source, other information has to be derived from the encoder by numerical differentiation, with significant quantization noise [105]. Direct measurement of the acceleration signal averts this problem and it can also be used to correct the quantization noise of the velocity signal as estimated from the encoder [106].

The major purpose of acceleration feedback control is to improve the disturbance rejection ability of the controlled loop. Hori and Lorentz both observed enhanced stiffness in speed control motors. Wittmann et al. present a hybrid current and acceleration control which is equivalent to a disturbance observer and discussed the noise sensitivity and load sensitivity [107]. Tian et al. extended the acceleration control concept to a magnetic levitation system and showed that the sinusoidal disturbance is attenuated [108]. Different arrangement of the current loop and acceleration loop has been tested and compared with cascaded PI controller by Griese and Maas [109]. Dumanli et al. fused the acceleration and encoder signals by kinematic state observer to estimate the acceleration and jerk and then a full state feedback is realised. He has observed enhanced stiffness at the anti-resonant and resonant frequencies but didn't pay attention to the stiffness at other frequency ranges [110]. Katsura et al. proposed the PAIDO idea in [111], where the authors use the displacement and acceleration signals to compose the disturbance observer in a way similar to a complimentary filter. Although the major purpose of adopting acceleration feedback is to reduce the errors caused by forces, it is also proved to be helpful in suppressing crosstalk from other slides in lithography machines [112].

There are also other ways to incorporate acceleration signal in control loops. Acceleration signal is used to actively suppress structural chatter vibration [113], [114].

Abir et al. used the acceleration signal to estimate the machine tool frame vibration and tried to compensate for it in the controller [115], [116].

Despite the proved system resistance to disturbances with acceleration feedback, it has not been widely adopted in cutting systems. For one reason, the additional sensor and conditioning electronics will raise the cost. Another very importance reason is that in many cases the enhanced dynamics stiffness can also be achieved by simply designing the slide with a larger inertia. However, a large inertia is not applicable for fast tool servo applications because that will require huge amount of motor force to drive the stage at high frequencies.

Nowadays the performance of acceleration sensors has been dramatically improved and is promising to broaden their applications in precision field. Pritschow et al. has even developed a new sensor based on Ferraris principle, which can measure the relative acceleration rather than the absolute acceleration [117]. Previous studies have been focusing on the variations of controller structures and the estimation of acceleration. Few have pointed out how the stiffness changes over the whole frequency range regards to the sensor bandwidth. In addition, the error caused by the additional feedback sensor noise is another important factor to be considered in ultra-precision positioning application. This topic has not been discussed in the literature yet.

## **2.5 Summary**

In this chapter, the current machining configurations for freeform surfaces and the associated position control technologies are reviewed. The complexity of those freeform shapes requires the machine tool slides to move at fast speed and even sudden change of directions. This is very challenging especially when the error is required to be small for good surface finish. The mechanical parameters, such like moving mass and damping coefficients, change a lot depends on the application. This added to the difficulties of the controller tuning and establishing of a deterministic design approach.

In order to accurately control the tool position along all degree of freedoms under high dynamics, various active control structures has been proposed by researchers. The active control method can also be used to improve the stiffness and correct geometric errors of the machine tool. Those active structures all feature with various sensors and

actuators. Among them, the structure with direct measurement of tool position and direct force actuating on the tool is pursued, which is not easy to achieve with off-the-shelf parts.

The control algorithms used the current machine tools are mostly PID structure, which is based on a very simple system model. The system dynamics are more complex in practice. Model-based controlling algorithms together with multi-sensor feedback are theoretically capable of improving the system performance but they are not adopted in ultra-precision scenarios due to hardware limitations and uncertainty caused by the new sensors.

# CHAPTER 3

## A novel-concept stiff-support positioning system design and its prototyping

### **3.1 Introduction**

In this chapter, a new design of fast positioning system, which reduces the structural loop compliances by incorporating a metrology frame and a stiff force loop, is proposed for high-speed ultra-precision machining.

Firstly, the basic concepts in precision machinery design are introduced. Different machine tool configurations are compared and their pros and cons are discussed. Variations of turning machine configurations are studied which finally lead to the design of a new stiff-support structure.

Then a fast positioning stage is designed based on this concept. The detailed design and calculation of the flexure bearing, magnet track and the motor coil parameters are carried out. The influences of several key design parameters are analysed by Finite Element Analysis (FEA) simulation.

Finally, the parts are built and a prototype of the positioning system is assembled. This prototype will form the testing platform for the subsequent study.

### **3.2 Basic concepts in precision machine tool design**

#### **3.2.1 Dynamic errors and machining accuracy**

The cutting process is a combination of interactions among the cutting tool, the work-piece and the machine tool. Therefore, many factors can contribute to the finished part errors. These factors can be grouped into three groups. The machined part dimensions depend on how accurate the cutting tool is positioned relative to the part, shape of the cutting tool where cutting occurs and how materials are removed by the

tool. This corresponds to three major research topics in the mechanical manufacturing area as shown in Figure 3-1. The first factor is determined by the performance of the machine tool and the last two factors correspond to tooling and cutting mechanism study.

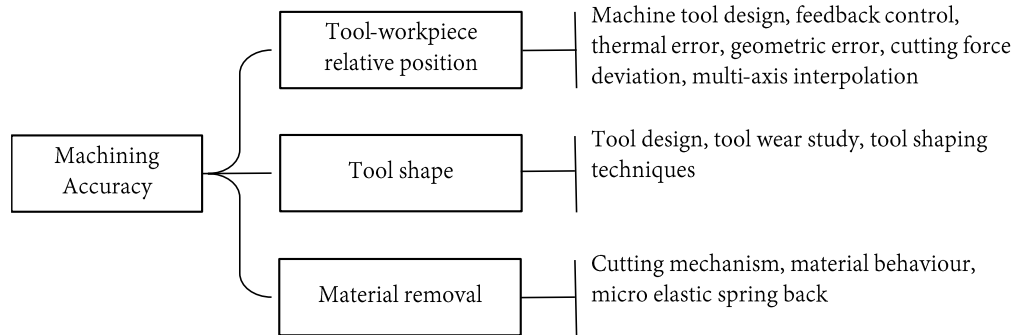


Figure 3-1: Influencing factors for machining accuracy and corresponding research topics

Cutting tools made from diamond are widely used in ultra-precision manufacturing. The diamond material is super hard and thus the cutter shape and edge sharpness can maintain stable for a long cutting distance when cutting some non-ferrous materials. The shape of the cutter, either a round profile or straight profile, can be accurately described to tens of nanometres level [118]–[121].

When the precision cutter is engaged into the workpiece substrate following a commanded trajectory, the materials are removed from the workpiece. However, not all the materials in the path are removed. Because the cutting occurs within a small area with high pressure, the material under the cutter deforms both elastically and plastically. The plastically deformed materials flow to the side of the cutter and will not flow back. This phenomenon is called plastic side flow and is more obvious in cutting of soft materials [122],[123], [124]. The side flow phenomenon severely affects the form accuracy of micro structured surfaces [125], [126].

The tool-workpiece positioning errors can influence the size, shape and surface roughness of the machined parts, depending on the spectrum of the errors. Normally these errors can be classified into two groups: static errors and dynamic errors. Here it is preferred to catalogue the error sources into geometric ones when no force is exerted and the dynamic ones in response to all the dynamic disturbances like cutting

forces, even at zero Hertz. Geometrical errors mainly depend on the geometry of individual machine component, relative position of each component and the temperature distribution. Dynamic error is the frequency response of the machine structure under both internal and external excitations, which may come from cutting forces, gravity, environmental vibration, inertial force (spindle unbalance), ripple forces from motor, hydraulic force from coolant, bending of cables, friction of covers, turbulences of fluids for hydrostatic/aerostatic bearings et al. It should be pointed out that the structure dynamic characteristics are highly dependent on geometric interaction of the bearing parts, e.g. clearance of aerostatic bearings. The tool positioning error is the major source of machining inaccuracy. Therefore, the focus of this thesis is placed on the control of tool position.

### **3.2.2 Structural loop stiffness**

Structural loop stiffness indicates the amount of tool position deviation relative to the workpiece under a certain cutting force. In multi-axis machine tools, the motion of each axis is guided by linear or rotary bearings to constrain the movement only to the desired direction. However, these bearings are not infinitely stiff along other directions and these compliances constitute the basis of the structural loop stiffness of the machine tool.

The positioning stiffness along the movement direction of each axis is finite and this is called the servo stiffness. It is determined by the response of the closed-loop system to cutting forces, which involves both the mechanical parts and the active control action. This will be discussed later in this thesis. There also exists some compliance in the frame structures. The combination of bearing stiffness, structural compliance and servo stiffness forms a flexible force loop from the cutting tool to the workpiece, as shown in Figure 3-2.

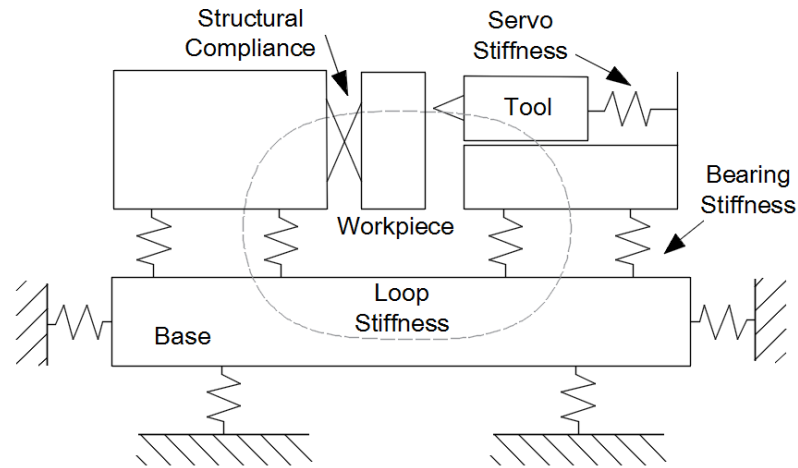


Figure 3-2: Illustration of structural loop stiffness

The importance of high structural loop stiffness varies from application to application. In non-contact machine tools such as optical measuring apparatus and laser machining machine tools, there exists no cutting force during the whole process. One typical example is the lithography machines used in semiconductor industry. Lithography machines require fast movement and sub-nanometre positioning stability. The major disturbances come from ground vibration and sensor noise. Therefore, the design emphasis is put on how to isolate the environmental disturbances and how to avoid sensor noise amplification rather than increasing the structural loop stiffness.

In contact cutting machine tools, such as turning, milling and grinding machines tools, there are additional disturbances resulting from the interaction between the tool and the workpiece. For some hard and brittle materials, the cutting force can be as high as several Newtons in diamond turning and the forces are even higher in grinding process. The high forces not only affect the surface quality of the machined parts, in some cases where the structural loop stiffness is not high enough, the cutting process might be unstable [127], [128]. In this case, the design should be focused on increasing the loop stiffness to counteract the force disturbances.

There is no clear boundary between a measuring apparatus and a machine tool in the ultra-precision research field. Usually, the metrology grade measuring devices are installed in temperature-controlled labs with vibration isolation measures to achieve minimum measuring uncertainty. In the ultra-precision machining field, machine tools are also located in well-controlled environments with extremely sensitive feedback sensors. The same numerical controlled motions are found in both measuring devices and machine tools. What's more, there is an increasing demand that the measuring devices to be integrated onto a machine tool so as the machining errors can be measured and compensated online without repositioning of the workpiece.

This integration brings some challenges to the designers because there are different design emphasises for measuring machines and machining machines. An increased loop gain helps achieve higher loop stiffness, but the sensor noise will also be amplified at the same time. Therefore, there should be a certain optimal trade-off for each application scenario depends on the relative strength of error sources. This will be discussed later in this thesis.

### **3.3 Machine tool configurations**

There are many possibilities to arrange the relative orientations of the motion axes in a multi-axis machine tool. For a turning machine tool, two common configurations are the cross-slides configuration and T-based configuration [129].

#### **3.3.1 Cross-slides configuration**

In the cross-slides configuration, the X and Z slides are stacked together. The X slide beam is fixed onto the machine base and a carriage block moves along it. The Z-axis beam slides through the X carriage block from the perpendicular direction. Therefore, the two-axis motions are realised [130]. In fast tool freeform machining, the FTS module is a special device that can move at fast speed and usually this tool module is mounted on the top slide, as shown in Figure 3-3.



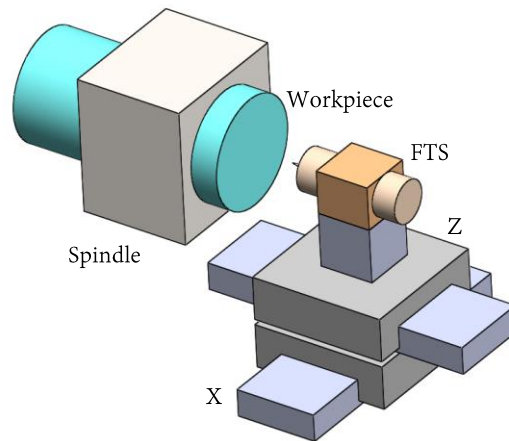


Figure 3-3: Cross-slides turning configuration with FTS

One example is shown in Figure 3-4 where the linear slides are of dovetail air-bearing type. In order to analyse the dynamic behaviours of this configuration, a multi-body dynamic model is established using the MATLAB Simscape Toolbox<sup>1</sup>. The bearing interfaces are represented by spherical joints and the moving bodies are simplified into single masses. A sweep sinusoidal driving force is exerted between the Z slide beam and the carriage block. The Z position feedback is recorded at the same time. The simulated frequency response plot and the vibration modes at different frequencies are shown in Figure 3-4 as well.

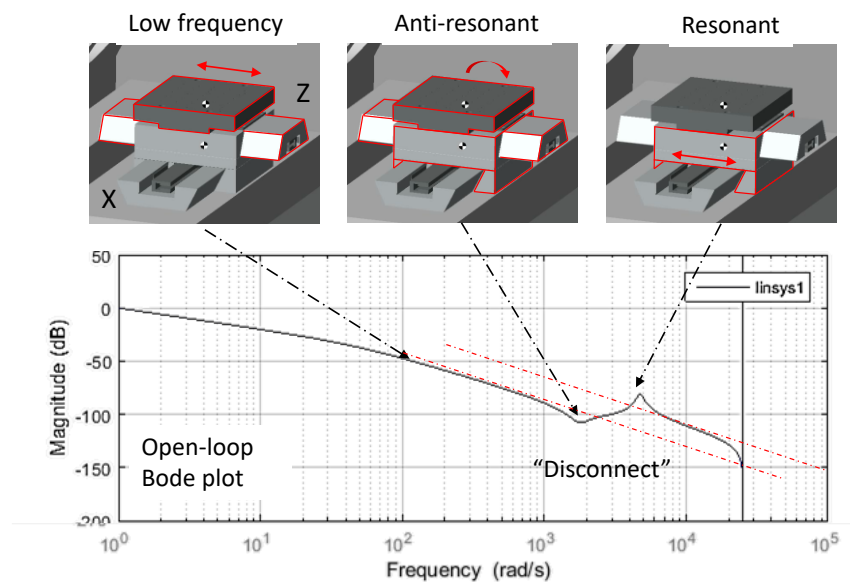


Figure 3-4: Z-axis frequency response of a cross-slides configuration

<sup>1</sup> Documents can be found at <https://uk.mathworks.com/products/simscape.html>.

It can be seen from this graph that the Bode plot curve possess an anti-resonant dip and a resonant tip. This is a typical response shape when the structural loop has some compliance. At the low frequency range, the Z slide beam alone moves back and forth as expected. At the anti-resonant frequency, the X carriage block and the Z beam start to vibrate in the angular direction together. Although they are vibrating, the change of the relative position between them is small and thus the frequency response curve shows a low value. When the frequency is increased to the resonant frequency, the carriage block vibrates horizontally while the Z slide beam hardly moves. The driving energies are mostly transported to the carriage block.

These dynamic behaviours influence the tool position accuracy and the controllability of the Z slide. The angular vibrations of the carriage block cause the tool deviate from the commanded position and this cannot be detected by the encoder at the motor position, thus the dynamic errors caused by angular bending will not be compensated by servo system. From the controller point of view, the open loop gain is increased after the resonant frequency. Virtually the effective moving mass is smaller beyond this point and it is called “mass disconnect”. The raised high frequency response tends to affect the gain margin of the closed-loop system and limit the maximum gains.

Another problem associated with the cross slides structure is that when the Z slide moves across the travel range, the centre of gravity of the moving mass changes. This introduces a varying torque onto the X slide bearing. The torque will cause some angular deviations of the tool. In addition, the closed-loop vibrations of the lower axis might be transferred to the upper axis. This phenomenon has been observed in many experiments.

Despite all the disadvantages mentioned above, the stacked configurations are used in many machine tools. The major reason is that it is difficult to avoid when the number of motion axis is large, or the space is constrained.

### **3.3.2 T-based configuration**

For diamond turning machine tools, there are only two linear axes. This makes it possible to avoid the cross slides structure, although this also means the spindle has to

be stacked onto one linear axis. Stacking a rotary motion onto a linear motion is easier than stacking two linear motions. Therefore, the T-based arrangement of X-axis and Z-axis has been widely adopted in ultra-precision machine tools [55]. Two typical T-based arrangements for a turning machine with FTS are shown in Figure 3-5.

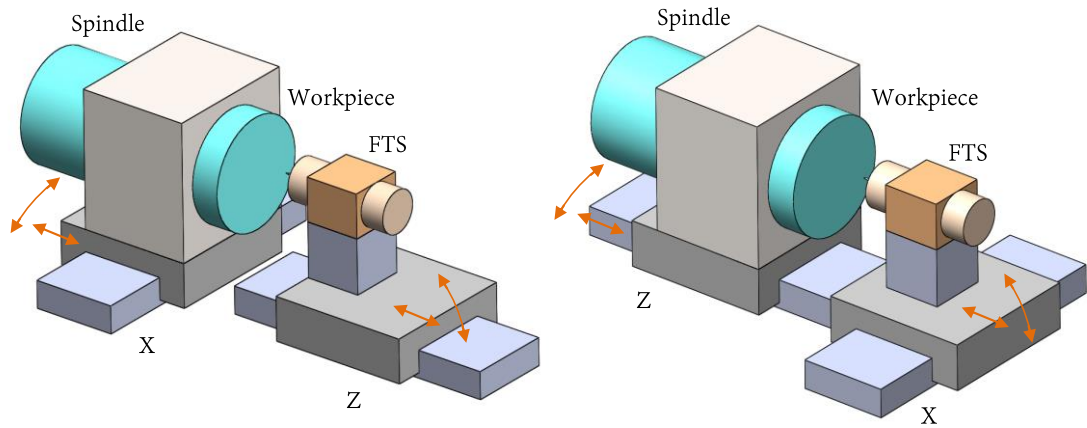


Figure 3-5: Typical T-based diamond turning machine with FTS

The T-based configuration avoided some of the problems of the cross-slides structure but the problems for the FTS module remain the same. In these cases, The FTS module is installed with a certain elevated height above the slides. Therefore, there exist at least one angular and one translational degree of freedoms, which are less stiff. Because of the finite stiffness of the underneath bearing or servo system, the base of the FTS module will vibrate during high frequency cutting.

The disturbances mainly come from two sources, one is the inertia force of the moving tool assembly, and the other is the cutting force. In most FTS systems, the first source is addressed by introducing an equal amount of mass moving in the opposite direction. This cancellation comes with either reduced motion bandwidth or doubled system cost. Nevertheless, the cutting force still poses a problem. What's more, the feedback sensor only measures the displacement of the tool in reference to the module base. The base vibration cannot be sensed by the control system.

The angular compliance problem can be circumvented by aligning the linear axes in such a way that the spindle centre line passes through the area formed by the bearing surfaces [131], [132]. Two such arrangements are shown in Figure 3-6. The X-axis is aligned in the vertical plane with two bearing rails at the top and the bottom of the base.

Independent metrology frames can be used to establish the dimensional linkage between the spindle position and the feed position.

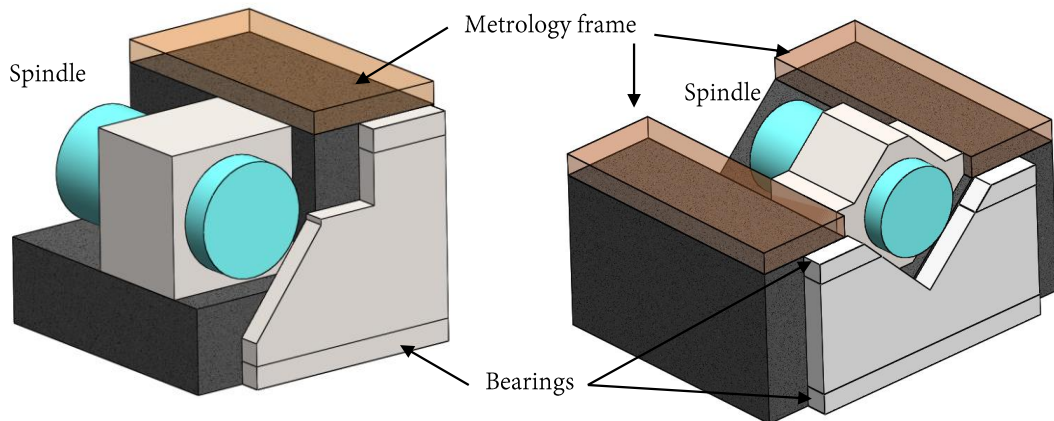


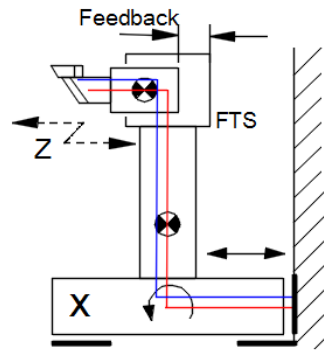
Figure 3-6: T-based turning machine configuration with minimum angular compliance

### 3.4 A novel stiff-support design

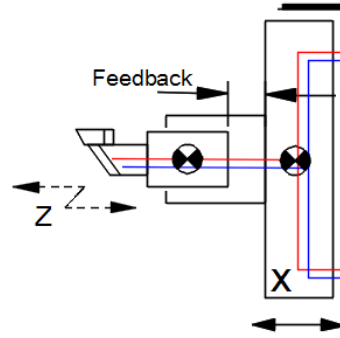
The metrology paths and the force paths for the above configurations are shown in Figure 3-7. It can be seen that in the conventional FTS configuration on T-based turning machine in Figure 3-7 a), the metrology and force paths go through all the bearing interfaces in the system. Any change of bearing clearance caused by force will affect the positioning accuracy of the tool. Especially a small angular motion will cause significant movement at the tool point. The minimum angular compliance design in Figure 3-7 b) partially solved this problem by eliminating the angular degree of freedom and only the translational compliance remains.

With the addition of the metrology frame close to the cutting tool, as shown in Figure 3-7 c), this error movement can be detected because it will cause linear motion error at the tool point. The force is still transmitted through all the bearing interfaces to the machine base. The excited vibration will be treated as disturbances to the control system. It is up to the motion controller to compensate for this error.

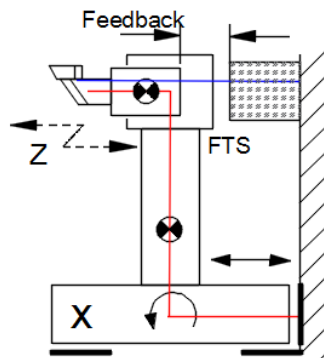
In this study, a new configuration is proposed, as shown in Figure 3-7 d). The inertial force and cutting force are directed to the fixed machine base. With no flexible modes prone to be excited by the forces, the requirement on balancing is greatly reduced. The dynamic characteristics are expected to be simpler, reducing potential modelling difficulties.



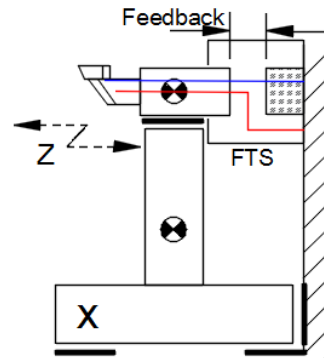
a) Conventional FTS



b) Minimum angular compliance design



c) FTS with metrology frame



d) Proposed stiff-support design

— Bearing    ▨ Reference    — Metrology loop    — Force path

Figure 3-7: Metrology paths and the force paths for different FTS configurations

This configuration is made feasible by the design of flat Lorentz actuator, as shown in Figure 3-8. Single-phase Flat Voice Coil Motor (FVCM) is extended along the X direction to release the motion degree of freedom, which is usually constrained in traditional voice coil motor design. Short-stroke high frequency motions are achieved in Z direction with flexure guidance. The flexure guidance is fixed on the carriage of the X guide slide. The motion along X direction is driven by a linear motor and guided by ball-bearing linear slide. A metrology straight edge is used as the position reference and a capacitive displacement sensor is measuring against it. The diamond cutter is fixed in the same line as the displacement sensor and the motor centre. In this way, the force pass through the gravity centre and the Abbey principle is obeyed, which is very important in reducing machine tool errors [133], [134]. The detailed assembly design of the motor and the bearing structure is shown in Figure 3-9.

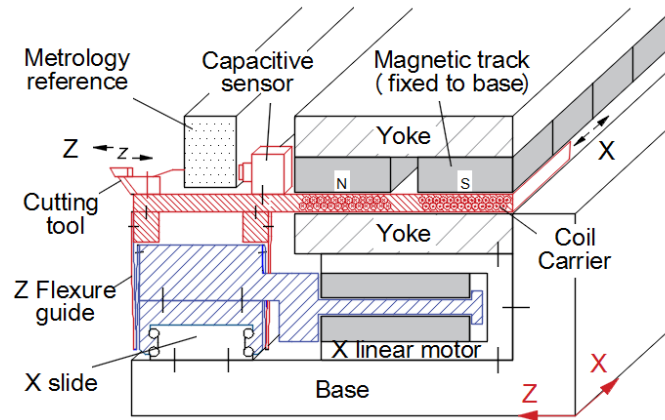


Figure 3-8: Stiff-support structural design (Parts in red move in the Z direction and parts in blue move in the X direction together with the red parts.)

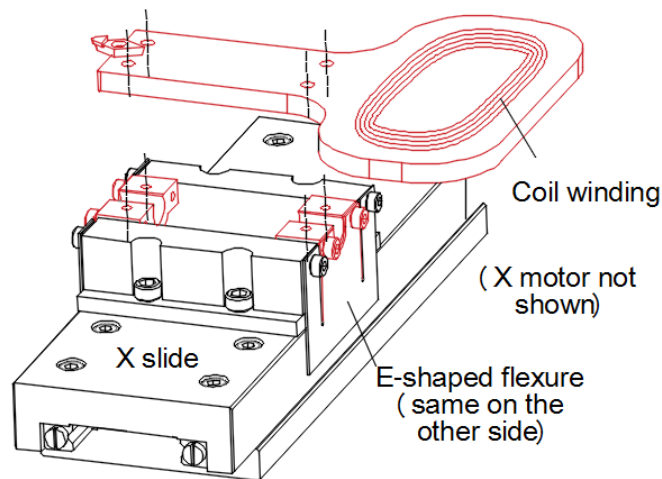


Figure 3-9: Detailed design of the flexures

Two machining setup with the designed device are shown in Figure 3-10 and Figure 3-11 for diamond turning and ruling respectively. In the diamond-turning configuration, the large range slow or inaccurate motion is provided by the spindle support. The small fast Z2 motion can be used to correct the other errors. The spindle is also supported in centre plane. In the ruling engine configuration, the workpiece is mounted on a vertical axis. The depth of the ruling cut can be accurately controlled and thus to machine various groove shapes and linear lens array structures. In both setup configurations, the designed module is fixed to the machine bed directly. The metrology frame connects the cutting tool and the workpiece and forms the shortest metrology loop.

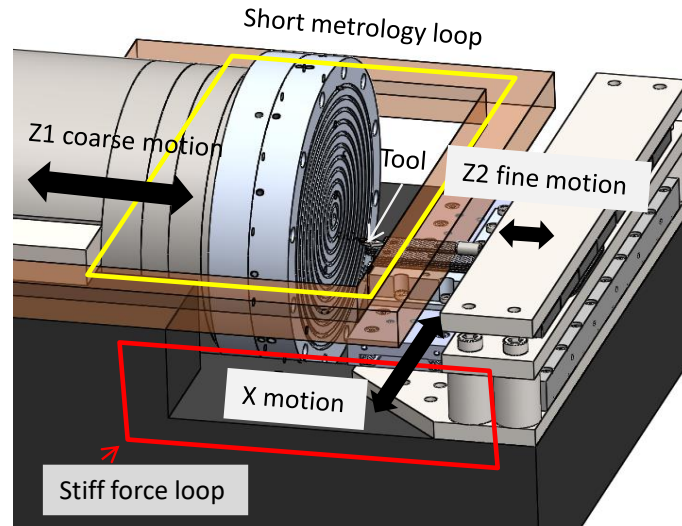


Figure 3-10: Diamond turning configuration with the proposed device

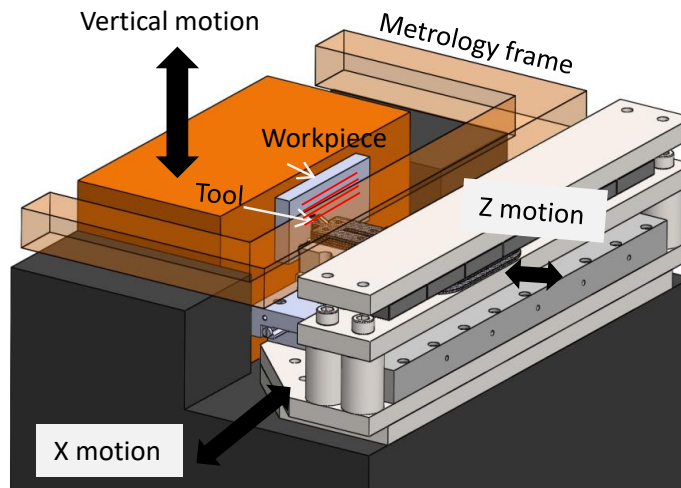


Figure 3-11: Precision ruling configuration with the proposed device

One of the significant advantages for this design is that the straightness and stiffness for the X linear slide is not important anymore. Conventional machine tool relies on the fluid bearing to provide the required precision. However, there are many factors can influence the slide precision, like the motor heat, fluid pressure change, fluid heat, turbulence or weight change on the slide. In the proposed design, the metrology frame is free from heat sources and forces. The other disturbances are firstly suppressed by the control action before affecting the tool position. This makes it possible to use low cost ball-bearing slides as the X-axis bearing and easy to achieve compact size. Furthermore, if there exists a kind of sensor can measure the relative position between the rotating chuck and the metrology frame in the turning setup, the spindle errors will



not be important any more. The fast motion bandwidth will be high enough to compensate for the spindle error motions. In addition, the stiff support design reduces the need for balancing the inertia force in FTS.

Three key components of this design are the coil and sensor assembly, the magnet track assembly and the flexure bearing. Next, the detailed design and calculation procedures will be presented.

### 3.4.1 Flexure bearing design and stiffness calculation

The parallel flexure bearing structure as shown in Figure 3-13 are used to support the moving tool and motor coil. The parallel structure ensures that the vertical movement is small when the parts are moving. A pair of E-shaped flexure hinge is cut from 0.5 mm-thick beryllium copper sheet. The stiffness of the bearings can be tuned by selecting the geometry and the dimensions of the shape.

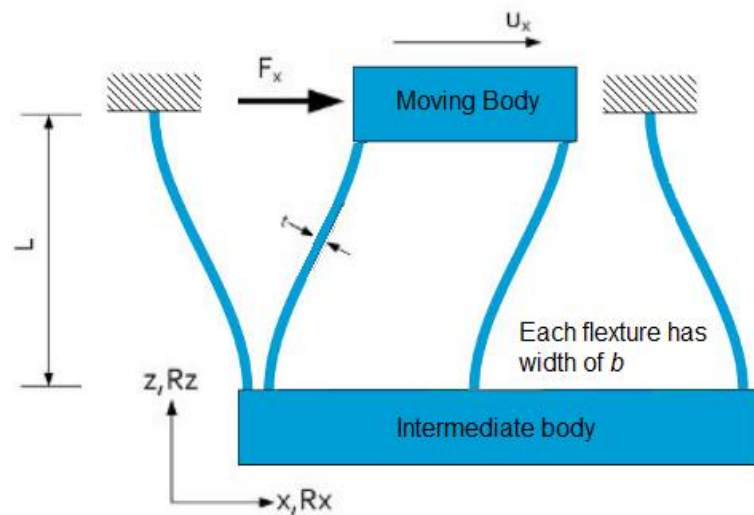


Figure 3-12: Double parallel leaf spring bearing

The effective length of the flexure leaf is  $L$  with thickness of  $t$  and the width of each leaf is denoted as  $b$ . Then the stiffness along the X direction can be calculated as<sup>2</sup> :

$$K_x = \frac{Ebt^3}{L^3} \quad (3-1)$$

<sup>2</sup> Detailed information from <https://www.janssenprecisionengineering.com/page/flexure-guiding-2-leaf-springs-in-parallel/>



Where:  $E$  is the elastic modulus of the material, 125 GPa for beryllium copper. The width  $b$  is selected as 20 mm (the centre column width is equal to the sum of the side columns) based on the space constraints. The effective length of the flexure is selected as 20 mm, and then the calculated stiffness is 37500 N/m.

A FEA model is established in Solidworks to analysis the stiffness of the designed bearing. The contacting surfaces are defined as bounded since a screw will be used to fasten them. A unit force along the Z direction was applied to the moving part and the resulted deformation is 0.02573 mm. The stiffness of the bearing structure is calculated as 38865 N/m.

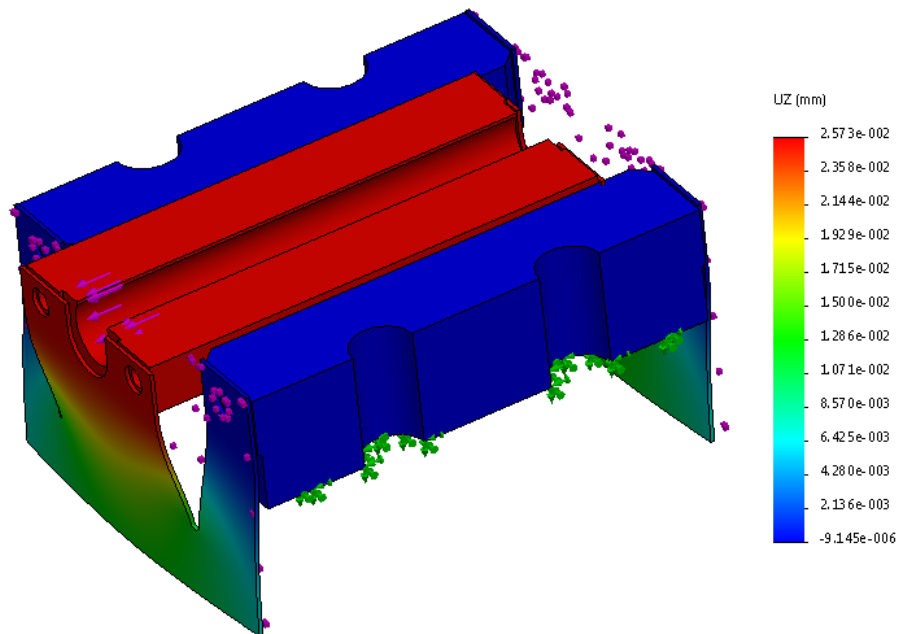


Figure 3-13: Deformation of the flexure hinge with unit force

### 3.4.2 Magnet track design and calculation

Fourteen magnets are bonded onto two steel bars to form the magnet track as shown in Figure 3-14. The magnet is selected of N52-grade NeFeB material, which is the highest strength permanent magnetic material on the market. The size of the magnets is selected as 40 mm × 20 mm × 10 mm, due to commercial availability. The steel yokes must be thick enough to reduce the magnetic reluctance. Here the thickness is selected as 12.5 mm. The majority of the loop magnetic reluctance is caused by the air gap and the magnets, which has similar permeability as air (relative permeability of 1.05). Therefore, the air gap distance between the magnets and the opposite steel bar

is the key parameter that determines the maximum magnetic field strength. The FEA model of the magnet track is established in ANSYS. A parallel boundary box of  $1\text{ m} \times 1\text{ m}$  size is defined and the magnetic lines are constrained in it. The size of the boundary box is large enough in order to simulate an infinite space condition. A parameterised 3-D model of the magnet track is built. The key parameters are changed to study how strong magnetic field can be achieved with the current setup.

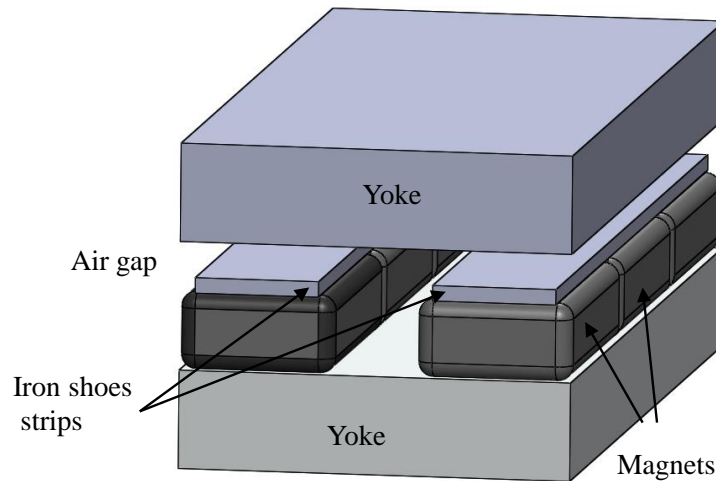


Figure 3-14: Diagram of the magnet track design

Firstly, the air gap distance is changed from 4 mm to 10 mm. The simulated magnetic field strengths are plotted in Figure 3-15. As expected, when the air gap is decreased, the average magnetic field strength is higher. A higher magnetic field is desired for high motor force with the same amount of motor current and coil windings. However, the reduced air gap limits the number of coil windings that can be inserted into the magnetic field. In addition, the coil assembly must be thick enough in order to be reasonably stiff. Based on these considerations, the air gap distance is selected to be 6.2 mm. the thickness of the coil assembly is designed to be 6 mm and 0.1 mm free play is left on each side ensuring no contact occurs between the two.

The commercial magnets are all made with fillets on their corners because the NeFeB material is brittle. However, the magnetic fields at those corners will not be uniform. When the motor coil moves in this field, the output motor force will change unexpectedly. In order to achieve a uniform magnetic field, two steel strips (iron shoe) are attached to the surface of the magnets. The high permeability of the steel material helps to smooth out the magnetic fields.

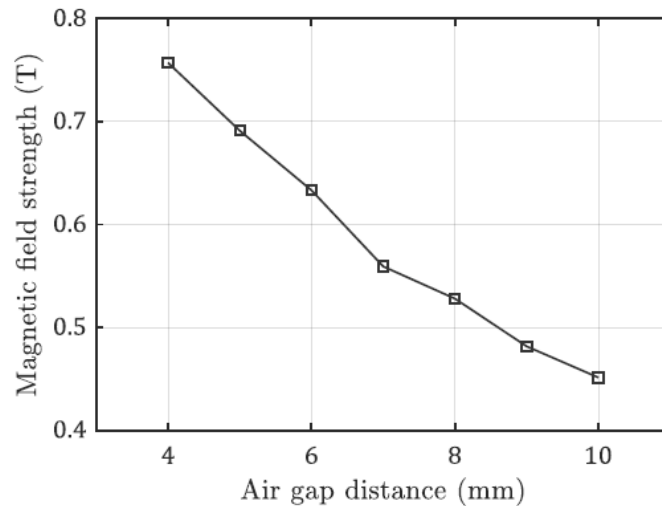


Figure 3-15: Average magnetic field strength changes with different air gap distances

The strip thickness is another key parameter that affects the field strength. A larger strip thickness has better averaging effects but the leaking magnetic field between the two strips will reduce the field strength in the air gap. The leaked flux lines in the air space are clearly visible in Figure 3-16.

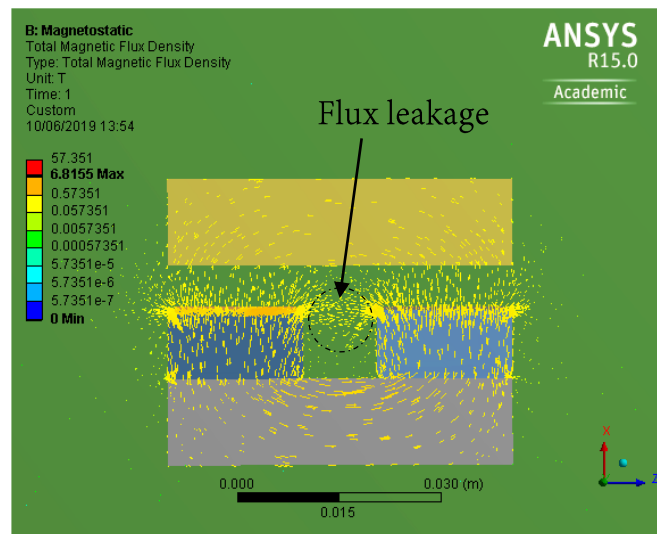


Figure 3-16: Using iron shoes to smooth the magnetic field and the leakage problem

The achievable magnetic field strength with different strip thicknesses are studied in the simulation and the results are plotted in Figure 3-17. The air gap distance is kept the same of 6 mm. It can be seen that the field strength decreases with a thicker strip. In this thesis, the thickness is selected as 0.05 mm, which is readily available on the market.

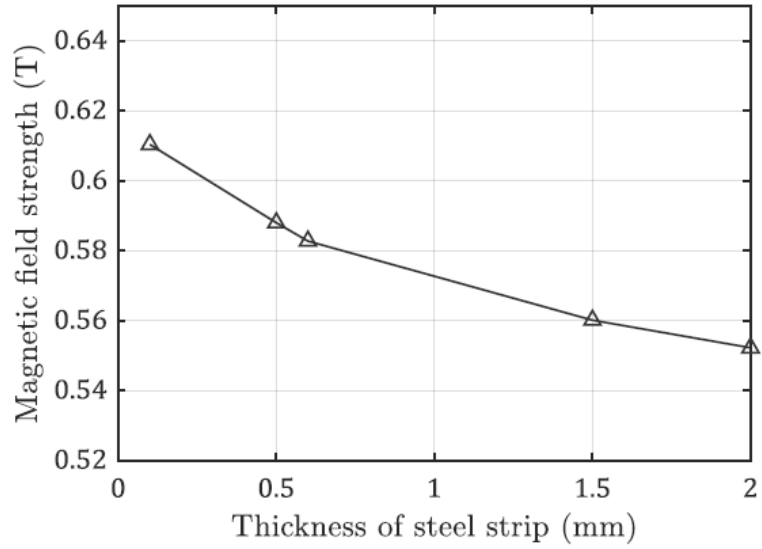


Figure 3-17: Average magnetic field strength changes with different iron shoe thicknesses

The magnetic field distribution with the designed parameters is shown in Figure 3-18. Only three pairs of magnets are shown in this simulation. The field strength is found to be uniform and with a strength of 0.61 T. This magnetic field will be used to convert the motor currents into motor forces.

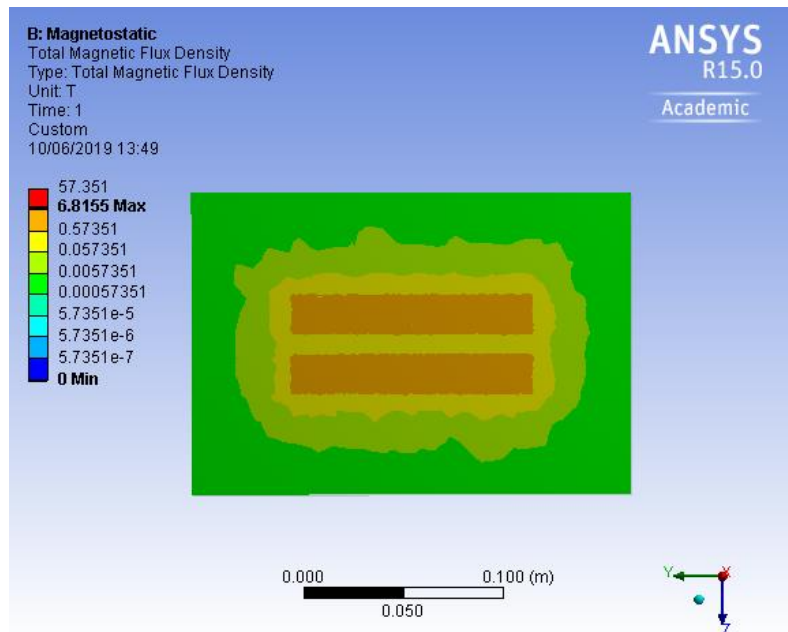


Figure 3-18: Cross section of magnetic field distribution with the selected parameters

### 3.4.3 Calculation of FVCM parameters

The motor coil assembly consists of the coil backbone and the coil. Only the coil portion contributes to the generation of force, therefore the support structure should be made as light as possible. Linear motor suppliers usually select resin to hold the motor coil, but this method requires a specific moulding process, which is not viable in small batch application. In addition, the elastic modularity of the resin material is usually low. In this thesis, the coil backbone is made out of four layers of carbon fibre sheets to minimise the mass of the non-force-generating parts. The carbon fibre sheets are unidirectional ones with the highest elastic modularity direction along with the motor force direction. Each layer is bonded with high strength resin epoxy. The bonding layer is intended to increase the damping of the support structure. The thickness of the carbon fibre sheet is 1.5 mm.

The 3-D model and the photo of the assembled part are shown in Figure 3-19. The motor coil can be modelled as an inductance in series with a small resistor and a voltage source. The material of the coil can be copper or aluminium. The copper winding has the advantage of lower resistance and therefore lower heat generation. The aluminium coil winding is lighter with the same size but with higher coil resistance. A high coil resistance is usually not desired due to its thermal effects. But it is also beneficial in that the electrical time constant of the motor coil, which is the ratio between the coil inductance and coil resistance, will be lower. A smaller electrical time constant means the current in the coil will reach the desired value faster, which is important in fast positioning applications. Base on this, the coil material is selected as aluminium with enamelled insulator. The maximum allowed temperature is 180 °C for effective insulation.



Figure 3-19: Model and photo of the multi-layer carbon-fibre coil assembly

The volume for the coil winding is limited to a fix space with 3 mm thick as shown in Figure 3-20. Within the same volume, the diameter of the wire determines the number of coil turns. Assumptions are made that the coil wires are close to each other.

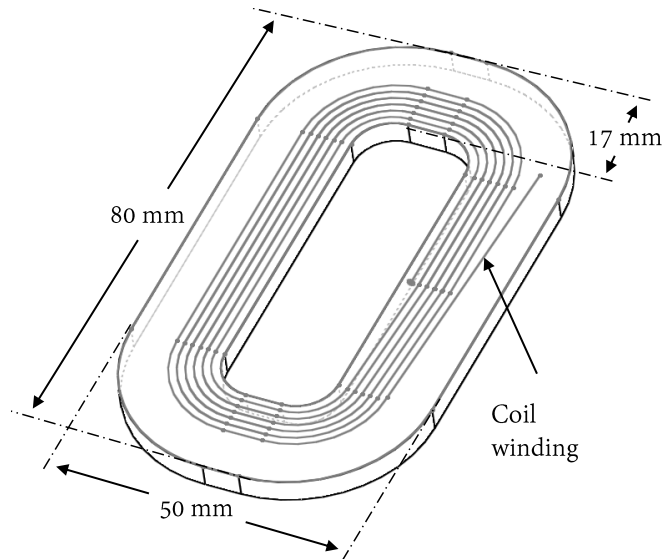


Figure 3-20: Coil winding design with key dimensions

The inductance  $L_{coil}$  and resistance  $R_{coil}$  of the coil is related to the shape of coils, diameter of the wire and coil material. The effective length of the coil, which cuts the magnetic lines when the motor moves, is also determined by the wire size. The coil resistance is easily calculated by the conductivity of aluminium and the size of the wire. The inductance of the coil is approximated by the round coil model in free space as follow<sup>3</sup>:

<sup>3</sup> Calculated according to <https://www.allaboutcircuits.com/tools/coil-inductance-calculator/>

$$L_{coil} \approx N_{coil}^2 \mu_0 \mu_r \left( \frac{D_{coil}}{2} \right) \left[ \ln \left( \frac{8 \times D_{coil}}{d_{coil}} \right) - 2 \right] \quad (3-2)$$

Where:  $N_{coil}$  is the number of coil turns,  $D_{coil}$  is the approximated equivalent loop diameter,  $d_{coil}$  is the diameter of the wire,  $\mu_0$  and  $\mu_r$  are the permeability of free space and the relative permeability of the medium, the air in this case.

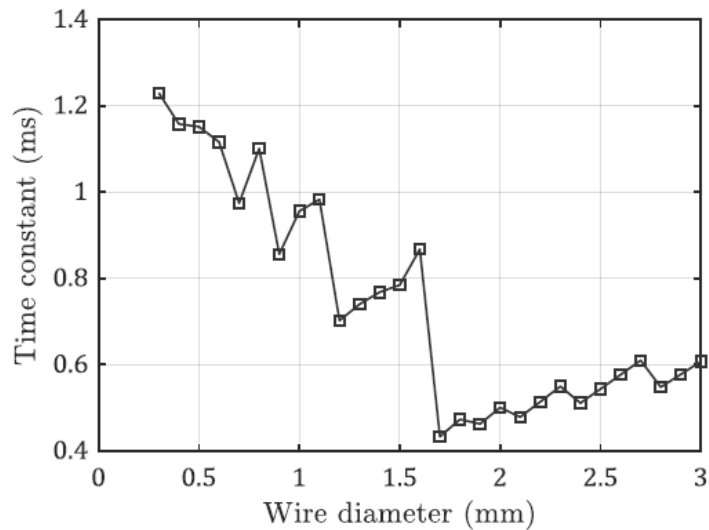


Figure 3-21: Calculated electrical time constant with different wire diameters

The calculated electrical time constant and the motor force constant under 0.61 T magnetic field strength under different coil wire diameters are shown in Figure 3-21 and Figure 3-22. It can be seen that a larger wire diameter usually means a smaller electrical time constant. The discontinuities in the graphs are caused by the vast change of coil turns when the layer number changes. The motor force constant keeps decreasing because it is proportional to the number of coil turns. The wire diameter is selected as 0.9 mm, which corresponds to a reasonably small time constant and large force constant. The force constant at this point is 3.914 N/A. The coil resistance and inductance are 0.3657  $\Omega$  and 0.3131 mH respectively, corresponding to 0.8563 ms electrical time constant.

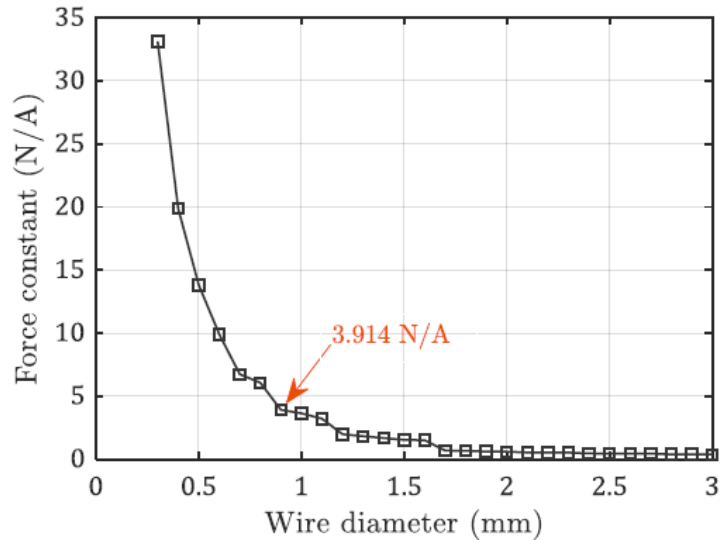


Figure 3-22: Calculated motor force constant with different wire diameters

### 3.5 Prototype assembling

A motion system prototype is developed according to the stiff-support structural design. A capacitive sensor from Lion Precision (CPL190) is fixed to the moving coil assemble via a block and targeting a precision flat surface. This flat surface is used as the position metrology reference. The accuracy of the metrology reference is fundamentally important in this design. The geometrical errors of the metrology frame can be treated as a change of position command. Ideally, a straight edge with optic grade surface should be used. However, in this paper a precision ground then lapped surface is used due to practical limitations. In the latter of this thesis, it is very interesting to find that it is possible to get very good surface smoothness even with this relatively rough reference. This is because the sensing area of the capacitive sensor (2 mm diameter) averages out the small scratches of the lapped surface.

A linear cross roller bearing from THK Ltd. is used as the X guide. The X-axis position is measured through a Renishaw encoder. A linear motor from Aerotech is used to drive the X-axis and to close the position loop. The Z motion range is 50  $\mu\text{m}$ , limited by the measurement range of the capacitive sensor. The assembled sensor and magnet track assembly are shown in Figure 3-23 and Figure 3-24. The finished motion prototype is shown in Figure 3-25 as well.



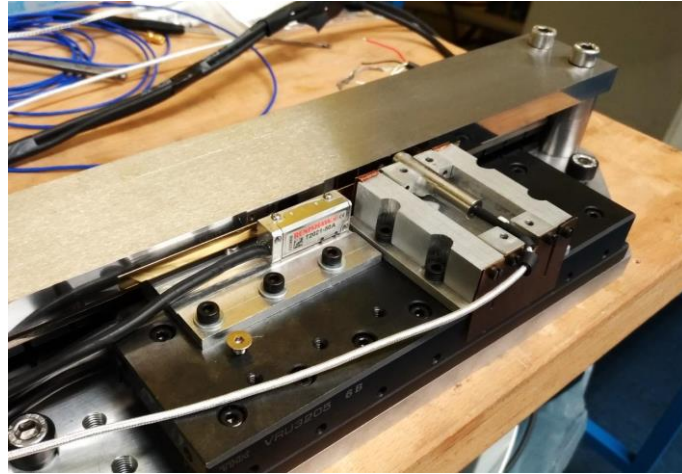


Figure 3-23: Photo of the capacitive sensor and encoder assembly

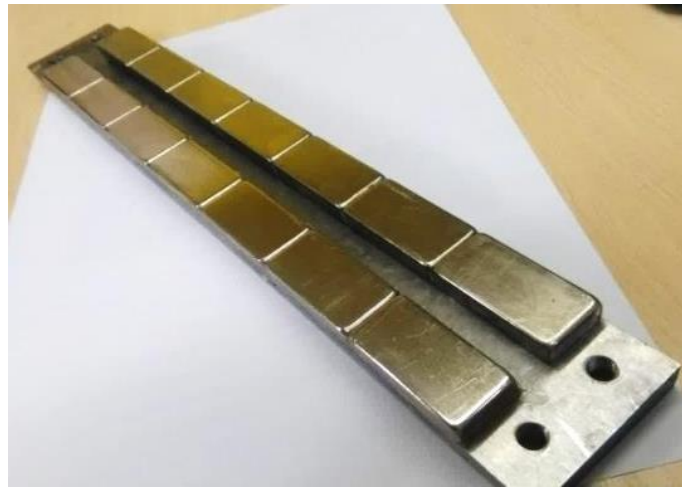


Figure 3-24: Photo of the magnet track assembly (Iron shoe strip not fitted)



Figure 3-25: Finished assembly of the developed motion system

### **3.6 Summary**

In this chapter, a novel stiff-support concept is proposed which eliminates the structural and bearing compliances in the stiffness loop. The new design has also adopted the metrology frame structure with shortest path and it obeys the Abbey principle as well. Those design considerations make it promising to improve the performance of the cutting system, even with low cost components. The controller design will also be made easier with the new system.

This structure is made feasible by a modified flat voice coil motor design. The influences of several parameters have been revealed by FEA modelling. Although there are some practical limitations when selecting the parameters, the quantitative results provide guidance for designing precision mechatronic systems. The developed mechanical system will be the basis for the future controlling and analysis studies. The system design has been made as simple as possible and the servo stiffness is the major factor that determines the dynamic performance of the positioning system.

# CHAPTER 4

## Signal chains in digital controller and power amplifier

### 4.1 Introduction

The servo controller is the second stage in the control system loop and its dynamic performance is equally important in the design of high dynamic positioning system. In this chapter, the digital controller is built and the signal transfer paths within the digital controller are clarified. Then the time delays associated with these transmissions are analysed according to the hardware specifications. This time delay information helps get a more accurate model of the system and it also helps to identify the bottleneck stage for improving the performances. The detailed design and tests reveal the noise sources in the electronics. The noise level of the controller board is tested.

Then a power amplifier board is developed by the author. The power stage noise is minimised by selecting a linear power amplifier. Different compensation circuits for the closed-loop current controller are studied and compared. The performance of analogous current controller is then verified by frequency response tests.

### 4.2 Overall structure of the electronic system

The function of the controlling electronics can be divided into a controller and a power amplifier. The controller is responsible for three tasks: reading the sensor signals, calculation of the control algorithm and then output a command voltage. The electrical signal in this portion falls within a low voltage and current range. This low power signal usually cannot be used to drive a motor and thus a power amplifier stage is necessary. The power stage simply outputs a large voltage with large current capability, which is proportional to the command voltage from the controller. The design of the power stage and controller board is shown in Figure 4-1. The digital

controller consists of a Digital Signal Processor (DSP), Analogue to Digital Convertors (ADC), Digital to Analogue Convertors (DAC) and corresponding power supply and booting circuits. The power stage is designed based on an integrated linear power amplifier. Due to the large output power of the amplifier, the amplifier will generate a significant amount of heat during large loading conditions. Therefore, a dedicated water-cooling block is designed. The block is made of aluminium with many water-cooling channels. An analogue PID current controller board is also designed in order to regulate the output current.

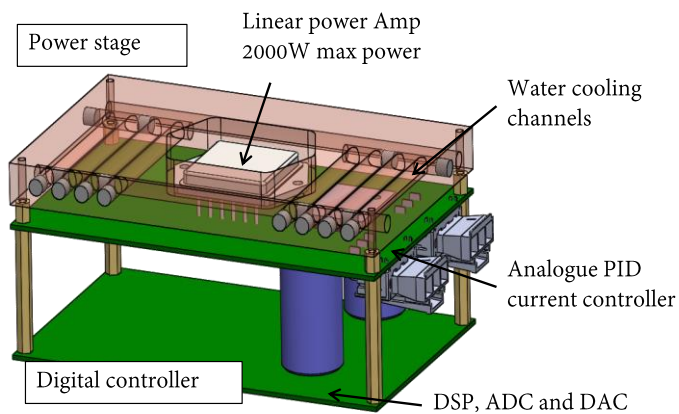


Figure 4-1: Model of the designed controller and power amplifier stage

The photograph of the built electronic system is shown in Figure 4-2 (image is flipped to show the details of the board). The detailed structure of the power stage circuits and the digital controller circuits will be discussed in the following sections.

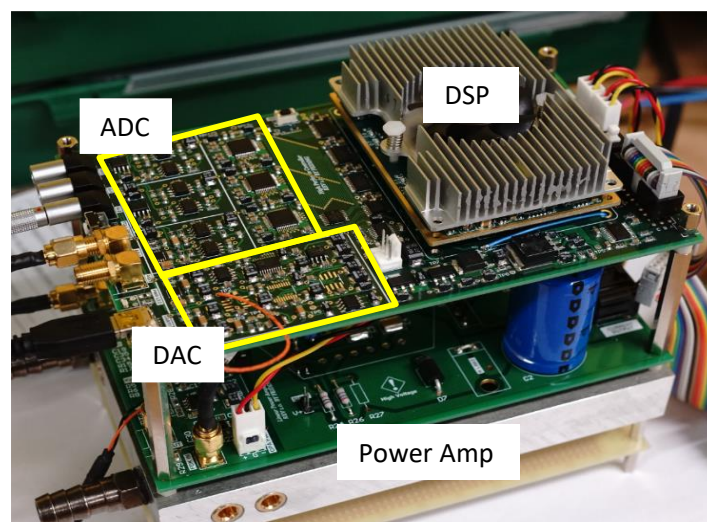


Figure 4-2: Photograph of the built controller and amplifier electronics

Specifications of the developed controller and amplifier board are shown in Table 4-1.

Table 4-1: Specifications of the developed controller and amplifier board

Parameters	Value
Computing power	Two cores, 20G flops per core
ADC	16 bit, differential input
Sampling rate	Up to 2 MHz per channel
DAC	18 bit, 1 $\mu$ s settling time
Peak current	20 A
Bus voltage	Up to 95 V

### 4.3 Development of digital controller board

The digital controller is aimed for reducing the calculating time of servo loop with minimum sampling and output noise. Although there are many commercial controller boards available from vendors like the dSPACE and National Instruments, it has been determined to build one from scratch. One of the reasons is that by designing the system step-by-step, the delays and noise sources can be identified and sometimes reduced. This is the foundation of the error analysis and controller design approaches covered in Chapter 5 and Chapter 6 in this thesis.

#### 4.3.1 Function block diagram of the digital controller board

The digital controller board is built around a dual-core floating-point DSP from Texas Instruments (Model: TMS320C6657). The power management and boot circuits (the small PCB board in Figure 4-2) for this DSP chip are from Tronlong Electronics, ShenZhen. The AD/DA board is developed by the author.

Each of the three ADC chips (Model: ADS8422) is mapped to the one of last three Chip Select (CS#1~3) of the 16-bit parallel External Memory Interface (EMIF). The first chip select (CS#0) is connected to a 128 MB NAND flash. Multi-channel Buffered Serial Port (McBSP) is configured to communicate with a serial-port DAC (Model:

AD5781). Detailed information on ADC and DAC interfacing circuits with DSP can be found in Appendix B. The controller board communicates with a host PC through Universal Asynchronous Receiver/Transmitter (UART) serial port and the General Purpose Input/Output (GPIO) interface.

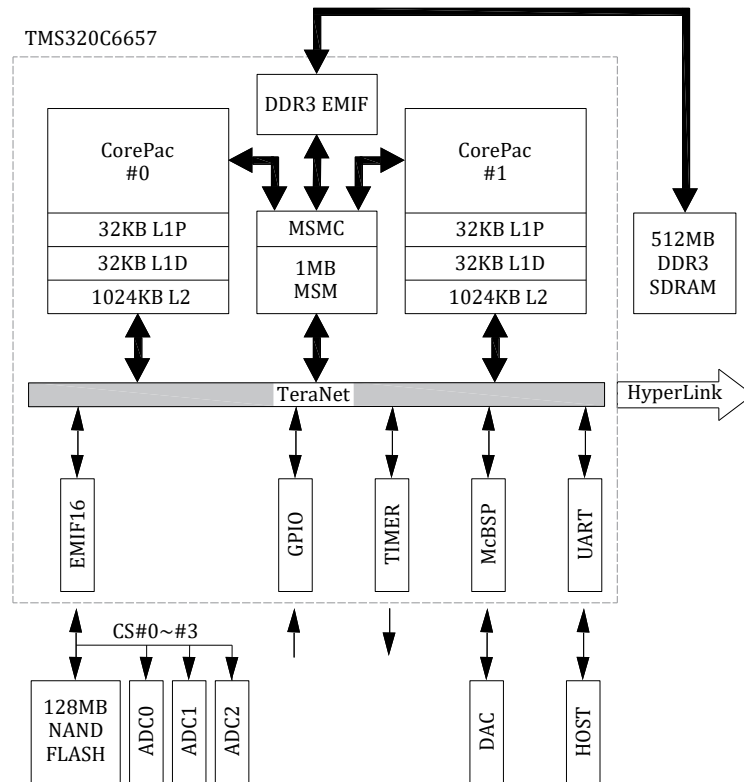


Figure 4-3: System function block diagram and data flow paths

### 4.3.2 On-chip hardware resources of the DSP

Two identical C66x processing units (CorePacs) are integrated on a single silicon chip. The CPU cycle time is 1ns at 1GHz operating frequency. This frequency can be increased to 1.25GHz at most but with higher power consumption and heat generation. According to the datasheet of C6657 chip from Texas Instruments, there are eight functioning units (.M1, .L1, .D1, .S1, .M2, .L2, .D2, and .S2) running parallel in each CorePac<sup>4</sup>. So that eight instructions in total can be executed in a single CPU cycle. The .M unit is responsible for all the multiply operations and it can finish one single-precision multiply operation in one cycle or one double precision multiply operation

<sup>4</sup> Details can be found at <http://www.ti.com/product/TMS320C6657>.

in four cycles. The .L and .S units perform arithmetic and logical operations. One double-precision addition or subtraction can be finished in one CPU cycle<sup>5</sup>. The .D unit is mainly for manipulating data between the memory and the CorePac register files. Some of the eight units may be idle while others are executing instructions. The programmer is responsible to optimise his codes to make full use of the hardware resources.

Outside the CorePacs are local memories for programs and data storage. The central processing unit keeps fetching instructions and data from the memory, do the operation and then push the results back to the memory. Therefore, it is vital that the CorePac has instant access to these local memories.

A two-layer cache structure is used in this digital processor, namely L1 cache and L2 cache. The L1 cache is physically closer to the CorePacs and the processor can read or write data to this cache layer within one CPU cycle. The programme data can be buffered into this memory space in order to boost read and write speed. However, the size of this cache is very limited, 64 KB in this case. Therefore, a secondary L2 cache (1 MB) is used to buffer data into L1 cache. The L1 cache space is divided into data cache (L1D) and programme cache (L1P). The L1 and L2 caches are unique to corresponding core. The C6657 DSP also features a 1 MB size shared Multi-core Shared Memory (MSM). The different cores of the DSP chip can access the same memory space. This provides an effective way to exchange data between the cores. There exists a Multi- core Shared Memory Controller (MSMC) unit to coordinate the data flow so that the reading and writing actions will not conflict with each other.

There is also a dedicated high-speed bus within the DSP chip, called TeraNet. This bus inter-connects the CorePacs and all the peripherals. When the CorePac reads data from the peripheral registers, the data must firstly go through the data bus. Since there are multiple data sources and destinations on the bus, the data flows are managed by a dedicated control unit. This data bus structure will introduce delays, which will be discussed in Section 4.4.

---

<sup>5</sup> According to the C66x CorePac User's Guide from Texas Instruments at <http://www.ti.com/lit/ug/sprugw0c/sprugw0c.pdf>

### **4.3.3 Coordination of multi-core tasks**

The DSP has two independent processing cores and thus the computing power is doubled. However, the servo calculation routine is a seamless serial process, which means the sampling, computing and output voltage procedures have to be finished in chronological order. In order to make the full use of the computing capability of the DSP, the servo routine is divided into several tasks and the tasks are run on separate cores. The tasks are synchronised by the inter-core interrupts.

The tasks of sampling and processing of the signals from the feedback sensors are accomplished by the Core 1. The other Core 0 is responsible for the servo calculation and DAC output functions. The remaining time of the Core 0 is also used to communicate with the host PC.

## **4.4 Delays in the digital signal chain**

In this section, the delays in the controller are discussed in detail. The reason to study the delays is that the amount of time delay of a closed-loop system determines the maximum bandwidth without the loss of stability. For example, a time delay of one microsecond corresponds to 0.36-degree phase loss at 1 kHz in the servo loop while it will cause 90-degree phase loss at 250 kHz. The typical phase margin for a properly tuned loop is around 25 degree to 60 degree and the phase loss will pose great difficulties in tuning the loop gains.

In a digital control system, the controller uses the old information from the last sampling time measurement to calculate the current action to be taken. On the other hand, the control action might not be delivered to the end effector in time. Therefore, the delays in the control loop can be classified as sensor delay and actuator delay [135].

In practice, digital control system always has a certain amount of sensor delay caused by the sampling and hold mechanism and the processing time. The actuator delay may come from the backlash in the transmission chain, which is not common in direct drive motions. In this thesis, the mechanical system is deemed as free from time delays and only the delays in the controller board are studied. The digital delays can be classified into transmission delay, calculation delay and sampling delay.



#### 4.4.1 Transmission delay

The data flow from the feedback sensor to the controller output voltage is shown in Figure 4-4. The position change of the stage causes a voltage output from the capacitive sensor. Delays in the control board exist outside of the DSP chip. This includes the ADC conversion time, transceivers, and the serial data transmission out of McBSP.

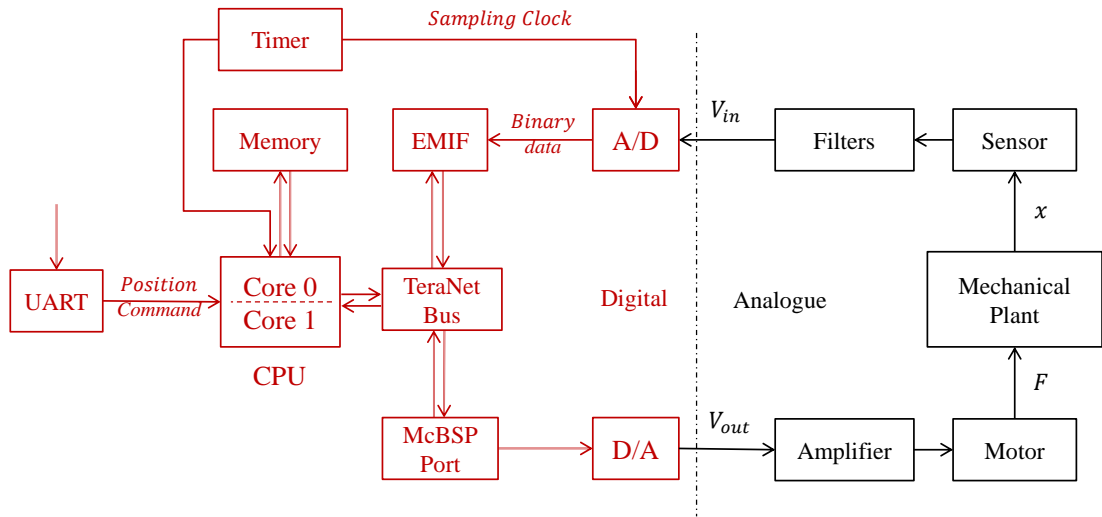


Figure 4-4: Data flows in the digital control loop

The working data flow for closed-loop control is described as below:

1) The timer is configured to generate pulse trains from one digital output port at a fixed time interval. This pulse trains are used as the sampling clock to the ADC. All the three ADCs share the same clock signal and thus the sampling actions are synchronised. After the initialization process during the power up stage, the timer runs autonomously. The timer also triggers the CPU Core 1 to start an acquisition task routine upon each pulse generation.

2) The ADC chip starts to acquire and convert the analogue voltage on its pins into binary data after receiving the sampling clock with a delay of 3 ns (called aperture delay). The conversion time for the selected ADC chip is 180 ns ( $T_{CONV}$ ). The converted data will be available on the bus at 225 ns after the sampling pulse. There exist a further approximately 10 ns delay in the voltage level translation chips between the ADC and the DSP.

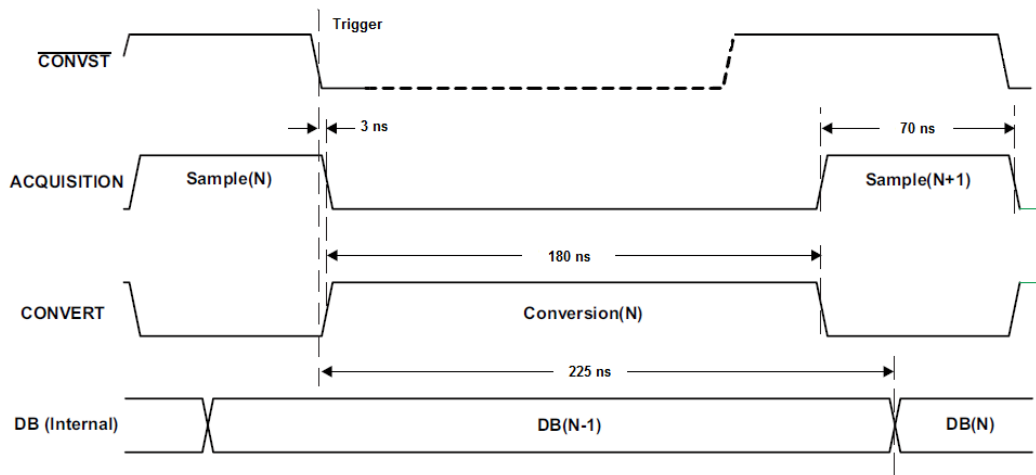


Figure 4-5: Timing delay diagram of the ADC input

3) Concurrently with step 2), the CPU Core 1 starts reading the data. Since the ADCs are connected to the EMIF16 peripheral, the CPU Core 1 sends a read command to the EMIF16 module requesting the ADC converted data to be put on to the data bus. As shown in the system block diagram in Figure 4-3, the CPU cores are connected to the EMIF16 peripheral through a TeraNet bus and the instruction signal has to pass through the bus before reaching to the EMIF16 register. The timing is configured such that when the instruction signal reaches the EMIF16 module, the ADC conversion is finished, and the output data is ready to be read.

The TeraNet bus consists of five sections and each section runs at a different clock rate with the core. This switch mechanism causes delays when the CPU reads or writes data through the peripherals. For example, when the CPU reads data from a peripheral register, for example, the timer register, the instruction goes through a chain of paths as in Figure 4-6. The instruction sent by the core goes through the TeraNet 3P\_A, TeraNet 3P\_B and TeraNet 6P\_B sections respectively. TeraNet 3P\_A and TeraNet 3P\_B are updated at one third of the CPU rate. TeraNet 6P\_B is updated at one sixth of the CPU rate.

The return data will also go through the same path back to the CPU cores. So the single read operation cost nearly 116 CPU cycles or 116 ns at 1GHz CPU frequency ( $T_{EMIF}$ ). A read from the EMIF16 module goes through a similar process. The maximum frequency of a timer interrupt is tested to be around 2.8MHz where the only

task in the interrupt service routine is clearing the timer interrupt flag (one bit in the timer register).

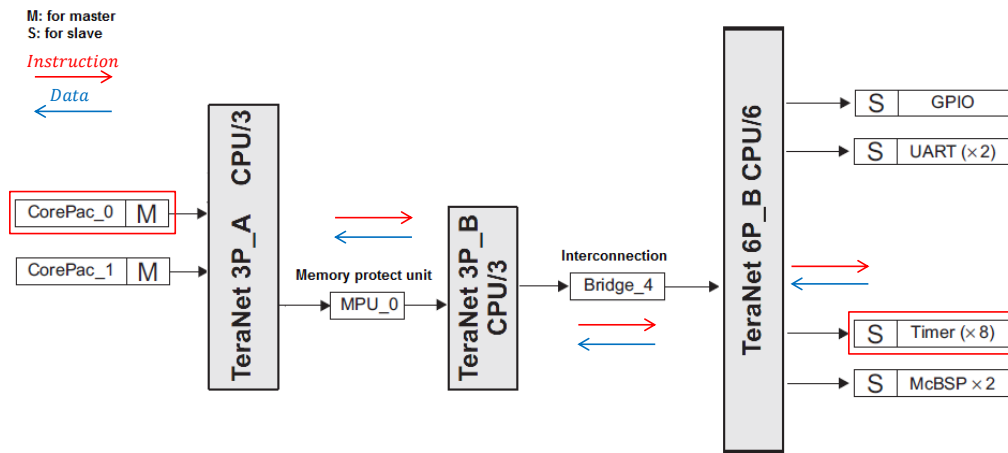


Figure 4-6: Information flow of read action from the peripheral through the TeraNet bus

4) Then the CPU Core 1 starts to pre-process the sampled data. The raw binary data read from the bus is of 16-bit integer type ranging from 0 to 65535. This data is then converted into float point format because the CPU can calculate float point data directly. The pre-processing task involves simple data averaging and then the result is passed onto the next stage ( $T_{AVG}$ ). It is supposed to distribute the computation burdens evenly onto the two cores.

5) Once the Core 1 finished the pre-processing of the signal, it triggers the Inter-Process Communication (IPC) interrupt to notify the other core to take over the job. The IPC interrupt generation takes some time ( $T_{IPC}$ ) to be completed. Then it clears the timer interrupt flag bit and gets ready for the next sampling and processing cycle. The timer interrupt flag bit is on the timer peripheral and the CPU also has to go through the TeraNet bus to clear it, which requires 116 ns.

6) The other Core 0 receives the IPC notification and starts the servo calculation ( $T_{SVR}$ ). At the same time, the position command is read to the local memory. A servo output value is calculated based on the control algorithm and the difference between the command position and the feedback position. Then the output value is converted back to integer type and sent to the McBSP serial port registers<sup>6</sup>. Again, McBSP

<sup>6</sup> In some servo systems, fixed-point type is directly used in the calculations to save CPU time but with more programming difficulties.

registers can only be accessed through the TeraNet and the same amount of CPU cycles is needed as in 3).

This simultaneous parallel processing technique, or pipeline technique, distribute the tasks onto two CPU cores and improves the servo update rate as shown in Figure 4-7. However, the total transmission delay between the input signal and the output signal remains the same as single core processing.

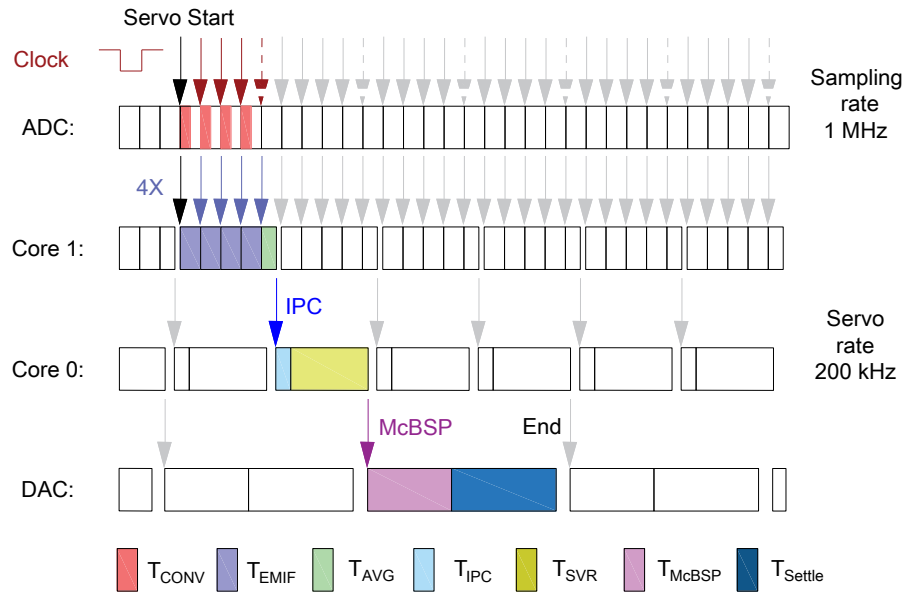


Figure 4-7: Parallel processing to improve the servo update rate

7) After the McBSP register received the binary data, the data bits are shifted out to the DAC chip one by one. The clock rate of the serial port is configured as 18 MHz<sup>7</sup>. One output contains 24 bits including the 18-bit data and other controlling bits. Therefore, it takes 1.33  $\mu$ s to transmit the whole voltage data ( $T_{McBSP}$ ). The output voltage will start to change at 130 ns after the completion of the data transmission. The output of DAC chip needs some time to settle down to the desired value. The settling time of the selected DAC chip is 1  $\mu$ s ( $T_{Settle}$ ) when the output is a 10 V step change within a tolerance of 0.02%.

<sup>7</sup> The DAC accepts up to 35 MHz clock rates, but it is not achieved in this thesis due to the PCB routing imperfections.

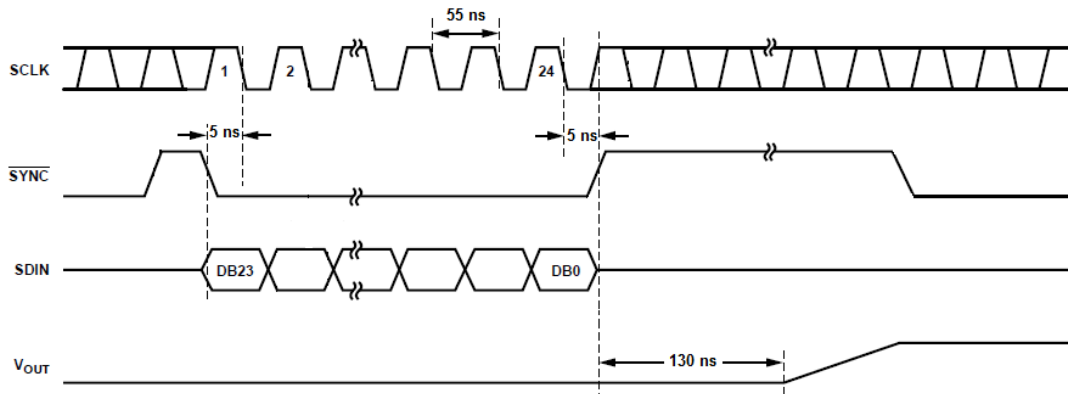


Figure 4-8: Timing delay diagram of the DAC output

The amounts of time delays spent on each stage are listed in Table 4-2. As we can see, the majority of CPU time is spent on the communication to registers through the TeraNet. This accounts for a major portion of the total delay time. An alternative approach is to introduce a FPGA to trigger the ADC and read the data to its own memory. Then the FPGA transfer the data to the DSP core through dual-port memory, bypassing the TeraNet bus. This is something can be improved in the future.

Table 4-2: Time spent on data transferring

Transmission stage	Time delay ( $\mu$ s)
ADC sampling	0.235
Read from ADC (TeraNet)	0.116
Clear Timer flag (TeraNet)	0.116
Core 1 notify Core 0 (TeraNet)	0.116
From Core to EMIF16 (TeraNet)	0.116
Shift data from EMIF16 to DAC	1.46
DAC settling time	1
Total time delay	3.159

#### 4.4.2 Calculation delay

Apart from the time spent on data transmissions, the calculations in the CPU also take some time. The calculations mostly happen in the preprocessing stage (taking average) in Core 1 (noted as  $T_{AVG}$ ) and the servo calculations stage in Core 0 ( $T_{SVR}$ ). A general arithmetic calculation involves three steps: fetch the program and data from the local memory, do the calculation in the function units and then push the results back to the local memory.

Table 4-3 below lists the CPU cycles needed to read a data from different memory locations or registers. The closest memory space to the CPU core is the L1 cache, which requires one CPU cycle to read or write. However, since the programme code is located on the shared L2 memory for the reason of multi-core operation, the reading or writing operation takes 3 CPU cycles. Therefore, a simple add operation of two double-precision numbers takes 7 CPU cycles, or 7 ns when the CPU is run at 1 GHz. Real world servo calculations can be made up of lots of such simple arithmetic operations and the total calculation time is dependent on the complexity of the control algorithm.

Table 4-3: CPU cycles required to read a single-precision data from different memory locations

Read from	CPU cycles required
Local L1P/L1D	1
Shared L2	3
DDR3	4
EMIF16	58

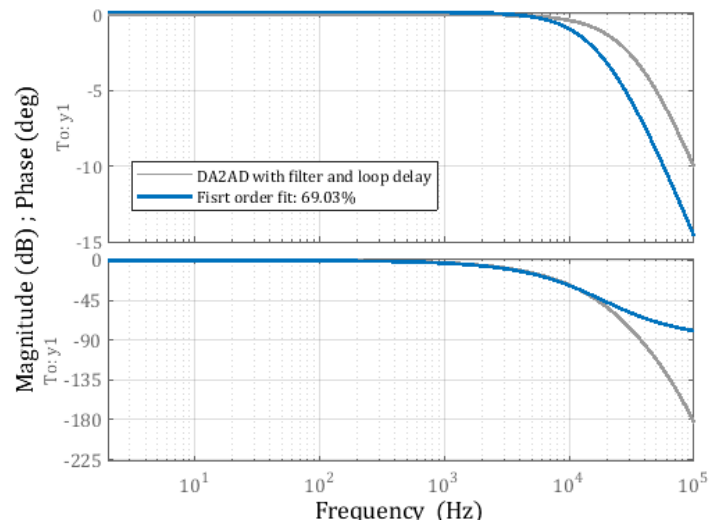
#### **4.4.3 Sampling delay**

Due to the nature that a digital sampling system only measures the sensor data at discrete time intervals, the physical change can only be sensed at the next sampling instant. This will cause a certain delay before the transmission delays in the loop. The delay time varies from zero to the sampling period. A higher sampling rate will help reduce this delay.

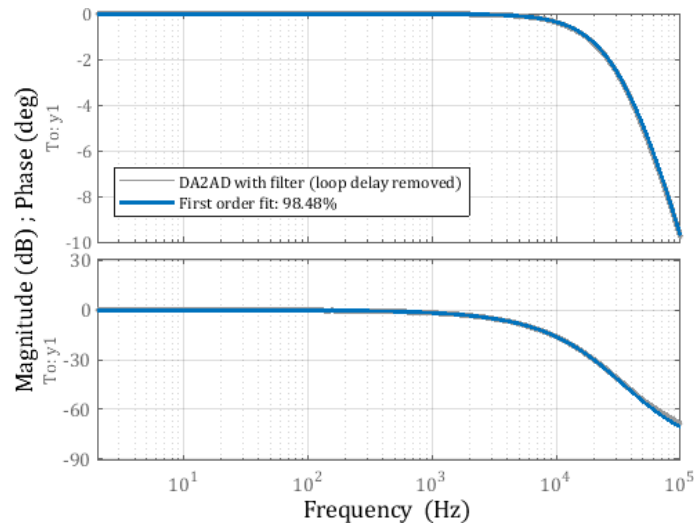
However, the maximum sampling rate is limited by the CPU time required to manipulate the data through the buses. It has been tested that the achievable sampling rate is up to 2.5 MHz for single channel sampling and 1 MHz for three-channel sampling. Ideally, each sampling should be followed by the servo calculation routine, but the servo update rate in Core 0 cannot be so high due to the complexity of servo calculation. Therefore, the sampled data is firstly averaged for every four samples, which are acquired at a rate of 1 MHz. This oversampling strategy will help increase sampling resolution as discussed later.

#### **4.4.4 Measured loop frequency response with delays**

The loop delays are measured by directly connecting the output of the DAC to the input of the ADC. Sweep sinusoidal voltages are sent from the DAC and the feedback results are used to calculate the frequency responses. In this test, the sampling is conducted once without the oversampling procedure. Since the anti-aliasing filter between the output and the input are deemed to be a linear first-order system, discrepancies from this response shape is mostly caused by the nonlinear delays in the loop. The measured responses curve is shown grey as in Figure 4-9 a). It can be seen that the phase curve of the measured response drops rapidly after 20 kHz. Direct first order system fit only shows 69.03 % agreement with the measurements. When a delay of 3.5  $\mu\text{s}$  is removed from the data and then redo the fitting, the result shows 98.48 % fitness to the measured data.



a) Direct first-order fitting of the measured loop response without considering the delays



b) First-order fitting of the measured loop response with delay removed

Figure 4-9: Accurate delay estimation helps improve modelling accuracy

## 4.5 Noise in the digital signal chains

This section deals with the electrical noise in the digital signal chains. The feedback sensor voltage is sampled by the ADCs in the digital controller. The controller output is delivered through DAC and thus the noise performance of the ADCs and DACs are important factors to be considered. There are other electromagnetic interferences from the environment through the cabling of the signals.



#### 4.5.1 ADC noise spectrum

The ADC sampling noise comes from two sources: the electrical noise of the op amps, which are used to regulate the input impedance, and the quantization noise. The op amps are of high speed and the noise floor is usually higher than precision op amps. The selected operational amplifier has a voltage noise floor of 1.6 nV/ $\sqrt{\text{Hz}}$ . The quantization noise is caused by the nature that the digital sampling system can only represent a voltage number with fixed memory size. The selected ADC chip is of 16-bit, which means one analogue voltage is represented by a 16-bit binary number. This small representing errors show up as a white noise with uniform probability distribution. The quantization noise Power Spectral Density (PSD) can be calculated as:

$$PSD_{AD} = \left(\frac{V_{IN}}{2^{16}}\right)^2 \times \frac{1}{12f_N} \quad (4-1)$$

Where: the input voltage range  $V_{IN}$  is  $\pm 4.096$  V and  $f_N$  is the Nyquist frequency, which is half of the sampling rate. The performance of the developed ADC circuits is measured by shorting the input pins of the ADC with a low value resistor. The measured time domain signals and the corresponding power spectrum density are shown in Figure 4-10. It can be seen that the minimum resolvable voltage is 0.0625 mV and the measurement results are stable to within  $\pm 3$  bits. The spectrum shows a flat top with no obvious peaks, this is a good indication that the noise is almost white.

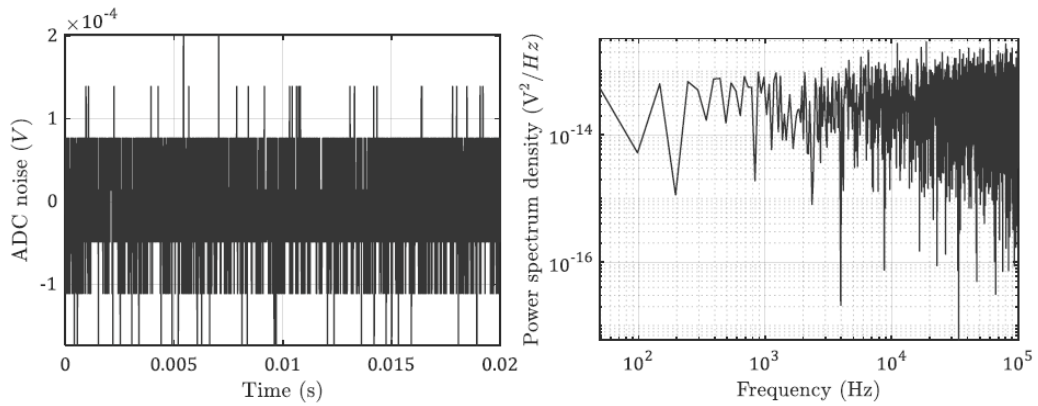


Figure 4-10: Noise spectrum of ADC with  $4 \times$  oversampling without anti-aliasing filter

#### 4.5.2 Displacement sensor noise spectrum

The feedback voltage from the sensor also has a certain noise floor. However, this noise level is mostly determined by the instrument electronics and not so much can be done on this, except choosing a better instrument. Anti-aliasing filter is used to limit the broadband noise. Thirty-two samples of the voltage signal are measured with the developed ADC board under stationary conditions. The calculated PSD functions are averaged to reduce measurement variance. The measured sensor noise and the spectrum are shown in Figure 4-11. It can be seen that the noise floor of the sensor electronics are much higher than the ADC noise. And it is also clear that the anti-aliasing filter helps suppress the high frequency sensor noise.

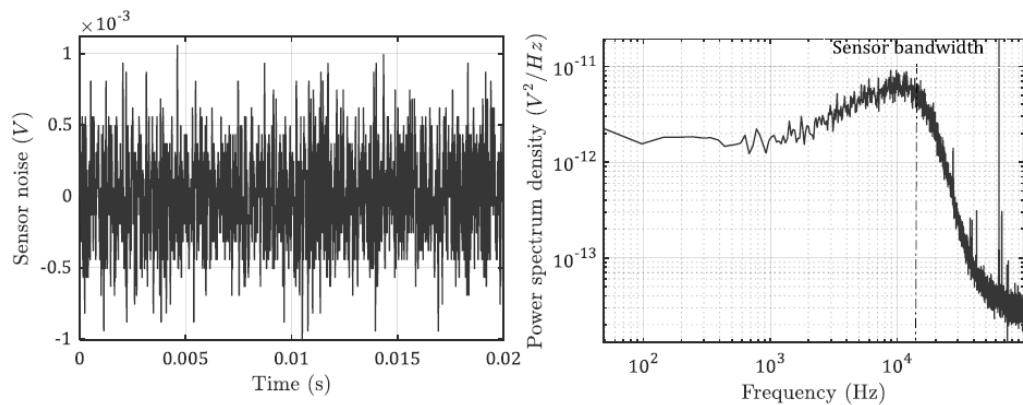


Figure 4-11: Measured displacement sensor noise with anti-aliasing filter

#### 4.5.3 DAC output noise

The output quantization noise can be calculated in the same way as ADCs, the difference is that the DAC is of 18-bit and the output voltage range is  $\pm 10$  V. Apart

from the quantization noise, the DAC also has the output glitch noise which source from the inner structure of the chip.

To test the DAC noise, a sinusoidal voltage is output from the DAC and the voltage is sampled by the ADC. The readings are shown in Figure 4-12. There are clear peaks superimposed on the sine wave with magnitudes of tens of millivolts. Since the ADC noise floor is much lower than this value, the peaks are traced to the DAC circuits. This is caused by the glitch impulses problems of high speed DACs. When the DAC input code transits from one to another with a large number of bits to be changed, the synchronization of those changes of many bits is not perfect. This will cause temporary incorrect outputs<sup>8</sup>. These glitches usually last for a very short time and can be effectively attenuated with a low-pass filter.

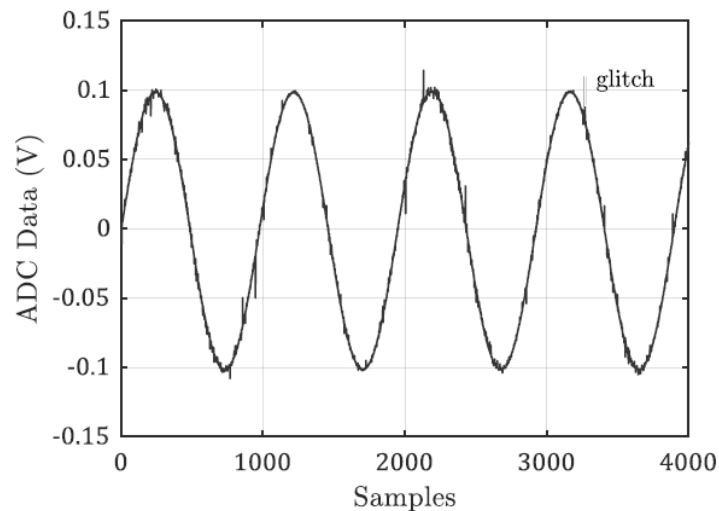


Figure 4-12: DAC Output glitch sampled by ADC when no filter is applied

## 4.6 Power amplifier stage design and tests

This section discusses the design of the power amplifier stage. The power amplifier stage is used to convert the low power control signal into high power controlled energies. The purpose of the current loop is to suppress the variations of motor parameters since motors are designed to be run within wide temperature range. The cascade current loop simplifies the system dynamics seen by the position controller.

---

<sup>8</sup> Further information can be found in the article below:

<http://www.analog.com/media/en/training-seminars/tutorials/MT-013.pdf>. (accessed 11/06/2019)

#### 4.6.1 High-power driving techniques

The driving forces in machine tools mostly come from electrical motors, although there are some exceptions where hydraulic cylinders are used. The high power can either be high voltage, like in piezo actuators, or high current, as in the case of motors.

In the electronic circuits, voltage is easier to be manipulated and thus most electrical rules are based on voltage directly. The current can be measured and controlled according to the Ohms law. There are two schemes to adjust the current in the motor winding. The most common method is the Pulse Width Modulation (PWM) driving technique. The output voltage from the power stage can only be two states: the positive bus voltage and the negative bus voltage. The output power is controlled by changing the pulse widths as shown in Figure 4-13. The inductive load acts as a low-pass filter and then the current in the motor winding is continuous [136]. However, the working principle of linear power amplifier is quite straightforward: the output voltage is strictly proportional to the command input [137].

Although widely used in the industry, the PWM switch drivers have some disadvantages in precision applications, such as the current ripples in the motor coil and severe electromagnetic interferences to other sensitive instruments. The ripple current is related with the driver bus voltage, switch frequency and motor inductance. The amplifier bandwidth is also limited by the switch frequency of the drive. There are reports saying that increasing switch frequency helps achieving improved positioning performance [136]. Linear amplifier driver does not have this problem but the max power is relative smaller. In this thesis, an integrated linear power amplifier from Apex Microtechnology (Model PA04) is adopted to drive the motor.

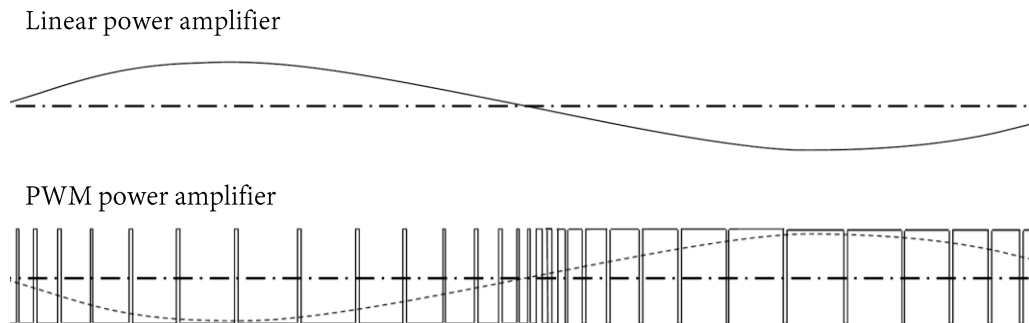


Figure 4-13: Comparison of voltage waveforms from linear and PWM power amplifiers [138]

Direct current amplification can be achieved through power bipolar junction transistors as shown in the book [138]. The differences between voltage amplifier and current amplifier can be described by their output impedance. For an idea voltage amplifier, the output voltage should remain at the same value no matter how much current flow through it. This means the voltage across the amplifier keeps constant (zero) and then it has to be of zero internal resistance. On the other hand, for an idea current amplifier, the output current should be independent on the output voltage. A voltage change did not cause any current change and this can only be achieved by infinite output impedance. Amplifiers in the real world are limited by their ability to provide current under voltage output or voltage under current output, so their output impedances are not zero or infinite. Therefore, specific closed-loop circuits are needed to achieve current control with voltage type amplifiers.

#### **4.6.2 Open-loop characteristics of voltage amplifier and coil**

Before closing the loop, the open loop characteristics of the voltage amplifier and coil must be established. The amplifiers cannot run at a large gain and at high frequency at the same time. As shown in Figure 4-14, the voltage amplifier has a -1 slope response as shown in the datasheet. The amplifier gain decreases with increased input frequency. Gain Bandwidth Product (GBP) of amplifiers is defined as the achievable product of open loop gain and bandwidth [139]. This relationship between open loop gain and frequency is often used to characterise the performance of the voltage amplifier. For example, if a voltage amplifier has a gain bandwidth product of 3 MHz, and it is expected to work in a 500 kHz bandwidth circuit, then the maximum open loop gain on this chip is limited to 6. If higher loop gain is required, more op amps should be used in series in this application. In this thesis, the selected power amplifier has a GBP of 2 MHz and the selected operational amplifiers in the compensation circuits have a GBP of 45 MHz.

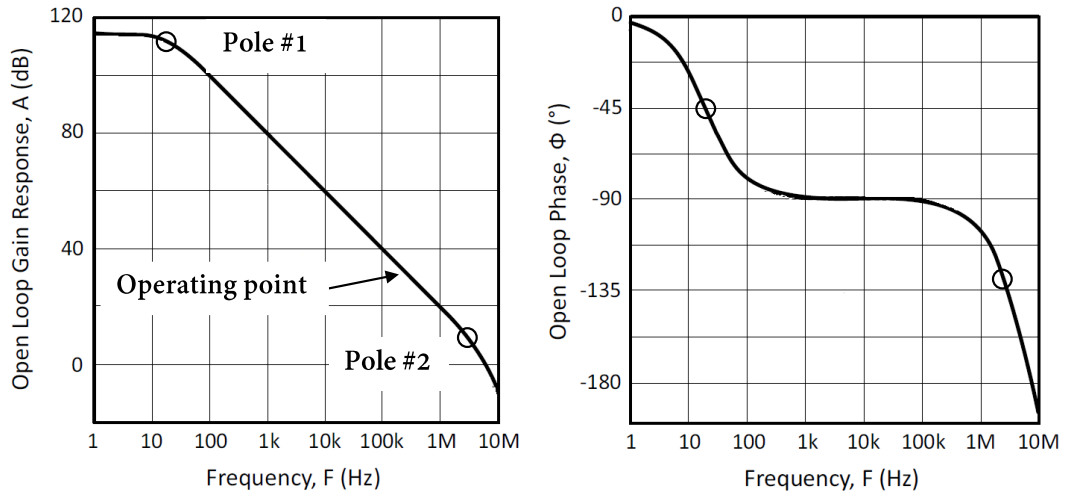


Figure 4-14: Open-loop gain of voltage amplifier PA04 (from Apex Microtechnology)

### 4.6.3 Closed-loop current control with linear voltage amplifiers

The circuits to build a current amplifier circuit from a low impedance voltage amplifier are shown in Figure 4-15. The current through the load is converted to a proportional voltage by a low value resistor in series with the load. The sensed voltage is feedback to the input pin of the voltage amplifier. This closed-loop structure tends to adjust the output voltage of the amplifier automatically until the voltage across the current sensing resistor is the same as the control input. Thus, the relationship between command voltage input and load current is established.

There are two options for the location of the current sensing resistor, either between the supply voltage and load, or between the load and ground. The former is called high-side current sensing and the latter is called low-side current sensing [140]. The high-side structure provides better fault detection ability but the feedback voltage rises on a high common-mode voltage, which is close to the bus voltage. This requires special high input common-mode voltage devices. One drawback of the low-side sensing is that the load reference is floated. Since the load voltage is not a concern in motor application, the low-side structure is adopted in this thesis.

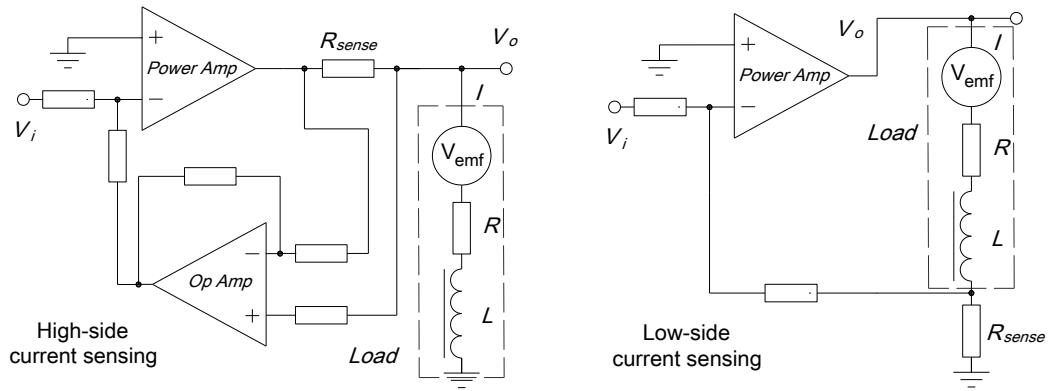
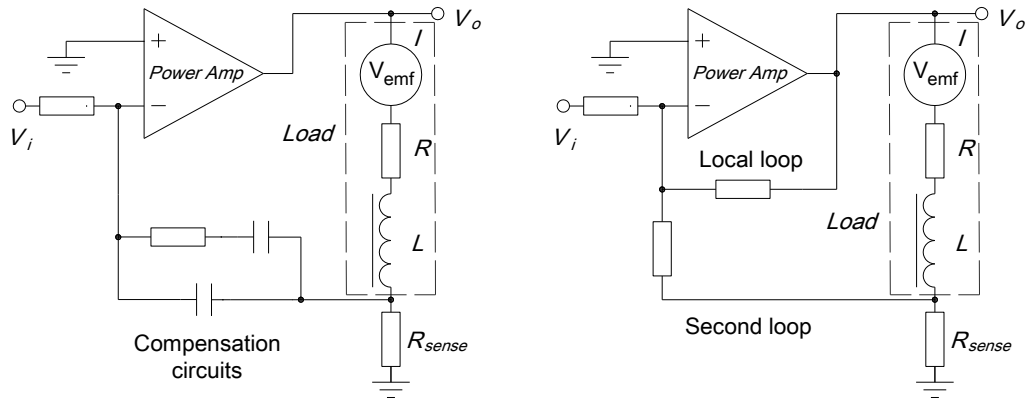


Figure 4-15: High-side and low-side current sensing in current control loop

However, the simple feedback structure in Figure 4-15 is not ready to be used. From Figure 4-14, it can be seen that the voltage power amplifier itself has a -1 slope response and 90-degree phase loss before the second internal pole. The load is composed of a resistor  $R_{coil}$  and an inductance  $L_{coil}$ , therefore, another pole exists at the angular frequency of  $R_{coil}/L_{coil}$ . Beyond this frequency, the magnitude of the frequency response has a -2 slope. The open loop system has a phase of -180 degree. This is a marginally stable situation and cannot be used in practice.

Many circuits can be used to compensate for the pole. One scheme is to introduce a pole in the feedback path by paralleling a capacitor with the feedback resistor as shown in Figure 4-16 a), according to Lu [40]. This pole functions as a zero in the forward path and this zero is designed to cancel out the pole of the load. In this way, the closed-loop stability is guaranteed, but the feedback voltage cannot reflect the load current accurately any more. Additional operational amplifiers are required to correct the voltage by lead networks [138]. This correction network is located outside the closed-loop and functions as a feedforward compensator. Any parameter deviations in the feedforward compensator caused by temperature drift and so on will lead to errors [138].



a) Compensation in the feedback path      b) Compensation with local closed-loop

Figure 4-16: Two schemes to compensate load poles

Another way is shown in Figure 4-16 b). Since the power amplifier will be stable in a closed-loop with a -1 slope response and 90-degree phase loss before the second internal pole, a localised voltage closed-loop can be established. This localised closed-loop will change its frequency behaviour. By feeding back the output voltage, rather than the voltage of the current sensing resistor, the closed-loop transfer function has a flat response up to several hundred kHz as shown in Figure 4-17. The simulation is done by the TINA software by Texas Instruments. The high frequency roll-off is limited by the GBP of the device. The amplifying ratio affects the closed-loop bandwidth and a higher closed-loop bandwidth corresponds to less phase margin.

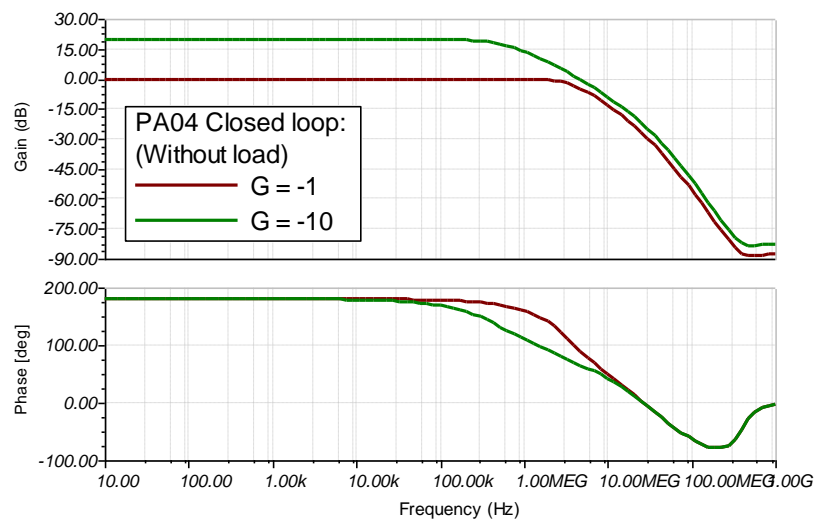


Figure 4-17: Closed-loop responses with different voltage feedback gains



Now the current control loop has enough phase margins to be closed. In this study, additional operational amplifiers are used to do the subtraction and multiplication jobs. This is because if a single amplifier is used to amplify a signal with large gains, the signal bandwidth is lower. This can be seen in Figure 4-17 as well, where the closed-loop bandwidth under gain of -10 is smaller than the one with unit gain. Each operational amplifier can be configured into summing joint, low-pass stage, lead stage and pure gain stages [138]. Thus, rather complex control strategy can be realised by combining those different amplifiers.

Figure 4-18 a) shows such an analogue current control loop arrangement. The first operational amplifier sums the inverted feedback voltage and the input reference with a proportional gain applied. This signal is further amplified by the voltage-feedback power amplifier. This is a simple proportional controller. The open loop transfer function and closed-loop transfer functions are plotted in Figure 4-19 a).

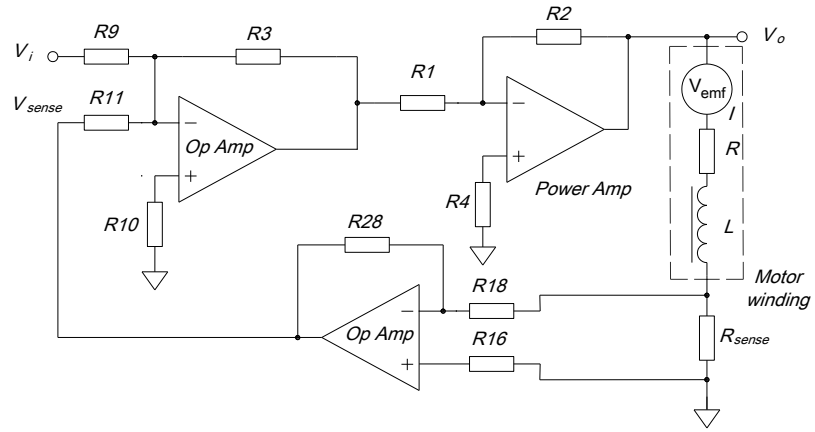
It can be seen that the closed-loop is stable and the output current tracks the input reference. However, the tracking performance is not satisfying. Because of the finite low frequency open loop gain, the closed-loop always has DC tracking errors. A proportional integration (PI) controller can be realised by placing the capacitor C10 in the feedback path, as shown in Figure 4-18 b). The integral action starts from DC frequency and ends at the corner frequency as calculated below:

$$\omega_{int} = \frac{1}{R_3 C_{10}} \text{ rad/s} \quad (4-2)$$

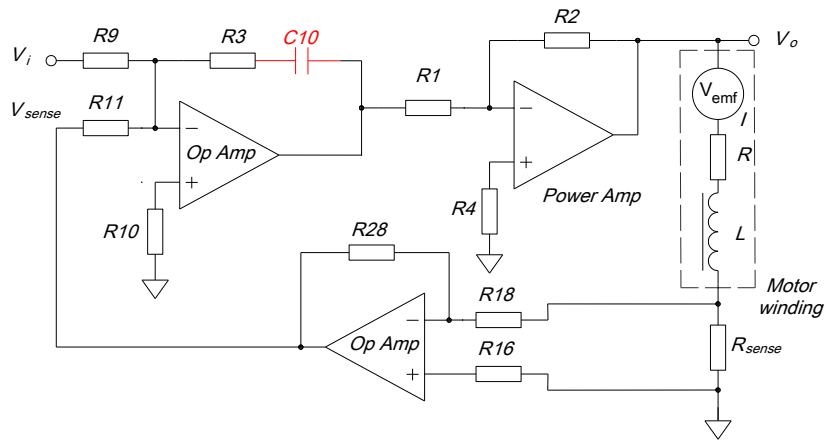
When the integral corner frequency is selected as the same as the pole of the coil, the open loop transfer function become a pure -1 slope line. The frequency response with the PI control can be seen from the frequency response curve as in Figure 4-19 b).

After the closure of the loop, the low frequency tracking performance is improved. The closed-loop gain remains close to one up to 100 kHz. The low frequency closed-loop response is -0.133 dB using P control while it approaches to 0 dB with the PI control. Therefore, the motor current can be accurately controlled to the reference command.

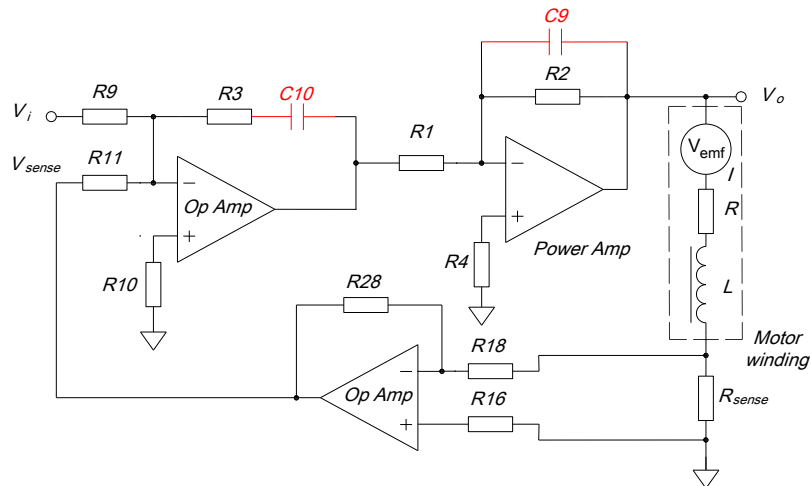
In order to limit the high frequency noise in the loop, an additional capacitor is added parallel to the feedback resistor of the power amplifier as shown in Figure 4-18 c). This arrangement created a pole at  $\omega_f = 1/R_2C_9$ , and then the high frequency gain rolls off quickly. The final frequency response with the PI and roll-off actions is plotted in Figure 4-19 c).



a) Analogue circuits for P compensation control

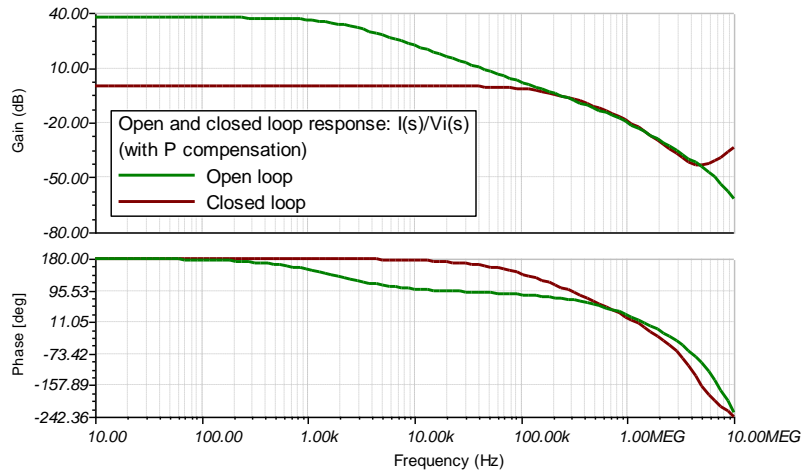


b) Analogue circuits for PI compensation control

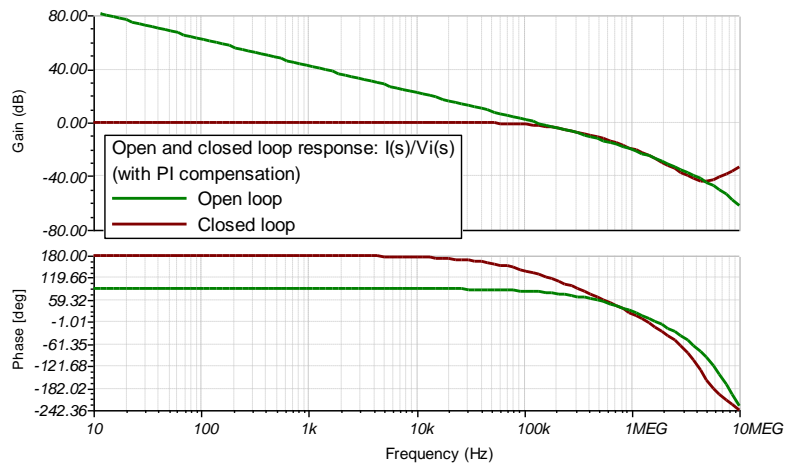


c) Analogue circuits for PI compensation control with low-pass filter

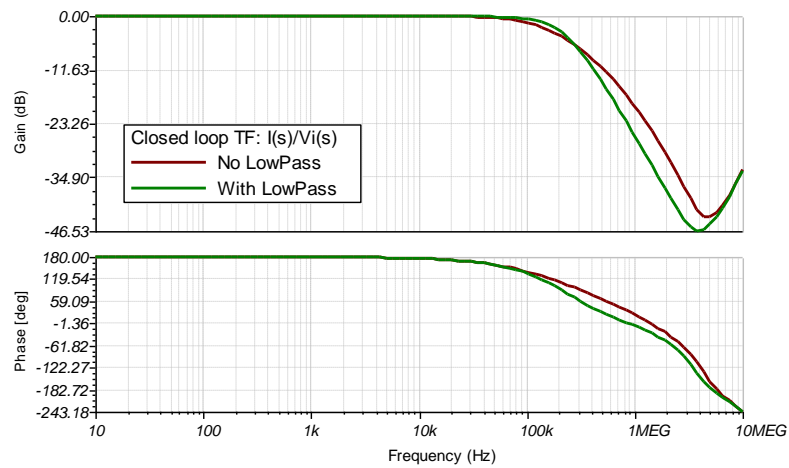
Figure 4-18: Different analogue compensation circuits for current closed-loop control



a) Open and closed-loop responses with P control



b) Open and closed-loop responses with PI control



c) Comparison of closed-loop transfer functions with and without low-pass filter

Figure 4-19: Simulated frequency responses with different analogue compensation circuits

#### 4.6.4 Experimental tests of the power amplifier stage

The developed controller board with cooling block is shown in Figure 4-20. The necessary protection circuits for the PA04 amplifier are adopted according to the part datasheet. A 2-ohm current sensing resistor is in series with the load, the resistor is capable to dispense heats at 30 W. Both the amplifier and the current sensing resistor are bonded to the cooling block with heat paste. The cooling block is made from a mono piece of aluminium with drilled channels in it. The power of the board is from two DC power supplies connected in a positive and negative form. The maximum voltage is limited to 36 V for safety concerns in these experiments.

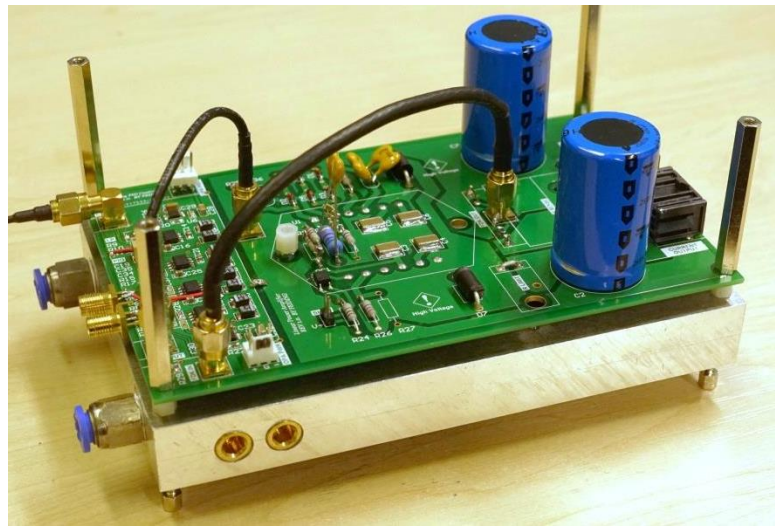


Figure 4-20: Photo of the developed current controller board with cooling block

Before the current control board is connected to the coil, the frequency response of the coil is measured first to identify the parameters and calculate the compensation components values. The test is conducted by injecting sinusoidal inputs to the coil assembly and measure the current in the coil. The tests are carried out both before the coil is inserted into the magnet track and after assembling. The measured results are shown in Figure 4-21.

It can be seen that in the free air, the response is close to that of a first-order model. However, the frequency response is not a first order low-pass shape when the coil is inserted into the magnet track. The inductance of the coil changes when it is close to the ferrous iron yoke. As the flat coil assembly is inserted into the magnet track assembly, the high frequency response is raised with less phase loss. This is caused by

the reaction between the coil and the iron yoke. On one hand, the present of low resistance magnetic path increases the self-inductance of the coil. On the other hand, the high frequency magnetic field induces eddy currents in the yoke and cause energy loss.

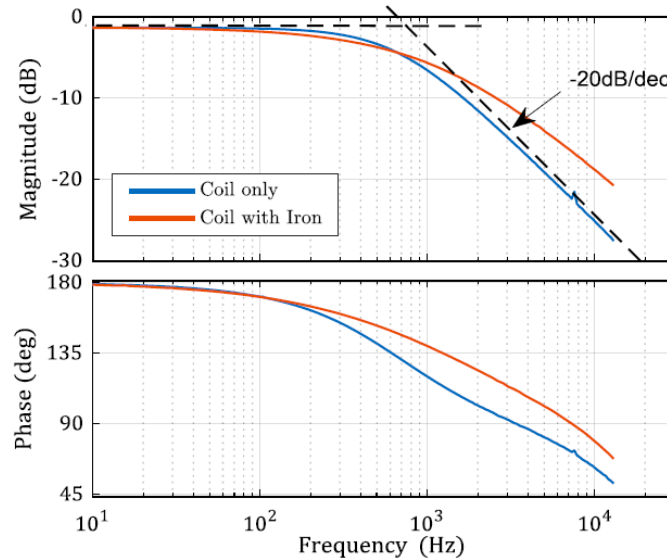


Figure 4-21: Frequency responses of the coil with and without core iron (units)

The mismatch of the model will affect the order of the closed-loop current transfer function. If the coil transfer function is a perfect first-order one, then the resulted current loop transfer function will also be of perfect second order. However, the designed analogue PI circuits can only ideally compensate for one pole. In this case, the overall coil response is still approximated by a first order system. The mathematical model is derived as:

$$H_{coil} = \frac{1.1179e + 05}{(s + 1.552e04)} \quad (4-3)$$

The estimated coil resistance is  $0.55 \Omega$  and the inductance is  $0.23 \text{ mH}$ , compared with the designed values in Chapter 3 of  $0.3657 \Omega$  and  $0.3131 \text{ mH}$ .

The pole in the coil frequency response is located at  $1.552 \times 10^4 \text{ rad/s}$ . A capacitor with  $8.2 \text{ nF}$  is selected as the  $C_{10}$  and thus the compensation resistor  $R_3$  is calculated as

$$R_3 = \frac{1}{1.552 \times 10^4 \times 8.2 \times 10^{-9}} = 7.857 \text{ k}\Omega \quad (4-4)$$

The resistor value is chosen to be 8 kΩ. The closed-loop response is shown in Figure 4-22. This resistor value is also changed to 1 kΩ to see how the PI compensation corner frequency mismatch affects the loop shape. It can be seen in Figure 4-22 that with a 1 kΩ resistor, a higher resonant response is observed. The sharper response is not desired since the noise in the previous stage will be amplified in this frequency region.

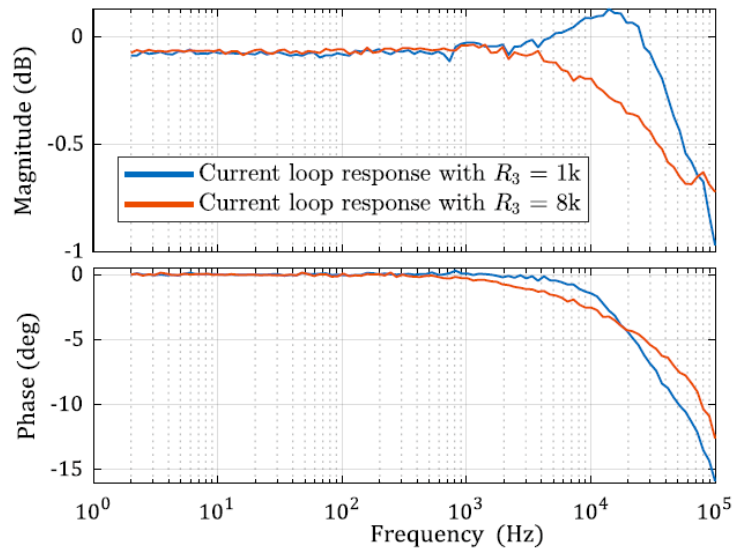


Figure 4-22: Current closed-loop response with different compensation resistors

When the loop proportional gain is increased by tuning the gain resistor  $R_2$ , the bandwidth of the current loop is increased as shown in Figure 4-23. However, the current regulation noise will also increase with a higher bandwidth. Therefore, a medium proportional gain of 0.5 is selected and the resulted closed-loop bandwidth is 400 kHz at -3dB. This bandwidth is high enough for most applications compared with the commercial motor drives of several kHz bandwidths.

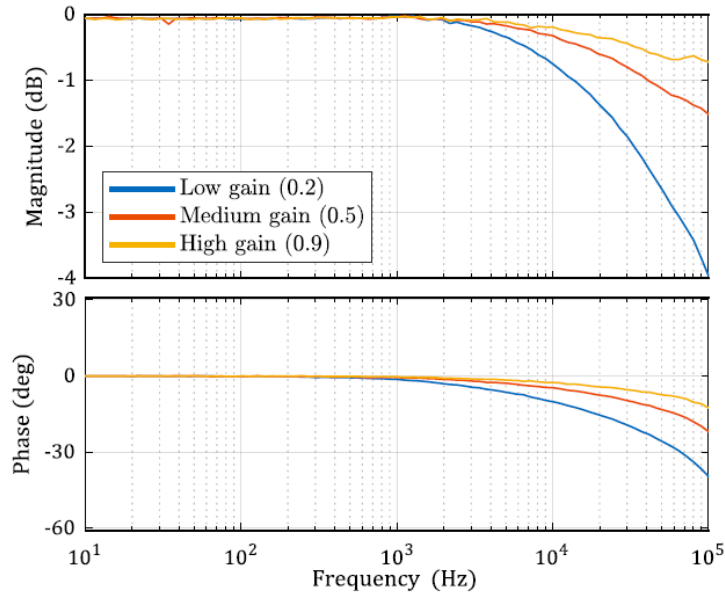


Figure 4-23: Measured current loop response with different proportional gains

The current outputs are measured under stationary condition and the current noise is shown in Figure 4-24. The measurements are conducted for 32 times and the spectrums are averaged with the same procedure as the sensor noise measurement. One clear peak at around 8 kHz is obvious in the spectrum, whose cause is not clear yet.

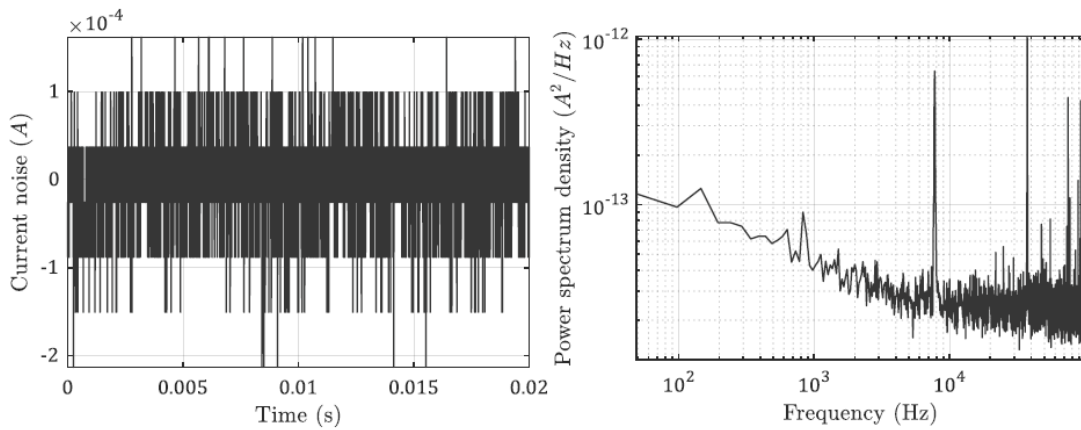


Figure 4-24: Measured current stage noise and corresponding spectrum

## 4.7 Summary

In this chapter, a high performance digital controller and a current control power amplifier are designed and developed for the fast tool positioning system. A very thorough understanding has been established on how the signals propagate within the



digital controller and how they are amplified to drive the motor. The voltage signal from the feedback sensor is delayed by the ADC sampling, reading, processing and DAC output stages. At the same time, the electrical noise is picked up and mixed with the signals. The root causes of those delays and noise are identified in this chapter and this lays the foundations for the future analysis of the positioning loop.

The analogue current controller, which amplifies the controller output into high power energies, is then built. The pure analogue design ensures a high bandwidth of 400 kHz. Different compensation circuits and their responses are studied. Finally, the PI compensation with low-pass filtering structure is adopted.

By going through all the design and developing procedures as above, the dynamic signal chains within the electronics are revealed, which are fundamentally important in determining the loop performance of high-speed control. This knowledge is not always available with off-the-shelf products. Potential improvements of the controller are identified for future revisions. In addition, electronics with higher performance than commercial products are realised with relatively low costs.

# CHAPTER 5

## Dynamic error analysis in single feedback control loop

### 5.1 Introduction

In this chapter, the previously developed stiff-support positioning device and the control boards are put into closed-loop control. The control law is based on PID control algorithm. A systematic error analysis approach, which reveals the contributions of disturbances on the tool positioning errors, is proposed and verified.

Firstly, the dynamic model of the mechatronic system is established. The frequency response function of the built device is measured by sweep sinusoidal excitation. The system parameters are estimated by comparing the experimental data with the theoretical model.

Secondly, the propagations of the disturbances and their contributions to the positioning errors in the closed-loop are analysed. Each disturbance source is treated as a stochastic process and these stochastic disturbances are synthesised in the frequency domain. The real tool positioning error, which is free from sensor noise, is revealed. The differences between following error and real positioning error are discussed and clarified. A series of closed-loop positioning tests under different moving masses and various bandwidth settings are conducted. The estimated following errors from the model are compared with the measured values at each condition and the error analysis approach is justified. The error spectrums are also decomposed, and the roots of these error spectrums are found out.

Lastly, the dynamic stiffness of the positioning system is discussed. The influences of cutting force are modelled and experimentally verified in the cutting experiments.

## 5.2 General model of single-feedback control loop

A single feedback closed control loop primarily consists of the actuator to be controlled, the controller and the feedback sensor. Below shows a generic block diagram of a control system where  $G$  represents the plant model. In control theory, plant is a term used to describe the combination of physical process and actuator that are under control.  $K$  block represents the control action, realised by either a digital controller or analogous circuits. The  $H$  block is used to describe the dynamics of the feedback sensor. The symbols  $r$ ,  $u$  and  $y$  represent the command input, controller output and the controlled output respectively. There are two disturbances injected into the loop shown as  $d$  and  $n$  in Figure 5-1.  $d$  is called input disturbance because it occurs at the same location as the input of the plant.  $d$  is of the same unit as the controller output. The disturbance  $n$  is the output disturbance (including sensor noise) in the same unit of the plant output. There are possible other disturbances but these two are the common ones and others can be equivalently converted to those inputs.

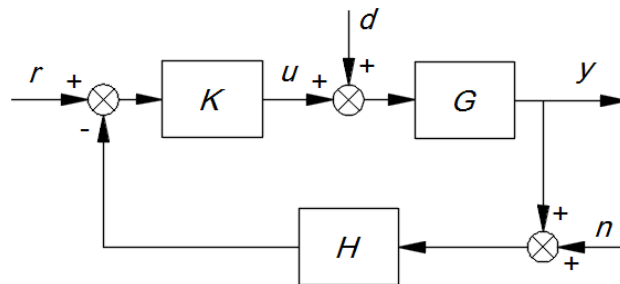


Figure 5-1: Typical single-feedback control loop configuration

The performance of an actively controlled loop can be evaluated by two merits: the reference tracking ability and disturbance rejection ability.

1. *Reference tracking*: The ability to keep the plant output  $y$  in track with the command input  $r$ .

The reference tracking ability indicates how well the tool follows the trajectory as the operator programmed in CNC machine tools. It is possible that the tool can follow the shape of the commanded trajectory quite well but with a certain time delay. This might be less a problem in single axis positioning application than in a multi-axis application [141]. Additional feedforward control actions can be used to correct the reference tracking performance.

2. *Disturbance rejection*: The ability to keep the plant output  $y$  unchanged despite all the disturbances.

The disturbances  $d$  and  $n$  tend to disrupt the plant output  $y$ . In manufacturing scenario, the disturbances may come from the cutting forces, cable forces, the environmental vibrations and some other unstable conditions within the machine tool. The paramount tasks of machine tool builders are to minimise the influences of these disturbances in order to achieve ultra-precision machining quality. In a broader point of view, the disturbances also include the process disturbances representing the changes of the plant characteristics. This may result from a change of the slide mass of the machine tool or change of motor winding resistance due to temperature variations.

The performances can be represented by the transfer functions from reference  $r$ , disturbance  $d$  and output disturbance  $n$  to the controlled plant output  $y$ . These transfer functions are shown as below. These three transfer functions also have the names of output sensitivity  $S$ , input sensitivity  $D$  and complementary output sensitivity  $T$  respectively. Output sensitivity  $S$  reflects the ability to reject sensor noise of the system and input sensitivity  $D$  reflects the ability to reject force disturbances.

$$\frac{y}{n} = \frac{1}{1 + KGH} \quad (\text{Output sensitivity } S) \quad (5-1)$$

$$\frac{y}{d} = \frac{G}{1 + KGH} \quad (\text{Input sensitivity } D) \quad (5-2)$$

$$\frac{y}{r} = \frac{KGH}{1 + KGH} \quad (\text{Complementary output sensitivity } T) \quad (5-3)$$

The purposes of closed-loop control are to minimise the disturbance sensitivity functions  $S, D$  and make  $T$  equal one across the frequency axis. If the open loop gain  $KGH$ , also known as  $L$ , is high enough then the output sensitivity  $S$  approaches zero and the complementary output sensitivity  $T$  approaches one. However, it will be a different situation for input sensitivity  $D$ . It depends on how open loop transfer function is increased. In fact, simply increasing the plant response  $G$  to command input will lead to a larger  $D$ . The proper way is to make  $G$  small and  $KGH$  large at the

same time. That means the product of  $KH$  largely determines how the closed-loop system response to the input disturbances and this job is mostly done on the controller.

### 5.3 Another point of view on the effects of the closed-loop control

The time domain response of the physical plant can be described by a series of differential equations, which turns to transfer functions after Laplace transform. The differential equations can also be described by the so-called state space representation. The state space representation unveils the connections between each variable. For the single degree of freedom mass-spring-damper system shown in Figure 5-2 a), one of its state space realizations is shown as black in Figure 5-2 b), where  $a$ ,  $v$  and  $x$  represents the acceleration, velocity and position of the moving mass respectively.

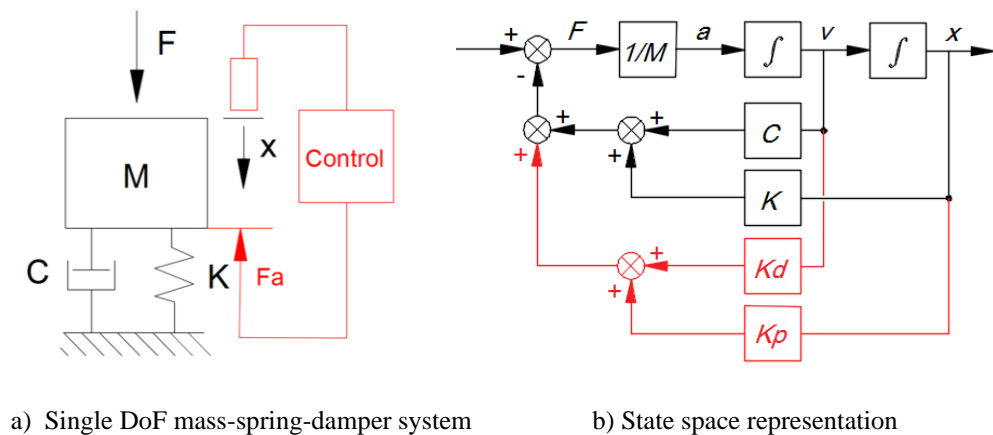


Figure 5-2: State space representation of a simple system under PD control

When a feedback control mechanism is deployed in the control loop, shown in red in Figure 5-2 b), the closed-loop system's behaviour changes and can be treated as new plant. Here a simple Proportional Differential (PD) control structure is shown. From the control aspects, the controller imitates the natural spring effect by reading the position signal and generating a proportional negative force on the moving body. Since the  $Kp$  term is in parallel with the original  $K$  term, they have the same effects in the closed-loop system. Then the new spring term of the system will be  $Kp + K$ . Similarly, the damping effect can be simulated by velocity feedback and virtual mass can be achieved by acceleration feedback. These adjustable terms form the new characteristic matrix of the closed-loop system [138].

Active control can simulate some non-existing effects in the natural world as well. For example, the integral action in the closed-loop helps achieving super spring effect with infinite static stiffness. What's more, the natural interaction forces only occur between two interacting bodies. In the active control method, the sensor measurement may come from other remote bodies. This brings more possibilities of the control effects. However, active control comes with its own imperfections. The sensor measurement always includes some noise. When a digital controller is used, the computation delay and sampling delay put a limit on the achievable closed-loop bandwidth.

#### 5.4 Modelling of the mechatronic system with error sources

The dynamic model of the mechatronic system is established in this section. This model is used for two purposes. One purpose is to compare the model with the real device response and get more accurate parameter estimation. The second purpose is to use this model as the basis for controller design and the analysis on error sources.

Figure 5-3 shows the closed-loop diagram of this tool positioning system. It mainly consists of a digital controller with A/D and D/A convertors, a power amplifier stage, the mechanical device with a motor and a displacement sensor.

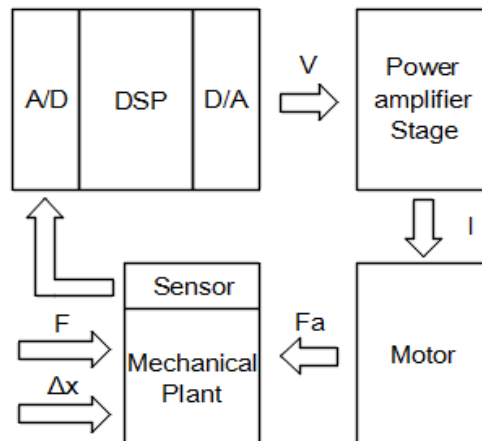


Figure 5-3: Closed-loop servo system diagram

The lumped-parameter model of the mechanical system is established as shown in Figure 5-4, according to mechanical structure designed in Chapter 3. The  $m_1$  block represents the tool tip flexibility and it is all about the dynamic performance of the tool

holder and coil support.  $k_1, c_1$  should always be designed as high as possible because the driving force has to go through this flexibility before reaching  $m_1$ , adding phase lag in the loop.  $m_2$  is the mass of the movable body including coil assembly and sensor. The  $k_2$  and  $c_2$  are the stiffness and damping of the flexure bearing.  $m_3$  represents the mass of the X carriage.  $m_4$  is any flexible mass that will disconnect from  $m_2$  at high frequency. Perhaps there are multiple  $m_3$  and  $m_4$  in practice but only the dominant one is modelled here.  $k_5$  and  $c_5$  are the stiffness and damping of the motor coil reference to magnets. Since Lorentz motors virtually have zero stiffness,  $k_5$  is almost zero.  $c_5$  can be changed by inserting conductors in the magnetic field and eddy current damping can be achieved.

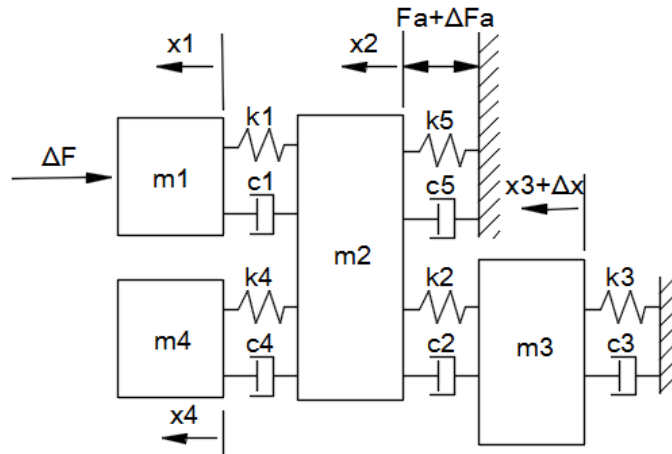


Figure 5-4: Lumped-parameter model of the mechanical system

The major disturbance sources in the mechanical setup are shown in Figure 5-4 as well. The disturbance sources are identified as cutting force  $\Delta F$  and environmental vibration  $\Delta x$ . The transfer functions from disturbances to tool tip position  $x_1$  are derived as in Appendix C and the results are listed as below ( $s$  is the complex frequency in Laplace transform,  $Z(s)$  is introduced to simplify the representation):

$$\frac{X_1(s)}{\Delta F(s)} = 1/[Z(s) \times (k_1 + c_1 s)/(Z(s) + k_1 + c_1 s) + m_1 s^2] \quad (5-4)$$

$$\frac{X_1(s)}{Fa(s)} = k_1/[Z(s)(k_1 + c_1 s + m_1 s^2) + (k_1 + c_1 s)m_1 s^2] \quad (5-5)$$

$$\frac{X_1(s)}{\Delta X(s)} = k_1(k_2 + c_2s)/[Z(s)(k_1 + c_1s + m_1s^2) + (k_1 + c_1s)m_1s^2] \quad (5-6)$$

Where  $Z(s)$  is denoted as:

$$Z(s) = \frac{(k_4+c_4s)m_4s^2}{k_4+c_4s+m_4s^2} + \frac{(k_3+c_3s+m_3s^2)(k_2+c_2s)}{k_3+c_3s+m_3s^2+k_2+c_2s} + k_5 + c_5s + m_2s^2 \quad (5-7)$$

The frequency response of the displacement sensor can be approximated by second order Butterworth low pass filters as

$$H_{capa} = \frac{V_{capa}(s)}{X(s)} = \frac{\omega_{capa}^2 S_{capa}}{s^2 + 2\omega_{capa}s + \omega_{capa}^2} \quad (5-8)$$

Where:  $\omega_{capa}$  is the measuring bandwidth (-3dB) of the sensor electronics and  $S_{capa}$  is the sensitivity of the capacitive sensor.

The current loop transfer function from controller output voltage  $V_{cmd}$  to motor current  $I$  can also be modelled with a low pass characteristic:

$$H_I = \frac{I(s)}{V_{cmd}(s)} = \frac{\omega_I^2}{s^2 + 2\zeta\omega_I s + \omega_I^2} \quad (5-9)$$

Where:  $\omega_I$  is the current loop bandwidth of 400 kHz and the damping coefficient  $\zeta$  is selected as 0.707 according to the shape of frequency response of the current loop.

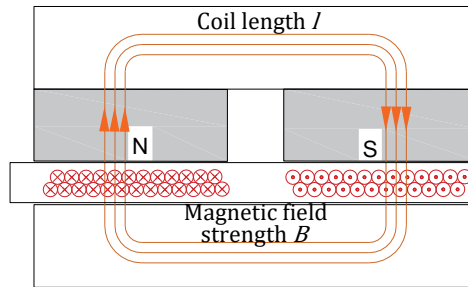


Figure 5-5: Flat voice coil motor structure

Then the output force from the flat voice coil motor can be obtained according to the force constant  $K_T$  and motor current  $I(s)$  as

$$F_a(s) = K_T \times I(s) \quad (5-10)$$



## 5.5 Plant parameter identification

System identification process is necessary because the built system may deviate from the designed parameters. The identification process is composed of input excitation, output measurement, estimation of frequency response function and fitting of the measured data with a model.

### 5.5.1 Input excitation sources and signal processing

The selection of a proper excitation signal type is very important in frequency response tests. The primary requirement on the input signal is that it must contain all the frequency contents in the interested frequency range. Either this can be done by a sweep manner or the test is done at all frequencies at one time. There are several signal types widely used in the modal test field and they are shown in Figure 5-6. There is a very comprehensive and useful booklet discussing the practical issues in frequency response testing written by Pete Avitabile [142].

The sweep sinusoidal signal in Figure 5-6 a) is a signal train consisted of many sinusoidal segments. Each segment has a stable frequency. At the beginning of each segment, the amplitude is designed to increase linearly from zero to the desired amplitude. This ramp ensures smooth transition from one frequency excitation to another and avoids stimulating unwanted dynamics. The sampling of data starts after a few of signal periods, called the settling time, in order to get stable response. The length of the settling time should be selected large enough to allow the lowest dynamics to settle down.

The chirp signal is also a sweep type sinusoidal excitation, but the frequencies are changed continually in the time domain as shown in Figure 5-6 b). This will increase the number of frequency test points but does not allow time for stable response conditions at each frequency.

Another type of excitation signal is the pure random signal as shown in Figure 5-6 c). Since the spectrum of a random white noise is flat, it can stimulate all the dynamics of the system under test. There are two factors associated with the pure random method that make it less preferable in high precision applications. One is that the start and end

of the signal are not zero, and this will cause leakage problem<sup>9</sup>. The amplitude of the peak response will be lower than real value because some of its power leaks to other frequencies and the measured results will show a higher damping. The other factor is that the amplitude of each frequency component cannot be made high enough at the same time due to the limited power of the exciter. With the same noise floor of the sensor, the Signal to Noise Ratio (SNR) with random based excitation method is lower than sweep method. Despite all these shortcomings, random signals are still used in industry because this method requires the shortest measuring time.

The leakage problem with pure random excitation, and may be other signals, can be alleviated by applying windows to the time domain signal. The idea is to force the start and end of the signal to be near zero by multiplying scaler coefficients. The time domain multiplication will distort the frequency content of the signal. Therefore, both the input and the measured output signals are applied by the same window. The equally distorted spectrums can still be used to reveal the frequency response function of the system.

Another way to avoid the leakage problem with random excitations is the burst random signal type in Figure 5-6 d). The random excitation is shunt after a certain time and let the output to settle down. The sampled data includes the zero start points and the zero endpoints. Therefore, signal windowing is not necessary.

The pulse impact method in Figure 5-6 e) is mostly found in modal testing of mechanical structures. In this method, an impact hammer with a force sensor is used to apply short lasting force to the structure and the vibrations are picked up by acceleration sensors or displacement sensors. The durations of the impact can be tuned by changing hammer tips with different softness. The last type of excitation is the step impact in Figure 5-6 f), which is often used in the time domain to estimate the rising time and damping of the system quickly.

---

<sup>9</sup> More information on spectral leakage at [https://en.wikipedia.org/wiki/Spectral\\_leakage](https://en.wikipedia.org/wiki/Spectral_leakage)

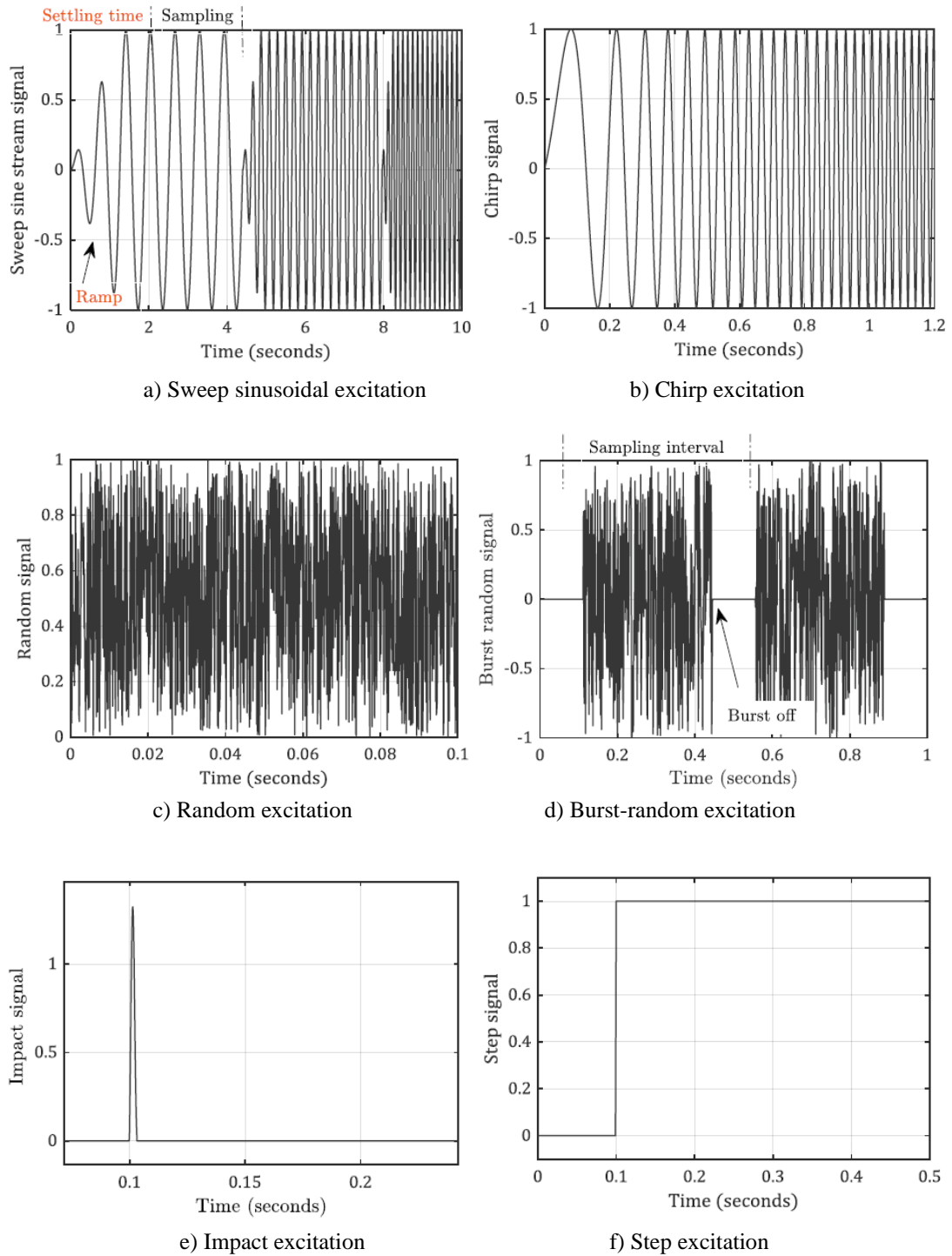


Figure 5-6: Typical excitation signals used in frequency response tests

The different input signal types reveal different aspects of the system characteristics. The sweep sinusoidal and chirp excitation signals are deterministic signals. The amplitude of each frequency contents can be controlled by changing the time series data. This characteristic differentiates these signal types from the other random

excitation ones. For a non-linear system, the system output is not only determined by the system transfer function, but also related to the input amplitude. The sweep sinusoidal and chirp inputs should be used when the nonlinearity of the system is of interest, while the random based excitations are to be used when the nonlinearity is not important. Impact excitation signal is a little different from the above. It can be determined both in the time domain and in the frequency domain. However, in the real tests, the impact is generated by hitting the part with a handheld hammer and the impact force amplitude is difficult to control accurately. Therefore, it is not suitable for characterizing the nonlinearity of a system. The characteristics of common excitation signal types are listed in Table 5-1.

Table 5-1: Characteristics of common excitation signal types

	Sweep Sine	Chirp	Pure Random	Burst Random	Impact
Signal to Noise Ratio	Very high	High	Fair	Fair	Low
Leakage control	No	No	No	Yes	Yes
Measuring time	Very long	Fair	Good	Very short	Very short
Characterize Nonlinearity	Yes	Yes	No	No	No

Based on the above discussion, the sweep sinusoidal signal is selected to test the response of the built positioning system. Sweep sinusoidal commands are sent from the D/A convertor and the response of the open loop system is measured by the capacitive displacement sensor. The settling time at the beginning of each segment is set to one second. After that, four periods of input and output signals are acquired at the same time. The sampling rate of the developed controller board is set to 200 kHz which mean the frequency response can be measured up to 100 kHz. The length of the data is strictly controlled to be integral numbers of signal periods. Before each test, a pre-test is conducted to get an estimation of the response shape. Then the input signal amplitudes are scaled accordingly such that the weak response dynamics can be excited effectively. In this way, the measurement SNR can be improved, especially at the high frequency range.

### 5.5.2 Calculation of frequency response functions

Once the input and output response data are sampled, the time domain data should be transformed into the frequency domain through the Discrete Fourier Transform (DFT) algorithm. This post processing procedure might also introduce some errors. The most popular method is the Fast Fourier Transform (FFT) algorithm. FFT is one type of DFT algorithms especially optimised for computational speed. There are several requirements for this algorithm can be used. One of them is that the number of sample points should be integral powers of two. In commercial computation software like MATLAB, the length of the data is either truncated or padded to the closest power of two if this condition is not satisfied. However, in the sweep sinusoidal method, the sampled signal length should be integral numbers of signal period. These two requirements cannot be satisfied at the same time because the sampling rate of data acquisition hardware cannot be set arbitrarily. The direct DFT algorithm does not require the “power of two” condition and the calculation equation is shown as below [143].

$$X_k = \sum_{n=0}^{N-1} x_n \cdot e^{-\frac{i2\pi}{N}kn} \quad (5-11)$$

Where:  $x_n$  is the time series data,  $N$  is the number of samples,  $X_k$  is the transformed complex value at frequency bin of  $k$ . After the direct DFT transformation is used to calculate the frequency spectrums, the frequency response function of the system is calculated as

$$H_k = \frac{Y_k}{X_k} \quad (5-12)$$

Where:  $X_k$  and  $Y_k$  are the Fourier transform of the input and output data respectively.  $H_k$  is the calculated complex frequency response value.

The measured frequency response functions from DAC output to the sensor voltage are shown in Figure 5-7. The frequency response measurements are repeated for two conditions with different moving masses. It can be seen that the response curve possess typical second order low pass characteristics. When the moving mass is increased from 0.075 kg to 0.175 kg, the mass line is lower at frequencies less than 7 kHz. However,

when the frequency is higher, the response curve no longer follows the same rules any more. This phenomenon indicates that the root causes of the frequency response at these two regions are different. The high frequency response is mostly dominated by the electrical crosstalk between the power line signal and the sensor feedback signal, while the low frequency response is predictable with the mechanical model.

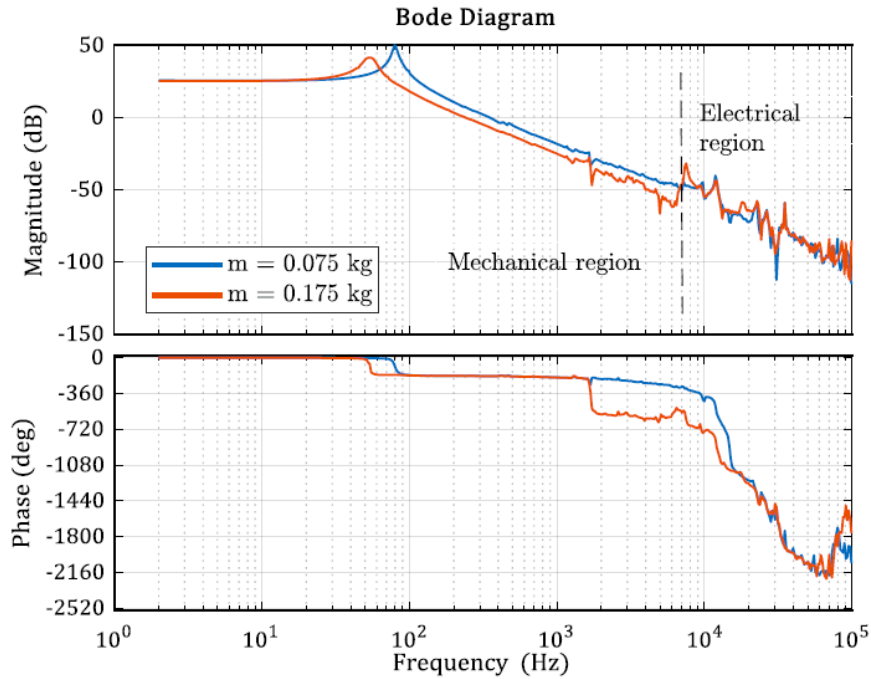


Figure 5-7: Measured frequency response of the built positioning system

A single frequency response curve is not sufficient to estimate all the plant parameters. For example, if the motor force constant and the plant response are scaled by the same amount, the resulted open loop response will remain the same. Before the system parameters can be estimated, the motor force constant is estimated in a separate test. In this test, the movable part is pushed against a dynamometer (Kistler 9129AA) and the force generated by the voice coil motor is measured. The motor current is controlled at a series of values. The measured force and current values are plotted in Figure 5-8. The linear fit reveals the force constant of the motor as 3.6658 N/A. This value is close to the calculated force constant value of 3.914 N/A in Chapter 3.

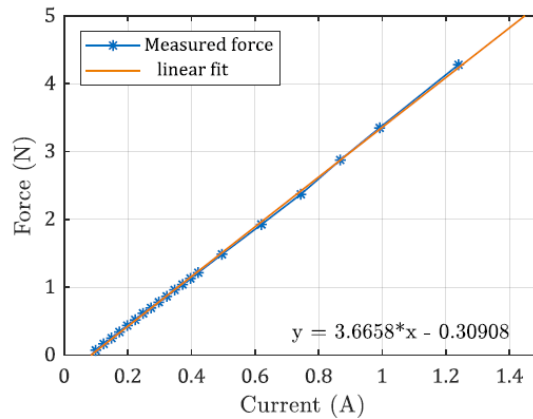


Figure 5-8: Linear fit results for the motor force constant calibration

### 5.5.3 Parameter estimation

There have been many studies on trying to estimate system parameters, like stiffness, damping, residues, from the measured FRFs [144]. The simple way is to pick the peak magnitudes and calculate the damping coefficient by the ‘half power point’ method. However, this method is not accurate enough. Some automatic calculation algorithms include least square complex exponential (LSCE), least square frequency domain (LSFD), eigenvalue reconstruction analysis (ERA), rational polyfit, frequency domain direct parameter identification (FDPI) and the most popular one, the poly-reference Least Squares Complex Frequency-domain (pLSCF) estimator [145]. Unfortunately, each estimator is not capable of estimate all the parameters at one time, and it is more difficult when the system has high damping or close poles.

In this case, the structure of the system is known and the mathematical model is used as the grey box model. The model parameters are then estimated by fitting the grey box model and the experimental data in MATLAB<sup>10</sup>. The estimated open loop transfer function is shown in Figure 5-9. It is seen to be of 97.7% fit to the measured data, which is evaluated by the normalized root mean square error between the model prediction and measured data.

The electrical crosstalk effects are modelled by extra residue terms. These terms remain unchanged when the plant parameters are changed to study the effects of influences of structural parameters later.

<sup>10</sup> More on greybox estimation in MATLAB: <https://uk.mathworks.com/help/ident/ref/greyest.html>

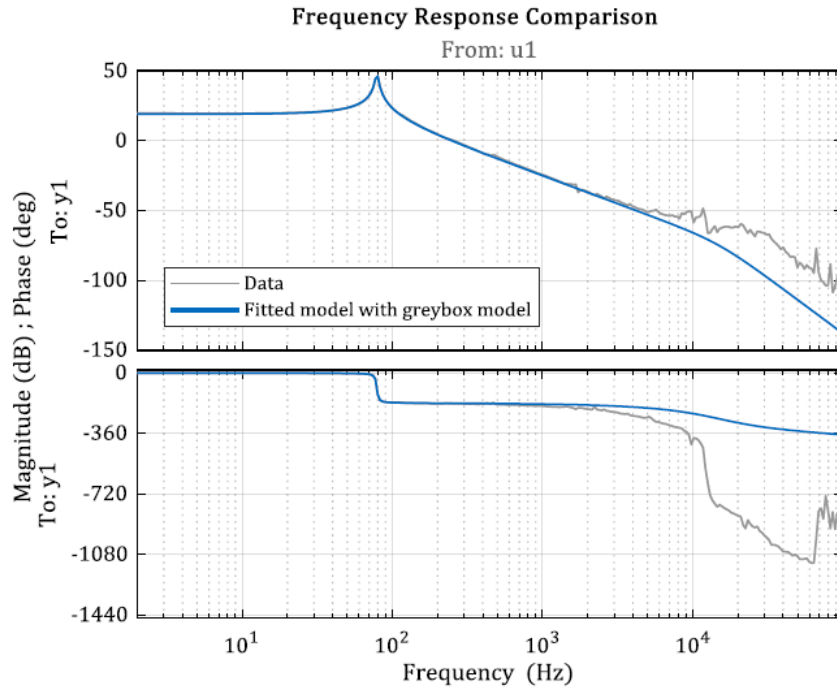


Figure 5-9: Fitted model with grey box model

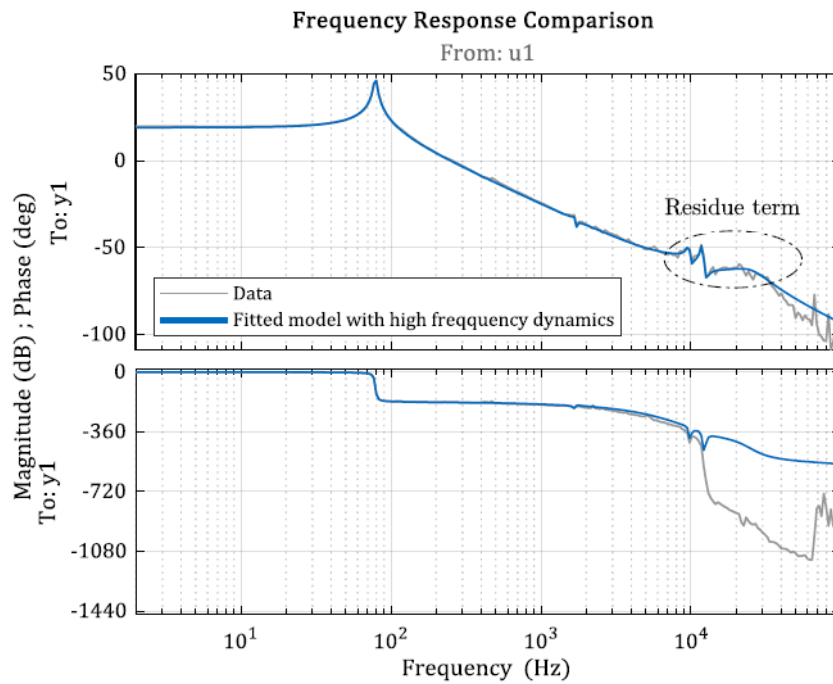


Figure 5-10: Fitted model with grey box model and high frequency residue terms

It can be seen that the fitted model can represent the frequency response of the system up to 10 kHz when the extra terms are used. Not all model parameters are identified because they are not apparent in the loop performance, such as the  $k_1$  and  $c_1$  parameters. The estimated variables are listed in Table 5-2. The accurate



modelling of the whole mechatronic system laid the foundations for the further deterministic control algorithm and error analysis approaches.

Table 5-2: Identified parameters of the positioning system

Parameters	Values
$m_1 + m_2$	0.074 Kg
$k_2$	21965 N/m
$c_2$	2.28 N/(m/s)
$m_4$	0.008 Kg
$k_4$	56285 N/m
$c_4$	6.18 N/(m/s)

## 5.6 Calculation of the PID controller gains

The established model will be used in calculating the controller gains and then study the error propagations. The control action in the digital processor is one of the signal chains in the closed-loop. Before the closed-loop transfer functions can be derived, the controller structure and parameters have to be determined first. In this chapter, the parallel PID structure as shown in Figure 5-11 is adopted and both electrical driving components and mechanical elements are closed in a single loop. The feedback is the tool position measured by the capacitive sensor.

The PID controller gains are calculated using the MATLAB patented algorithm based on the measured open loop transfer function [146]. A very comprehensive procedure for tuning a PID controller for positioning control can also be found in the JPE Precision Point booklet or on the website<sup>11</sup>.

<sup>11</sup> <https://www.janssenprecisionengineering.com/page/motion-control-basic-feedback-design/>. (Last accessed June, 2019)

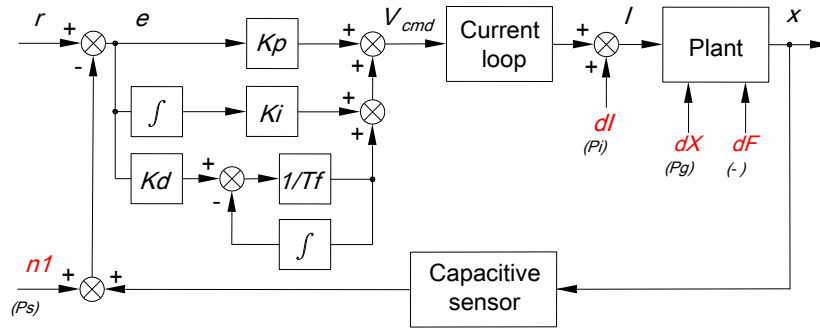


Figure 5-11: Block diagram of PID position loop

## 5.7 Error contribution analysis

### 5.7.1 Stochastic and non-stochastic errors

The positioning stability of a motion system describes its ability to maintain at commanded position despite all kinds of disturbances, like cutting force, ground vibration etc. The disturbances in Figure 5-11 can be treated as stochastic noise superimposed on slow varying non-stochastic components. The stochastic components do not repeat themselves in each measurement, but they pose stable statistics characteristic like PSD functions [147]. For example, the electrical noise from a sensor is random but its thermal drift is predictable and repeatable. The PSDs of the stochastic components of the disturbances from sensor  $n1$ , current noise  $dI$  and environmental vibration  $dX$  are denoted as  $Ps$ ,  $Pi$  and  $Pg$  respectively, which are all functions of frequencies. The cutting force disturbance is treated as non-stochastic of value  $dF$ .

The stochastic components of cutting force is set to zero at this point because cutting force is primarily determined by the cutting area. Very precise prediction model of cutting force has been realised by Zhu et al [148] and thus it is not considered stochastic. Although in practice there may be some random factors, like material impurity or micro grain boundaries, they are not considered here due to the difficulty of modelling and measurement. The disturbance values are listed in Table 5-3.

Both kinds of components contribute to the positioning errors and machining errors of a machine tool. Due to the different natures of the components, they are treated separately. The stochastic components are manipulated in the frequency domain since

they have stable PSDs. The non-stochastic components are analysed in the time domain.

Table 5-3: Decomposition of disturbance sources

Disturbance source	Stochastic components	Non-stochastic components
Displacement sensor noise	$Ps$	Treated as position command
Motor current noise	$Pi$	0
Environmental vibration	$Pg$	0
Cutting force	0	$dF$

A pre-requisition for analysing positioning errors is the knowledge of disturbance strengths. Thus, the disturbances are measured separately at each error source using data acquisition board and capacitive sensor. The PSD of the sensor noise ( $Ps$ ) has been measured in Section 4.5.2 and the current noise PSD ( $Pi$ ) has been discussed in 4.6.4 when the current controller is built. The third factor of noise from the environmental base vibrations is measured using the capacitive sensor over a long period. The measured vibrations and the corresponding PSD are shown in Figure 5-12.

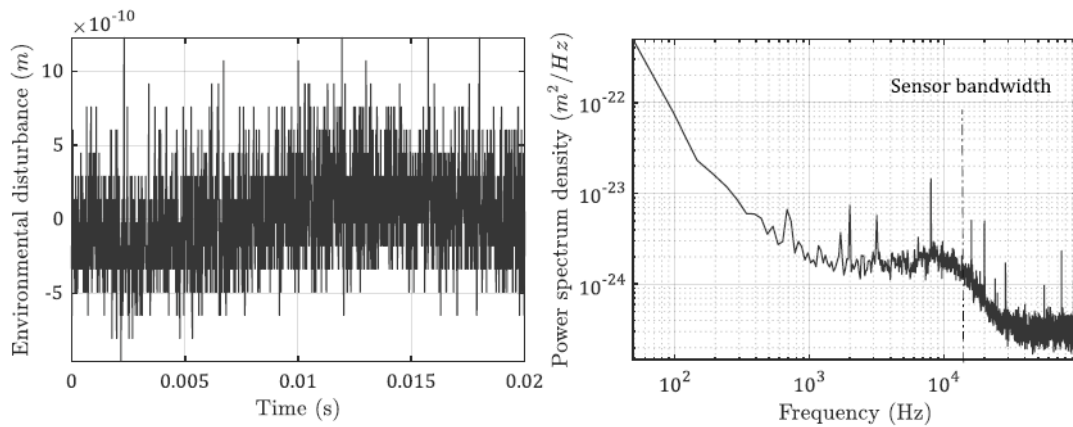


Figure 5-12: Environmental disturbance vibrations

### 5.7.2 Frequency domain synthesis of stochastic disturbances

The modelling of the whole positioning system and the calculated control algorithm makes it possible to analyse the noise propagation paths in the closed-loop system.

This is more comprehensive than considering the mechanical set-up or control algorithm alone. The disturbance propagation paths in the positioning system are shown in Figure 5-13. The stochastic components of each disturbance source are measured beforehand under stationary conditions.

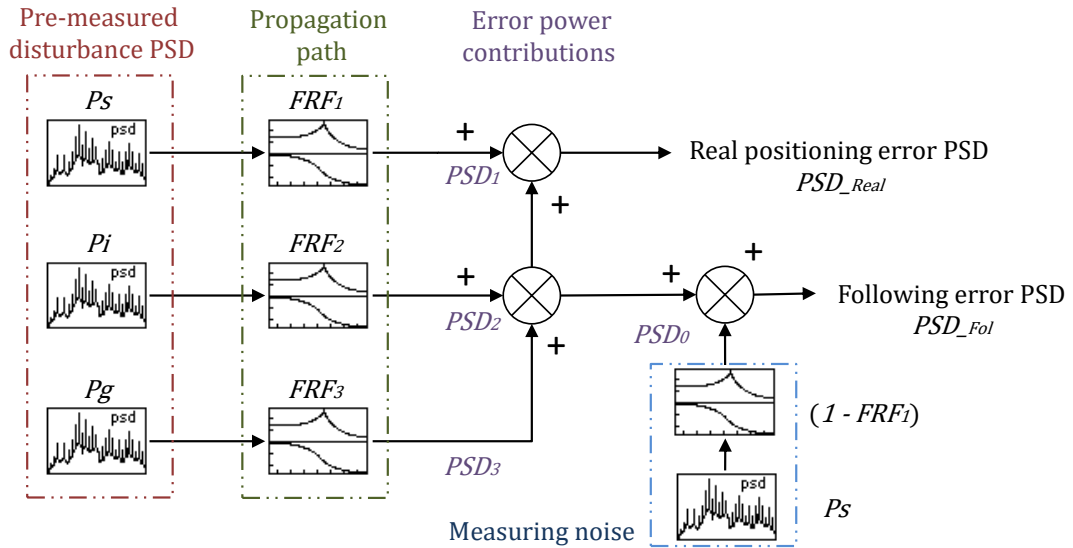


Figure 5-13: Diagram of stochastic disturbance propagations and measuring noise

In this diagram, the  $FRF_i$  represents the frequency response functions from each disturbance input to tool position, as modelled in Section 5.2. In order to get better positioning stability, these transfer functions should be made as low as possible. The error power contribution  $PSD_i$  from each disturbance to final position can be calculated according to [149] as:

$$PSD_i(v) = P_i(v) \times |FRF_i(v)|^2 \quad (5-13)$$

Where:  $i$  indicate the disturbance source number (from 1 to 3 with  $P_1, P_2, P_3$  representing  $P_s, P_i$  and  $P_g$ , respectively) and  $v$  is the frequencies. The  $PSD_i$  represents the power spectrum density of the position errors caused by each disturbance source distributed across the frequency axis. Since these disturbances are assumed mutually uncorrelated, their powers can be added to reflect the total error power. The synthesised tool position PSD is

$$PSD_{Real}(v) = PSD_1(v) + PSD_2(v) + PSD_3(v) \quad (5-14)$$

The function  $PSD_{Real}$  represents the true tool vibration spectrum. However, this value is not available in real applications. Most people use the position following error to indicate how accurate the tool is positioned. In a motion control system, following error is the instantaneous difference between the commanded position and the position as reported by the feedback sensor. It is commonly seen on the display screen of numerical control systems. Since every sensor has a certain level of noise floor, the reported position cannot represent the real tool position, especially in ultra-precision applications where the following errors is of the same level with sensor noise.

The following error can be estimated in a similar way as the real positioning error. The current noise and base vibration disturbance contribute the same amount of powers to the following error as to real positioning error. However, the sensor noise is treated differently. Since sensor noise is injected from the same location as the position reference in the loop, the sensor noise within the positioning bandwidth is tracked quite well and thus it does not show up in the following error. Only the difference between the sensor noise and the tracked sensor noise contribute to the following error. Thus, the following error PSD is calculated as

$$PSD_{Fol}(v) = P_s(v) \times |1 - FRF_1(v)|^2 + PSD_2(v) + PSD_3(v) \quad (5-15)$$

In order to estimate the time-domain error magnitude from the PSD values, the Cumulative Amplitude Spectrum (CAS) function is derived.  $CAS_i(v)$  is the square root of the integrated  $PSD_i(f)$  from 0 Hz to  $v$  Hz, shown in Eq.11.

$$CAS_i(v) = \sqrt{\int_0^v PSD_i(f)df} \quad (5-16)$$

The squared CAS value at Nyquist frequency is equal to the total power. The square of the time domain Root Mean Square (RMS) value is also the signal power. According to Parseval's Theorem [94], the signal power remains the same in the frequency domain and time domain. Thus, the error RMS value  $Err_{rms}$  is expressed as

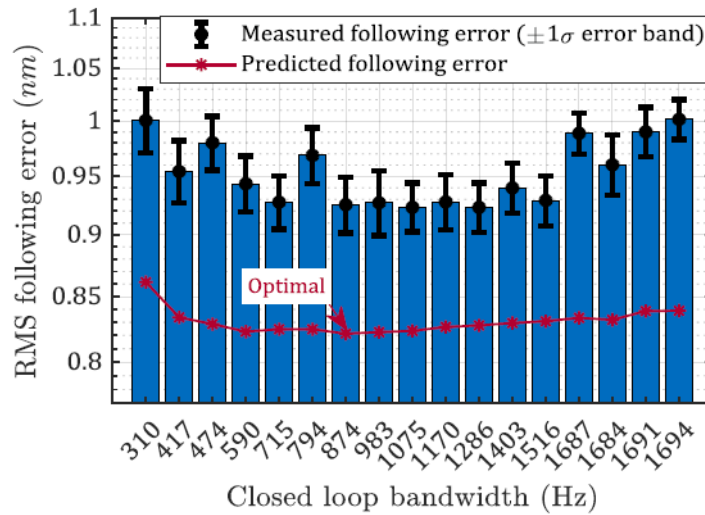
$$Err_{rms} = CAS_i(v_{Nyquist}) \quad (5-17)$$

Where:  $\omega_{\text{Nyquist}}$  is the Nyquist frequency. This relationship is used to link the estimated PSD function to time domain RMS error. The performance of the positioning system is evaluated by the RMS value of the real positioning error while the RMS following error is used to compare it with experimental results.

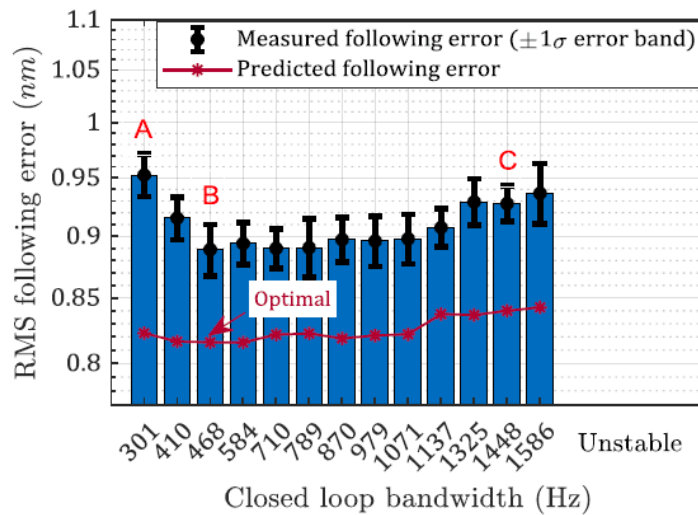
### 5.7.3 Closed-loop positioning error tests

The calculated controller action was transformed into C language codes and deployed in the developed controller board. The closed-loop update rate was set to 199.6 kHz and the following error was acquired at the same rate. Each acquisition includes 4096 samples. The moving mass was changed by gluing additional steel blocks onto the tool holder symmetrically, minimising the change of the centre of gravity. Two different moving masses, namely 0.075 kg and 0.175 kg, were achieved in this way. For each mass condition, the controller gains were adjusted from low to high, resulting in various cross over frequencies (or positioning bandwidths). Each following error measurement was repeated 32 times to reduce the influences of random factors.

As discussed before, the real positioning error of a motion system is not available. Thus, the following error readings from sensor feedback are used to verify the analysis approach. The RMS values of the following errors with two different moving masses are shown in Figure 5-14 a) and b) respectively. The error bar of each data point indicates the standard deviation of the 32 measurements. The predicted RMS following error is also plotted as a comparison. It can be seen that the estimated following error and the experimental data shows the same trends under both mass conditions. The optimal bandwidths of 874 Hz and 468 Hz agree with the measured data. There exists a constant difference of around 10 percent between the estimated value and the measured value, which is attributed to the modelling errors. It is evident that the following error has been reduced at bandwidths below 1 kHz with the larger moving mass. The following errors keep at the same level between the 1 kHz and 1.5 kHz range. Bandwidths higher than 1.6 kHz result in unstable loop for the 0.175 kg mass condition and thus the data is not available.



a) Following errors with 0.075 kg moving mass



b) Following errors with 0.175 kg moving mass

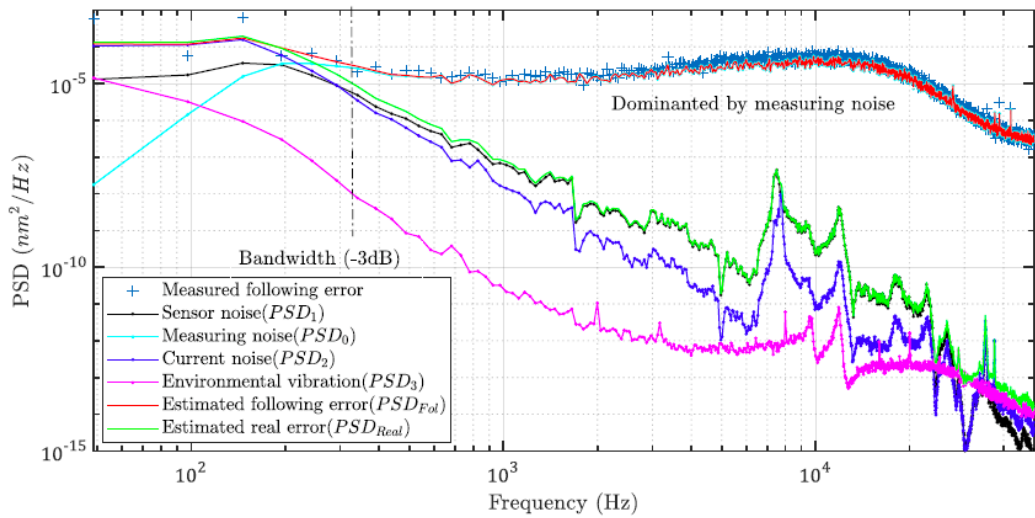
Figure 5-14: Comparison between measured following errors and estimated following errors with different moving masses and bandwidths

### 5.7.4 Spectrum analysis of measured errors

The frequency spectrums of the measured following errors at three bandwidths of 301 Hz, 468 Hz and 1448 Hz, marked as A, B and C in Figure 5-14 b), are shown in Figure 5-15. It can be seen that under all the three situations, the measured following error spectrum (blue cross) agrees with the synthesised following error spectrum (red) well. At low bandwidth as shown in Figure 5-15 a), the low frequency following error is dominated by current noise disturbance. While at high bandwidth as shown in Figure

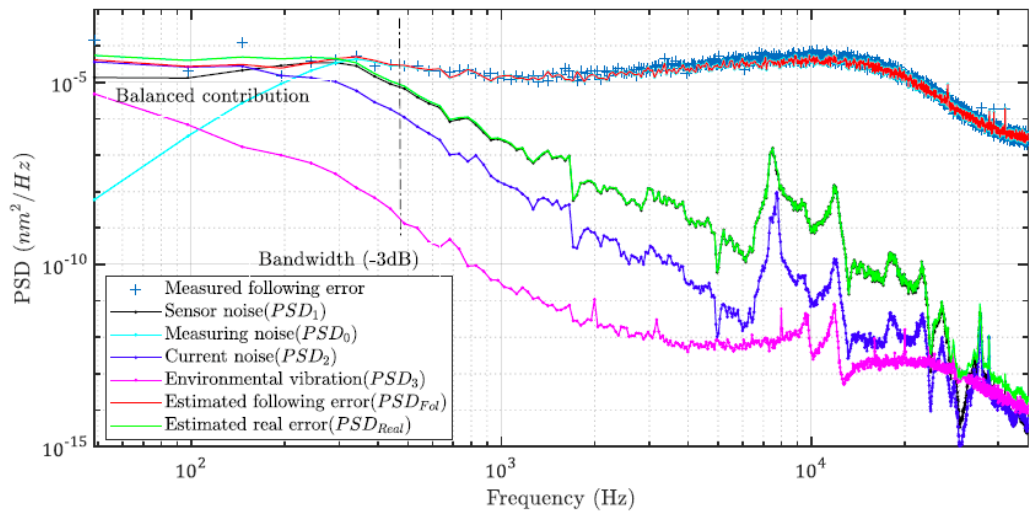
5-15 c), the low frequency following error is greatly reduced due to the better tracking ability, while noise around 1 kHz is greatly amplified. At the optimal bandwidth of 468 Hz in Figure 5-15 b), the error contributions from sensor noise and current noise are balanced. The agreed spectrums demonstrate that the error analysis method can predict the frequency components effectively.

With this approach justified, the real positioning error spectrum (shown in green) now can be estimated. There are many differences between the following error spectrum and the real error spectrum. Beyond the closed-loop bandwidth, the following error spectrum largely comes from the fake measuring noise. In fact, the tool only has very small physical vibrations at these frequencies. The differences are especially obvious at high bandwidth setting as in Figure 5-15 c). In the low frequency range, the following error is small, but the real positioning error is larger. In the high frequency range, the two real vibration peaks at 7.4 kHz and 11.7 kHz are buried in the measuring noise.

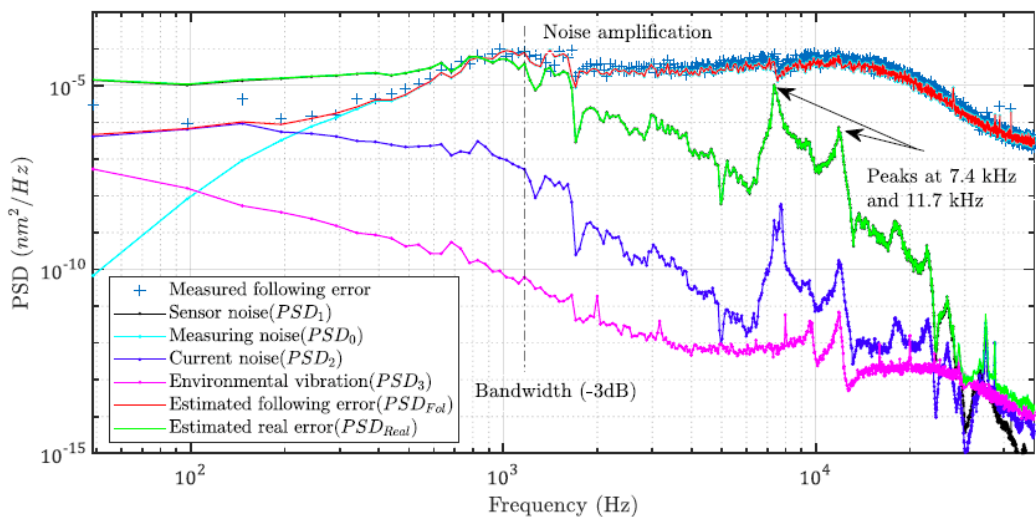


a) At 301 Hz bandwidth, the low frequency following error is dominated by current noise disturbance.





b) At the optimal 468 Hz bandwidth, the error contributions of PSD1 and PSD2 are balanced.



c) At 1448 Hz bandwidth, the low frequency following error is greatly reduced due to the better tracking ability, while noise around 1 kHz is amplified. High frequency components of real positioning errors are increased.

Figure 5-15: Spectrum analysis of predicted following errors and real positioning errors in comparison with experimental results

The results reveal that the following error signal hardly tells how the tool is vibrating. One sample of the time domain following errors at 468 Hz bandwidth is shown in Figure 5-16. This signal shows around 6 nm peak-to-valley value and the RMS value is 0.83 nm. In fact, the RMS real positioning error is estimated to be only 0.23 nm by the model prediction. The peak-to-valley value will be around 1.4 to 2.3 nm, which is 6 to 10 times of the RMS value as a rule of thumb.

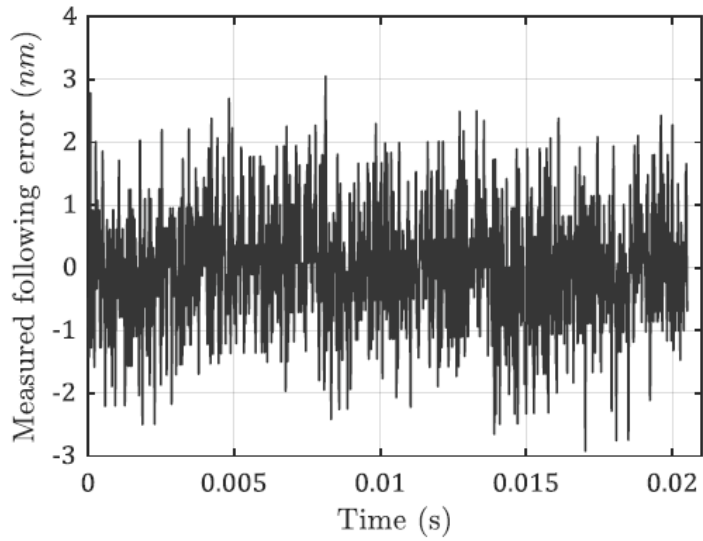


Figure 5-16: Following errors read from capacitive sensor feedback at 468 Hz bandwidth setting

The power percentages of real positioning errors contributed by each disturbance source are shown in Figure 5-17. It can be seen that the sensor noise contributes the largest portion of power when the bandwidth is higher than 1 kHz. This indicates that a high-quality sensor is essential for fast tool servo application. The environmental vibrations only contributed a very small fraction of power for every bandwidth setting. This is attributed to the stiff-support design and the low stiffness and damping of the flexure bearing. If an air bearing is used instead, the contribution will be even lower.

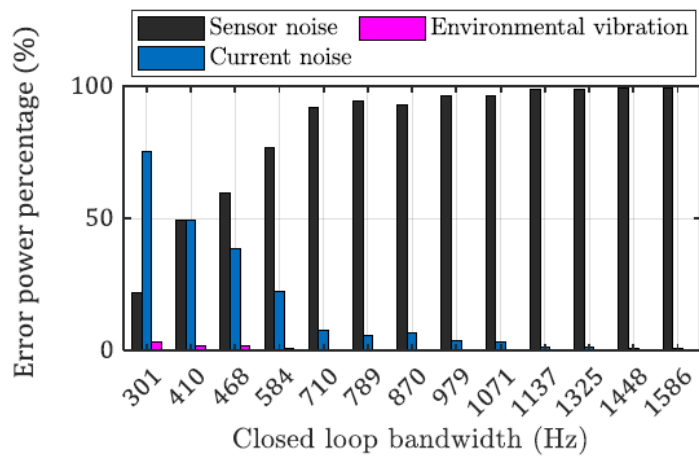


Figure 5-17: Error power contribution to the total real positioning error with different bandwidths

### 5.7.5 Time domain analysis of non-stochastic components

Different from the closed-loop positioning tests, the cutting force also plays a role in the cutting process. The non-stochastic component of the cutting force is predictable and repeatable. The time-domain disturbance signal is directly used as an input to the disturbance transfer function. The outputs are the displacement deviations caused by the disturbance. The time domain simulation is run on MATLAB. The measured and modelled frequency response function from cutting force (N) to sensor voltage (V) is shown in Figure 5-18. Please note that the 360-degree phase change is the same as zero phase change. The frequency response test is conducted in a similar way as the open loop frequency tests except that the PID control is enabled and the input test signal is superimposed onto the controller output.

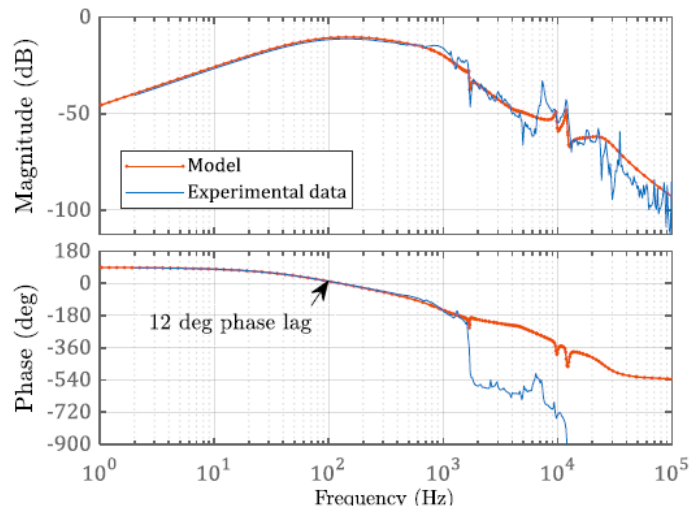


Figure 5-18: Frequency response from cutting force to sensor voltage

The error and cutting force evaluation experiment is conducted during the machining of freeform micro lens array and the cutting details will be covered in Chapter 8.5. The measured cutting force for the lenslet is shown in Figure 5-19. The force signal is applied as the input of the response model and the simulated tool deviation is shown in Figure 5-19 as well. It can be seen that the tool deviation gets larger and larger as the absolute cutting force increases. In addition, when the cutting section ends, there is a 180 nm overshoot in the opposite direction. The maximum deviation occurs after the maximum cutting force, or depth of cut. This corresponds to

the 12-degree phase lag at 100 Hz in the frequency response function in Figure 5-18. This lag is expected to be larger at higher frequencies than 200 Hz.

The simulation results are compared with the measured tool following errors. The following errors from the capacitive sensor are recorded during the machining experiment. Figure 5-19 shows the measured following errors in three cutting cycles. The error curve poses similar shape as the simulated results. The maximum error of 266 nm is comparable with the simulated value of 295 nm although the overshoot amount (34 nm) shows some discrepancies with the predicted value. This is attributed to the model mismatch at around 1 kHz.

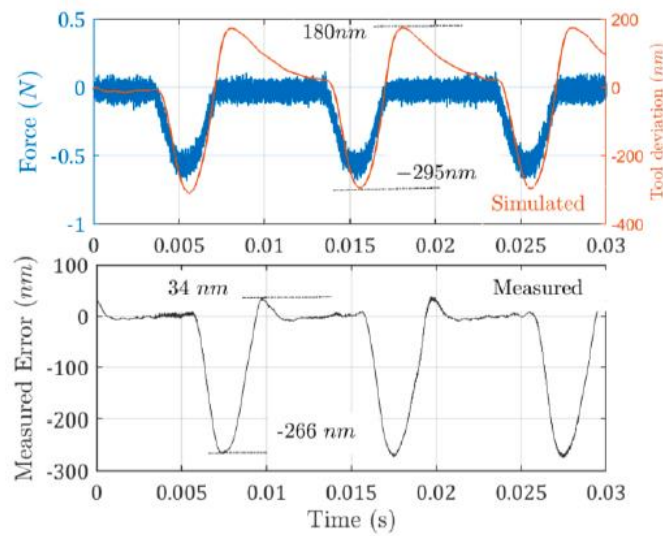


Figure 5-19: Simulated tool deviation with pre-measured force and measured following errors

## 5.8 Closed-loop dynamic stiffness and controller gains

The frequency response curve derived in Figure 5-18 reflects how much tool error will be caused by the cutting force. The ability to reject cutting force is also called dynamic stiffness. Therefore, the inverse of the curve is used to characterise the dynamic stiffness of the cutting system. This can be seen from the input sensitivity of  $D = G/(1 + KGH)$  as discussed in Section 5.2. Larger controller gains will make the  $K$  value large and therefore a higher dynamic stiffness. The loop will be unstable when the gains are too larger. The closed-loop stability is reflected in the open loop transfer function  $L = (1 + KGH)$ . Therefore, if the plant response  $G$  is reduced, then the control action  $K$  can be higher without loss of stability.

The input sensitivities  $D$  of the loop under low and high gains are plotted in Figure 5-20 and Figure 5-21, respectively. The results are calculated from the established model. It can be seen that cutting force disturbances are more suppressed at the low frequency range with a higher controller gain. At the resonant frequency, the disturbance is amplified and then it decreases rapidly after the resonance. It is also clear that the controller gains have negligible effects on the stiffness beyond the closed-loop bandwidth and the stiffness is almost the same as the plant response in this region.

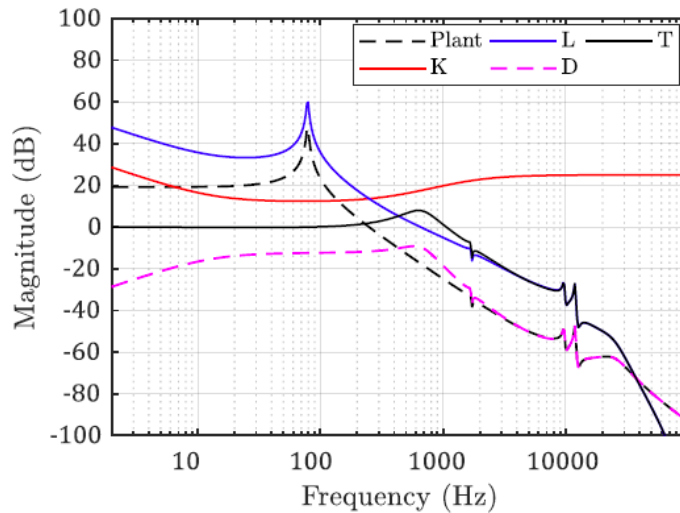


Figure 5-20: Stiffness curve with low PID gains

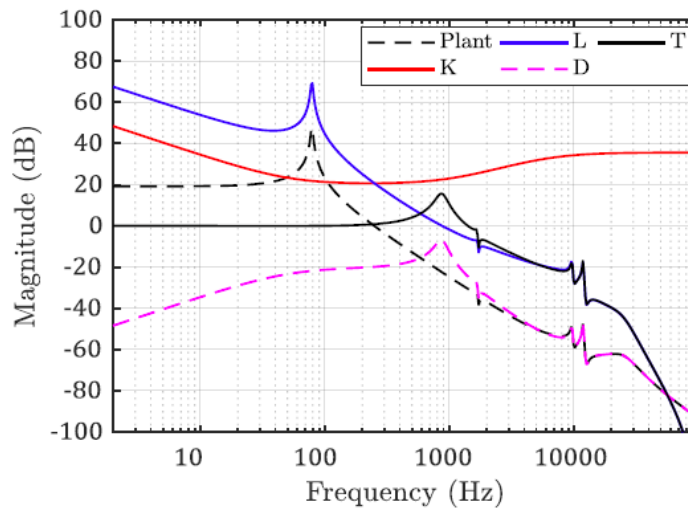


Figure 5-21: Stiffness curve with high PID gains

## 5.9 Summary

In this chapter, the transfer function model of the positioning system is established via frequency response tests and parameter identification method. A systematic error analysis approach is proposed and verified for the first time to reveal the contributions of disturbances on the tool positioning errors. The predicted following error spectrum agrees with the measured spectrum across the frequency range and this approach is justified.

The error analysis process reveals that the following errors read from the CNC software underestimates the real positioning error at low frequency while overestimates it at high frequency range. The error analysis approach successfully revealed the real tool positioning errors that are mixed with sensor noise.

It is found that a larger moving mass helps combating disturbances except the sensor noise. Increasing moving mass helps improving the positioning stability. The improvement is not obvious when the major error source is the sensor noise at high bandwidths. The optimal bandwidth, at which errors reach minimum value, turns lower with a larger moving mass.

The cutting force affects both the form error and surface quality in dynamic cutting. The maximum form error does not necessarily occur at maximum depth of cut. This can be predicted by analysing the positional response function to cutting force. The dynamic stiffness of the positioning system is determined by the controller gains. A higher moving inertia with high damping and stiffness will permit larger controller gains and then better stiffness can be achieved.

# CHAPTER 6

## Optimisation of control algorithm and study on influences of structural parameters

### 6.1 Introduction

The PID control algorithm used in the Chapter 5 has only four free parameters that can be tuned while the real world situation is much more complex. Filters can be used to cope with resonances but their locations and depths are not easy to determine. The control algorithm and gains are often selected based on human experiences through the “trial and error” process. Auto tuning methods can help us find the proper controller gains, but the controller structure is not optimised [150]. Therefore, it is unlikely to tell how much room for improvement exist for the selected controller gains that will result in minimum positioning error.

The difficulty of finding an optimal controller also poses difficulties to predict the positioning performance during the design stage. The positioning error tests show that the plant moving mass affects the achievable minimum positioning errors. However, there are many other parameters have not been studied yet and their influences are not clear. These parameters will be determined in the design stage of the positioning system and they are not easy to change once the prototype is built. Therefore, a systematic model that reveals the influences of plant structural parameters such as stiffness or damping is necessary in order to get a quantitative understanding on how to reduce errors from the design point of view.

In this chapter, the uncertainty associated with controller tuning is precluded by adopting H2 optimal control algorithm, which results in a control law minimizing positioning errors based on plant model and measured disturbances. The minimum positioning errors are predicted with different structural parameters. Then the

influence of each structural parameter is analysed. The analysis results reveal the optimal structural parameters and provide guidance on improving the dynamic performance of the tool positioning system.

The control effects of the optimal controller and the PID controller are compared through a series of positioning tests. Moreover, the practical issues such like computational load on the digital controller are discussed as well.

## 6.2 Optimal control theory

In modern control theory, optimal control has a broad range of meanings in that the word “optimal” may refer to minimum usage of fuel, minimum time to travel from one point to another, et al. In this thesis, the word “optimal” means achieving minimum tool real positioning error under all kinds of disturbances.

A standard closed-loop control system can be represented by a transfer matrix  $G$  and a controller  $K$ , as shown in Figure 6-1. Disturbances are modelled as input  $w$  and output performance to be evaluated is modelled as  $z$ . The controller senses the output  $y$  of the plant and then generates a control signal  $u$  to the plant. The column number of inputs  $w$  represents the number of disturbances. The transfer matrix  $G$  can be partitioned into four submatrices as in Figure 6-1. The submatrix  $A$  represents the characteristic matrix of the plant in state space denotation. The  $B1$  block is the input matrix for all the disturbances and the last column ( $B2$ ) corresponds to the control input  $u$ . The block  $C1$  is the output matrix for the errors to be minimized and the last row ( $C2$ ) corresponds to the output measurement.

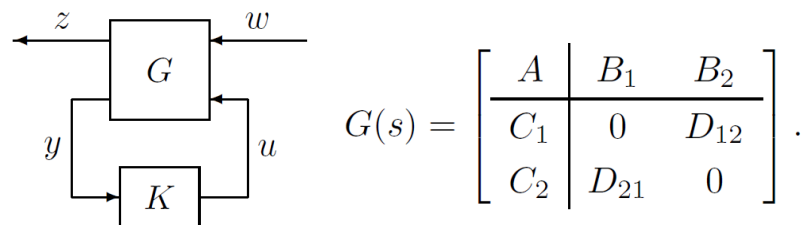


Figure 6-1: Standard representation of H2 optimal control problem [149]

As quoted from [149], the H2 optimal control algorithm can be described as:



“The H2 control problem is to find a proper, real rational controller  $K$  that stabilizes  $G$  internally and minimizes the H2-norm of the transfer matrix from  $w$  to  $z$ .”

There are four assumptions for H2 optimal control problem to be properly posed, The details of these conditions can be found in Zhou and Doyle’s book [149]. The H2-norm is a measure of the mean square deviations of a variable across the frequency range. The H2-norm of a Single-Input and Single-Output (SISO) system with transfer function  $J(s)$  is defined as:

$$\|J\|_2 = \left( \frac{1}{2\pi} \int_{-\infty}^{\infty} |T(j\omega)|^2 d\omega \right)^{1/2} \quad (6-1)$$

For multi-variable system with transfer function matrix of  $J(s) = [j_{mn}]$ , the definition generalises to [151]:

$$\|J\|_2 = \left( \sum_{mn} \|j_{mn}\|_2^2 \right)^{1/2} = \left( \frac{1}{2\pi} \int_{-\infty}^{\infty} \text{tr}[T(-j\omega)^T T(j\omega)] d\omega \right)^{1/2} \quad (6-2)$$

The matrix  $J(s)$  is the cost function, which is to be minimised in the optimization process. The selection of the cost function depends on the application requirements. In this case, the positioning error is to be minimised and thus the transfer function matrix formed by the transfer function of each disturbance source to the tool position should be the cost.

The controller output  $u$  is also included in the cost function to be constrained because there is hardware limits on the maximum controller output. The weights of the control output and the errors can be tuned. The optimal control design are realised by solving Ricatti equations in MATLAB with the function `h2syn` and finally a controller transfer matrix  $K_{opt}$  is calculated<sup>12</sup>.

This above representation assumes zero-mean white Gaussian noise disturbances with unit power spectrum. When the input disturbances have coloured spectrum characteristics as in this thesis, the input can be modelled as a white noise going through a particular weighting filter [151]. The benefit of using filters is to make these variables comparable and specify different frequency requirements even with different

---

<sup>12</sup> More details about this algorithm at <https://uk.mathworks.com/help/robust/ref/h2syn.html>.

units. Besides this, the weighting factor for controller output can also be selected as a frequency-dependent filter, rather than a scalar.

The transfer functions of the filters are then integrated into the plant model and an augmented transfer matrix  $G$  is formed as shown in Figure 6-2.  $W_e$  and  $W_u$  are the weighting filters for the positioning error and control output in the cost function.  $W_1, W_2$  and so on are the weighting filters for the disturbances.

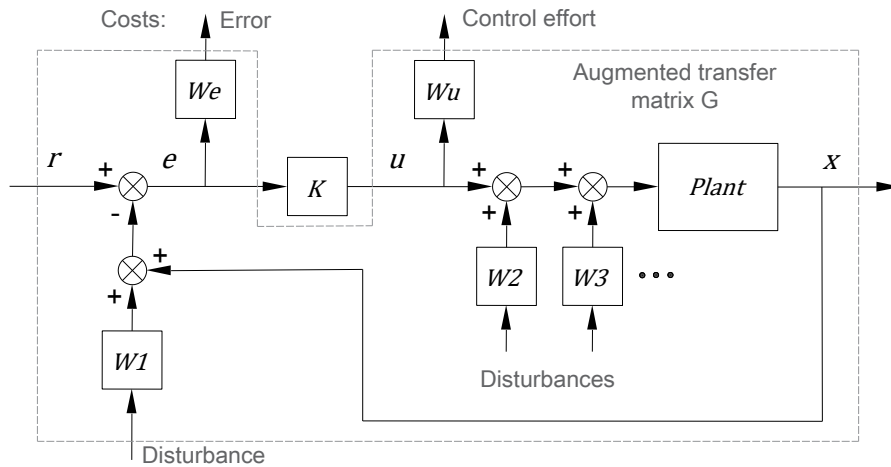


Figure 6-2: Augmented plant configuration for optimal controller design

## 6.3 Calculation of control algorithm

### 6.3.1 State space model of the closed-loop system

A state space model of the previous plant is established as shown in Figure 6-3. The transfer functions derived in Chapter 5 are used to form a Multiple-Input and Multiple-Output (MIMO) system. Each disturbance source is marked as an input in the diagram. The current loop noise in this case is injected before the motor.

In Figure 6-3, the  $W_s, W_i, W_{fc}$  and  $W_g$  are the weighting filters selected to represent the spectrum characteristics of the disturbance signal. The purpose of introducing the cutting force disturbance  $W_{fc}$  is to add a degree of freedom to adjust the dynamic stiffness curve. In addition, there are two more transfer functions to be determined for the optimal control setup.

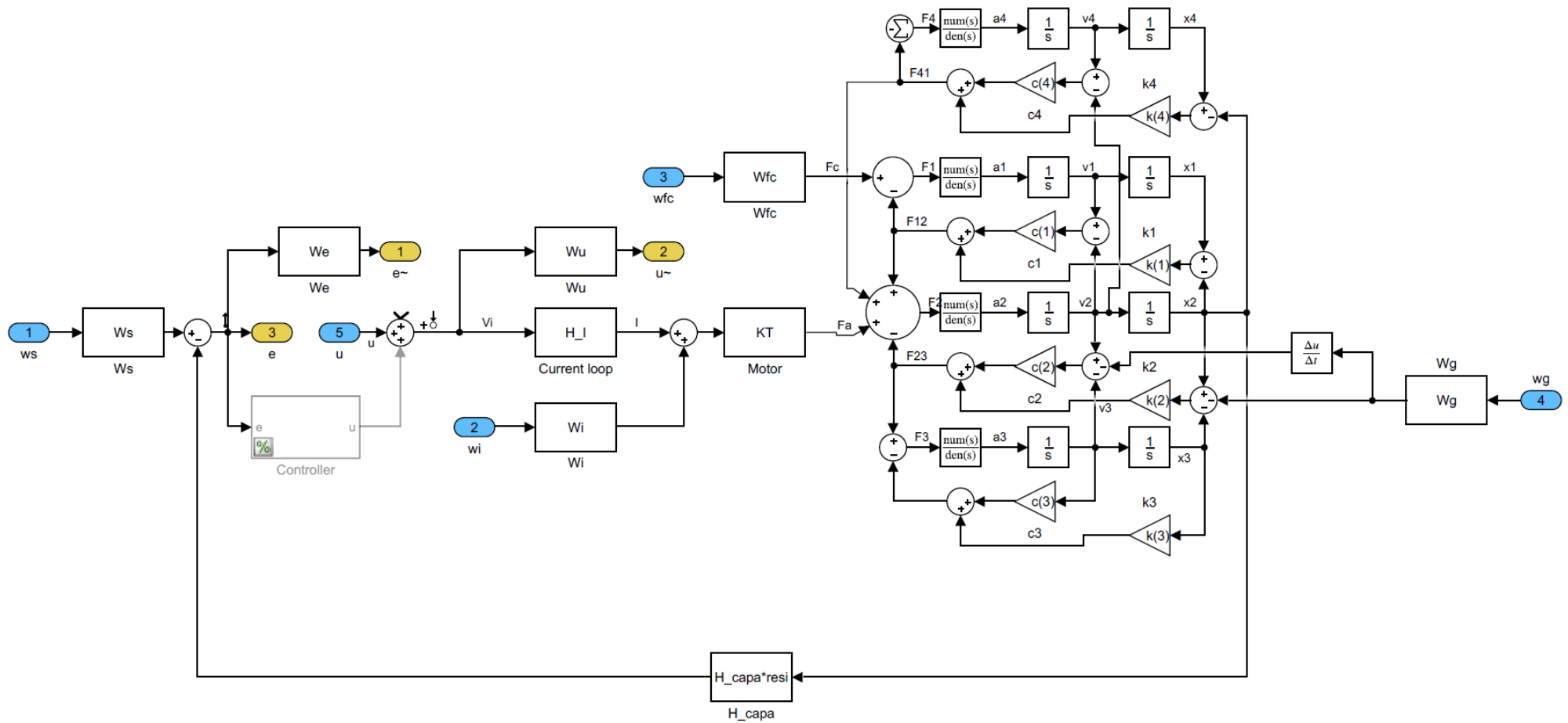


Figure 6-3: H2 optimal control model established in MATLAB for the developed prototype (state space model)

The weighting function for the following errors  $W_e$  controls the shape of the closed-loop sensitivity function. Since for a closed-loop system, the sensitivity at high frequency range is always close to unity,  $W_e$  is mainly for control the low frequency range sensitivity shape. According to [149], the weighting function is selected as:

$$W_e = \frac{s/M_s + \omega_b}{s + \omega_b \varepsilon} \quad (6-3)$$

Where:  $M_s$  limits the peak response near the cross over frequency.  $\omega_b$  is the intended closed-loop bandwidth.  $\varepsilon$  is an infinitesimal number and it is introduced to make the weighting function strictly proper. The  $M_s$  value can be calculated according to [149] as

$$M_s = \frac{\alpha \sqrt{\alpha^2 + 4\xi^2}}{\sqrt{(1 - \alpha^2)^2 + 4\xi^2 \alpha^2}} \quad (6-4)$$

Where:  $\alpha = \sqrt{0.5 + 0.5\sqrt{1 + 8\xi^2}}$ ,  $\xi$  is the intended closed-loop damping ratio. In this case,  $M_s$  is calculated to be 1.2721 for critical damping ( $\xi = 0.707$ ) and  $\varepsilon$  is set to  $1 \times 10^{-7}$  in this analysis.

The weighting function for the output of the controller  $W_u$  controls how much output will be commanded to achieve the desired performance. At high frequency range higher than intended bandwidth, the  $W_u$  is used to limit the control output by adding a pole, thus the response falls fast at high frequency, to suppress sensor noise. The weighting function is selected as:

$$W_u = \frac{s + \omega_{bu}/M_u}{\varepsilon_1 s + \omega_{bu}} \quad (6-5)$$

Where:  $M_u$  and  $\omega_{bu}$  limit the control output.  $\varepsilon_1$  is introduced to make the weighting function strictly proper.  $M_u$  and  $\omega_{bu}$  are set as large numbers ( $1 \times 10^8$ ) to indicate motor power is enough for static positioning.

### 6.3.2 Selection of weighting filters for coloured disturbances

As mentioned in Chapter 5, the disturbances are measured separately at each error source using data acquisition board and capacitive sensor. The disturbances are assumed stationary stochastic processes. The disturbance spectrums are approximated by a white noise going through a weighting filter. The selection of the filter equation is a complex procedure, which has drawn lots of research attention [152]. The weighting filters must be stable transfer functions. In this thesis, several typical low-pass filter, high-pass filter and resonant filters are used as the model to fit the disturbance spectrums. The spectrum beyond the sensor bandwidth is discarded in order to reduce the order of the fitted weighting filter. Since the measured disturbance spectrum might be in arbitrary shapes, the fitting accuracy is not expected to be high. The fitting emphasis is placed at the low frequency range.

The capacitive sensor noise is modelled as independent band limited white noise. The weighting filters are valued as the square root of the signal average PSD value. According to Figure 6-4 a), the weighting filter for sensor noise is selected as:

$$W_s = 1.36 \times 10^{-6} \text{ (constant)} \quad (6-6)$$

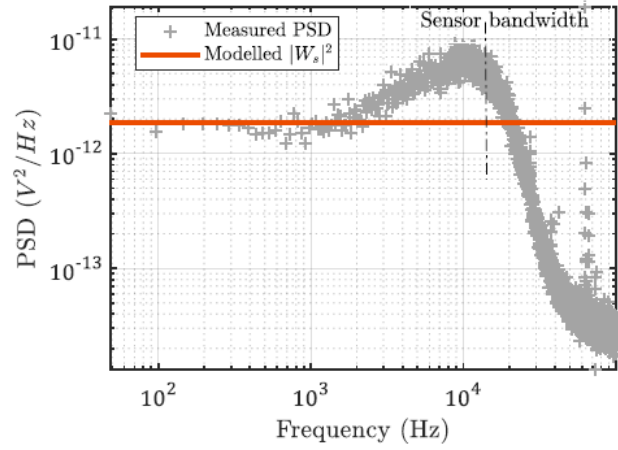
The current loop noise is modelled with large amplitudes at the low frequencies and the peak at 7748 Hz is modelled by a poorly damped second-order peak filter, as shown in Figure 6-4 b). The weighting filter is selected as:

$$W_i = 1.64 \times 10^{-7} \times \frac{s^2 + 0.1\omega s + \omega^2}{s^2 + 0.005\omega s + \omega^2} \times \frac{s - 200\pi}{s} \quad (6-7)$$

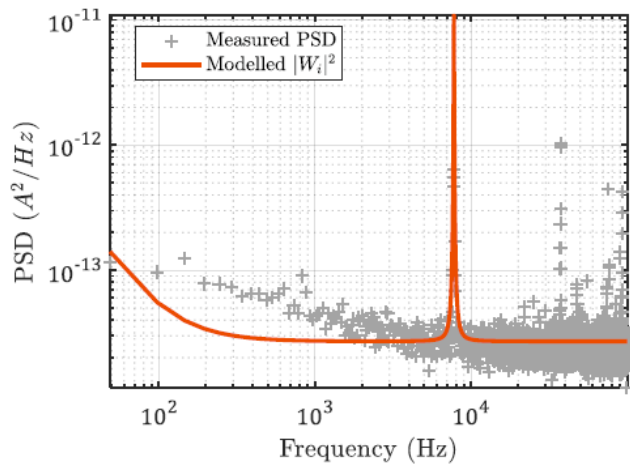
Where:  $\omega = 2\pi \times 7748$ . Then the environmental disturbance vibrations are chosen as:

$$W_g = \frac{2.83 \times 10^{-9}(s - 2000\pi)}{s} \quad (6-8)$$

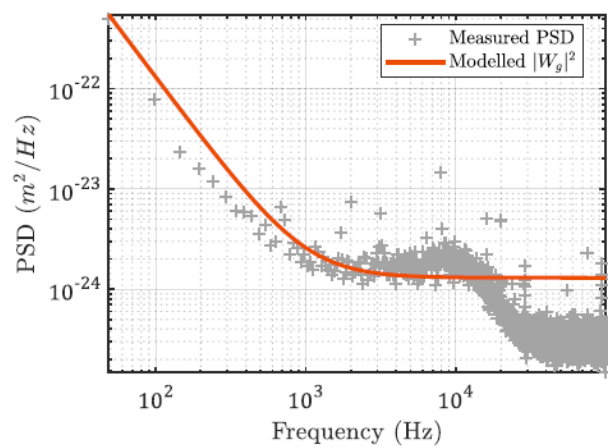
The squared values of the weighting functions are plotted in Figure 6-4 a) to c) for a clear comparison with the disturbance PSDs. The selection of those filters are trade-offs of model accuracy and complexity. If the models were chosen as high order functions, the resulted controlling function would be too computational intensive for real time control tasks.



a) Displacement sensor noise ( $W_s$ )



b) Motor current noise ( $W_i$ )



c) Environmental disturbance vibrations ( $W_g$ )

Figure 6-4: Disturbances measurement and modelling of the disturbance spectrum

Although there are some human factors in determining those filters, it is worth mentioning that those filters are kept unchanged throughout the optimisation process. Those filters represent the current environment and hardware conditions as the design inputs.

Now the plant parameters and the weighting transfer functions in the diagram Figure 6-3 are all available. The optimal control design can be realised by solving Riccati equations in MATLAB. The input is the augmented matrix and the output is the state space model of the optimal control algorithm. The resulted controller is a  $27 \times 27$  matrix in the state space form with 27 state variables. The open loop and closed-loop transfer functions of the modelled system with the calculated optimal controller are shown in Figure 6-5. Because no feedforward action is added, the closed-loop performance is nearly the same with open-loop transfer function beyond the control bandwidth. The crossover frequency of 870 Hz is resulted from the optimal control algorithm. Additional stiffness below 1 rad/s is added by setting  $\omega_b = 1$  for realizing zero static following error. This value can be tuned to add customise integral action to the control loop.

As a comparison, the same crossover frequency is achieved with a PID algorithm and the calculated controller functions are shown in Figure 6-6. There exists a structural resonant point at frequency of 1645 Hz, which has caused troubles when the PID gains are further increased. This peak has been successfully compensated in the optimal controller because the controller has more control degree of freedoms. The low frequency control actions are also different in that the optimal controller is fully determined by the disturbance strengths while the PID controller is calculated according to the phase margin set by the user. The control efforts function, which is the transfer function from reference  $r$  to controller output  $u$ , is calculated as [149]:

$$R = \frac{u}{r} = \frac{K}{1 + HGK} \quad (6-9)$$

This function shows the controller output amplitude in responds to an error signal at different frequencies, as plotted in red dashed lines in Figure 6-5 and Figure 6-6. Usually the output voltage of the digital controller falls within  $\pm 10$  V, corresponding

to the maximum motor force. At low frequency where  $K$  is large, the  $R$  value approaches to  $1/HG$ , the control effort is mainly for counteracting the spring force of the plant. The commanded motor force usually reaches its peak beyond the resonant frequency, where the plant  $G$  is dominated by the mass line with a  $-2$  slope. The controller has to compensate for it with a same positive slope and the motor output increase rapidly. At this region the control output might be very high if the required bandwidth is large, potentially saturates the motor. The  $Wu$  weighting function in Figure 6-3 is meant to limit the level of motor output in the controller design process.

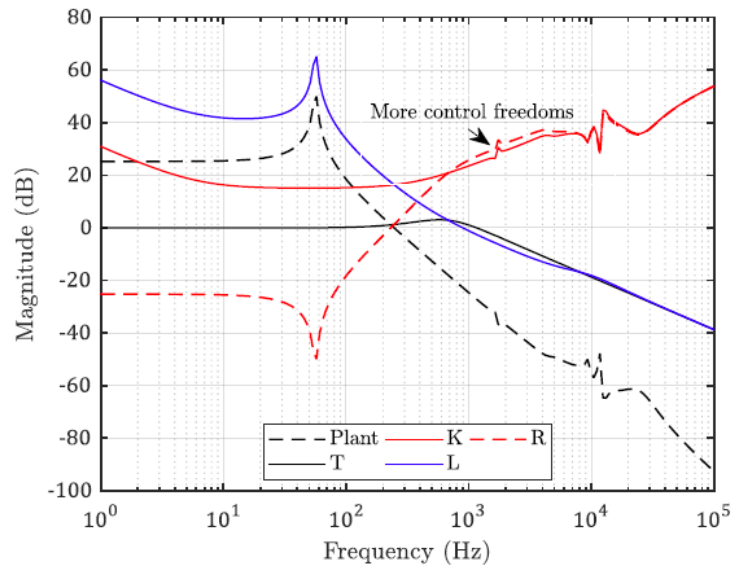


Figure 6-5: Calculated optimal controller and corresponding transfer functions

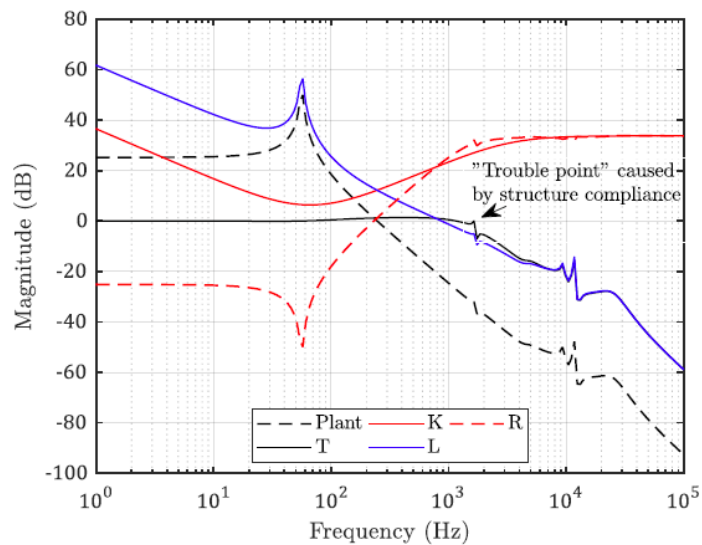


Figure 6-6: Calculated controller and transfer functions with PID control



The calculated optimal controller with a lower  $Wu$  weighting function with  $Mu = 1 \times 10^3$  and  $\omega_{bu} = 3 \times 10^3 \times Mu$  is shown in Figure 6-7. Compared to the results in Figure 6-5, the high-frequency control actions are greatly constrained. Therefore, the control efforts are reduced and this also helps to stabilise the loop. The corner frequency of 3 kHz is selected because the dynamics beyond 10 kHz is found to be the results of the electrical cross talks, which is not the real mechanical vibrations. Although the shape of the resulted control function is very similar to the one in the PID controller, the resonant peak at 1.6 kHz has been compensated effectively.

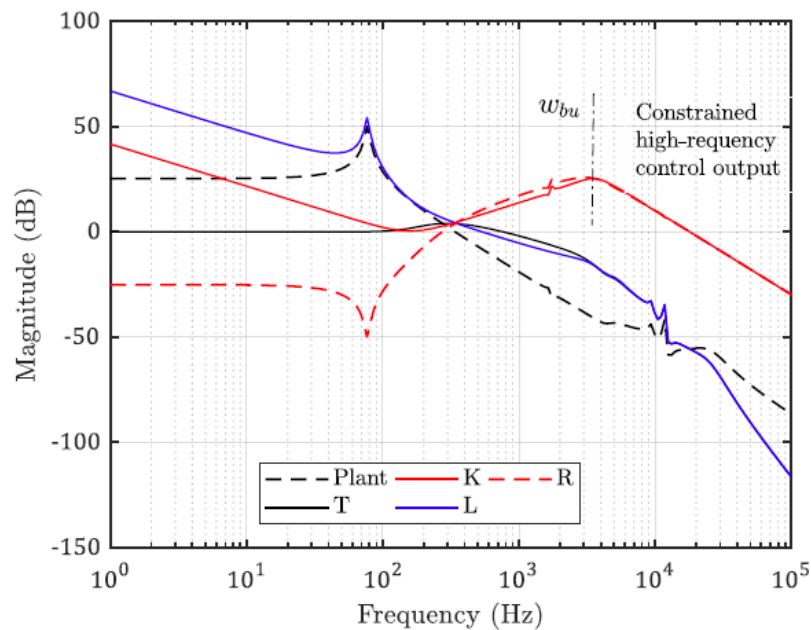


Figure 6-7: Calculated optimal controller with lower  $Wu$  weighting function

## 6.4 Closed-loop positioning test

The designed optimal control algorithm is deployed into the custom controller board developed in Chapter 4. As this control algorithm is a very different control structure with PID control, the programming routine is different.

### 6.4.1 Control algorithm deployment in hardware

The calculation is done by the time-domain state space function as shown in Figure 6-8. The designed control function consists of the state matrix  $A$ , input matrix  $B$ , output matrix  $C$  and the feedthrough matrix  $D$ . The state vector is a group of all the

variables in the system, which determines the state of the system uniquely, such as the position and velocity of each moving body. The new states at the next time step is calculated by the current states multiplied by the state matrix plus the input matrix timed by the position error  $e$ . Then the current controller output is calculated by multiplying the new states with the output matrix. The feedthrough matrix  $D$  is mostly zero in this case.

$$\begin{array}{l}
 \text{New states} \quad \text{Matrix A} \quad \text{Last states} \quad \text{Matrix B} \quad \text{Error} \\
 \text{States update:} \quad \begin{bmatrix} x_1' \\ \vdots \\ x_{27}' \end{bmatrix} = \begin{bmatrix} a_{11} & \cdots & a_{jj} \\ \vdots & \ddots & \vdots \\ a_{ii} & \cdots & a_{ij} \end{bmatrix} \times \begin{bmatrix} x_1 \\ \vdots \\ x_{27} \end{bmatrix} + \begin{bmatrix} b_1 \\ \vdots \\ b_{27} \end{bmatrix} \times e \\
 \\
 \text{Control output} \quad \text{Matrix C} \\
 \text{Output:} \quad y = [c_1 \quad \cdots \quad c_{27}] \times \begin{bmatrix} x_1' \\ \vdots \\ x_{27}' \end{bmatrix}
 \end{array}$$

Figure 6-8: Iterative calculation of the optimal control algorithm in hardware

The above procedures are programmed in C language and then the algorithm is run in real time. The required CPU time to finish the controller calculation is tested in the hardware with the hardware profiling function. The results are listed in Table 6-1 and the CPU time for the traditional PID control structure is listed in the table as a comparison. It can be clearly seen that the optimal control algorithm requires much more computational power from the hardware. The required CPU cycle number increases from 3045 for a simple 8-order controller up to 28204 cycles for the full-size calculated controller. As a comparison, the PID control algorithm only takes 430 CPU cycles.

Table 6-1: CPU cycles required for the optimal and PID control algorithms

Size of controller matrix A	CPU cycles required
8 × 8	3045
13 × 13	7128
27 × 27	28204
PID	430

Because of the high computational burden of the new control algorithm, the servo loop rate has to be reduced. A practical servo rate of 20 kHz is selected after several onsite trials.

#### 6.4.2 Measured closed-loop response with optimal control

The measured closed-loop response of input sensitivity  $D$  is shown in Figure 6-9. The measurement is conducted by injecting disturbance voltages to the controller output when the position loop is closed. The measured data points are marked as cyan colour and the prediction of the model is plotted in magenta colour. It can be seen that the optimal control action behaves as expected up to 5 kHz.

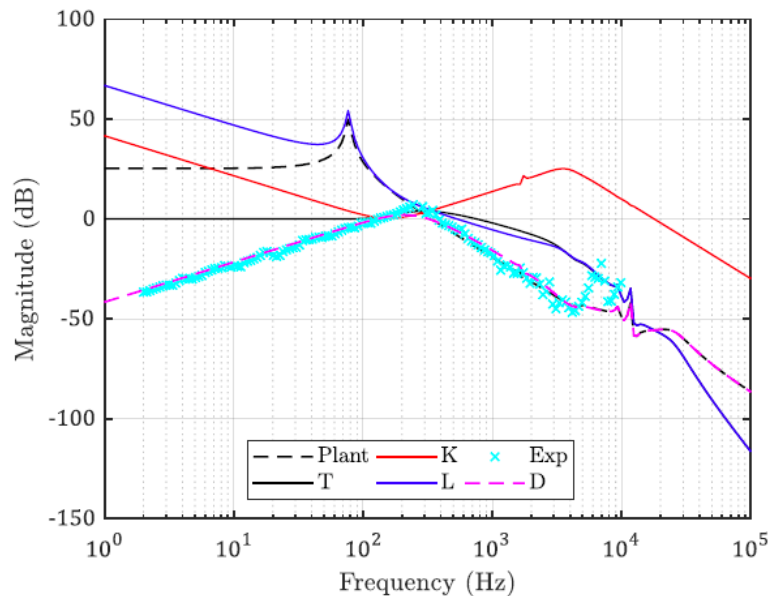


Figure 6-9: Measured closed-loop response of input sensitivity  $D$

The measured following errors with the optimal controller are shown in Figure 6-10. The position bandwidth (-3dB) is found to be around 1.1 kHz. The RMS value is 0.68 nm and the peak-to-valley value is 5.38 nm. Similar level of positioning stability has been achieved as described in Section 5.7.3, but with much lower position bandwidth of 468 Hz. As a comparison, the PID controller is tuned with the same sampling rate and a similar bandwidth (1.5 kHz) and the following errors are measured as shown in

Figure 6-11<sup>13</sup>. Because the sampling rate is kept the same, the measuring error contribution from the feedback sensor should be the same. The following errors are larger when the bandwidth is increased with the RMS value of 1.19 nm and peak-to-valley value of 7.65 nm with PID control. These results show that the optimal controller indeed helps achieve better positioning stability.

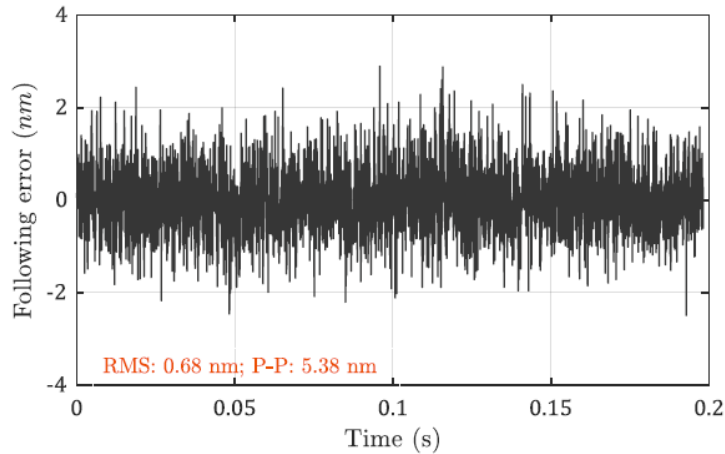


Figure 6-10: Measured following error with optimal controller at bandwidth of 1.1 kHz

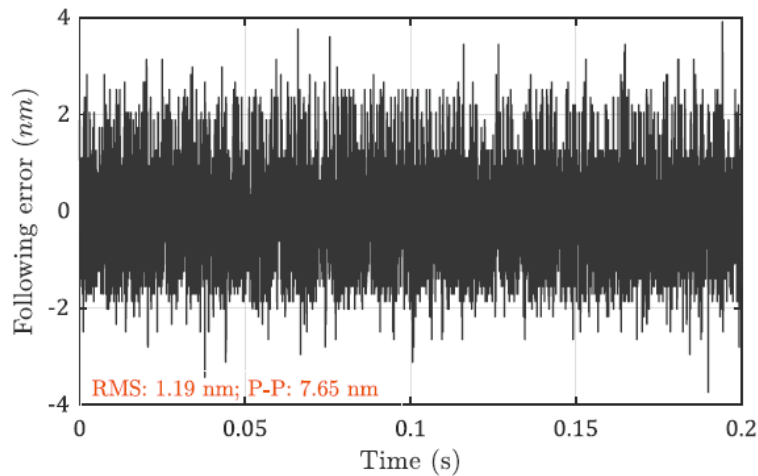


Figure 6-11: Measured following error with PID controller

The FFT spectrums of the two error signals are shown in Figure 6-12. It can be seen that the error spectrum is more evenly distributed when the optimal controller is utilised. The high-frequency noise is higher when the PID controller is used.

---

<sup>13</sup> The bandwidth is difficult to be tuned exactly same with the two different control methods because of the irregular dynamics at around 1.6 kHz.

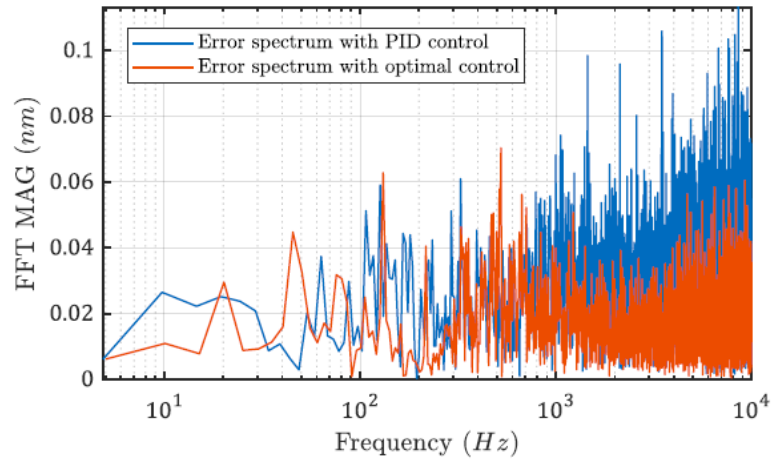


Figure 6-12: FFT spectrum of the two error signals with different control algorithms

## 6.5 Study on influences of plant parameters

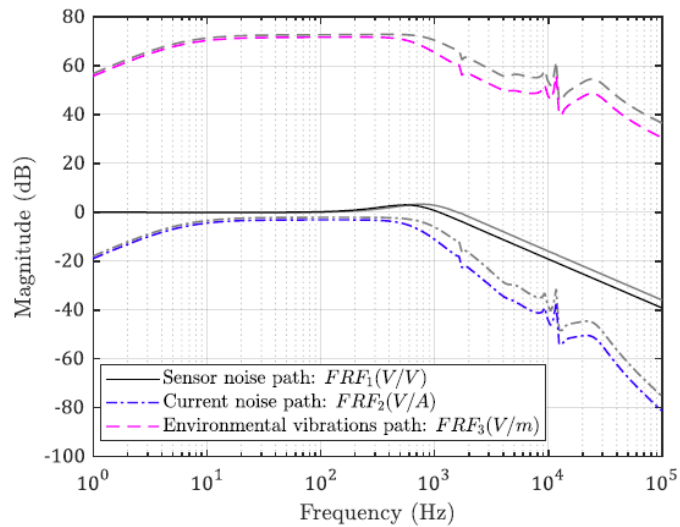
From the control point of view, the controller has theoretically done its best to suppress these errors. If the disturbances cannot be reduced from the roots, it is worthwhile to study how to reduce the system response to the disturbances by changing the structural parameters like mass, damping etc.

Several selected parameters are studied for their influences on the positioning following errors based on the closed-loop model, including the total mass of the moving part, flexure stiffness and damping, and motor force constant. The effects of changing plant parameters are not necessary to be linear. So the current system design is used as the “operating point”. The structural parameters are changed and the resulted following RMS errors are used to compare the sensitivities. This helps to figure out the most effective way to optimize the performance.

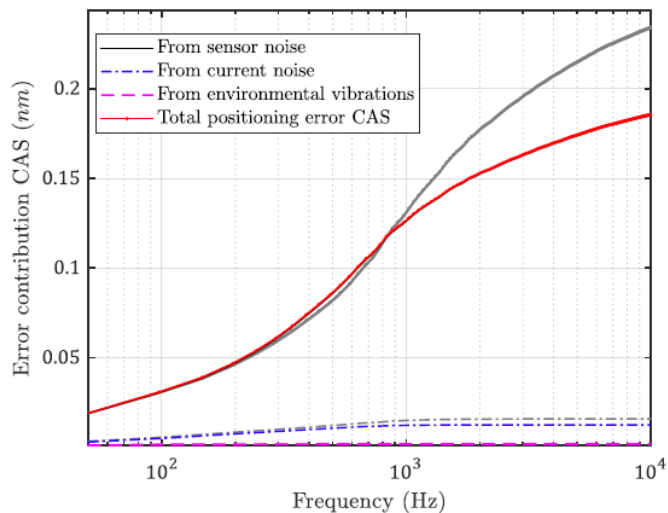
### 6.5.1 Influence of moving mass

In Chapter 5 with conventional PID control, it has been demonstrated that an increased moving mass helps reduce the positioning errors by experiments. Only two conditions are tested and the underlining mechanism has not been discussed. What’s more, the PID controller is difficult to be tuned to the optimal state. In this section, the new control algorithm will be used instead. The transfer functions from error sources to the position signal are plotted in Figure 6-13 a).

When the total moving mass  $m_1 + m_2$  is doubled based on the current configuration, all high frequency noise is reduced, shown in Figure 6-13 a). The cutting force and current noise transfer functions are notably reduced at high frequencies. Base vibration errors are also reduced at high frequency. The side effect of increasing moving mass is that more force is needed to achieve the same acceleration. This means bigger motor will be used and then more heat will be generated. The CAS plot in Figure 6-13 b) also shows the positioning errors are lower.



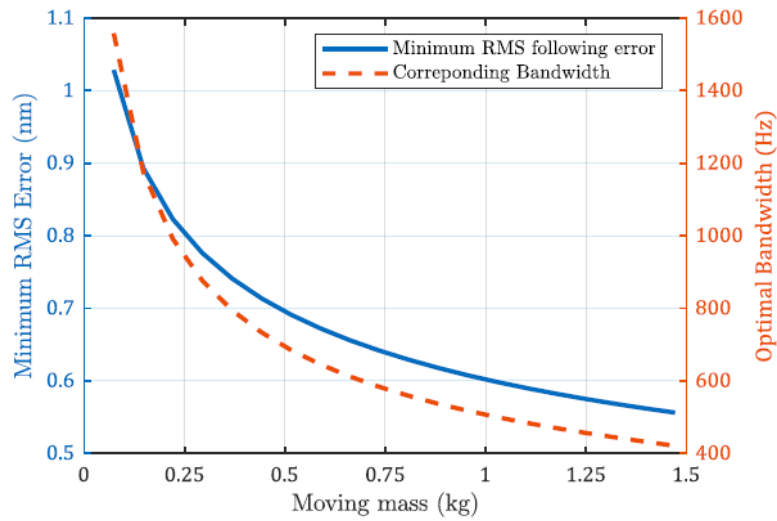
a) Noise transfer functions



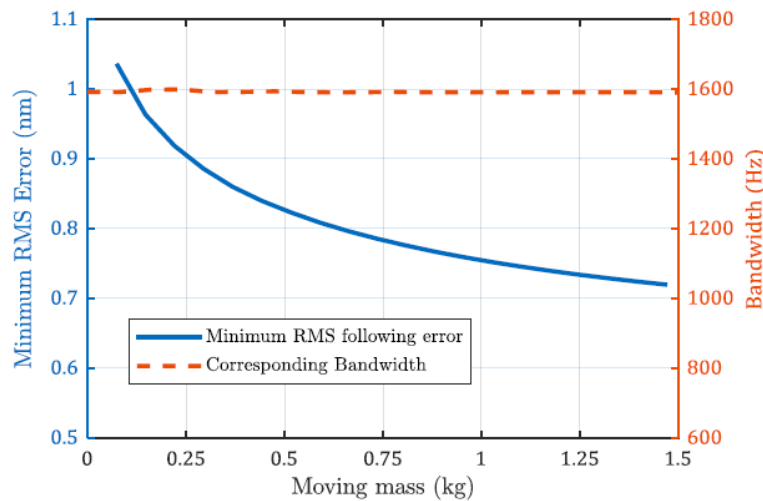
b) CAS plots for each error source

Figure 6-13: Performance with increased moving mass (grey -- before, coloured -- after)

The achievable minimum positioning errors with different moving masses are shown in Figure 6-14 a). It can be seen that the errors decrease with larger mass and the bandwidth (-3dB) decreases as well. In fast positioning applications, the bandwidth is required to be not less than a certain value. Thus  $\omega_b$  is tuned in the optimal control setup to achieve constant bandwidth, 1.6 kHz in this case. The achievable minimum error is plotted in Figure 6-14 b). The RMS error also decreases with increased moving mass but it is larger than that in Figure 6-14 a) because it deviates from the optimal bandwidth.



a) Errors with variable optimal bandwidth



b) Errors with constant bandwidth

Figure 6-14: Achievable minimum positioning error decreases with larger moving masses

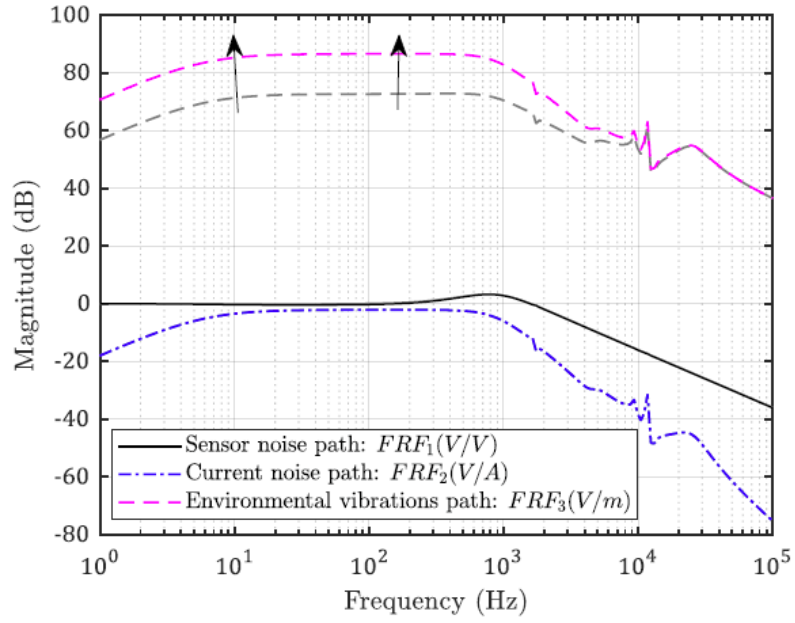
### 6.5.2 Influence of flexure bearing stiffness and damping

The flexure bearing in the designed system is the only path that outside vibrations can travel to the tool. Therefore, the stiffness  $k_2$  and  $c_2$  affect how much base vibration will be transferred to the tool tip. Meanwhile, they also affect the rejection ability of force disturbances. This can be seen in the Figure 6-15 a) and Figure 6-16 a). When the flexure stiffness  $k_2$  increases, the transfer function from base vibrations is raised at low frequency. While when the damping  $c_2$  increases, more high frequency base vibration is transmitted to the tool. However, the errors caused by the current stage noise are reduced in both cases. The optimal closed-loop bandwidth is decreased slightly as well.

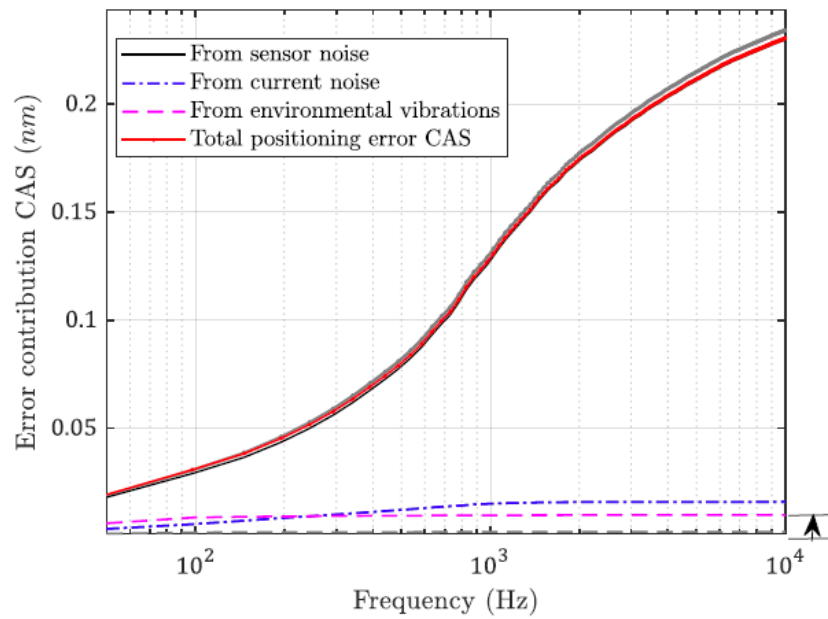
The CAS functions are plotted in Figure 6-15 b) and Figure 6-16 b). The total following error is decreased since the contribution of the base vibration is so small. This is not always true. When the stiffness or damping is increased to such a level that the base vibration contribution is comparable to the reduction of current stage noise contribution, the total error will be increased.

There exists an optimal pair of flexure stiffness  $k_2$  and damping  $c_2$  under this disturbance situation, which minimizes the following errors. This can be seen in Figure 6-17. In this analysis, the stiffness  $k_2$  and damping  $c_2$  are adjusted within a large range and the total RMS following error is plotted. As the stiffness and damping coefficients are increased, the following error decreases first and then starts to rise higher. According to Figure 6-17, the minimum following error of RMS 0.96 nm is achieved when  $k_2$  is equal to  $1.1 \times 10^5$  N/m and  $c_2$  is equal to 237.7 N/(m · s<sup>-1</sup>). Apparently, this optimal stiffness and damping value is dependent on the relative strength of the disturbances. That is to say, an optimal structure cannot be determined until the disturbances are identified.



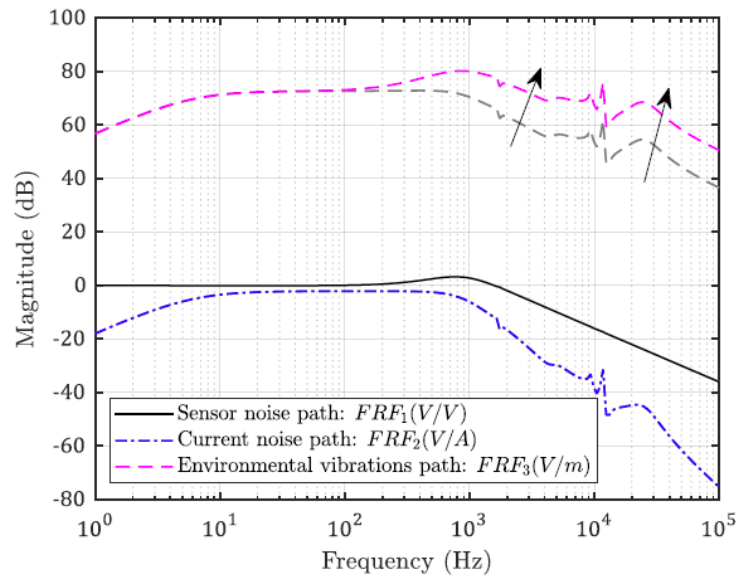


a) Noise transfer functions

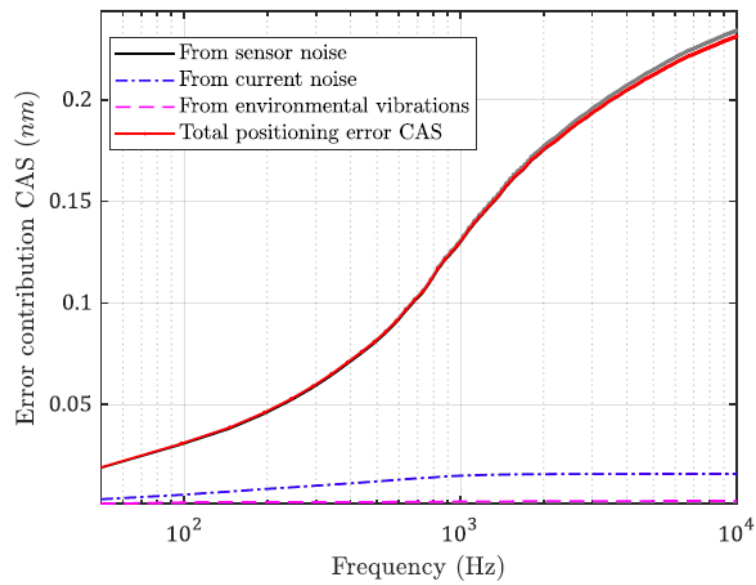


b) CAS plots for each error source

Figure 6-15: Performance with increased flexure stiffness  $k_2$  (grey -- before, coloured -- after)



a) Noise transfer functions



b) CAS plots for each error source

Figure 6-16: Performance with increased flexure damping  $c_2$  (grey -- before, coloured -- after)

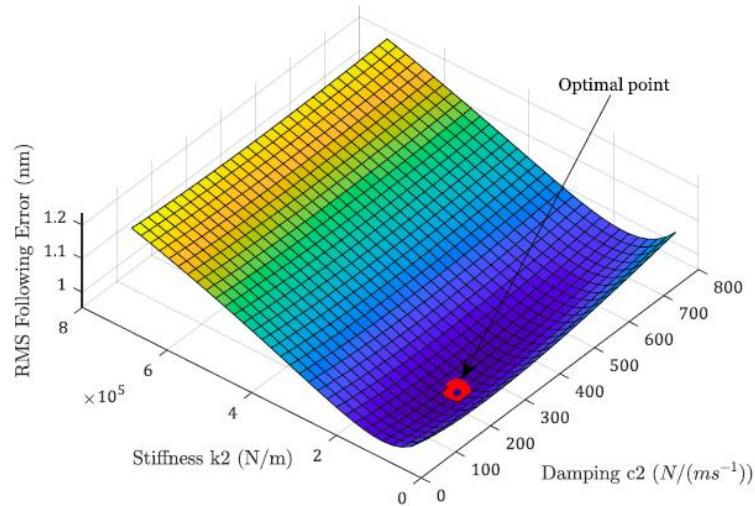
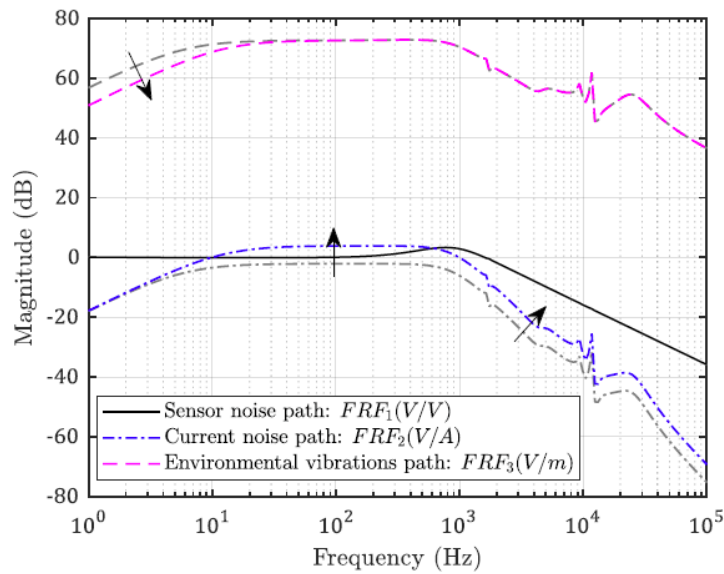


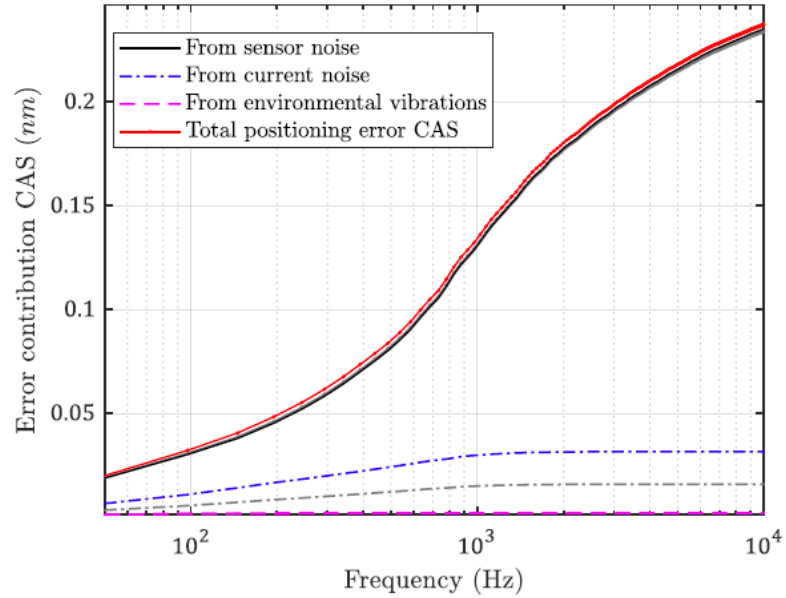
Figure 6-17: Optimal bearing stiffness and damping

### 6.5.3 Influence of motor force constant

The motor force constant is the block before the mechanical plant in the model as shown in Figure 6-3. In practice, this parameter is related to the selection of the motor. When the other stage parameters are not changed, only the motor force constant is increased, the noise transfer functions are shown in Figure 6-18 a). The error caused by the current loop noise will be larger in the middle and high frequency range. This is because the same amount of current corresponds to more force in this case. It is also found that low frequency vibrations are less transmitted to the tool.



a) Noise transfer functions



b) CAS plots for each error source

Figure 6-18: Performance with increased motor force constant  $K_T$  (grey -- before, coloured -- after)

## 6.6 Summary

In this chapter, a deterministic controller design approach is adopted to preclude the uncertainty associated with controller tuning, which results in a control law minimizing positioning errors based on plant model and disturbance model. The influences of mechanical parameters such as mass, damping and stiffness are investigated within the closed-loop framework. It is found that there exist optimal bearing stiffness and damping coefficients under a given disturbance condition. Larger moving inertia helps reduce all disturbances at high frequencies, which agree well with the positioning experiments in Chapter 5. A quantitative understanding on how plant structural parameters affect positioning stability is thus shown in this chapter. This provides helpful design guides to reduce error sources from the design point of view. Cutting force is not yet included in the analysis because of its dependence on work material, cutting tool, feed rate et al. If the cutting force shows stable spectrums then it can be modelled and analysed in the same way as other disturbances.

# CHAPTER 7

## Acceleration feedback control for enhancement of dynamics stiffness

### 7.1 Introduction

In this chapter, control algorithm with additional acceleration feedback loop is studied to enhance the dynamic stiffness of the fast tool cutting system without the need for adopting a large inertia, which is strictly limited in fast tool servo devices.

The influences of acceleration feedback on the closed-loop stiffness and the positioning errors caused by the added sensor are studied in details. An analytical model of the dynamic stiffness is established. The effects of the low-pass characteristics in the acceleration loop are discussed. The error contribution of the acceleration sensor is analysed and experimentally verified. The dynamic stiffness is tested through both frequency response test and intermittent diamond turning experiments. The following errors and the form errors of the machined surfaces are compared with the estimation from the model. The analysis model provides a theoretical basis for adopting acceleration feedback technique and tuning the stiffness curve to suit for different disturbance situations, paving the way for its practical implementations in ultra-precision applications.

### 7.2 Limitations with feedback control

In Chapter 6, an optimal controller structure has been proposed. However, the improvement to the dynamic performance of the system is quite limited. This is due to the fundamental limitations of feedback control scheme [149].

In the feedback control scheme, the open loop transfer function consists of all the poles and zeros ranging from low frequency to high frequency. The output sensitivity  $S(j\omega)$  indicates how the system output will be affected by the feedback

sensor noise. If the  $S$  function shows a value larger than 1, the sensor noise at this frequency range will be amplified, and vice versa.

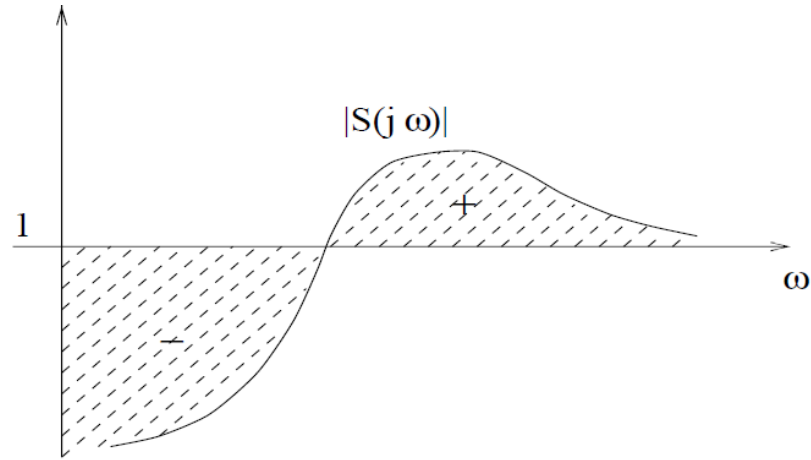


Figure 7-1: Illustration of the Bode sensitivity integral relationship (water bed effect) [149]

It can be proved that the Bode sensitivity integral, which is the integral of the output sensitivity function  $S(j\omega)$  along the frequency axis, is always equal to the summation of the real parts of the Right Hand Plane (RHP) poles  $p_i$  in the open loop function  $L(j\omega)$ . The relationship is shown in the equation below according to [149].

$$\int_0^{\infty} \ln|S(j\omega)| d\omega = \int_0^{\infty} \ln \left| \frac{1}{1+L(j\omega)} \right| d\omega = \pi \sum_1^m \text{Re}(p_i) \quad (7-1)$$

In the case when there are no right-hand poles, the integral equals zero. Then the Bode sensitivity integral can be interpreted that any attempts to increase the low frequency attenuation will result in larger sensor noise amplifications at the middle frequency range. Zhou et al. has elaborated on the mathematical proofs on the limitations of feedback control in chapter 6 of the book [149].

Another important consideration in cutting system is the dynamic stiffness. The dynamic stiffness of a closed-loop positioning system can be described by the input sensitivity  $D(j\omega)$ . As discussed in Chapter 5, the difference between the input sensitivity and the output sensitivity is that  $D(j\omega) = S(j\omega)G(j\omega)$ . Therefore, the limitations on the output sensitivity  $S(j\omega)$  also apply to the input sensitivity  $D(j\omega)$ . The integral of the total stiffness is always equal a fixed amount, which is determined by the response of the plant. Any attempts to increase the dynamic stiffness at one

frequency range by controller tuning will inevitably lead to deterioration of the dynamic stiffness at other frequencies. Reducing the response of the plant to forces by designing large stiffness, damping or inertia will help increase the overall dynamic stiffness.

Acceleration feedback has the similar effects of increasing the mass of the motion system [153]. However, since the above limitations apply to any closed-loop stable system, the dual feedback approach is not intended to circumvent this limitation, but explore opportunities to relieve those constraints.

### 7.3 Control schemes with acceleration feedback

The conventional motion control scheme consists of a cascade current loop within the position and velocity loops, as shown in Figure 7-2. The current loop is closed upon a current sensing resistor in series with the motor windings. Therefore, the current feedback only depicts how much force is generated by the motor. Other disturbances such as cutting forces or cable-induced forces cannot be sensed until they induce errors on the velocity signal or position signal. The estimation of disturbance force from velocity signal is a first order differentiation process and this will introduce a half sampling period delay. In most case, the velocity signal is derived from the position sensor by numerical differentiation. This means another delay in the loop [105]. It means fast response to these disturbances is not feasible.

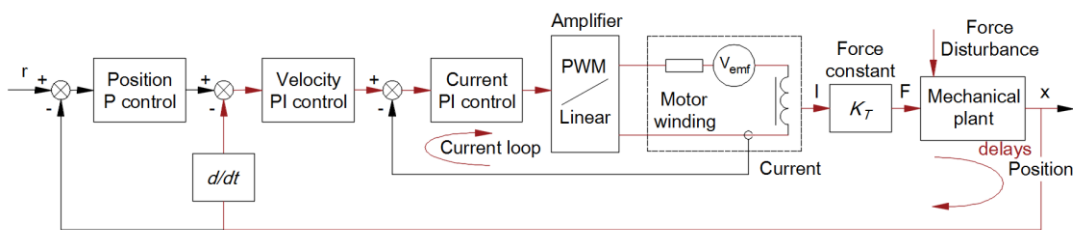


Figure 7-2: Conventional motion control with position feedback (Red arrows show the shortest path from disturbance to controller)

Acceleration feedback technique can detect momentum stage acceleration. The acceleration signal is strictly proportional to the net force including disturbances. Thus the controller can compensate the disturbance force before it affects positioning

accuracy, creating a ‘virtual mass’ effect. This is the basic idea of using acceleration signal to enhance dynamic stiffness of FTS.

There are two forms of control structures adopting acceleration signals in the control loop: the cascade acceleration loop and the disturbance observer structure [154].

### 7.3.1 Cascade acceleration feedback loop

As shown in Figure 7-3, the cascade acceleration loop is closed by feeding back the measured acceleration signal in a separate path to the controller. The output of the position or velocity loop serves as the set point of the acceleration loop. In this way, the controller in each loop is simpler. Because the simplified control structure, the inner loop can be closed at far higher bandwidth, which is only limited by the largest poles in the local loop. The position and velocity loop controllers are combined as one block since they usually share the same position sensor in this case.

Depending on the relative location of the current loop and acceleration loop, there are varieties of structures found in the literature. In some case, the current loop is totally replaced with an acceleration loop [155], and in other case, the acceleration loop is closed upon a current loop. Some other researchers proposed the parallel current and acceleration control structure [154].

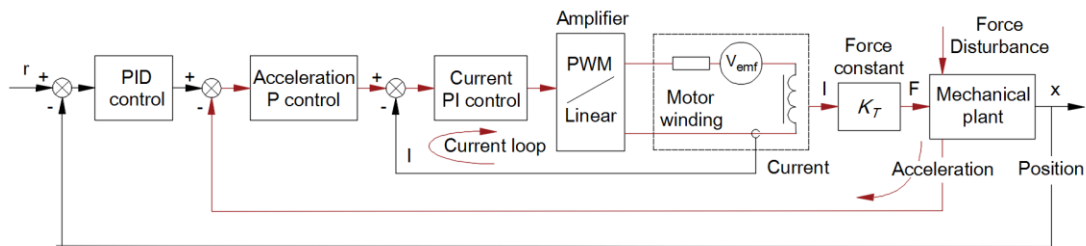


Figure 7-3: Motion control with cascade acceleration feedback (Red arrows show the shortest path from disturbance to controller)

### 7.3.2 Disturbance observer and compensator

Another control structure incorporating the additional acceleration signal is the Disturbance Observer (DOB) structure shown in Figure 7-4 [156]. The acceleration signal is used to calculate the total force acting on the tool and the motor output force



is deducted from the total force resulting in the disturbances. The estimated disturbance is feedback to the control loop and then compensated by the control output.

This concept has been studied in many papers but the acceleration signal is derived from either speed feedback or position feedback [102]. There are two problems associated with this method. The first is the noise amplification problem and the other is the differentiation delay [109]. These two problems limited the performance of disturbance observer used in industrial applications.

An acceleration sensor can be installed to measure the momentum acceleration with minimum time delay, which is typically one servo period. The measurement noise is far smaller than the double differential method. The dynamics of the motor can be circumvented by directly measuring the coil current with a current sensing resistor. The motor force is proportional to the coil current with no time delay.

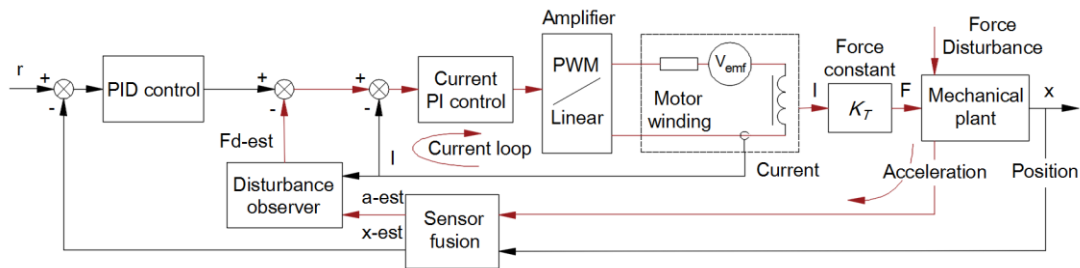


Figure 7-4: Motion control with DOB acceleration feedback (Red arrows show the shortest path from disturbance to controller)

### 7.3.3 Comparison of the two feedback configurations

The diagrams of the two feedback loops can be simplified into the following forms as shown in Figure 7-5. The blocks  $G_1$  and  $G_2$  are the plant transfer functions of the inner and outer loops.  $C_3$  is the feedback controller for the outer loop and  $C_1$  is the feedforward function multiplied by the control function. In this representation, the output of  $C_1$  is in the same unit of controller output, so as to the input disturbance  $d_i$ . The effect of  $C_3$  is the same in the two configurations, for closing the PID position loop.



$$y(s) = \frac{C1'G1G2}{1 + C3G1G2}r(s) + \frac{G1G2(1 + Q)}{1 + C3G1G2}d(s) \quad (7-3)$$

In Equation (7-3), it can be seen that the  $C1'$  function only appears in the reference path and the  $Q$  function only affects the disturbance function. This means they can be selected independently without affecting the other functions. When the  $C1'$  and  $Q$  are selected as below, the same output response and the disturbance response for these two configurations can be achieved.

$$C1'(s) = \frac{1 + C3G1G2}{1 + C2G1 + C3G1G2}C1 \quad (7-4)$$

$$Q(s) = \frac{-C2G1}{1 + C2G1 + C3G1G2} \quad (7-5)$$

Although these two configurations can be proved to be mathematically the same with different physical interpretations, Hori found that the cascade acceleration form performs better than the disturbance observer form in experiments [102]. This is because the DOB method requires a model of the plant  $G1$ . If the model is not accurate enough then the estimated disturbance will be wrong, which is a common problem for model-based method. We have also observed similar results in the preliminary tests. Thus, the acceleration control form is selected in the next-step analysis.

## 7.4 Analytical model of acceleration feedback control

An analytical model is established for the cascade acceleration-feedback structure. As shown in Figure 7-6, the position loop is closed by a typical PID control algorithm with first-order low-pass actions on the derivative term. The mechanical plant is simplified as a single body mass-spring-damper system with moving mass  $M$ , support stiffness  $K$  and damping coefficient  $C$ . The acceleration of the moving mass is directly measured with an accelerometer. The frequency responses of the accelerometer and the capacitive displacement sensor are denoted by  $H_{acc}$  and  $H_{capa}$  respectively. The  $H_I$  represents the transfer function of the closed current loop and  $K_T$  is the force constant of the motor.  $K_a$  is the tuneable acceleration feedback gain and  $H_a$  is an optional shaping filter on the acceleration signal with DC gain of 1. The sensor noise

$n1$  and  $n2$  are injected as disturbances in the units of sensor voltage. The cutting force  $dF$  and position reference  $r$  are also inputs of the closed-loop system.

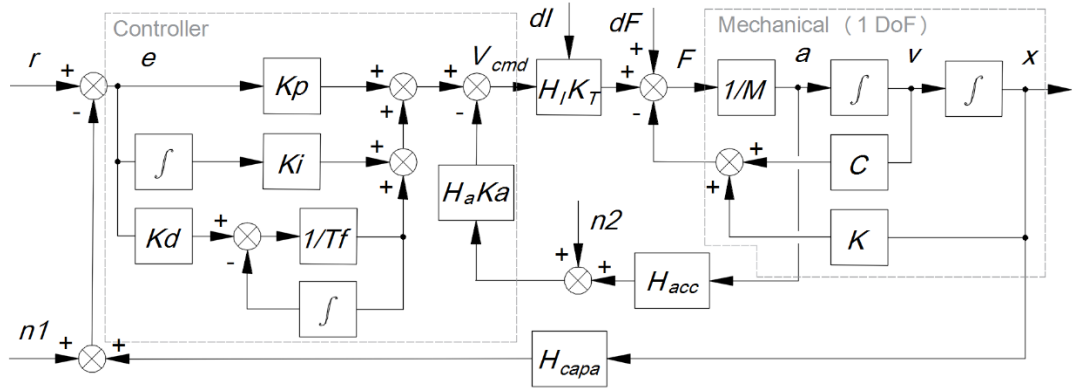


Figure 7-6: Analytical model of acceleration feedback control along with PID position controller

According to the Newton's law, the dynamics of the moving body can be written as:

$$\frac{X(s)}{F(s)} = \frac{1}{Ms^2 + Cs + K} \quad (7-6)$$

$$F(s) = H_{ctr}(s)[r(s) - H_{capa}X(s) - n1]H_IK_T - H_aKa[H_{acc}X(s)s^2 + n2]H_IK_T + dF(s) \quad (7-7)$$

Where:  $H_{ctr}(s)$  is the transfer function of the PID controller, written as

$$H_{ctr}(s) = K_p + \frac{K_i}{s} + \frac{K_d s}{T_f s + 1} \quad (7-8)$$

Where:  $K_p$ ,  $K_i$  and  $K_d$  are the PID gains respectively.  $T_f$  is the time constant of the first order low pass action on the derivative term (D).

#### 7.4.1 Analysis of dynamic stiffness with acceleration feedback

The stiffness of a tool positioning system is evaluated by the amount of tool deviation caused by unit external force. It is a function of frequency because the stiffness value usually changes under excitations at different frequencies. Based on the analytical model in the last section, the dynamic compliance function from cutting

force disturbance  $dF$  to tool position  $X$ , which is the inverse of the dynamic stiffness, is derived as

$$\frac{X(s)}{dF(s)} = \frac{1}{(M + H_a K_a H_{acc} H_I K_T) s^2 + \left( C + \frac{K_d}{T_f s + 1} H_{capa} H_I K_T \right) s + (K + K_p H_{capa} H_I K_T) + (K_i H_{capa} H_I K_T) \frac{1}{s}} \quad (7-9)$$

Compared with Equation (7-6), it can be seen that the closed-loop position control system can be treated as a new mechanical plant. The disturbance force is the input and the tool position changes in response to the force acting on it. The smaller the response is, the higher the dynamic stiffness is achieved. With the control action taking effects, the new plant has quite different behaviours at different frequencies. The equivalent mass, spring and damping terms in the new plant are listed in Table 7-1.

Table 7-1: Equivalent terms of the closed-loop behaviour

Name	Original	Equivalent in acceleration feedback control
Mass term	M	$M + H_a K_a H_{acc} H_I K_T$
Damping term	C	$C + \frac{K_d}{T_f s + 1} H_{capa} H_I K_T$
Spring term	K	$K + K_p H_{capa} H_I K_T$
Super spring term	--	$K_i H_{capa} H_I K_T$

As illustrated in section 3 of the book by Schmidt et al [138], the spring term governs the low frequency response, the damping term controls the response near the resonant and the mass term determines the positional response beyond the closed-loop bandwidth.

Table 7-1 shows that the equivalent mass of the plant has been changed from  $M$  to  $M + H_a K_a H_{acc} H_I K_T$  with acceleration feedback control. It is clear that no PID gains show up in the new mass term and this means the position loop gains have no effects on the dynamic stiffness beyond the position closed-loop bandwidth. There is a new super spring term introduced by the integral gain, which does not exist in the original plant. This super spring effect is desired because it helps to achieve infinite

DC stiffness. The damping and stiffness terms can also be changed by adjusting the  $K_d$ ,  $T_f$  and  $K_p$  gains.

The reference tracking ability and disturbance rejection ability of a closed-loop control system is mutually related. That means changing a single parameter will affect both the two transfer functions. This is not desired because the motion control bandwidth is a benchmark in fast tool servo applications. It should not be sacrificed in exchange for stiffness improvement. In order to compare the dynamic stiffness with different acceleration gains under the same reference tracking bandwidth, the reference tracking bandwidth is kept as unchanged as possible by adjusting the PID gains. The reference tracking function is derived as

$$\frac{X(s)}{r(s)} = \frac{\left(K_p + \frac{K_i}{s} + \frac{K_d s}{T_f s + 1}\right) H_I K_T}{(M + H_a K_a H_{acc} H_I K_T) s^2 + \left(C + \frac{K_d}{T_f s + 1} H_{capa} H_I K_T\right) s + (K + K_p H_{capa} H_I K_T) + (K_i H_{capa} H_I K_T) \frac{1}{s}} \quad (7-10)$$

The reference-tracking transfer function and the disturbance-rejection transfer function share the same denominators. In the ideal case when the current loop has flat response characteristic and the acceleration sensor has infinite measurement bandwidth with  $H_I = H_a = 1$ ,  $H_{acc} = S_{acc}$ , then the new mass term is a scalar. The numerator and denominator of equation X can be multiplied by the global factor of  $Kg = M/(M + H_a K_a H_{acc} H_I K_T)$  at the same time without changing the reference tracking function. In Lorentz type motion system, the original plant damping  $C$  and stiffness  $K$  are usually small compared with the control action  $K_d$  and  $K_p$ . Thus, this is equivalent to increasing the PID gains by the same ratio of  $Kg$ . In the case when the new mass term is not a scalar but a function of the complex frequency  $s$ , the DC gain of this complex function will be used to calculate the increase factor.

Figure 7-7 a) shows an example analytical result for a positioning system with ideal acceleration feedback control. The dashed lines indicate the responses with PID

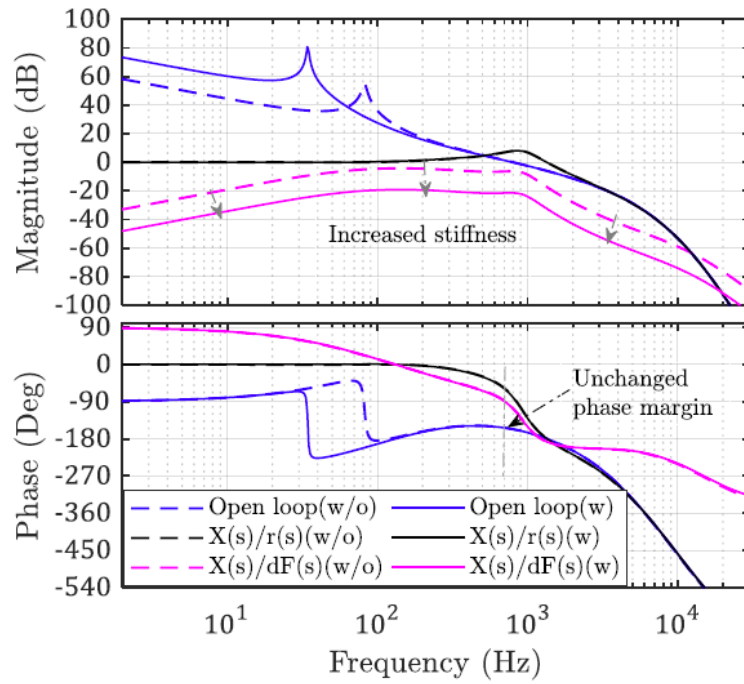
control only and the solid lines show the responses with PID and acceleration feedback control. By introducing acceleration feedback and increasing the PID gains at the same time, the dynamic compliance function  $X(s)/dF(s)$  is seen lower, means an increased dynamic stiffness across all the frequency range. The reference tracking function  $X(s)/r(s)$  and the closed-loop phase margin are not changed at all. This means the acceleration feedback technique can theoretically improve the high frequency dynamic stiffness of a positioning system without the need for a larger moving mass.

#### **7.4.2 Influences of low-pass characteristics within the acceleration loop**

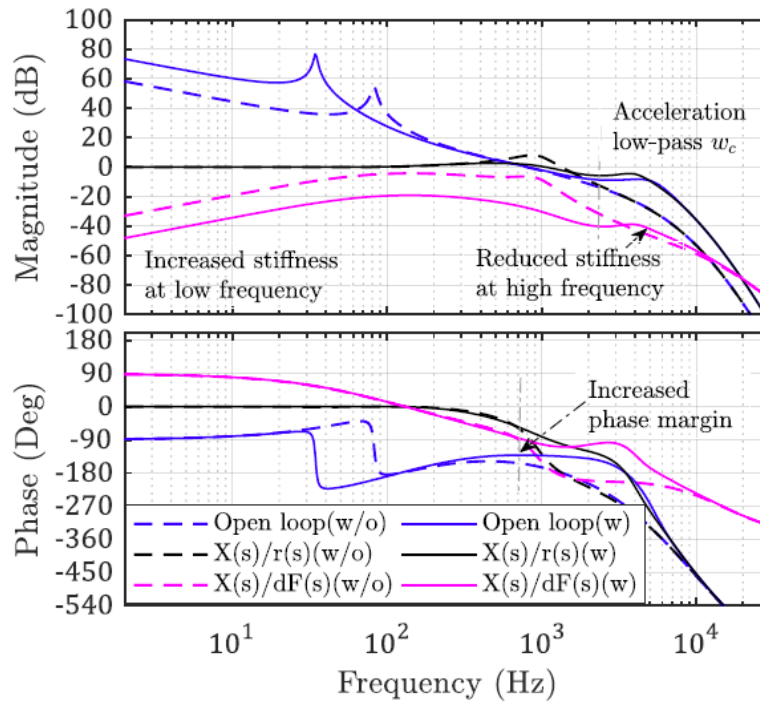
In practice, the acceleration measurement always has a low-pass feature limited by the bandwidth of the sensor and conditioning electronics. Moreover, the  $H_a$  filter can be set by the user to maintain closed-loop stability. The filters acting on acceleration signal will change the shape of the stiffness curve. When these low-pass characteristics exist in the acceleration loop, the transfer functions are plotted in Figure 7-7 b).

The PID gains are increased by the same ratio as in Figure 7-7 a). It can be seen that in the low frequency range, the dynamic stiffness is increased by the same level as in Figure 7-7 a). However, at frequencies just after the measurement bandwidth of the sensor, the dynamic stiffness deteriorates, showing larger amplitude. At even higher frequency, the stiffness remains unchanged because the sensor cannot response to such high frequency motion any more.

Although the high frequency dynamic stiffness is not enhanced, the open loop transfer function shows larger phase margin compared with no acceleration feedback scenario, and therefore the system is more stable. With the larger phase margin available, the PID gains can be increased further because the bandwidth of the position loop is limited by the available phase margin. This helps to achieve both better low frequency disturbance rejection and larger reference tracking bandwidth.



a) Acceleration feedback with ideal sensor



b) Acceleration feedback with low-pass characteristics

Figure 7-7: Comparison of loop transfer functions with (w) and without (w/o) acceleration feedback



### 7.4.3 Error contributions of the added acceleration sensor

The additional acceleration control helps increasing the low frequency dynamic stiffness. However, the acceleration-measuring sensor will inevitably bring some sensor noise, which will contribute to the following errors of the tool. In ultra-precision manufacturing scenario the tool positioning errors directly affects the surface quality of the finished parts [157], [158]. Thus, it is necessary to study how much error will be introduced by the new sensor, providing a guideline for comparing the benefits of a higher stiffness and the side effects of the sensor noise.

The transfer functions from the two sensor voltage noise  $n1$  and  $n2$  to the closed-loop tool position  $X(s)$  is found to be

$$\frac{X(s)}{n1(s)} = \frac{X(s)}{r(s)} \quad (7-11)$$

$$\frac{X(s)}{n2(s)} = \frac{X(s)}{dF(s)} H_a K_a H_I K_T \quad (7-12)$$

It is found that the noise transfer function from displacement sensor is the same as the closed-loop reference tracking function. The noise transfer function from acceleration sensor is similar to the dynamic compliance function, except the term of  $H_a K_a H_I K_T$ . In fact, the noise of the acceleration sensor voltage can be treated as a disturbance force after multiplied with  $H_a K_a H_I K_T$ . That is to say, the acceleration feedback approach reduces the system response to the force disturbance but also introduces more disturbances at the same time.

A third disturbance source is the current noise  $dI$  from the current loop controller as discussed in Chapter 5. The currents in the motor winding will instantaneously generate force disturbances on the moving parts. Therefore, the current disturbances transfer function is

$$\frac{X(s)}{dI(s)} = \frac{X(s)}{dF(s)} K_T \quad (7-13)$$

The transfer functions of the three disturbance sources with different acceleration feedback depths are shown in Figure 7-8. The dashed lines are for a small acceleration gain (0.001) and the solid lines are for a larger acceleration gain (4). It can be seen that with a larger acceleration gain, the current noise disturbance is suppressed within the bandwidth of the acceleration sensor, showing similar shape with the dynamic compliance curve in Figure 7-7 b). While the transfer function from the acceleration sensor noise shows significant increase with a larger acceleration gain. The noise from the capacitive sensor is redistributed from the middle frequency range to a higher frequency range.

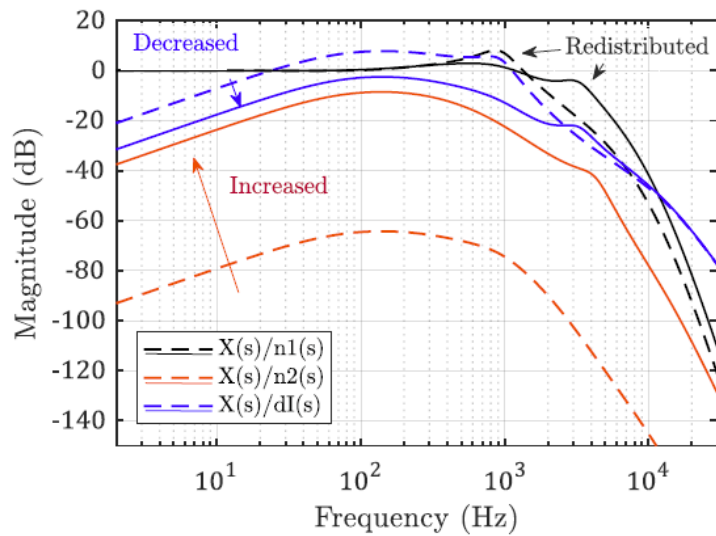


Figure 7-8: The transfer functions of the three disturbance sources with increasing acceleration feedback depths (Dashed: small acceleration gain; Solid: large acceleration gain)

Those error transfer functions together with pre-measured spectrums of the disturbances can be used to estimate the tool positioning error and following errors. The model of synthesising all the disturbance sources has been established in Section 5.7. This approach is used in the error contribution analysis of the new acceleration sensor. A fourth error contribution PSD to the tool position from the acceleration sensor is defined as

$$PSD_4(v) = P_a(v) \times |FRF_4(v)|^2 \quad (7-14)$$

Where:  $P_a$  is the pre-measured sensor noise spectrum,  $v$  is the frequency bins in Hz.

## 7.5 Experimental verification of the acceleration feedback model

### 7.5.1 Acceleration sensor characteristics

Two single-axis accelerometers from PCB Electronics (Model 333B50) are used to measure the acceleration of the cutting tool. One is used to measure the vibration of the machine base and the other is used to measure the tool vibration. Then the difference between the two is the measured relative vibration. The sensor signals are amplified by a conditioning module, made by FYLDE electronics, UK.

In order to maximise the measurement bandwidth of the acceleration signal, the low-pass filters cut-off frequency in the ADC circuits are selected as high as possible (half of the sampling rate). The typical frequency response of a piezo accelerometer is shown in Figure 7-9. The sensor has a mechanical resonant  $f_r$  at around 10~30 kHz. In the low frequency range, the lower limit  $f_L$  is caused by the finite insulation resistance in the sensor. It can be used up to 50% of the resonant frequency for 3dB accuracy.

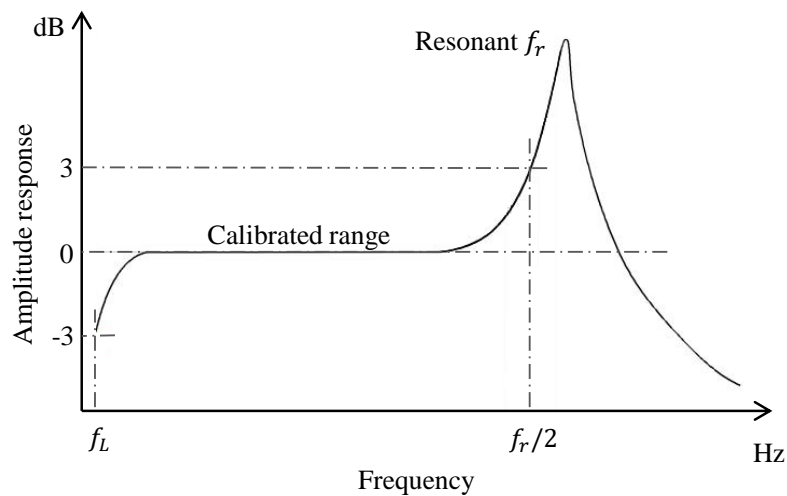


Figure 7-9: Typical frequency response of piezo accelerometers

The detailed specifications of the acceleration sensor used in this study are listed in Table 7-2. The resonant frequency is above 20 kHz and thus the bandwidth of the acceleration sensor was set as 10 kHz in the conditioning electronics. The sensitivity of this sensor is 1000 mV/g and the input voltage range of the controller is  $\pm 4.096$  V, therefore the maximum acceleration can be measured is  $\pm 4.096$  g. This acceleration

is not high for fast tool servo devices but still acceptable for studying the effects of the new feedback loop.

Table 7-2: Specifications of the acceleration sensor

Performance	Value
Sensitivity ( $\pm 10\%$ )	1000 mV/g
Discharge Time Constant	0.7 to 2 sec
Frequency Range ( $\pm 5\%$ )	0.5 to 3000 Hz
Resonant Frequency	$\geq 20$ kHz
Phase Response ( $\pm 5^\circ$ )	2.5 to 3000 Hz
Spectral Noise (1 Hz)	$15 \mu\text{g}/\sqrt{\text{Hz}}$
Spectral Noise (10 Hz)	$3.8 \mu\text{g}/\sqrt{\text{Hz}}$
Spectral Noise (100 Hz)	$1.1 \mu\text{g}/\sqrt{\text{Hz}}$
Spectral Noise (1 kHz)	$0.4 \mu\text{g}/\sqrt{\text{Hz}}$

The spectral noise performance of the sensor is also listed in the table. However, this is only the sensor performance under laboratory conditions. In practical applications, the conditioning electronics and cabling contribute noise to the signal. Therefore, the spectrums of the measurement noise are measured on site.

In this measurement, the movable parts are temporally fixed by glue and the necessary electronics like the current loop is powered off. The environmental conditions are kept as quiet as possible. Thus, the measured acceleration feedback signal will reflect the noise floor of the sensor and the conditioning electronics. Again, this measurement includes the noise from the ADC sampling circuits. The measured time domain signal and the PSD are plotted in Figure 7-10. It can be seen that the measured results show some randomly distributed peaks caused by the environmental interferences.

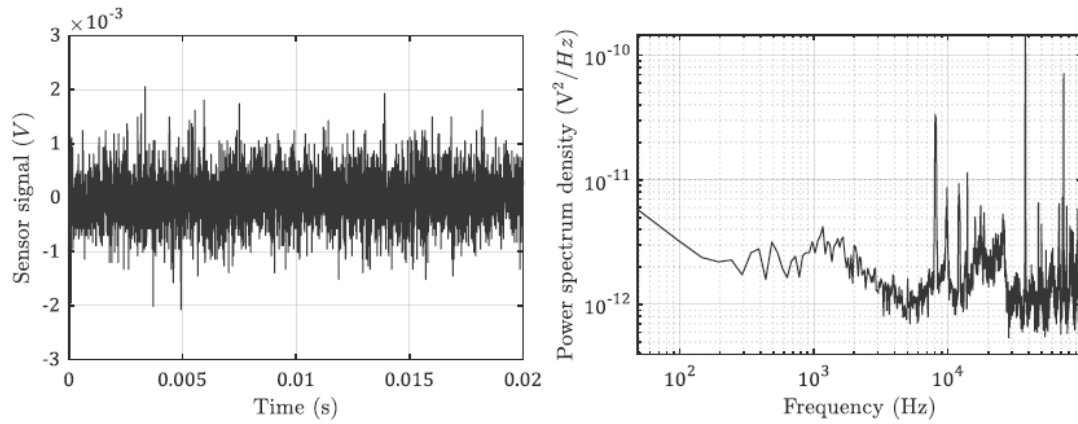


Figure 7-10: Measured sensor noise of the acceleration sensor

Both the displacement and acceleration open-loop response of the system are plotted in Figure 7-11, from force ( $N$ ) to tool position ( $m$ ) or tool acceleration ( $m/s^2$ ). The double integrated acceleration frequency response is plotted in comparison with the displacement response curve and with a gain of 10.8995, the acceleration response agrees with the displacement response well. The deviation below several Hertz on the acceleration curve is caused by the low signal noise ratio when the movement frequency is low. The acceleration is so low that the signal is buried in the noise floor of the sensor electronics. The acceleration sensor has lower phase loss at high frequency than the capacitive displacement sensor. This is evident from the phase graphs of the two Bode plot.

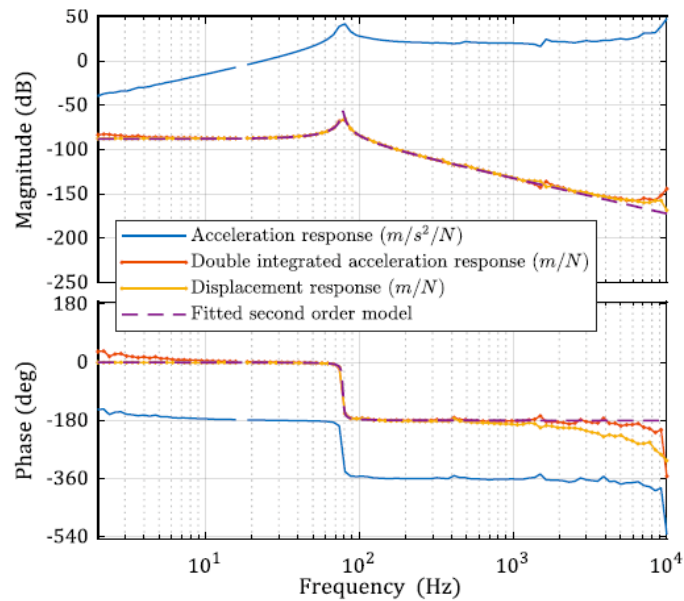
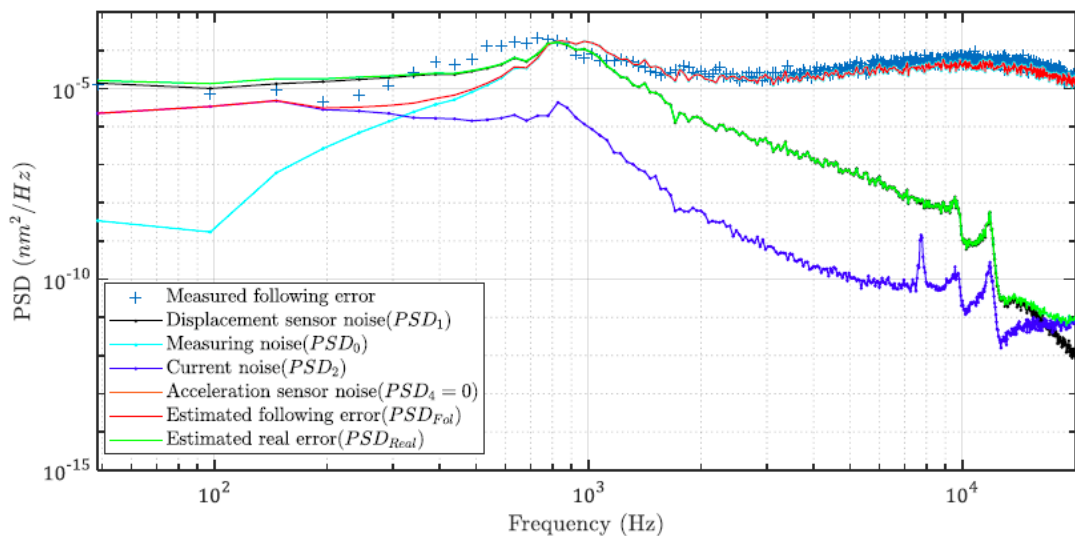


Figure 7-11: Measured frequency responses of the displacement sensor and the acceleration sensor

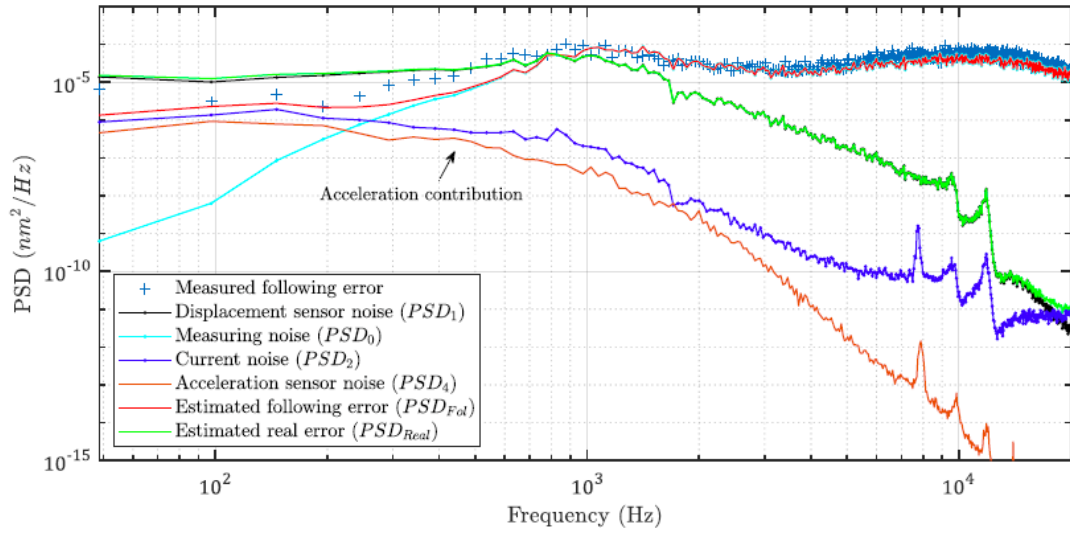
### 7.5.2 Positioning errors introduced by the acceleration sensor

The control algorithm was run on the custom-built DSP board. The control servo loop was run at 199.6 kHz rate. The following errors of the tool position are acquired from the capacitive feedback sensor.

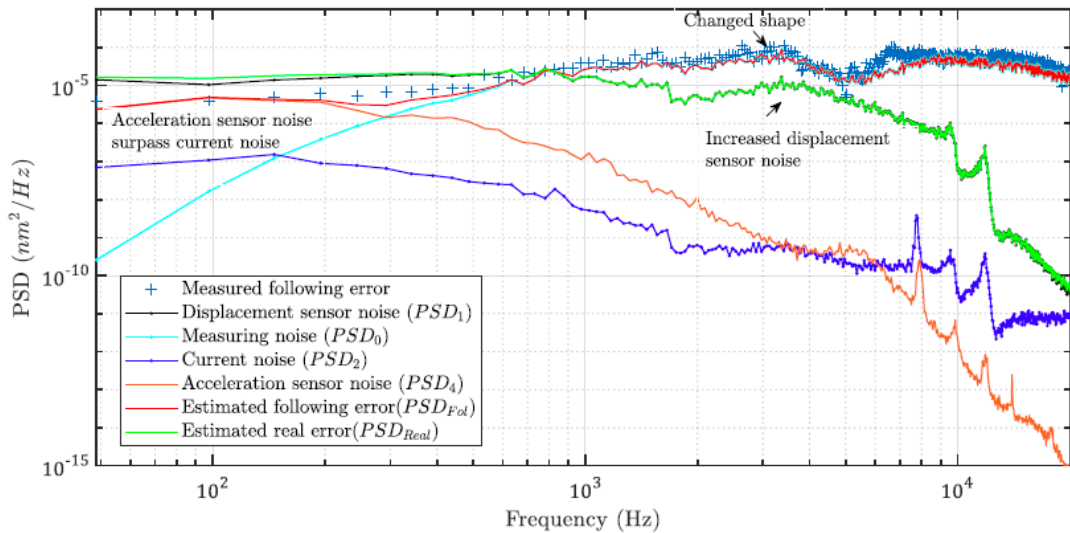
The PSD of the error signal is plotted in Figure 7-12. The additional error source from the acceleration sensor is added to the model, besides the sensor noise, the measuring errors and the current noise as demonstrated in Chapter 5. In Figure 7-12 a), the acceleration feedback is disabled by setting the feedback gain  $Ka = 0$ . In this case, the transfer function from the acceleration sensor noise to the tool position is virtually zero according to Equation (7-12) and the error contribution from the acceleration sensor is zero. When the acceleration feedback gain is set as 0.5 in Figure 7-12 b), the contribution of the acceleration sensor starts to show up as comparable level with the current noise. When the acceleration gain is increased further to  $Ka = 4$  as in Figure 7-12 c), the error contributed by the acceleration sensor noise surpasses the current noise and become the major error source. At the same time, because the reference-tracking curve is raised near 5 kHz frequency range, more noise from the capacitive sensor are transmitted to the tool position within this frequency range. This is clearly shown from the change of the overall shape of the measured following error PSD in the Figure 7-12 c).



a) Measured following error with  $Ka = 0$



b) Measured following error with  $Ka = 0.5$



c) Measured following error with  $Ka = 4$

Figure 7-12: Error contributions with different acceleration gains

### 7.5.3 Dynamic stiffness with acceleration feedback control

The dynamic stiffness is tested by injecting a sweep sinusoidal disturbance voltage onto the control output. This disturbance voltage is considered proportional to disturbance force since the current loop bandwidth is as high as 400 kHz and the interested frequency range is 10 kHz. Figure 7-13 shows the measured frequency response from disturbance force to position output with two different acceleration gains ( $Ka = 0$  and  $Ka = 1$ ) and fixed PID gains ( $Kp = 1.65, Ki = 562, Kd =$

$9.5 \times 10^{-4}$  and  $Tf = 9.6 \times 10^{-5}$ ). The modelled responses are plotted as well to compare with the measured data. It can be seen that the measured data agrees with the model prediction for both cases. When the acceleration gain is increased, the response to cutting force at around 1 kHz is more damped and thus the dynamic stiffness at this point is enhanced.

The stiffness at the low frequency range keeps the same despite the higher acceleration gains. This is because the spring term and the super spring term in Equation (7-9) are only related to the PID gains, which are not increased in this case. The increased damping is equivalent to a larger phase margin and it permits larger PID gains without loss of closed-loop stability.

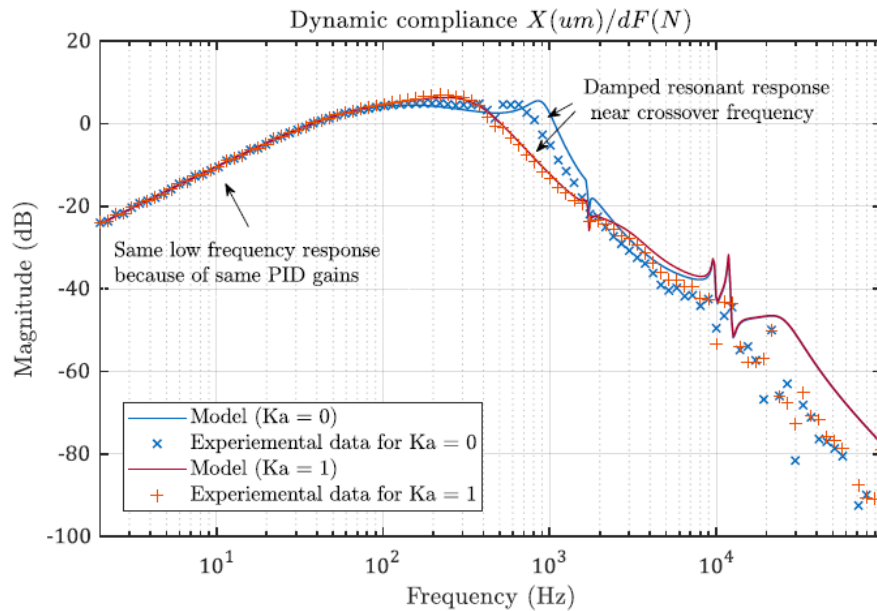


Figure 7-13: Dynamic compliance function with increasing  $Ka$  and fixed PID gains

When the PID gains are simultaneously increased by a global factor  $Kg$  as depicted in Section 7.4.1, the measured and modelled dynamic compliance curves are shown in Figure 7-14. The low frequency stiffness is increased with larger controller gains and the measured response data proved this. It is worth mentioning that the increased PID gains cannot be used without the acceleration gain because they will cause instability. Despite the improved low frequency stiffness, the stiffness at around 5 kHz frequencies is worse than the no acceleration feedback scenario. This is due to the low-pass feature of the acceleration measurement, as discussed in Section 7.4.2.



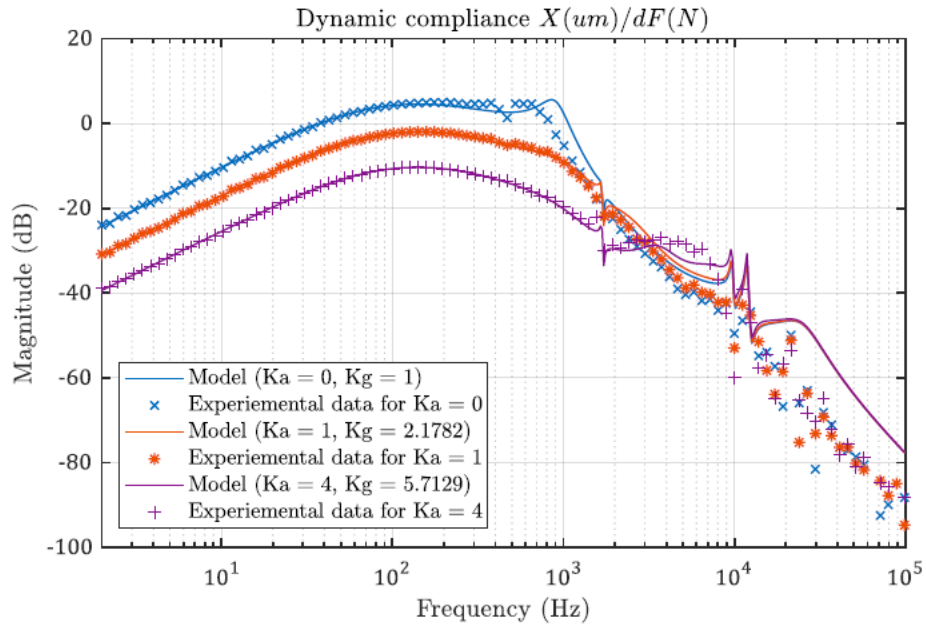


Figure 7-14: Dynamic compliance function with increasing  $Ka$  and proportionally increased PID gains

## 7.6 Intermittent cutting experiments

### 7.6.1 Intermittent cutting setup

An intermitted cutting experiment is designed to test the dynamic stiffness during cutting. The built experiment device was mounted on a diamond turning machine bed as shown in Figure 7-15.

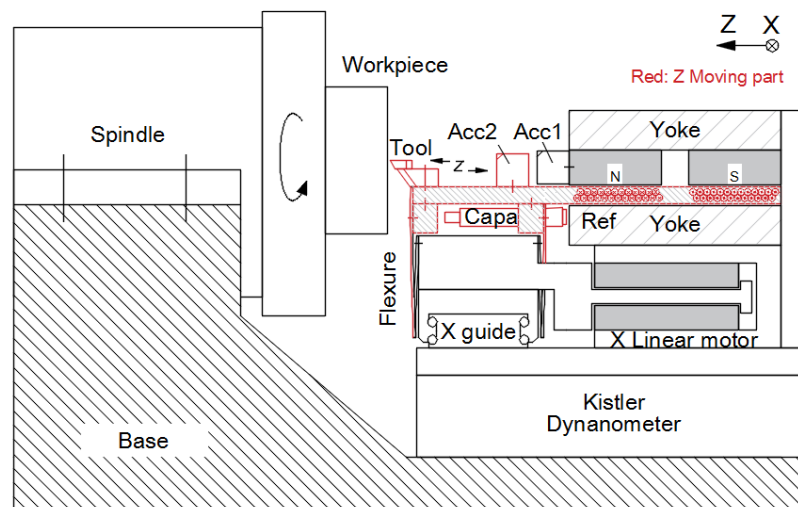


Figure 7-15: Diagram of the acceleration feedback control experimental setup

A precision air-bearing spindle was used to hold the workpiece for a face cut. A copper sample was designed with a step change in height by milling half of the surface lower. Therefore, the cutting only occurred during half of the spindle revolution and the cutting force changed abruptly. This step-changed force was used as the input for evaluating the dynamic stiffness of the cutting system. The turning parameters are listed in Table 7-3. The machined surface was measured by a white light interferometer (ZYGO CP300).

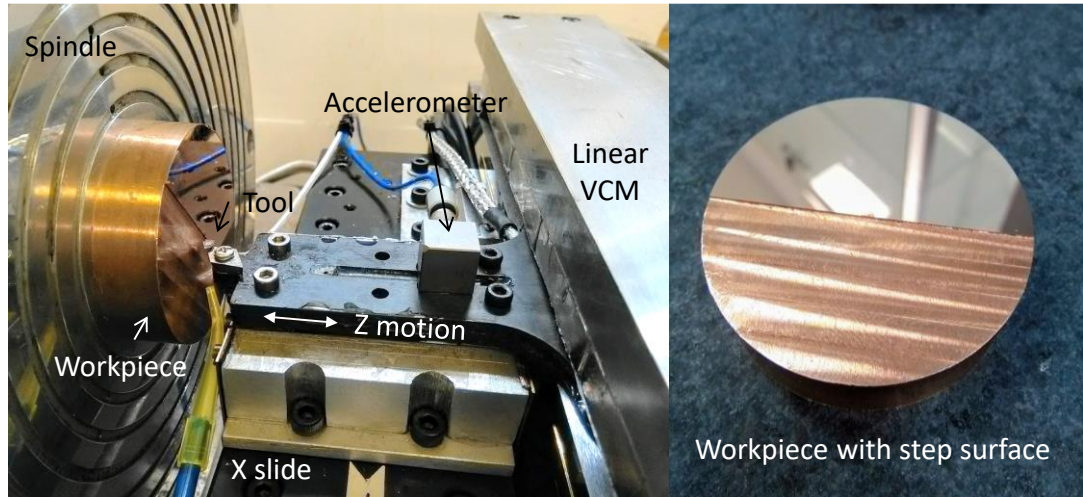


Figure 7-16: Photo of the acceleration feedback control experimental setup

Table 7-3: Experimental conditions for intermitted cutting tests

Name	Value
Workpiece material	Copper
Tool radius	0.5 mm
Rake angle	0 degree
Feed rate	8 $\mu\text{m}/\text{rev}$
Depth of cut	2 $\mu\text{m}$
Spindle speed	250 rpm
Lubricant	Thin layer of mineral oil

## 7.6.2 Intermittent cutting results

The different parameters are deployed in the controller and used in the face cutting experiment. The acquired following errors from the displacement sensor during the intermittent face cutting are shown in Figure 7-17. The acceleration gains are increased from 0 to 4 and the PID gains are increased accordingly in Figure 7-17 a) to d). Higher gains resulted in ringing noise and thus not shown here.

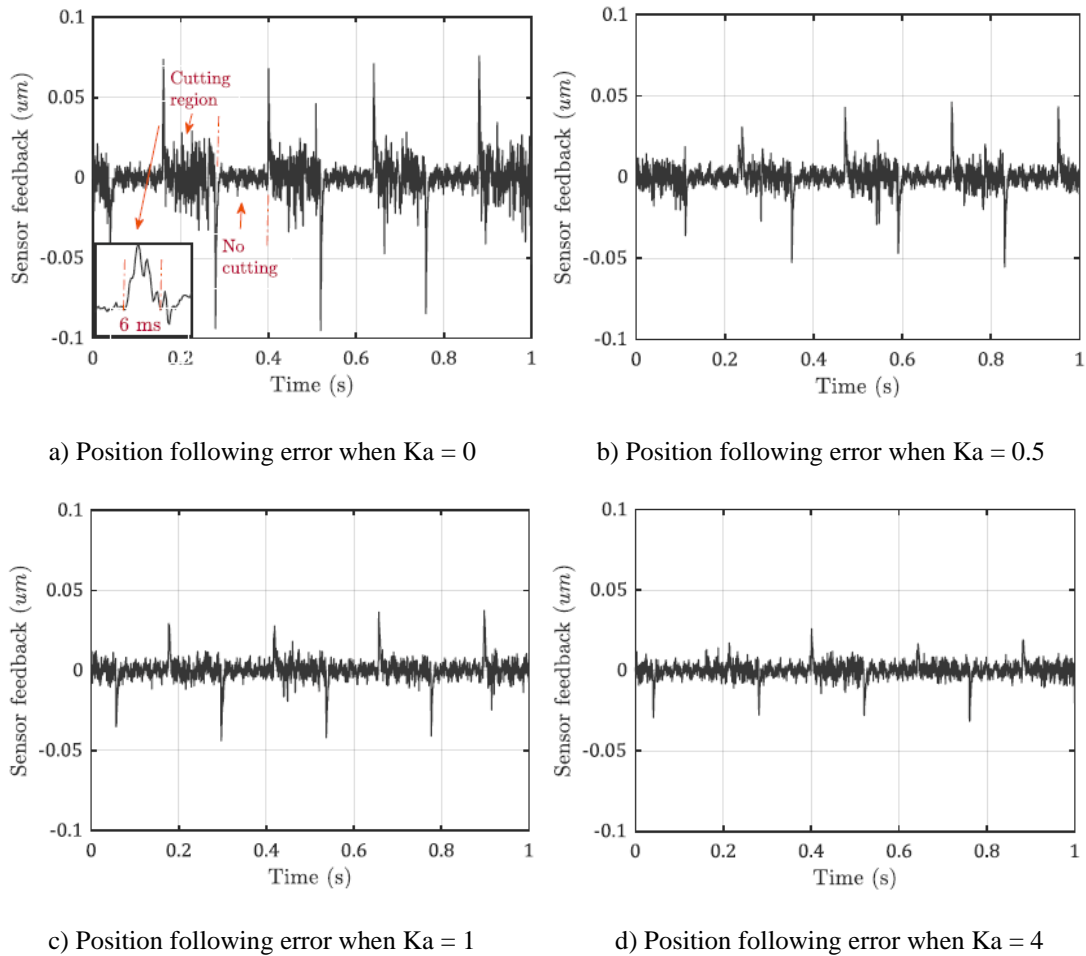


Figure 7-17: Following error caused by cutting force with different acceleration gains

It can be seen from the first graph that when the tool enters the cutting region, there exists a sharp rise of the following error due to the sudden change of cutting force. Since the positive direction of the position sensor is defined as the direction away from the workpiece, this means less material will be cut. Then the tool was quickly controlled back to the commanded position. The duration of the peak is approximately 6 milliseconds for every peak. When the tool leaves the cutting region, there exists an opposite error peak due to the disappearance of the cutting force. The following error

shows larger peak-to-valley values in the cutting region than the air cut region, which is reasonable because there is an extra disturbance source. As the acceleration gains are increased, the value of the peak error decreases from 75 nm ( $Ka = 0$ ) down to 25 nm ( $Ka = 4$ ). The peak-to-valley errors during cutting are also seen lower with larger acceleration gains.

Four circular tracks of 1 mm width are turned on the workpiece surface with the above four groups of gains. The measured surface form is shown in Figure 7-18. The picture on the left is a stitched image with a 5X objective (numerical aperture of 0.13, 25% overlap), which covers a surface area of 6.80 mm  $\times$  5.15 mm and the pictures on the right show detailed surface form at the step edge of the first and last track measured with a 20X objective covering a field of view of 0.35 mm  $\times$  0.26 mm (numerical aperture of 0.4). Therefore, both low frequency and high frequency form errors can be captured. The cross sectional profiles along the cutting path (marked 4, 3, 2 and 1 in Figure 7-18 left) for the four cuts are shown in Figure 7-19. The profile is evaluated by averaging the cross sections within 0.2 mm width to the track centre in order to average out the random factor. The four tracks are found of slightly different height offset, which is considered as results of the thermal drifts between the cuts. The radius of the four tracks are 16.5 mm, 17.5 mm, 18.5 mm and 19.5 mm, corresponding to surface speed of 431 mm/s, 458 mm/s, 484 mm/s and 510 mm/s, respectively.

The cross sectional profiles #4 in Figure 7-19 shows obvious higher surface form close to the edge. This is attributed to the tool deviation caused by intermittent cutting force. As calculated from the 6 ms peak following error in Figure 7-17 a) and the surface speed of the workpiece, the surface form error should last for 2.586 mm. This agrees with the measured profile shape. As the acceleration gains are increased, the height of this form error is reduced from 106 nm ( $Ka = 0$ ), 68 nm ( $Ka = 0.5$ ), and 42 nm ( $Ka = 1$ ) down to 27 nm ( $Ka = 4$ ). This demonstrates that the increased gains help to achieve better low frequency stiffness.

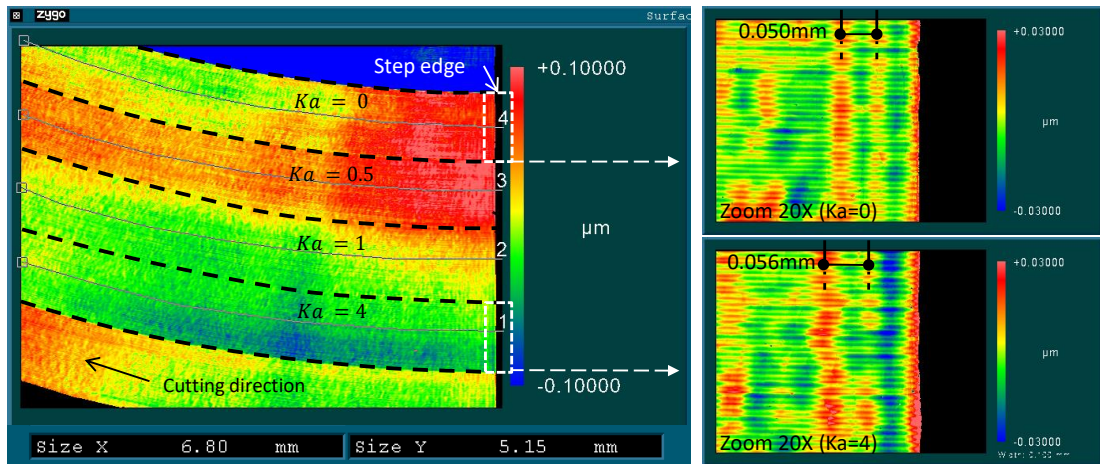


Figure 7-18: Measured surface profile with different acceleration gains and the detailed image at the edge

The detailed form errors for the track #4 and track #1 on the right in Figure 7-18 show obvious tool vibrations. The 0.05 mm and 0.056 mm error wavelength correspond to 8.62 kHz and 9.1 kHz tool vibrations respectively. It can be seen from these two graphs (with same colour bar setting) that the form is worse with a higher acceleration gain at the high frequency range. This result agrees with the measured stiffness curve in Figure 7-14. This experiment reveals that higher controller gains do not guarantee a better surface finish. Improvement of stiffness in some frequency ranges also means deteriorated stiffness in other frequency ranges due to the nature of closed-loop control. A properly tuned system is such that the stiffness is tuned higher where disturbance force is dominant, and the stiffness is allowed to be lower where the disturbance is negligible. The added acceleration sensor did not break the law but expanded the tuneable frequency range to further than the position loop bandwidth. The step-changed force disturbance in this experiment is an extreme example since in some applications the cutting force might be increased smoothly by changing the depth of cut gradually. If the cutting force can be constrained within a low frequency range by proper programming, the acceleration feedback approach will be beneficial in improving machining quality.

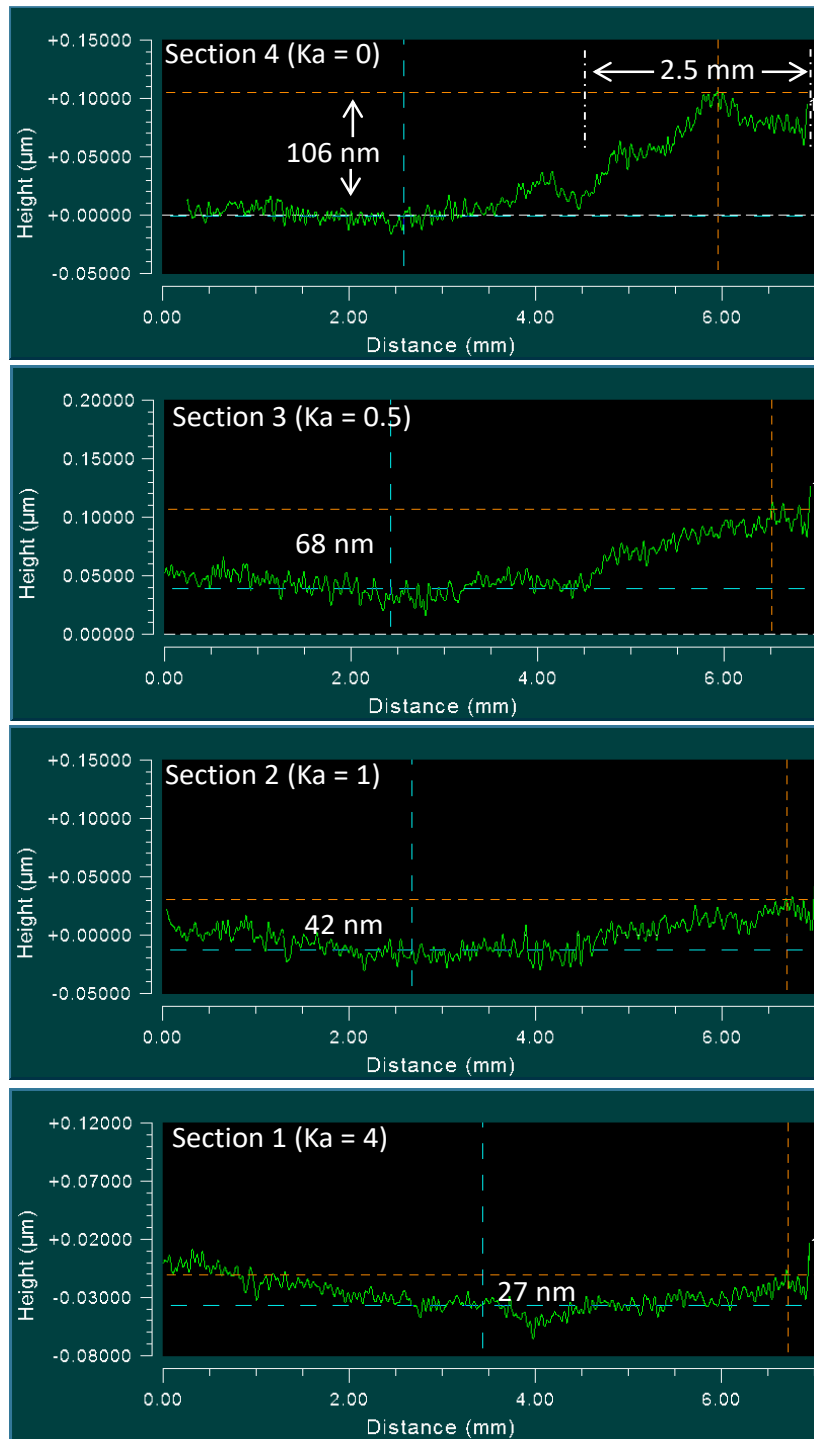


Figure 7-19: The averaged cross sectional profile along the cutting path

## 7.7 Summary

In this chapter, control algorithm with additional acceleration feedback loop is studied to enhance the dynamic stiffness of the fast tool positioning system.

Theoretical model of the dynamic stiffness and error propagations are established and verified in the positioning and cutting experiments. The practical issues of acceleration feedback technique in ultra-precision machining applications are discussed.

Acceleration feedback method increases the loop phase margin and the PID gains can be increased further. By doing this, the dynamic stiffness within the acceleration sensor bandwidth is proportionally improved. However, the stiffness is worse at frequencies just beyond the acceleration sensor bandwidth, due to the existence of low-pass characteristics in the acceleration feedback loop. The acceleration feedback technique does not suppress the force disturbance at all frequencies but expands the frequency range where the stiffness curve can be tuned, according to the spectrum of disturbance. The stiffness analysis results have been verified in the intermittent face cutting experiments. The measured surface form errors can be mapped to the low frequency and high frequency vibrations cause by the cutting force.

The additional acceleration sensor brings new error source to the closed-loop and its contribution increases with a larger acceleration gain. At the same time, the other disturbances are suppressed except the displacement sensor noise. There is a point where the increased acceleration error contribution surpasses others and starts to dominate, which is the upper limit for the practical acceleration gains.

# CHAPTER 8

## Geometric error mapping and freeform machining experiments

### 8.1 Introduction

In this chapter, the developed positioning system and the control algorithms are deployed in machining of typical freeform surfaces to test their performance.

Firstly, the experimental setup is established based on a custom-built diamond-turning machine. The original X and Z slides are replaced with the newly designed device. Only the precision air-bearing spindle was used throughout the cutting experiments. The rotational accuracy of the air-bearing spindle is evaluated before the cutting trials with a modified multi-probe error separation method. Radial, tilt and axial error motions are all obtained in this experiment.

Then the synchronisation between the spindle position and the fast tool motion is discussed. A hardware triggering mechanism is adopted to ensure deterministic timing. A flat face cut on NiP alloy material is carried out to demonstrate the achievable surface quality with this setup. After that, several freeform shapes are also machined and the following errors are evaluated. The surface forms are measured using white light interferometer.

### 8.2 Diamond turning experimental setup

A home-built diamond-turning machine is used as the machining platform with some modifications. The machine adopts a traditional lathe layout as it has very large air bearing spindle, as shown in Figure 8-1. The air-bearing spindle is fixed on a granite machine base. The workpiece is clamped on the spindle by vacuumed air. The X and Z linear axes are designed as a dovetail shaped air-bearing structure [159].



The developed positioning device was installed on the diamond-turning machine with its original slides disabled. Only the precision air-bearing spindle was used in this experiment, as shown in Figure 8-2. The stationary magnet track of the device was fixed to the spindle housing through two enhancing bars to increase the structural rigidity. A dynamometer (Type: Kistler 9129AA) was also mounted under the device to measure the cutting force profile of predefined shape when the enhancing bars are not fitted.

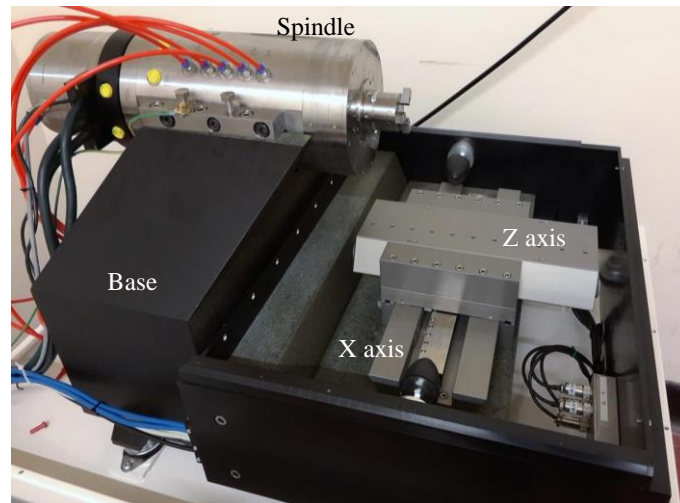


Figure 8-1: Photograph of the diamond-turning machine before modification

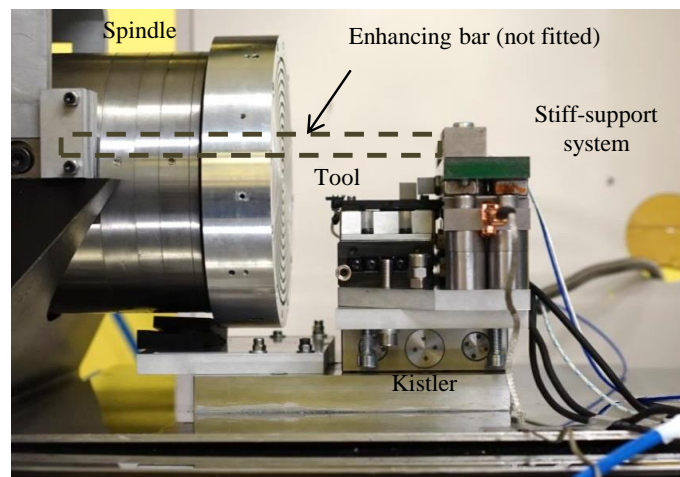


Figure 8-2: Machining setup on diamond turning machine with the developed device

The spindle unit is equipped with a 6000-lines optical encoder. After 4X interpolation in the controller, the spindle angle can be resolved to  $0.015^\circ$ . The key specifications of the work spindle are listed in Table 8-1. The control system is based on an open architecture controller structure (Type: A3200) from Aerotech.

Table 8-1: Specifications of the work spindle

Specification name	Value
Motor	Frameless brushless motor
Feedback	Optical encoder (6000 lines)
Air supply pressure	6 bar
Axial load capacity	136 kg
Radial load capacity	82 kg
Axial stiffness	150 N/ $\mu\text{m}$
Radial stiffness	63 N/ $\mu\text{m}$
Angular stiffness	4.1 Nm/ $\mu\text{rad}$
Maximum rotational speed	10000 rpm

### 8.3 Synchronisation of position command to spindle angle

For freeform turning, the cutting depth commands must be synchronised to the spindle angle in every revolution. Otherwise, the machined form will be distorted. Therefore, the spindle angle information must be transmitted to the digital controller with deterministic timing. Then the controller determines the position command according to the spindle angle.

The spindle angular information is only accessible from the A3200 controller, which is physically isolated from the fast positioning module. The A3200 controller hardware provides several industrial standard interfaces to communicate with the developed controller board. The Position Synchronized Output (PSO) feature of the A3200 controller is very useful in synchronising other devices with the spindle motion. The PSO function tracks the encoder reading and outputs synchronized pulses to the digital output ports. The latency of the output pulse is 120 ns and the maximum output frequency is 5 MHz.

The output pulses are used to trigger the developed controller and get the information transmitted. The pulse signal is routed to one of the GPIO port of the controller board. Each rising edge will trigger an interrupt task in the DSP. In the interrupt service routine, the count number is increased by one and then the CPU clears the interrupt flag and is ready for next edge.

The trigger rate puts a limit on the spindle speed and the angular pulse numbers. A small pulse number in each revolution means that the resolution of spindle angular position will be poor. For the GPIO interrupt method, the maximum trigger rate is measured to be 800 kHz without affecting the servo calculation. The spindle angle information is also used in the measurement of the spindle error motions.

## **8.4 Measurement of spindle error motions**

Because the rotation of workpiece is the only motion required to generate a freeform surface besides the motions provided by the new positioning device, the rotation errors will contribute to the machined part accuracy. Therefore, it is worthy to evaluate the errors of the spindle. Another reason for measuring the spindle errors is that the designed device has the ability to compensate for the spindle errors due to its fast response time, although this has not been done in this thesis due to time limit.

The ultimate idea is to measure the rotational errors in real time in reference to the metrology frame and use this signal as the feedback of the fast actuating motion. Then the requirements on the spindle accuracy will be reduced.

### **8.4.1 Measurement of radial and tilt error motions**

The key issue of spindle metrology is how to separate the true rotor error motions from the measured sensor data, which includes the imperfection of the measurement standard. Reversal, multi-probe and multi-step methods are the three most commonly used separation techniques for spindle metrology [160]. Reversal method typically involves the repositioning of both the artefact and probe, which will inevitably introduce extra measuring uncertainty. Multi-probe and multi-step methods have the same problem of harmonic suppression which derives from the algorithm used to separate the artefact profile [161], [162]. In this thesis, the radial motion errors of the

spindle are measured using a revised complementary multi-probe method, as described in Appendix D.

The measurement setup is shown in Figure 8-3. Three displacement sensors are pointed to the rotating artefact from three different angles. The artefact is fixed to the spindle rotor and the error motions of the spindle together with the imperfection of the artefact are detected by the displacement sensors. In practice, the shape change of the artefact caused by thermal variation and centrifugal force is negligible. Thus, the circumference profile of the artefact is assumed constant throughout the measurement cycle. The artefact profile signal is imposed on the error motion signals with different phases at different probe angles. This makes it possible to separate the artefact errors from the sensor signals. The detailed measurement procedures and data processing can be found in Appendix D.

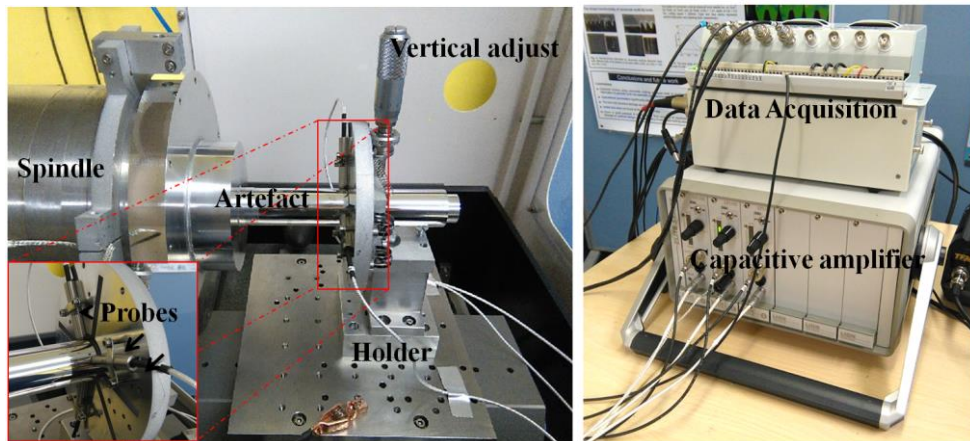


Figure 8-3: Experimental setup for radial and tilt error measurement

The tilt errors are calculated by measuring the radial errors at different locations along the spindle axis. Linear curve fit is applied at each rotary position and the results are plotted in Figure 8-4. The measured trajectories at different axial locations show good linear relationship. The fitted lines are then used to calculate the tilt errors of the spindle. The calculated tilt errors about the X and Y axis are shown in Figure 8-5. The angular deviations about the X and Y axis are within  $\pm 0.1$  arc-seconds for the full spindle revolution.

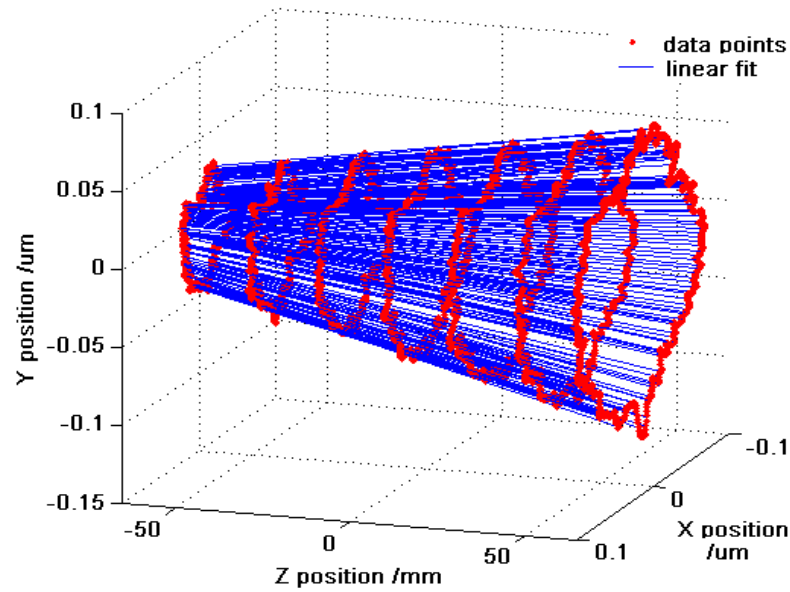


Figure 8-4: Trajectories of spindle rotating centre line with linearly fitted data

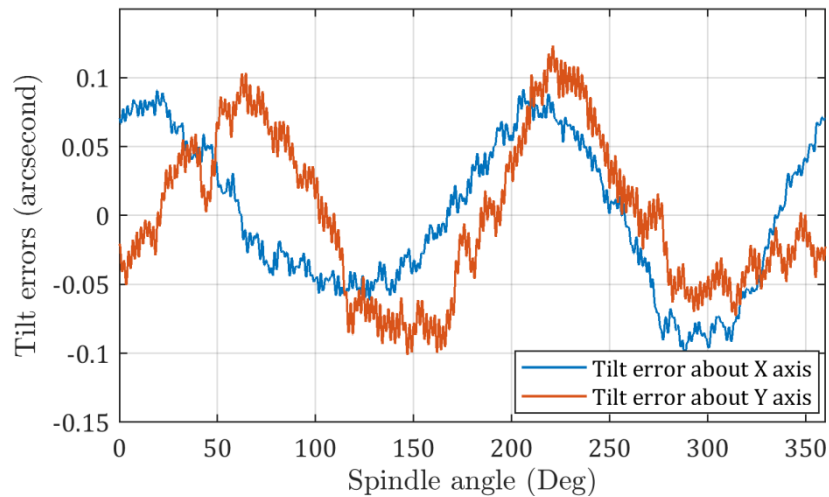


Figure 8-5: Calculated tilt errors about the X and Y axis in one full spindle revolution

#### 8.4.2 Measurement of axial error motions

The axial error motions of the spindle directly affect the surface profile of the diamond turned parts. Different from the radial error measurements where the artefact form error has to be separated first, the axial error of the artefact is of less importance. A precision spherical artefact is used in this measurement as shown in Figure 8-6. Firstly, the artefact is adjusted co-axial (within 1 µm) to the spindle rotational axis with a precision dial gauge. Then a capacitive probe, the same as the ones used in the radial error motion measurement, is targeted at the top of the sphere. The vertical and

horizontal position of the probe is adjusted manually until the readings reach a minimal value. The artefact form error and spindle radial errors will contribute a bit to the measured axial error results, but due to the small slope at the sphere top, the results are less sensitive to these factors.

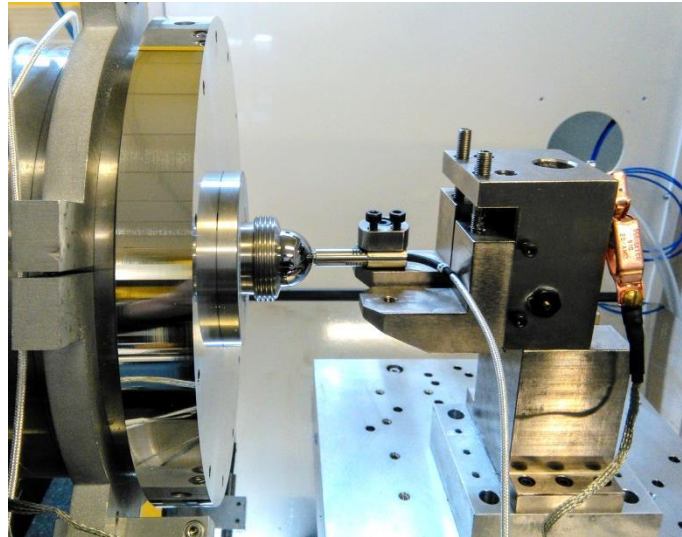


Figure 8-6: Setup for axial error measurement

The measured axial spindle error motions are shown in Figure 8-7. A total number of 960 data points are acquired within one revolution of the spindle. The spindle error falls within  $\pm 0.05\mu\text{m}$  band within one revolution.

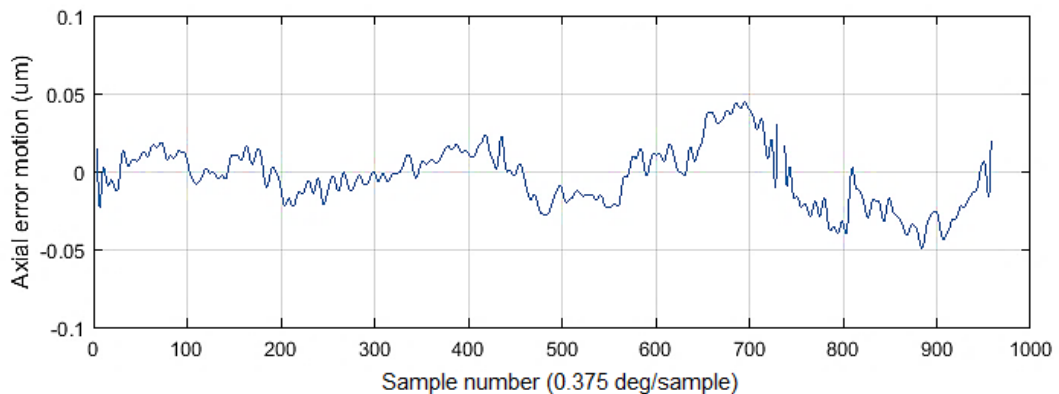


Figure 8-7: Measured axial error motions of the spindle

So far, the radial, axial and tilt spindle error motions are all quantitatively evaluated through the above experiments. The measurement results are ready to be programed into the motion controller and the repeatable errors in the Z direction can be compensated by the fast positioning system in the future.

## 8.5 Machining trials with the developed system

In order to verify the machining performance of the developed tool positioning system, several typical simple and freeform surfaces are machined with the diamond turning machine setup. The machining trials are started with a flat surface to test the positioning stability and the best optical surface quality that can be achieved. The finished parts were measured by a white light interferometer (ZYGO CP300) using a 20X objective lens. The numerical aperture of this objective is 0.4.

### 8.5.1 Flat surface turning

The flat turning trial is conducted on two different materials, the electroless plated NiP alloy and fine grain aluminium. A single crystal diamond tool from Contour Fine Tooling is used in this process. The geometry of the tool and the cutting conditions are listed in Table 8-2. The same diamond tool is used throughout the freeform turning experiments in this thesis. In addition, the lubrication condition is kept the same with a thin layer of mineral oil.

Table 8-2: Experimental conditions for flat diamond turning

Name	Value
Tool material	Diamond
Workpiece material	Electroless plated NiP alloy and Aluminium
Tool radius	0.5 mm
Rake angle	0 degree
Clearance angle	15 degree
Flat cutting feed rate	2 $\mu\text{m}/\text{rev}$
Flat cutting depth of cut	5 $\mu\text{m}$
Flat cutting spindle speed	250 rpm
Lubricant	Thin layer of mineral oil



The machined aluminium part is shown in Figure 8-8. The surface measurement result for the NiP part is shown in Figure 8-9. The flat surface shows surface roughness of 1.2 nm (Ra) with no filter applied within a measurement area of 0.36 mm × 0.27 mm. This demonstrated the good positioning stability of the designed cutting system.

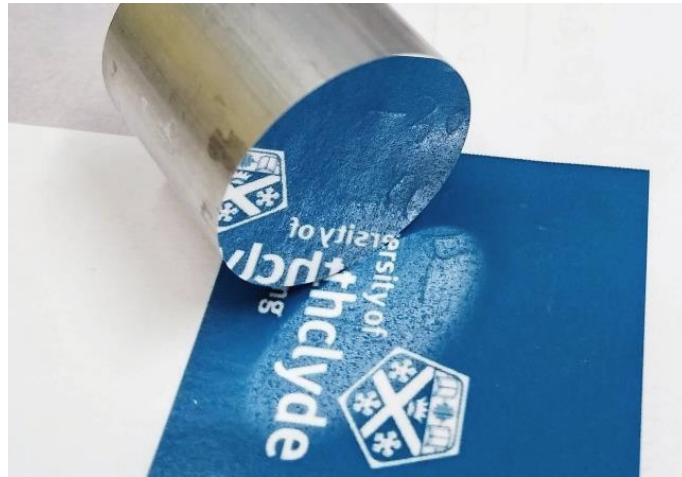


Figure 8-8: Photo of flat turning sample

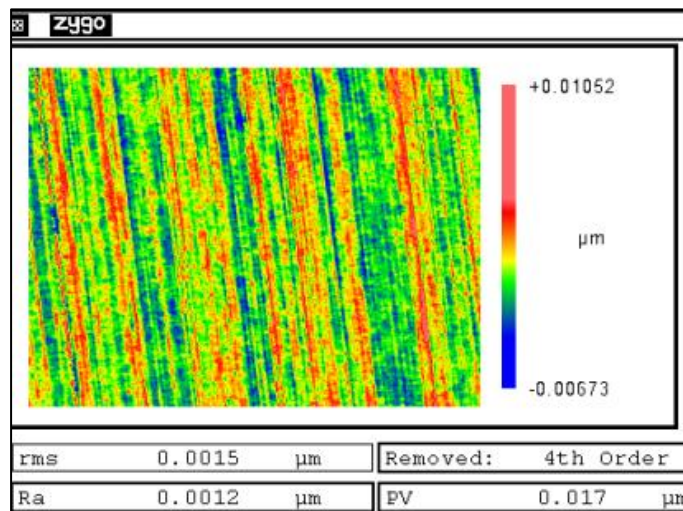


Figure 8-9: Measured flat surface topography on NiP substrate

### 8.5.2 Micro-lenslet cutting

Micro-lenslet structures are machined onto the top face of the workpiece. Firstly, a round diamond tool was used to cut a flat surface with slow feed rate. Then the same tool was programmed to move in a sinusoidal way and the material was cut at the far end of the trajectory as shown in Figure 8-10. The depth of cut was selected as half of



the sinusoidal amplitude and the cutting length was controlled to be the same with cutting width by adjusting the spindle speed. Therefore, each lenslet is a good approximation of a micro spherical shape. Because each lenslet can be formed in a single tool path, the machining efficiency for this method is much higher than multi-pass contouring method [163], [164].

The challenge for this cutting method is that the cutting force is larger than typical diamond turning. The cutting width is several hundred microns compared to the typical cutting width of tens of microns in multi-path cutting. The cutting force will play a part in the final form errors. Therefore, this method requires much higher dynamic stiffness from the cutting system.

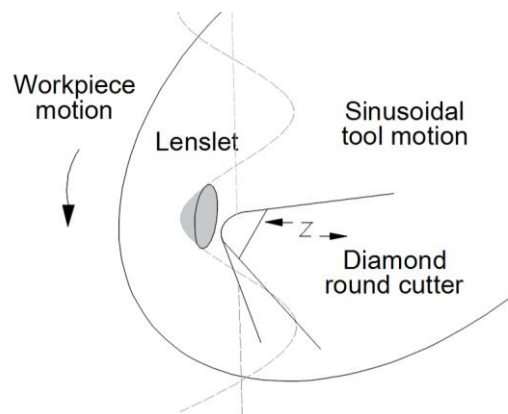


Figure 8-10: Diagram of micro-lenslet cutting trajectory

Table 8-3: Experimental conditions for micro-lenslet cutting

Name	Value
Workpiece material	Electroless plated NiP alloy
Sinusoidal motion frequency	100 Hz
Sinusoidal motion amplitude	10 $\mu\text{m}$
Lenslet depth	5 $\mu\text{m}$
Spindle speed	16 rpm

The experimental conditions are summarised in Table 8-3. The machined micro-lenslet surface and the microscopic photo are shown in Figure 8-11.

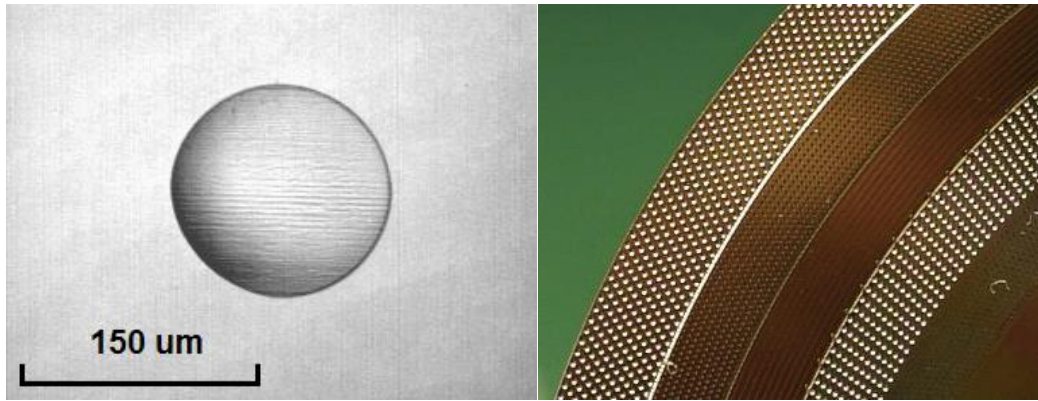


Figure 8-11: Photo of the micro lens and the micro-lenslet part with different depths

The surface form is measured by the 20X objective on ZYGO white light interferometer, same conditions as previous measurement. The form error of the machined micro lens along the cutting direction is shown in Figure 8-12. The cross section is selected at the largest diameter points along the cutting direction. The nominal motion amplitude is 5  $\mu\text{m}$  but because the closed-loop response has 0.6 dB overshoot at 100 Hz, the amplitude of 5.2  $\mu\text{m}$  is used as the form reference. The form error curve shows obvious non-symmetric shape. The maximum error of 200 nm lags behind the maximum depth of cut. This agrees with the calculated tool deviation under cutting forces in Section 5.7.5.

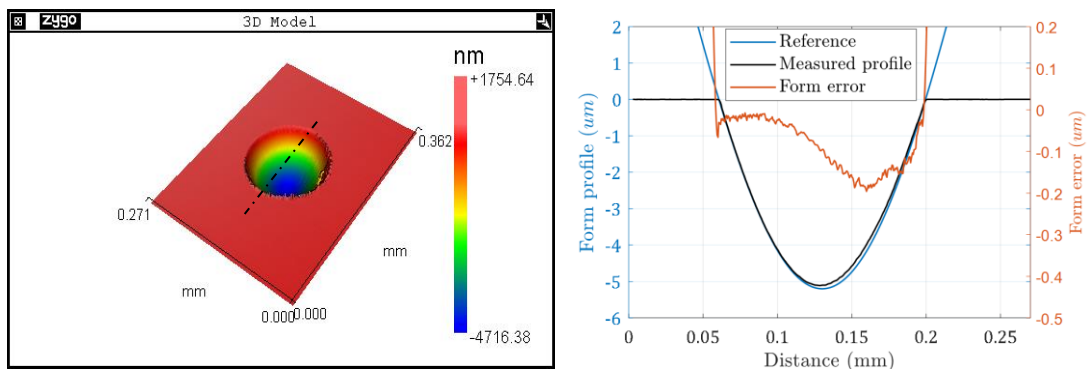


Figure 8-12: Form error of the machined micro lens

### 8.5.3 Beam integrator surface cutting

In this section, non-rotational symmetrical surfaces are to be machined. A sample of a beam integrator freeform shape is shown in Figure 8-13. It is formed by a 2-D array of small concave lenslets. Because it is not rotational symmetrical, the cutting depth is both related to the X-axis position and the spindle angular position.

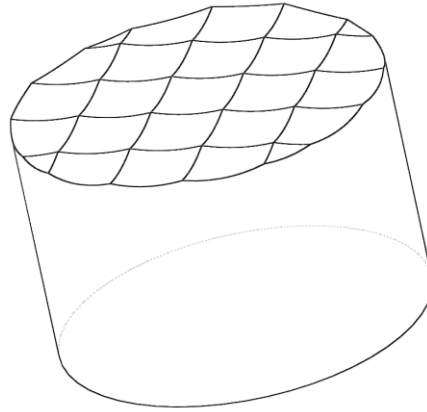


Figure 8-13: Freeform beam integrator surface

There are two ways to represent the surface profile information in the controller. When the surface is of arbitrary shape, point clouds with the coordinate of each point have to be used to define the shape. If the surface is of regular shape and can be described by mathematical equations, then several parameters are enough to define the surface. This makes a difference when transmitting the information from host PC to the controller. A small number of data can be easily stored in the memory of the controller board while large amount of data has to be transmitted during cutting.

The beam integrator surface is well defined by the dimensions of each lenslet and the spaces of the lens arrays. The equation parameters are programmed in the controller and the depth of cut is calculated directly according to the position feedback of X-axis and the spindle. The DSP controller calculates the next position during each servo update cycle. Since the position coordinate is updated at the same rate of the execution speed, no interpolation is required and thus the tool path has minimum cord errors.

The calculation programmes are shown below in MATLAB scripts. The same processes are programmed in C language in the controller.

```
X = r * cos(theta);
y = r * sin(theta);
x_local = x - floor(x/L)*L - L/2;
y_local = y - floor(y/L)*L - L/2;
z = (R - sqrt(R^2 - (x_local^2+y_local^2)));
```

Where: *theta* is the spindle angle, *r* is the X-axis position, *R* is the spherical radius of each lenslet and *L* is the pitch of the array structure. The calculated surface form is shown in Figure 8-14.

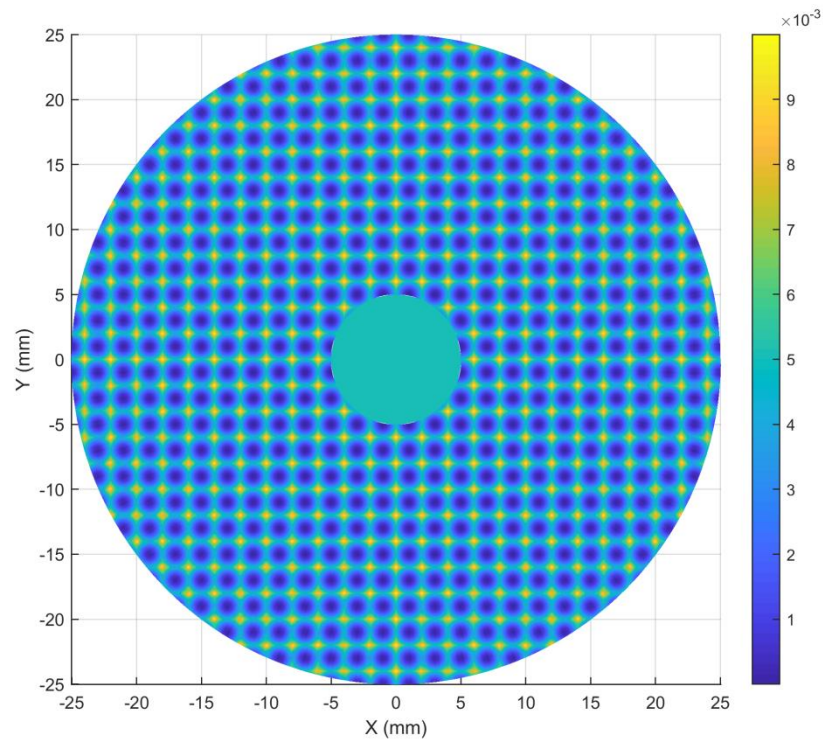


Figure 8-14: Designed beam integrator surface (Height in millimetres)

Table 8-4: Experimental conditions for beam integrator surface

Name	Value
Material	OFC Copper
Sphere radius ( $R$ )	100 mm
Edge length ( $L$ )	2 mm
Depth	10 $\mu\text{m}$
Feed rate	5 $\mu\text{m}/\text{rev}$
Spindle pulse number	80000
Spindle speed	120 rpm
Processing time	45 mins

The machining parameters are listed in Table 8-4. The workpiece material is Oxygen-Free Copper (OFC) and the diameter of the workpiece is 50 mm. A segment of the real-time trajectory and the position commands are plotted in Figure 8-15. It can

be seen that the following error at the transition of two lenslets is large. There exist around  $0.4 \mu\text{m}$  overshoot at every transition corner. The overshoot is caused by the absence of the feedforward control. After the transition corner, the tool follows the position reference well. The tool trajectory is very smooth with no visible noise peaks.

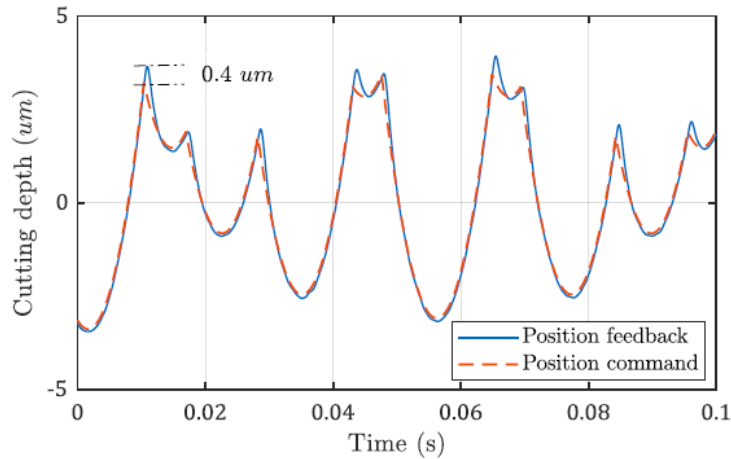


Figure 8-15: Tool trajectory during cutting of beam integrator surface

The photo of the machined part is shown in Figure 8-16. A rectangular area as marked in the picture is measured using white light interferometer with 5X objective (NA: 0.13), stitched with 36 images. The surface form shape is shown in Figure 8-17. It can be seen that the shapes of the lenslets are consistent. The average depth of the lenslets in the field of view is measured to be  $5.218 \mu\text{m}$  (compared to nominal depth of  $5 \mu\text{m}$ ). The pitch is  $2.003 \text{ mm}$  (compared to nominal pitch of  $2 \text{ mm}$ ). The surface roughness is measured to be  $3 \text{ nm}$  at five randomly chosen locations.

One of the lenslets as shown in Figure 8-17 is picked to study the form error. A sphere with  $100 \text{ mm}$  radius is fitted and subtracted from the data by ZYGO software. The resulted surface error is shown in Figure 8-18. It can be seen that at the beginning of the cut, the surface shows larger heights (around  $0.5 \mu\text{m}$ ). This result agrees with the tool following error in Figure 8-15.

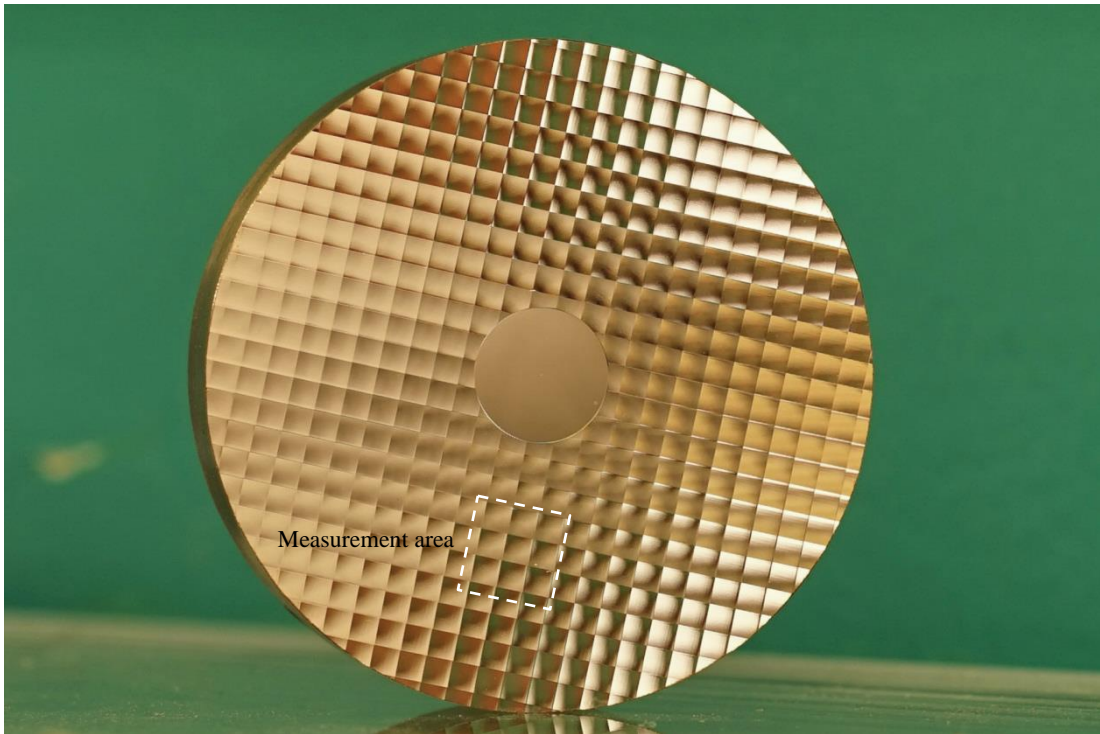


Figure 8-16: Machined beam integrator surface

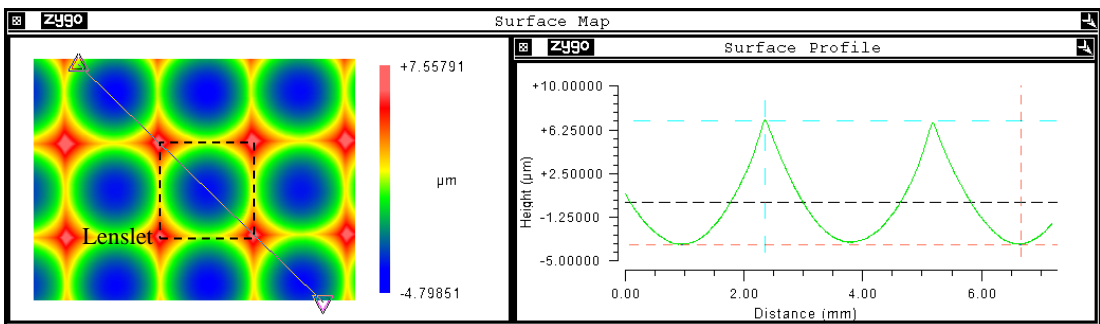


Figure 8-17: Measured beam integrator shapes and the cross section profile

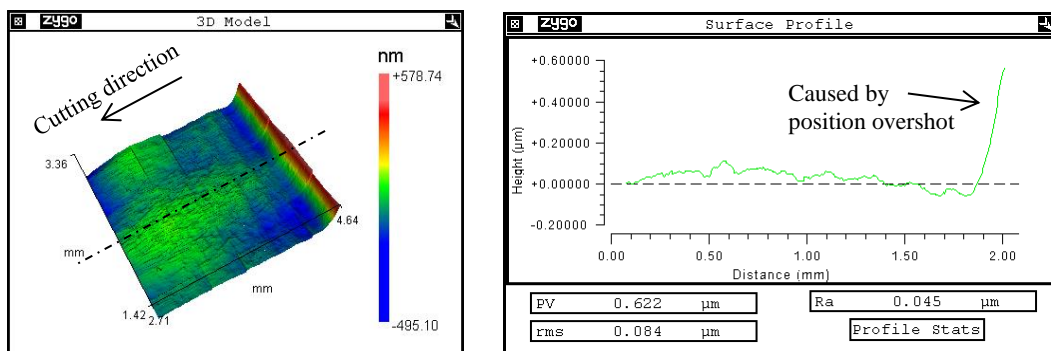


Figure 8-18: Form error of the spherical lens element and the cross section profile



### 8.5.4 Sinusoidal grid cutting

In a similar way as the beam integrator machining, a sinusoidal grid surface is designed and machined as well. The pitch of the grid is smaller which means the tool has to move at faster speed. The mathematical expressions used to calculate the depth of cut is as below:

$$\begin{aligned}x &= r * \cos(\theta); \\y &= r * \sin(\theta); \\z &= A_x * \sin(2 * \pi * x / \lambda_x) + A_y * \sin(2 * \pi * y / \lambda_y); \end{aligned}$$

Where:  $\theta$  is the spindle angle,  $r$  is the X-axis position,  $A_x$ ,  $A_y$  are the amplitudes of the sinusoidal wave along X and Y directions,  $\lambda_x$  and  $\lambda_y$  are the wavelengths of the sinusoidal structure along two directions. The calculated surface form is shown in Figure 8-19.

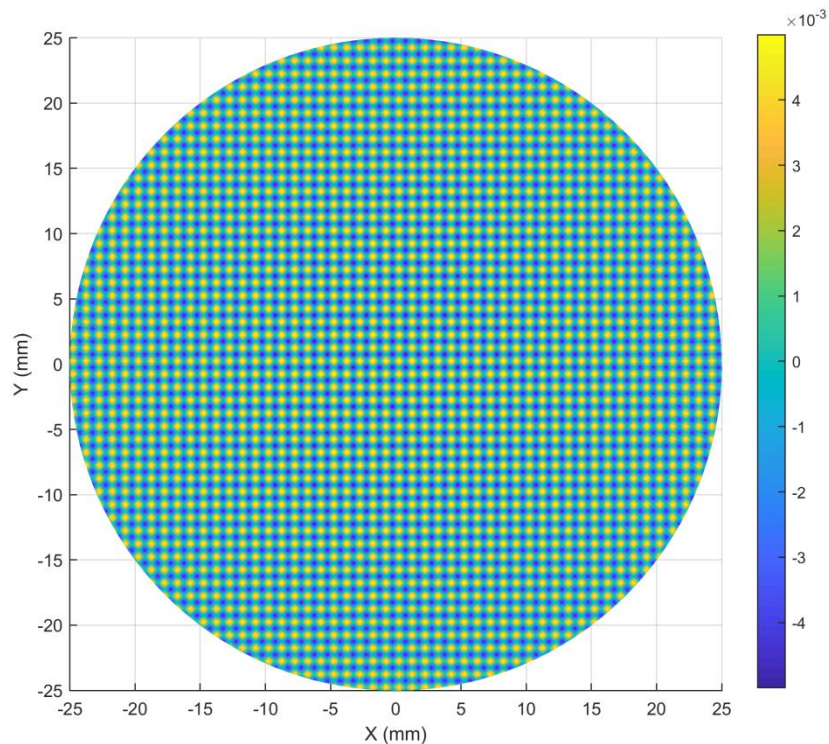


Figure 8-19: Designed sinusoidal grid surface (Height in millimetres)

The machining parameters are listed in Table 8-5. The maximum depth of cut is controlled to 10  $\mu\text{m}$ . The spindle speed is reduced to 60 rpm. Under this condition, the tool motion frequency is about 200 Hz at the edge of the part. When the cutter goes near to the centre of the rotation, the motion frequency is greatly reduced. This

inconsistency may affect the surface quality. It indicates that the freeform turning method has some disadvantages when the size of the part is large. The ruling configuration as mentioned in Section 3.4 does not have this problem.

Table 8-5: Experimental conditions for sinusoidal grid turning

Name	Value
Material	OFC copper
Wavelength (X, Y)	1 mm
Amplitude (X, Y)	$\pm 5 \mu\text{m}$
Feed rate	5 $\mu\text{m}/\text{rev}$
Spindle pulse number	80000
Spindle speed	60 rpm
Processing time	90 mins

The real-time tool trajectory and the position commands for the far side and central side cutting are plotted in Figure 8-20 and Figure 8-21 respectively. It can be seen that the following error is large at 200 Hz motions due to the uncompensated feedforward path. However, this error is reduced to within 25 nm when the motion frequency is around 20 Hz.

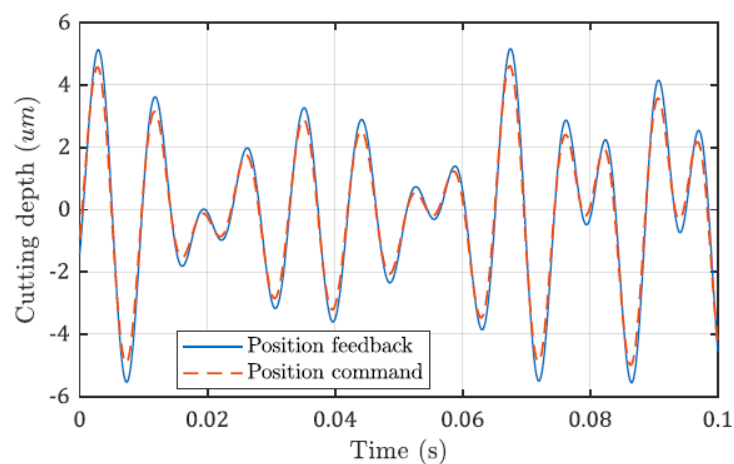


Figure 8-20: Tool trajectory during cutting of sinusoidal grid surface at 200 Hz



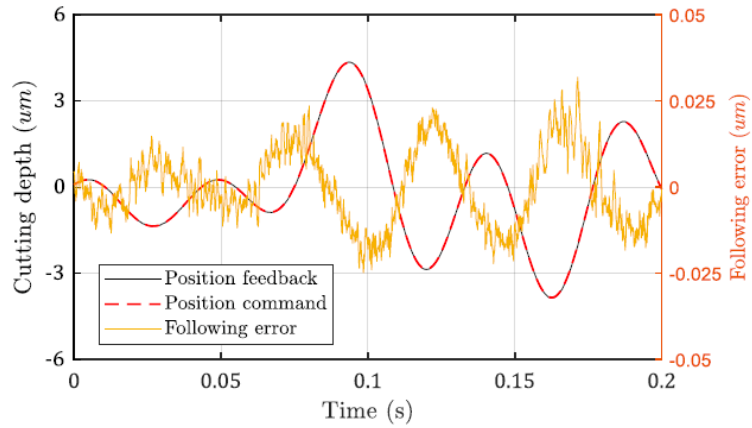


Figure 8-21: Tool trajectory during cutting of sinusoidal grid surface at 20 Hz

The photo of the machined part is shown in Figure 8-22. The surface measurement is conducted at two locations: near the centre and at the edge, with 5X objective. The measured form shapes are shown in Figure 8-23 for the edge measurement and the centre measurement is shown in Figure 8-24. The nominal peak-to-valley amplitude is  $10\ \mu\text{m}$ . However, this value is measured to be  $11.18\ \mu\text{m}$  at the edge due to the lack of feedforward control. This error can be easily compensated [165]. As a comparison, the peak-to-valley amplitude is very accurate at the centre ( $10.02\ \mu\text{m}$ ), showing that the tool error can reflect surface form error.

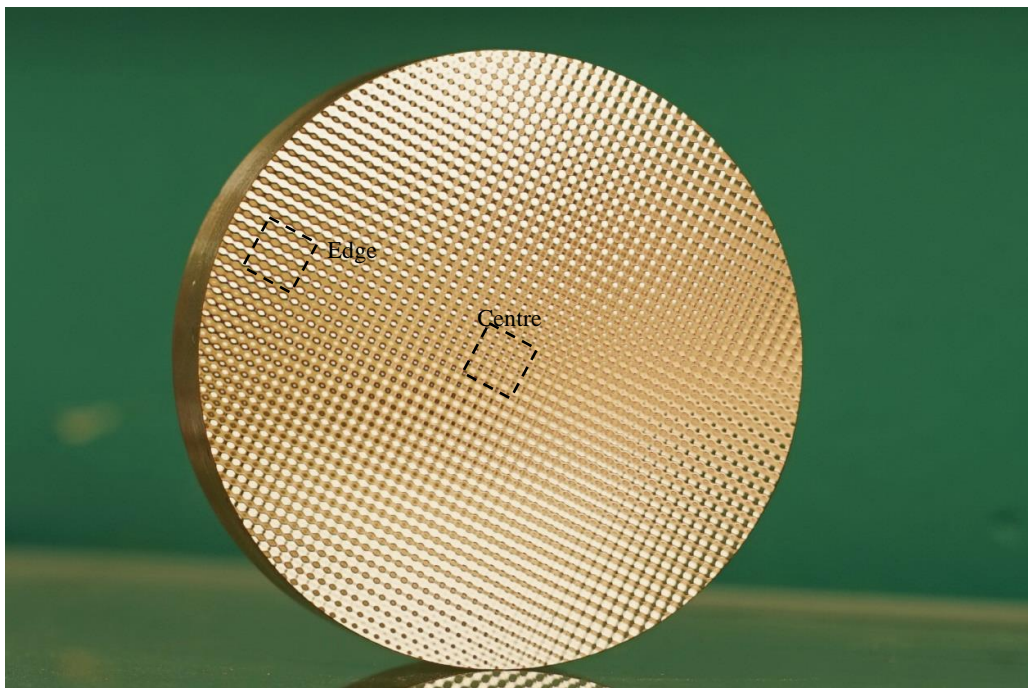


Figure 8-22: Machined sinusoidal grid surface

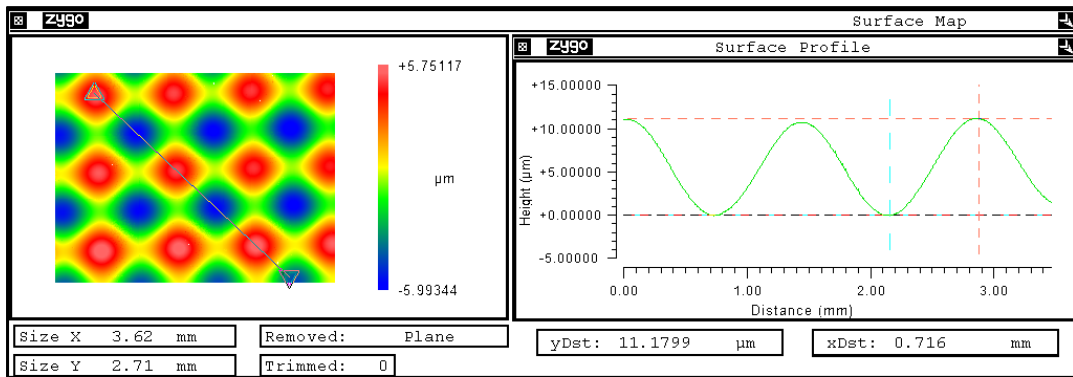


Figure 8-23: Measured sinusoidal grid shapes and the cross section profile (edge)

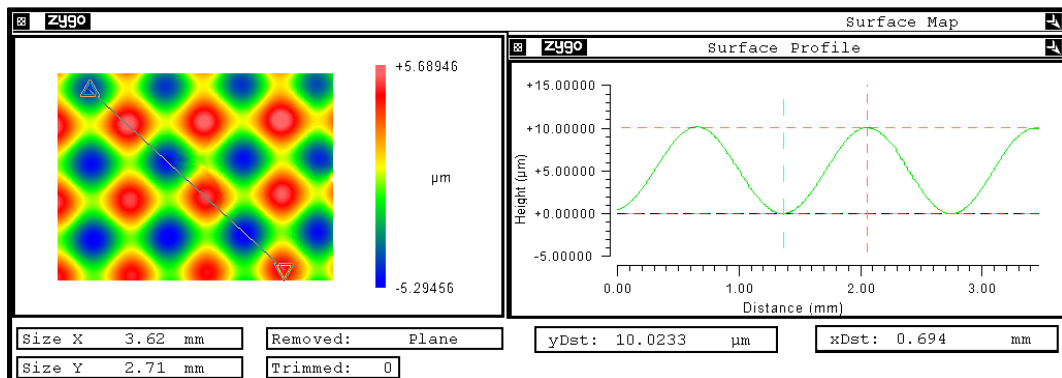


Figure 8-24: Measured sinusoidal grid shapes and the cross section profile (centre)

### 8.5.5 Arbitrary freeform machining

Unlike the regular shapes as discussed above, arbitrary freeform surfaces can only be fully defined by point coordinates. Therefore, arbitrary freeform machining requires significant large numbers of data points to be transmitted to the controller without interrupting the servo loop. The servo rate is as high as 199.6 kHz, which means the controller consumes 199600 data points per second. In industrial applications, the data rate is compressed via the interpolation process. The host PC only sends a fraction of the data points and then the controller interpolate the other points based on some rules [166]–[168]. The data amount is still large even with this approach, so high-speed data transmission interfaces are necessary.

The required high-speed communication interface is currently not available in this setup. Therefore, an alternative method is proposed in this thesis. In this method, a map of the form heights in Cartesian coordinate is used to calculate the tool positions. The map is digitalised into small pixels and the height within one pixel is assumed the

same. A typical map in this form is an image. Therefore, the programming process is simply downloading the image data into the controller. The image pixel number and the part size determine the lateral resolution of the form shape.

As shown in the Figure 8-25, the controller reads the spindle angular position  $\theta$  and the X-axis position  $r$  in real time. Then the polar coordinate is converted into the Cartesian  $x, y$  in workpiece coordinate. This process is the same as the analytical method mentioned above. Then the current coordinate is rounded into the nearest pixel location and the height value is extracted from the map.

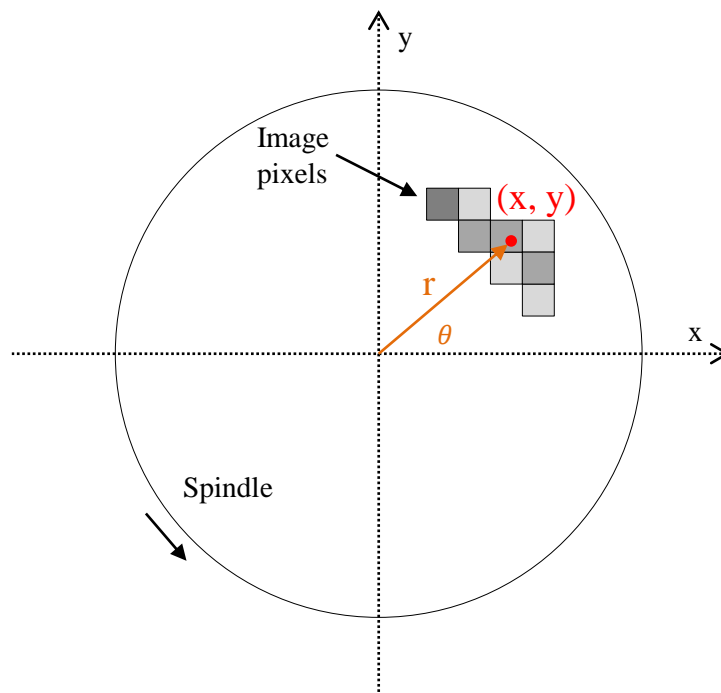


Figure 8-25: Calculation of tool position in arbitrary freeform machining

In this case, a picture of Chinese poem calligraphy is used as the sample image to be machined into the part. The image is firstly converted into greyscale format. Since the darkness of each pixel is represented by an unsigned integer number, which ranges from 0 to 256, the height of the freeform at corresponding point is calculated through the darkness of each pixel. The heights are then scaled into 0 to 5  $\mu\text{m}$ , as shown in Figure 8-26.

A two-dimensional data array in the memory is allocated to store the image data in the controller. The size of the data array is proportional to the pixel numbers of the image. The data is firstly written into the non-volatile flash of the controller through

serial port transmission. Upon powering on, the data file is then copied into the DDR memory from the flash. This procedure ensures that the file data will not be lost after power off and the slow data transmission process is needed only once. Because the data transmission speed is relatively slow, the image pixel number is limited to  $1000 \times 1000$ .

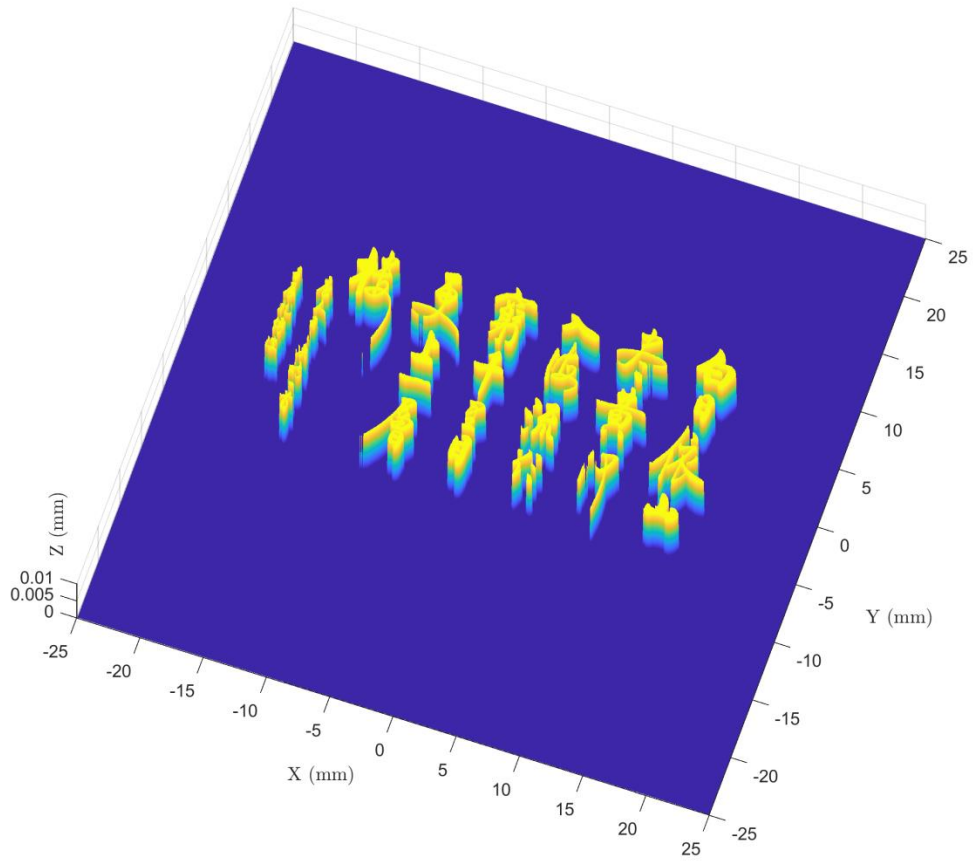


Figure 8-26: Freeform shape derived from sample image

Table 8-6: Experimental conditions for arbitrary freeform turning

Name	Value
Material	OFC copper
Max depth	5 $\mu\text{m}$
Feed rate	5 $\mu\text{m}/\text{rev}$
Spindle pulse number	80000
Spindle speed	30 rpm
Processing time	180 mins

The machining parameters are listed in Table 8-6. The maximum depth of cut is controlled to be 5  $\mu\text{m}$ . The spindle speed is reduced to 30 rpm. The machined surface is shown in Figure 8-27. It can be seen that the designed arbitrary graph is effectively copied to the surface of the workpiece. The trajectory is composed of many step changes of heights, which is very challenging for the cutting system. Overshoots has been observed and this effects can be reduced by applying low-pass filters in the servo routine in the future. The same structure can also be machined by diamond milling technique. However, the machining efficiency will be very low. The milling cutter should be very small in order to cut the small features, but it will be very challenging to obtain less than 10 nm surface roughness with such a tool on 50 mm diameter workpiece[59].

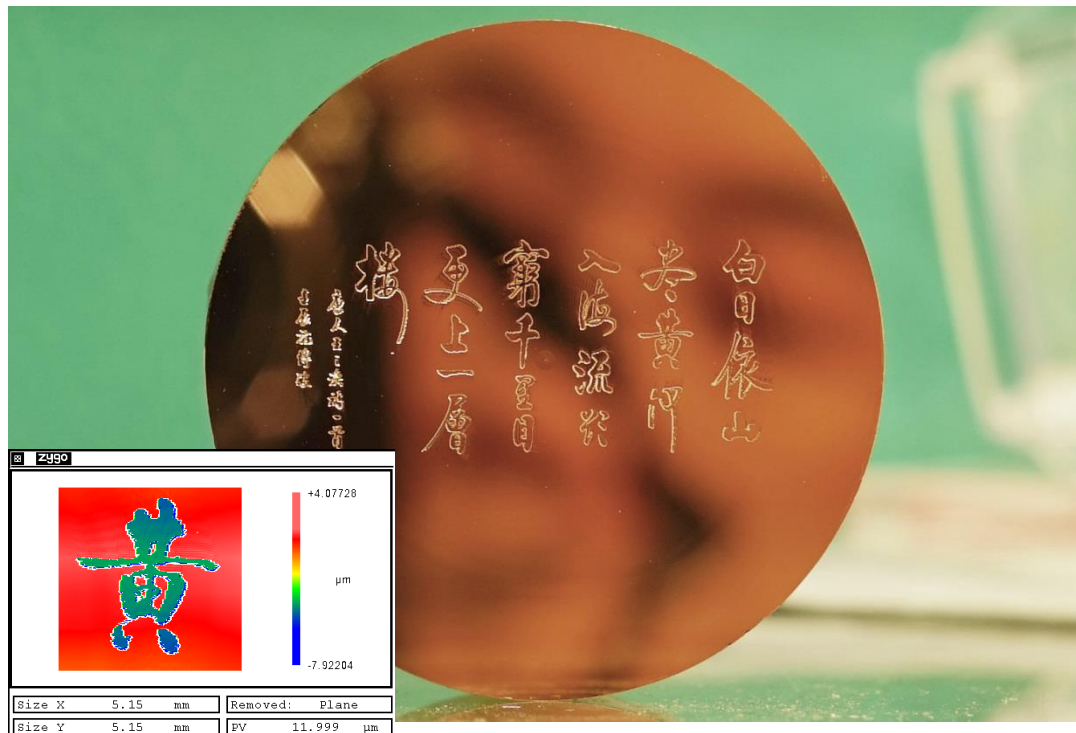


Figure 8-27: Machined freeform surface from an image

## 8.6 Summary

In this chapter, the developed fast positioning system is applied in the machining of several freeform surfaces.

Before the machining, the spindle error motions are measured with dedicated setups. A complimentary multi-probe error separation method is proposed to measure the errors without repositioning of the artefact. Both the radial and tilt error motions are obtained in this way. The axial errors are also measured. The measured error data shows good repeatability.

Then the spindle angular positions are transferred to the controller via digital interface. There exists a trade-off between the angular resolution and the spindle speed due to the limited data transfer rate. The maximum data transfer rate is around 800 kHz. The deterministic trigger mechanism ensured that the depth of cut is synchronised to the workpiece rotation, thus no distortion of the machined form.

Flat surface cutting on NiP alloy shows 1.2 nm surface roughness (Ra) and the high positioning stability performance is thus verified. The beam integrator and sinusoidal surfaces are then machined. Although the tracking performance at sharp corners is not

satisfying due to the lack of feedforward control, the experiments demonstrated the good positioning stability during dynamic motion. Following errors of less than 25 nm are achieved when the tool is moving at 20 Hz. A new scheme of storing the coordinates for arbitrary freeform surfaces is proposed without the complex path planning procedures. An arbitrary freeform surface is machined for demonstration.

# CHAPTER 9

## Conclusions and future work

### 9.1 Conclusions

A thorough design, analysis and control procedure of fast tool positioning system for ultra-precision freeform machining has been demonstrated in this thesis. The emphasis has been put on improving the positioning stability under all kinds of disturbances by feedback control loops. The mechanical structure and electronics have been specially designed for this purpose. Detailed modelling and discussion of the imperfections in the control loop laid solid foundations for the further analysis and optimisation of the system. Lastly, the developed fast positioning system is applied in the machining trials of several freeform surfaces. The developed system can achieve  $>1.5$  kHz closed-loop bandwidth with surface roughness less than 3 nm (1.2 nm for flat surface). This demonstrated the high-speed capability and good positioning stability of the system. The adoption of metrology frame concept in FTS devices has greatly reduced the requirement for high-precision slides and reduced the number of structural compliances. The knowledge obtained in this research is helpful in understanding of positioning system design in ultra-precision machining tools.

The conclusions for this research can be drawn as below:

- 1) A dynamically stiff structural loop is essential for a high dynamic precision machining system. Any bearing interface or angular compliance will make it difficult for feedback control and direct measurement of the tool position. In this thesis, a novel stiff-support concept is proposed which eliminates the structural and bearing compliances in the stiffness loop. The new design has also adopted the metrology frame structure with the shortest structural loop and it obeys the Abbey principle as well. Those design considerations make it possible to achieve 1.2 nm surface roughness with this machining system, even with low cost components.

- 2) The error analysis approach reveals that the following errors read from the CNC software underestimate the real positioning error at low frequency range while



overestimate it at high frequency range. The error analysis approach successfully revealed the real tool positioning errors that are mixed with sensor noise and it has been verified through a series of positioning tests. The detailed modelling of the whole system and the disturbance PSDs is the most vital procedure in this process. It is found that the high frequency response is mostly dominated by the electrical crosstalk, while the low frequency response is predictable with the mechanical model.

3) Mechanical parameters such as mass, damping and stiffness put a limit on the achievable performance within the closed-loop framework. A deterministic controller design approach precluded the uncertainty associated with controller tuning. The optimal bandwidth, at which errors reach minimum value, turns lower with a larger moving mass. There exist optimal bearing stiffness and damping coefficients under a given disturbance condition. A larger moving mass helps combating disturbances except the sensor noise and therefore helps improving positioning stability. The improvement is not obvious when the major error source is the sensor noise at high bandwidths.

4) The cutting force affects both the form error and surface quality in dynamic cutting. This can be predicted by analysing the positional response function to the cutting forces. The dynamic stiffness of the positioning system is proportional to the magnitude of the controller gains. A higher moving inertia with high damping and stiffness will permit larger controller gains and therefore better stiffness can be achieved.

5) Acceleration feedback method increases the loop phase margin and the PID gains can be increased further. By doing this, the dynamic stiffness within the acceleration sensor bandwidth is proportionally improved. However, the stiffness is worse at frequencies just beyond the acceleration sensor bandwidth. The acceleration feedback technique does not suppress the force disturbance at all frequencies but expands the frequency range where the stiffness curve can be tuned. The additional acceleration sensor brings new error source to the closed-loop and its contribution increases with a larger acceleration gain. There is a point where the increased acceleration error contribution surpasses others and starts to dominate, which is the upper limit for the practical acceleration gains.

## **9.2 Knowledge contributions**

The following contributions to the current knowledge base on ultra-precision machining system development have been made:

1) A novel stiff-support structural design concept for high-precision freeform machining has been proposed which achieved minimum compliances in the structural loop. This concept greatly lowers the requirements for ultra-precision components and costs.

2) A systematic error analysis approach has been developed which can predict the RMS positioning errors and revealed the real positioning errors (0.23 nm RMS) from noisy sensor measurements (0.83 nm RMS) for the first time.

3) Optimisation of control algorithm has been achieved which precludes the uncertainty associated with traditional PID controller tuning and make it possible to predict system performance with mechanical structural parameters at the design stage.

4) The knowledge on how structural parameters such as mass, damping and stiffness affect the achievable positioning stability and dynamic stiffness has been established. The existence of optimal structural damping and stiffness has been identified.

5) Enhancement of knowledge on adopting acceleration feedback technique for dynamic stiffness enhancement in ultra-precision machining has been achieved, considering the influences of sensor imperfections on positioning stability and dynamic stiffness.

## **9.3 Limitations and future work**

This research has studied the factors that affect the positioning stability of ultra-precision systems and the corresponding measures to reduce their influences. Since the positioning system is a rather complicated system, which involves multiple disciplines, there are some limitations and aspects to be improved for this work.

### 9.3.1 Aspects for future improvements

1) This thesis has only discussed the feedback control of fast tool positioning system. However, the feedforward control is very important in the tracking performance of fast positioning system. This work has not been done in this thesis due to time limit. The basic idea of feedforward control is to invert the closed-loop transfer function and then modify the position commands in the frequency domain. There has been quite a lot of research on feedforward control of closed-loop systems, especially for non-minimum-phase system where direct inversion is not possible. The established methods include Non-minimum-Phase Zero Ignore (NPZ-Ignore), the Zero-Phase-Error Tracking Controller (ZPETC) and the Zero-Magnitude-Error Tracking Controller (ZMETC) [169]–[171]. Industrial applications see input shaping technology. Nevertheless, the feedforward compensation should be designed after all the feedback controls have been finalised and tested, which is covered in this thesis.

2) In the freeform turning experiments, the diamond tool radius is not compensated in the calculation of tool trajectories. This is because the radius compensation algorithm is too complex for real-time calculation, at least impact the servo rate. This issue can be solved by switching to point cloud method. However, this method requires a high-speed data transfer interface and buffering mechanism, which is to be improved in the future.

3) There are some room for improvement in the mechanical design of the coil support structure. In addition, a dust cover is necessary to protect the metrology frame from cutting chips.

4) The system is treated as a linear system (except the delays) and all the modelling process is based on this assumption. In the frequency response tests, a little bit nonlinearity has been observed, which is caused by the plastic deformation of the leading wires. There are also some unexpected contacts between the coil and the magnets as well. In case that those factors cannot be eliminated by hardware modification, nonlinear control can be adopted in the future to address this problem.

### 9.3.2 More ideas

1) The primary feedback sensor in this work is a capacitive sensor from Lion Precision, USA. Although it is already an excellent displacement sensor, its measure range is limited to only 50  $\mu\text{m}$ . Recently, interferometric displacement sensors are available on the market with pico-meter noise floor and very small footprints. Their measuring range can easily reaches to hundreds of millimetres, which is preferred for wider applications.

2) The metrology frame is the datum of the position system. Therefore, its dimensional stability is very important, even more important than its straightness because the straightness can be measured and compensated via the reversal method. A thermally controlled metrology frame might be a solution for applications where utmost precision is required in uncontrolled environments.

3) The third idea is to measure the spindle error motions in real time, rather than going through the compensation routine. Then the repeatability of the spindle motion is not important any more. This requires a two DoF encoder and a new sensing technology.

4) Other advanced control theories like model predict control (MPC) or adaptive control has been applied in conventional milling machines to suppress chattering [172], [173]. Although chattering is not a common problem in diamond turning machine, the increased resistance to vibrations may help reduce the tool errors during cutting. Adaptive feedforward control can also be used to improve the tracking accuracy at changing motion frequencies [39].



# Appendix A

## Screen-shots of control software

The control user interface and the background communicating tasks are realised on MATLAB software platform. Four major modules are the main control panel with data acquirement, spectrum analysis module, frequency response test module and the controller tuning module, as shown in Figure A-1 to Figure A-4.

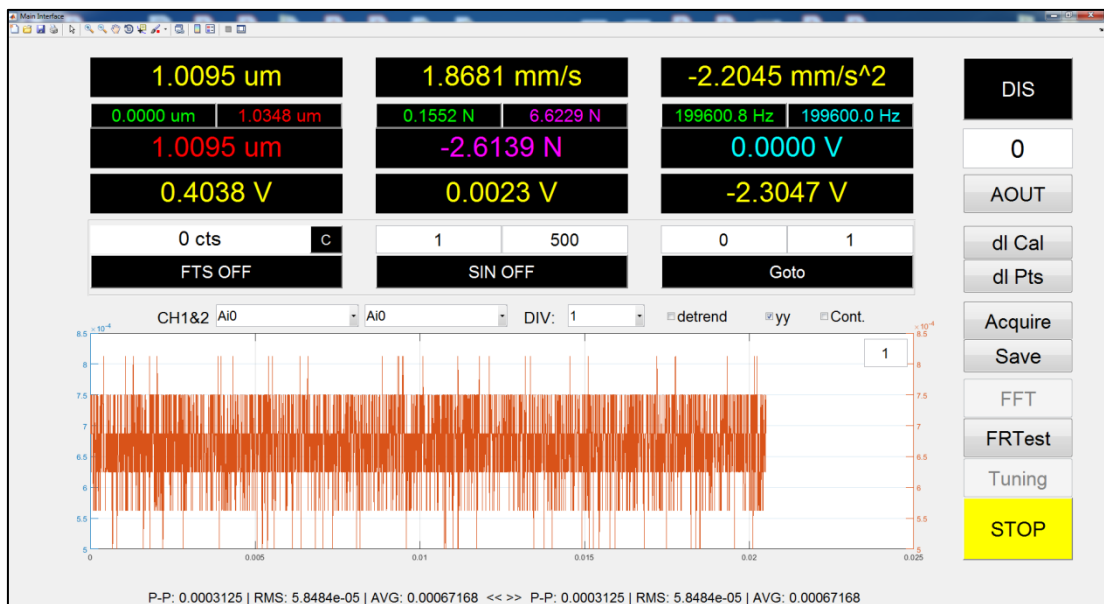


Figure A-1 Main control user graphical interface

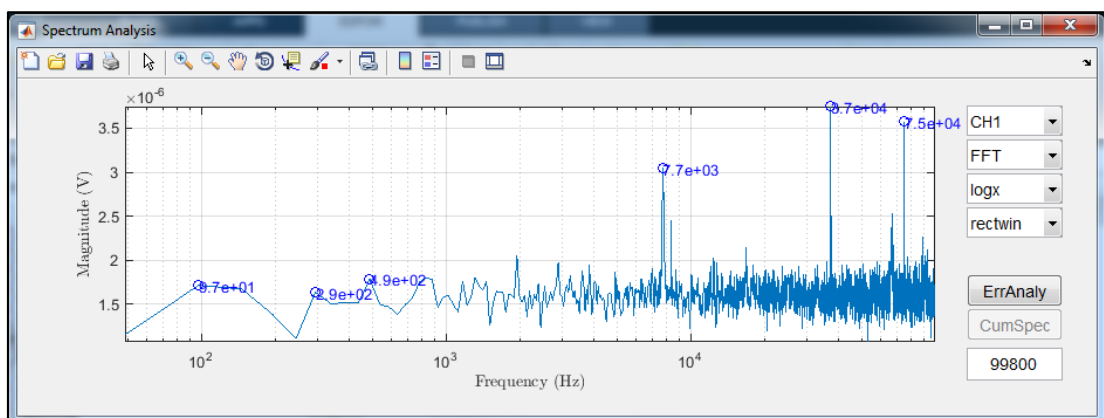


Figure A-2: Spectrum analysis user graphical interface

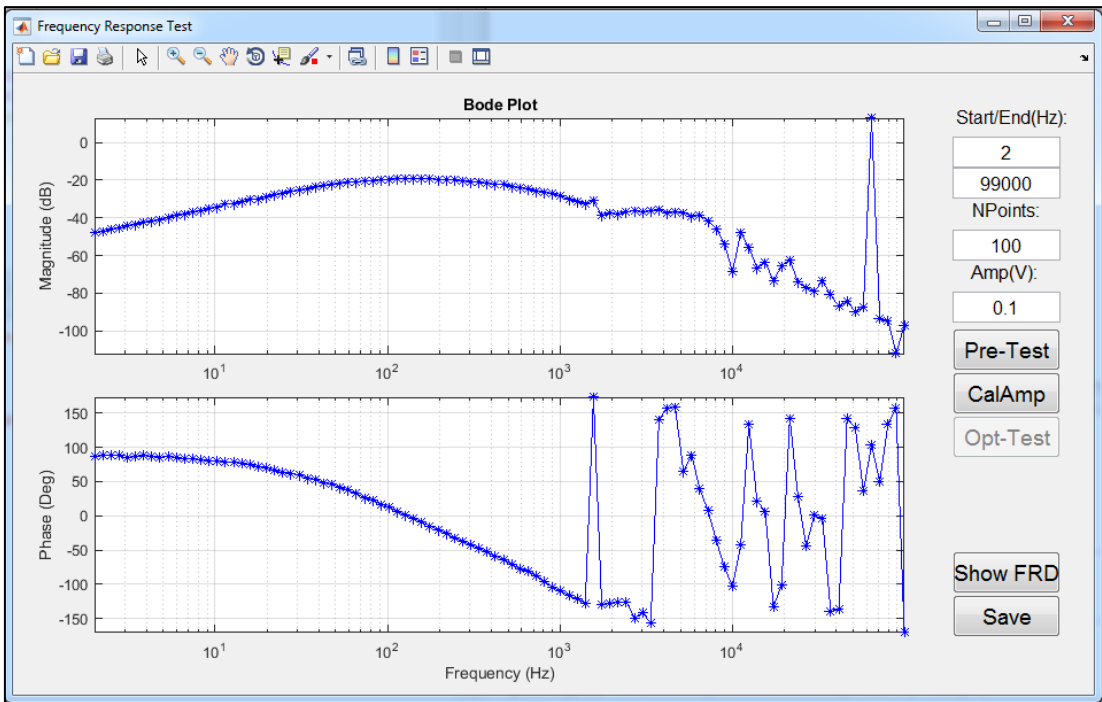


Figure A-3: Frequency response test user graphical interface

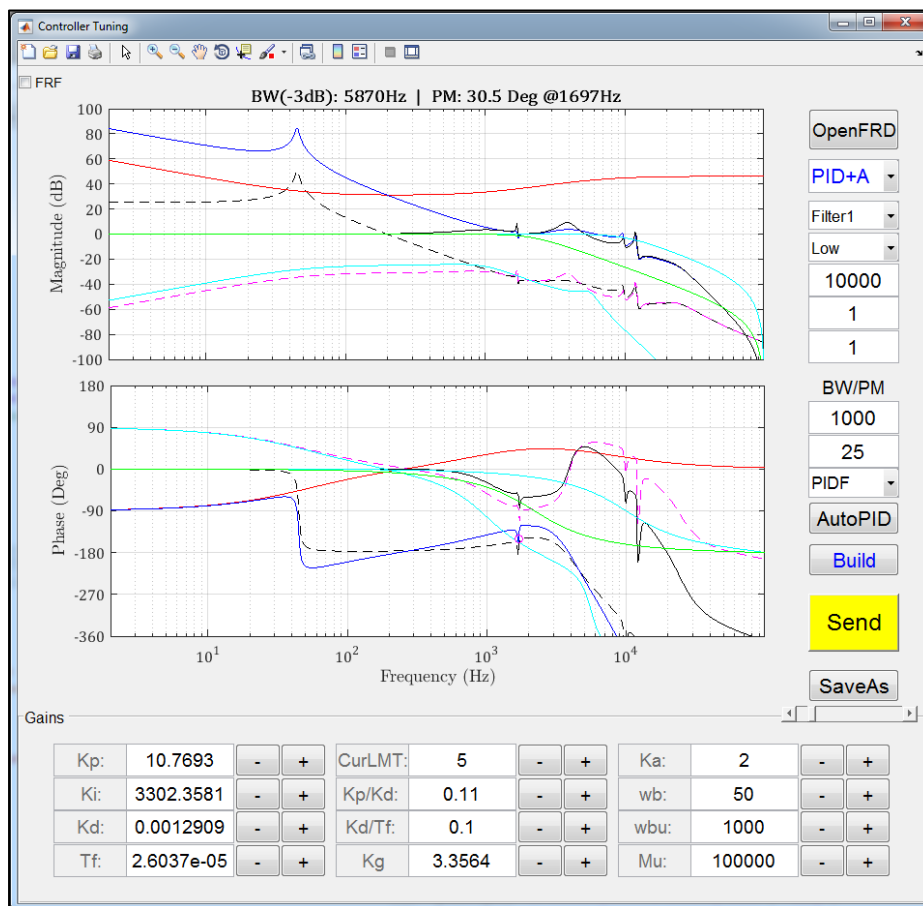


Figure A-4: Controller tuning user graphical interface

# Appendix B

## AD/DA interface circuits

### B. 1 A/D interface circuits

The DSP chip contains several communicate interface peripherals. The External Memory Interface (EMIF) is a 16-bit data bus designed for easy interfacing with asynchronous memory devices, such as NAND flash. In this thesis, it is used to read data from the parallel ADC. The ADC register is treated as an external memory location.

The interfacing circuits are shown in Figure B-1, two high-speed amplifiers THS4031 are used to buffer the input signal. The ADS8422 only accepts positive inputs within around two volts. A precision 4.096 V voltage reference chip is used to provide an offset voltage. In this way, the input voltage can be negative. Another voltage reference of 4.096 V is used to provide a precision reference for the ADC chip. This circuit is adopted from the recommended design from TI manual. The communication between the ADC and the DSP is bridged by an address decoder. The read operation from the DSP will generate high and low levels on the EMIF address bus and these levels are then converted into one single read pulse to the DAC. The data are then transferred to the DSP via the 16-bit data bus.

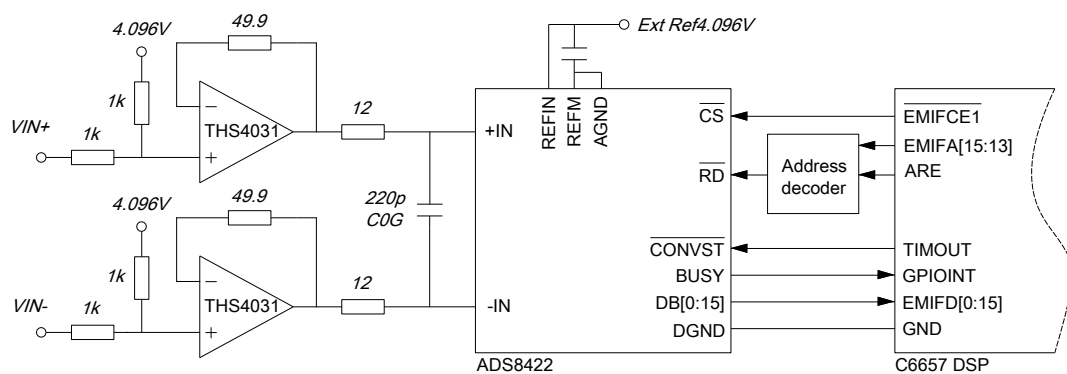


Figure B-1: ADC interface circuits



## B. 2 D/A interface circuits

Multi-channel Buffered Serial Port (McBSP) is an enhanced version of traditional serial port for transporting of large amount of data. In this case, it is used to communicate with a serial port DAC. The DAC is configured into “gain of two” mode to output bipolar voltage span with a single-ended reference. The voltage reference is of 10 V, buffered by two amplifiers. The voltage output of the DAC is also buffered via an amplifier to achieve current driving capability.

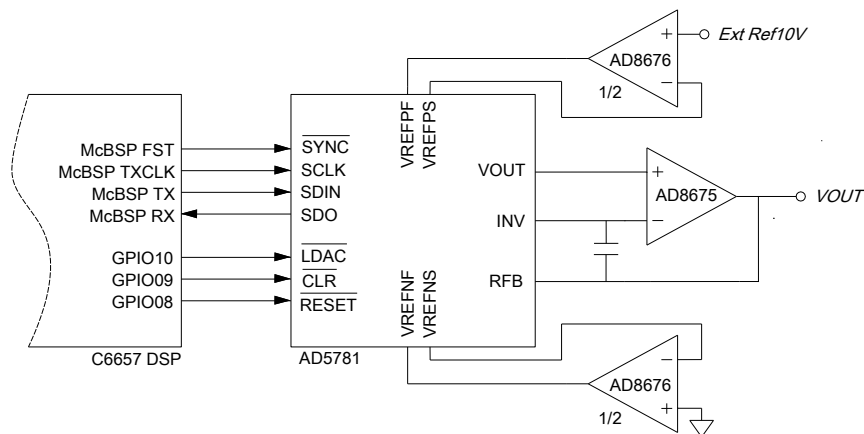


Figure B-2: DAC interface circuits

The PCB layout of the controller board with the above AD/DA interfacing circuits is shown in Figure B-3.

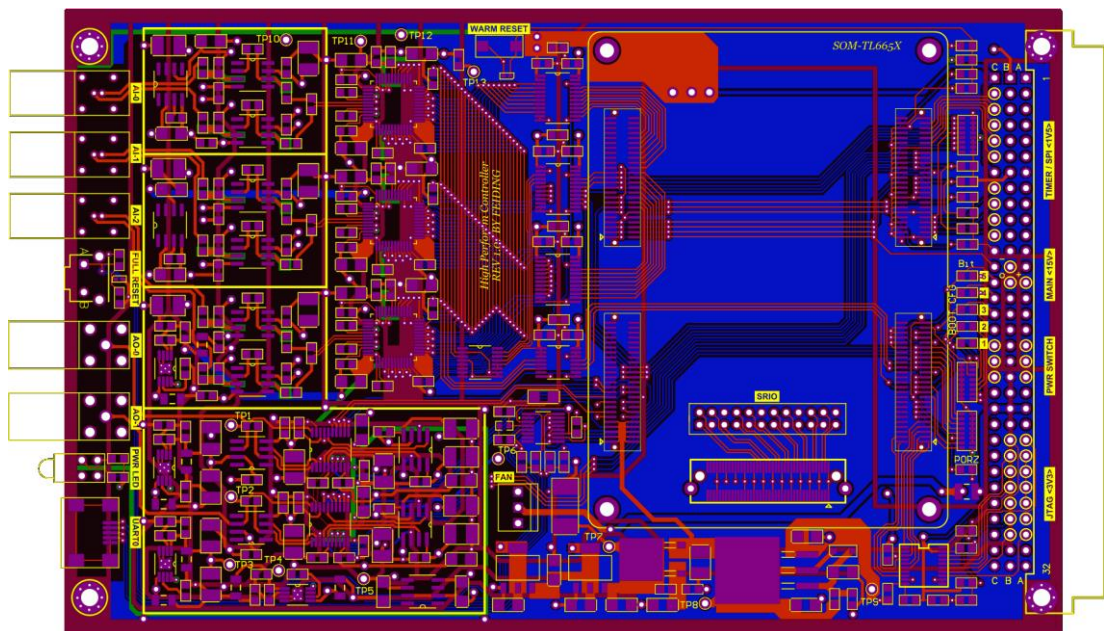


Figure B-3: PCB layout of the developed controller board

# Appendix C

## Lumped-parameter model

The transfer functions from disturbance sources ( $\Delta F, \Delta Fa, \Delta x$ ) to the tool tip position  $x_1$  are derived in this section. The Figure 5-4 is redrawn here for clarification.

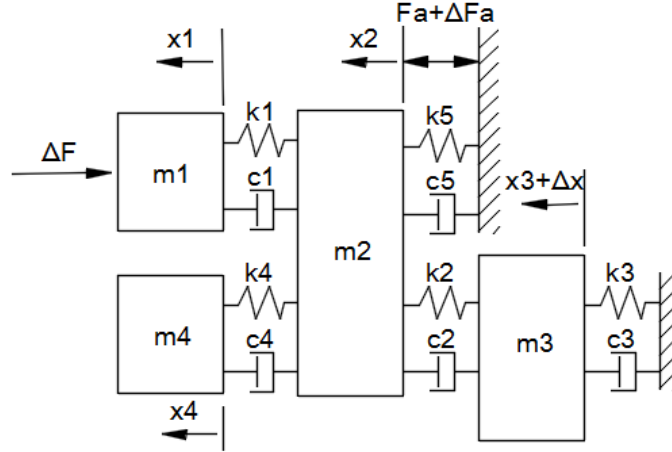


Figure C-1: Lumped-parameter model of the mechanical system

According to the Newton's Law, each body must satisfy the following relationship in the time domain:

$$m_1 \ddot{x}_1 - \Delta F - k_1(x_1 - x_2) - c_1(\dot{x}_1 - \dot{x}_2) = 0 \quad (\text{C-1})$$

$$m_4 \ddot{x}_4 - k_4(x_4 - x_2) - c_4(\dot{x}_4 - \dot{x}_2) = 0 \quad (\text{C-2})$$

$$m_2 \ddot{x}_2 + k_1(x_1 - x_2) + c_1(\dot{x}_1 - \dot{x}_2) + k_4(x_4 - x_2) + c_4(\dot{x}_4 - \dot{x}_2) - k_5 x_2 - c_5 \dot{x}_2 - k_2(x_2 - x_3 - \Delta x) - c_2(\dot{x}_2 - \dot{x}_3 - \dot{\Delta x}) + Fa + \Delta Fa = 0 \quad (\text{C-3})$$

$$m_3 \ddot{x}_3 + k_2(x_2 - x_3 - \Delta x) + c_2(\dot{x}_2 - \dot{x}_3 - \dot{\Delta x}) - k_3(x_3 + \Delta x) - c_3(\dot{x}_3 + \dot{\Delta x}) = 0 \quad (\text{C-4})$$

After applying Laplace transform on each equation, the second-order derivative  $\ddot{x}_i$  is transformed into  $X_i(s)s^2$  and the first-order derivative  $\dot{x}_i$  is transformed into  $X_i(s)s$ .

When solving for  $\frac{X_1(s)}{\Delta F(s)}$ , the other disturbances ( $Fa, \Delta Fa, \Delta x$ ) are set to zero. Since the equation number is equal to the number of variables, the solution can be found. The other transfer functions are solved in the same way.

# Appendix D

## Spindle error measurement

### D. 1 Method

The complementary multi-probe error separation method is established as below:

- 1) A precision cylindrical artefact is fixed to the spindle rotor.
- 2) Three displacement sensors are pointed to the rotating artefact from three different angles.
- 3) The error motions of the spindle together with the imperfection of the artefact are detected by the displacement sensors.
- 4) The spindle errors and the artefact form errors are separated via the multi-probe error separation method.
- 5) The error separation method cannot effectively separate the errors at some singular frequencies, which is related to the probe angles. Then two different sets of probe angle arrangements are used for another two measurements.
- 6) The data from three measurements are synthesised to get the true spindle errors.

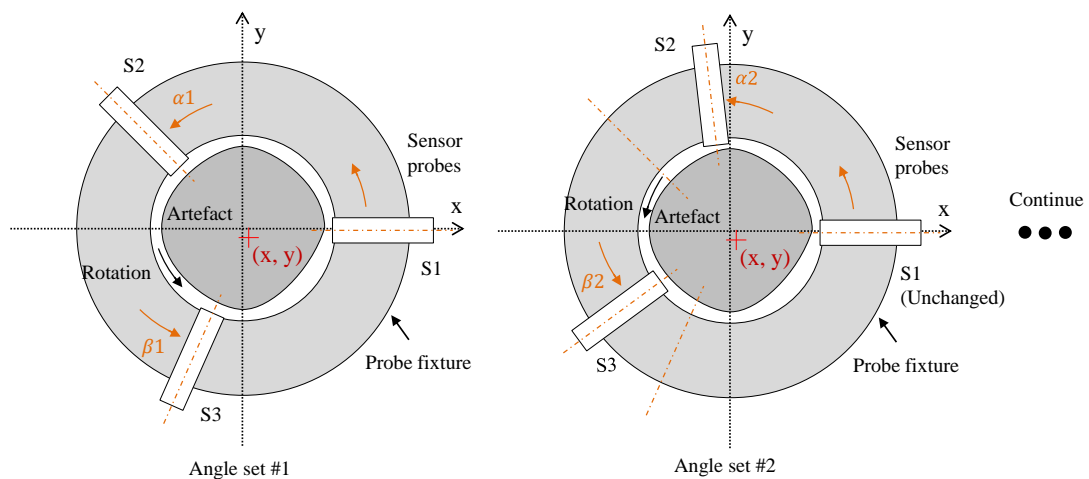


Figure D-1: Complementary multi-probe error separation method

## D. 2 Error separation algorithm

The error separation process is for removing the artefact form error from the measured signal and the spindle error motions can be revealed.

$S_1$ ,  $S_2$  and  $S_3$  are the displacement signals measured from the three sensor probes. The direction of the first probe is denoted as the X direction. The second and the third probes are arranged at  $\alpha$  and  $\beta$  angle reference to the X direction respectively. The rotor radial deviations along the X and Y directions are denoted as  $X(\theta)$  and  $Y(\theta)$ .  $\theta$  is the counter-clockwise angle starting from the X positive direction. The form error of the artefact at angle  $\theta$  is  $A(\theta)$ . Then the following relationships hold:

$$S_1(\theta) = A(\theta) + X(\theta) \quad (\text{D-1})$$

$$S_2(\theta) = A(\theta - \alpha) + X(\theta)\cos\alpha + Y(\theta)\sin \alpha \quad (\text{D-2})$$

$$S_3(\theta) = A(\theta - \beta) + X(\theta)\cos\beta + Y(\theta)\sin \beta \quad (\text{D-3})$$

Define the weighted summation of the three sensor outputs as

$$S(\theta) = S_1(\theta) + aS_2(\theta) + bS_3(\theta) \quad (\text{D-4})$$

Where

$$a = \frac{-\sin\beta}{\sin(\beta - \alpha)} \quad (\text{D-5})$$

$$b = \frac{\sin\alpha}{\sin(\beta - \alpha)} \quad (\text{D-6})$$

The harmonic weighting function  $H(k)$  is the transfer function from derived from artefact profile to the weighted summation of probe outputs. It can be described as:

$$H(k) = 1 + ae^{-jk\alpha} + be^{-jk\beta} \quad (\text{D-7})$$

Where:  $k$  is the harmonic order, in the unit of Undulations Per Revolution (UPR).

Low values of  $|H|$  will result in error amplification. However, it is difficult to find a pair of probe angles that makes  $H$  high enough for every harmonic. So, three sets of

probe angle combinations are selected to maximise the minimum value of  $|H|$ . The angle set #1 is selected according to Cappa's research [174]–[177]. A MATLAB script is written to search for the other two angle values at which the three combinations do not compress the same harmonics.

Table D-1: Designed probe angles

	Angle $\alpha$ ( $^\circ$ )	Angle $\beta$ ( $^\circ$ )
Angle set #1	100.4000	230.0333
Angle set #2	141.0333	270.7050
Angle set #3	139.3667	239.1200

The absolute values of  $H(k)$  at different harmonic orders for the three designed sets of angles are shown in Figure D-2. The minimum value is found of 0.1613 at 88 UPR.

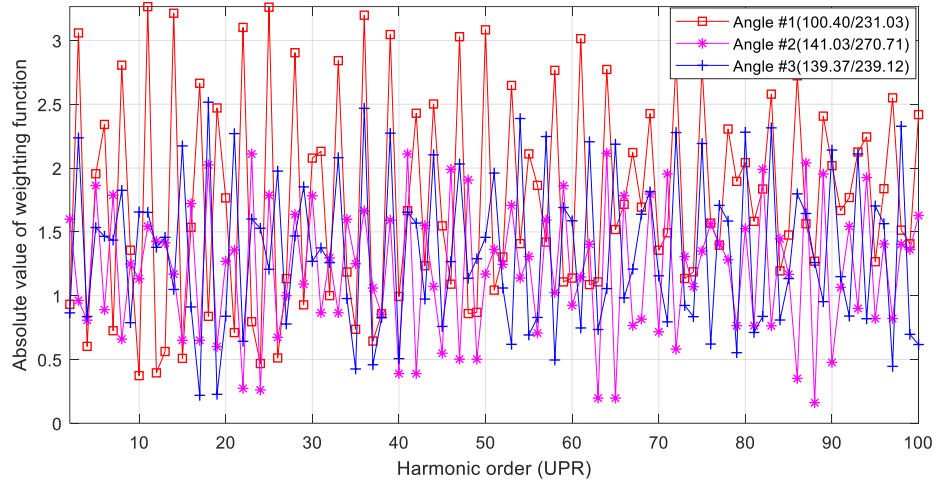


Figure D-2: Absolute values of  $H(k)$  at different harmonic orders for the designed three sets of angles

### D. 3 Measurement setup

An aluminium cylinder artefact is first turned with a diamond tool on the machine, thus a small runout is guaranteed. Three calibrated capacitive sensor (Lion Precision CPL190) are used throughout the measurement. The bandwidth of the amplifier is adjusted to 1 kHz to achieve a resolution of 0.3 nm (RMS).

The angles of the capacitive sensors are determined by a specially designed probe holder. Eight radial slots are machined onto a precision turned flat surface and then they are used to locate the probe body, as shown in Figure D-3 a). The nominal angles are taken from Table D-1.

Spindle error motion measurements are carried out at seven positions spaced by 21 mm along Z direction as shown in Figure D-3 b), each with three angular arrangements. The spindle error motions at different locations are later used to calculate spindle tilt errors. The probe mounting plate is adjusted perpendicular to the spindle rotating axis within 20  $\mu\text{m}$  and the influences of probe positional error are analysed in [178]. In order to reduce vibrations, the air bearing slides are cut off from air supply and rested on the machine bed after positioning the probe holder.

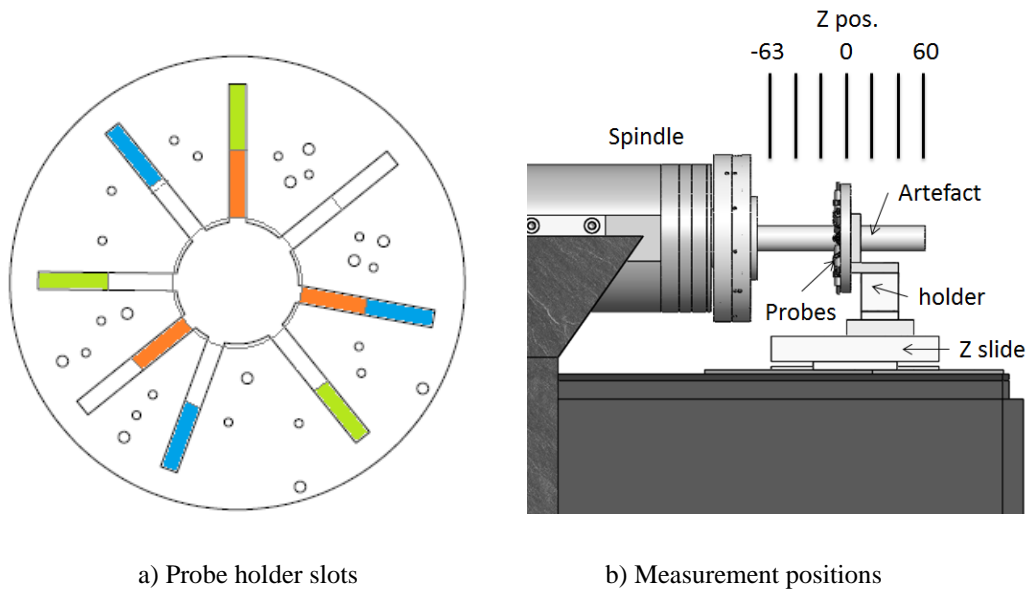


Figure D-3: Probe angle arrangement and the axial measurement positions

A 16-bit eight-channel simultaneous sampling board (MCC USB-1608HS) is used to sample the displacement signal. The data acquisition device is synchronised with the spindle angular position through the TTL pulses generated by the spindle controller as a clock signal. The spindle controller is configured to generate 10,000 pulses per revolution and the spindle rotation speed is set to 60 rpm.

Each measurement starts at the same spindle angular position from static and 200 consequent revolutions data is acquired. One sample of displacement measured by one of the three probes is shown in Figure D-4. It can be found that the sensor output is not

repeatable for each revolution at the beginning of the test, which is attributed to the unstable rotational status of the spindle axis under start-up motor torque. Thus, only the last 32 rotations are considered in the following spindle error tests.

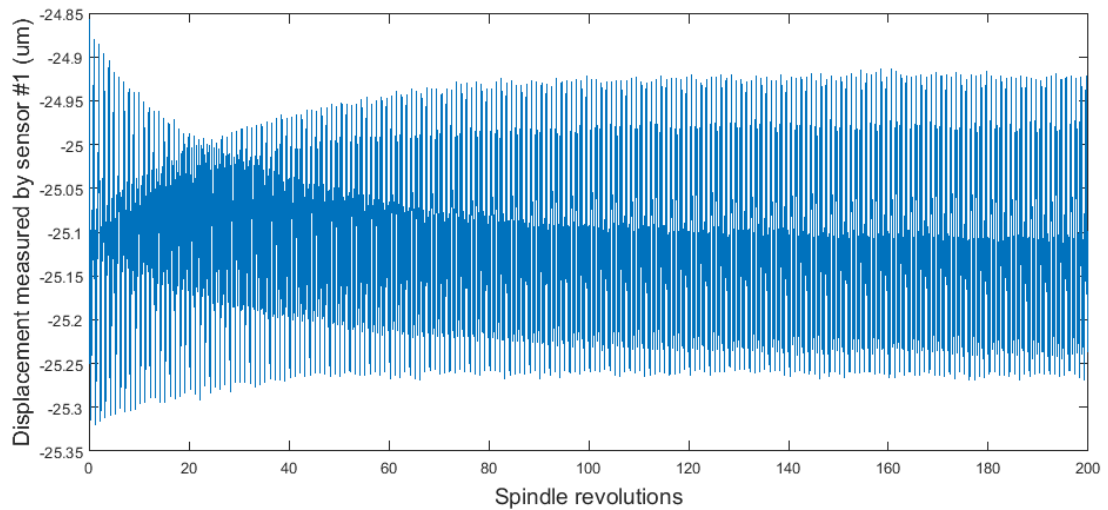
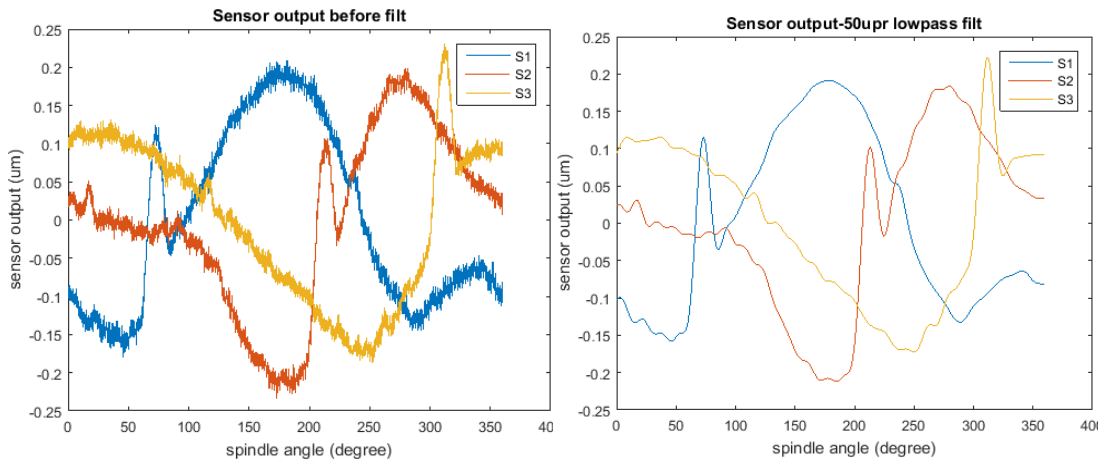


Figure D-4: Sensor readings for the first 200 revolutions after start-up

The exact angles between the three probes are critical for the correct separation of artefact form error and spindle error motion. Although many efforts have been made in selecting the different angles, there will be positioning errors when the probes are mounted on the sensor holder. The angle deviations will not be so large as to affect the overall shape of the weighting function, so the aforementioned design process is still necessary. The question is how to determine the actual angles after the probes are mounted.

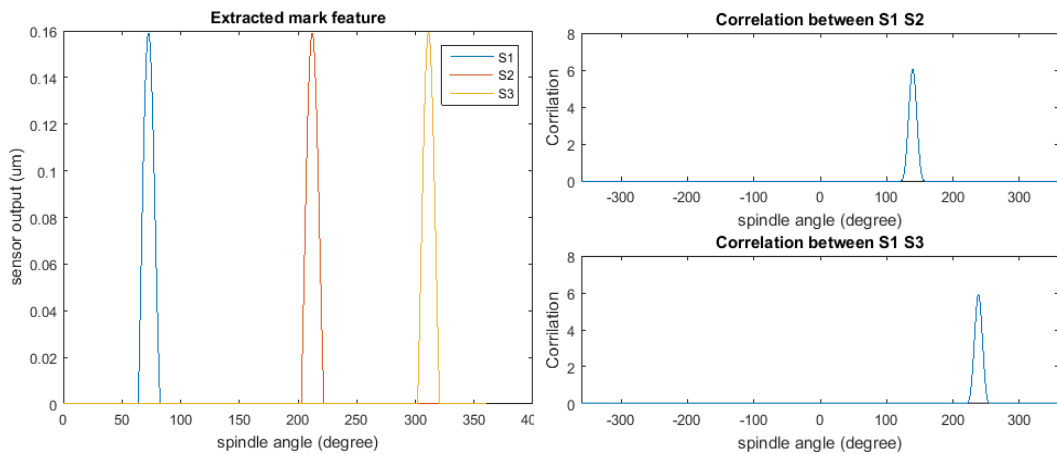
In this experiment, a special mark on the artefact is used to determine the relative angles between each probe. The output of the three probes should pose similar profile for every cycle with phase differences and correlation algorithm can be used to find relative phase angles. As the spindle error motion is superimposed on the form profile including the designated mark, the mark feature has to be extracted before applying the correlation method. The extraction process is shown below in figure. Firstly, the sensor output is filtered at 50-UPR cut-off frequency with zero-phase forward and reverse Infinite Impulse Response (IIR) filter. Then a low order polynomial (8th order) is subtracted from the curve to remove the large wavelength while keep the narrow mark signal dominates. After that, mark features for each probe are extracted with

same height from the peak and mutual correlation is calculated to determine phase differences.



(a) Sensor signal output

(b) 50µm low-pass filtered signal



(c) Extracted features by polynomial fitting

(d) Correlation calculation

Figure D-5: Steps for calculation of actual probe angles with an ink mark

The angles are calculated once a cycle and 96 cycles are calculated in total. The actual probe angles are listed in Table D-2, together with the standard deviations. The results show good repeatability and it seems the limitation is the number of the pulses generated per revolution by spindle.



Table D-2: Actual probe angles after probe mounting

	Angle $\alpha$ (°)	Standard deviation	Angle $\beta$ (°)	Standard deviation
Angle set #1	100.15	0.0052	230.12	0.0314
Angle set #2	140.90	0.0052	269.92	0.0173
Angle set #3	139.33	0.0131	238.31	0.0144

## D. 4 Data processing

The three harmonic weighting functions calculated from the measured angles are shown in Figure D-6. Several unexpected small absolute values of  $H$  can be found at harmonics around 35 UPR and 60 UPR, which is not desirable. This also demonstrates the necessity for using more than one angle combination to recover components that are missed out in a single measurement.

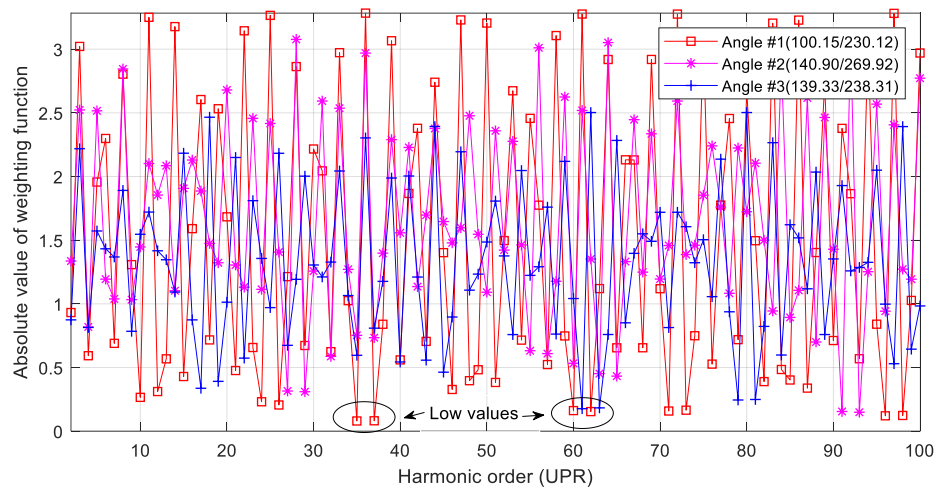


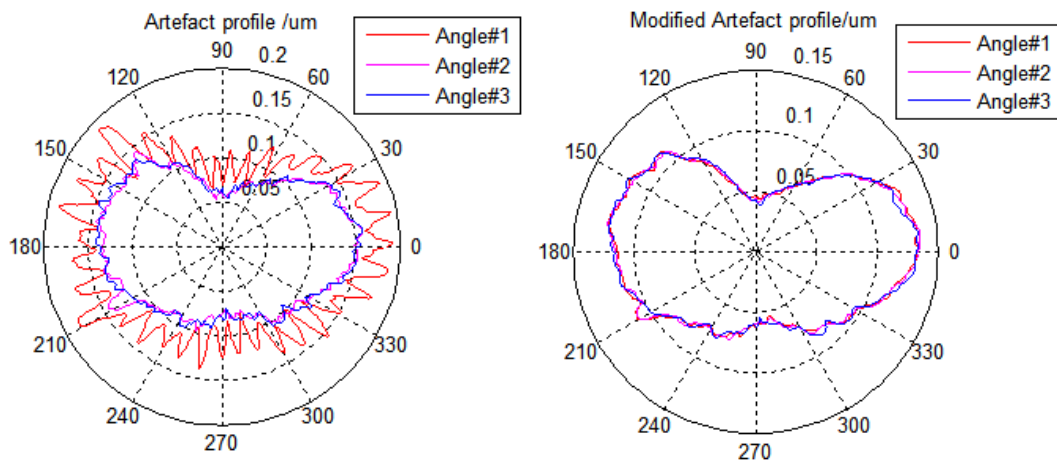
Figure D-6: Harmonic weighting functions after probe mounting

Three measurements with different angles at  $Z = -42$  mm (approx. 100 mm from the spindle bearing location) are evaluated to verify the frequency-domain modification approach. Analysed harmonic range is set from 2 UPR to 100 UPR and asynchronous errors are removed by averaging 32 revolutions.

Figure D-7 a) shows the separated artefact profiles from three measurements. The profile measured by angle set #1 poses much higher undulations than angle #2 and #3, which is caused by the error amplification effect of low  $H$ . The FFT results of the three

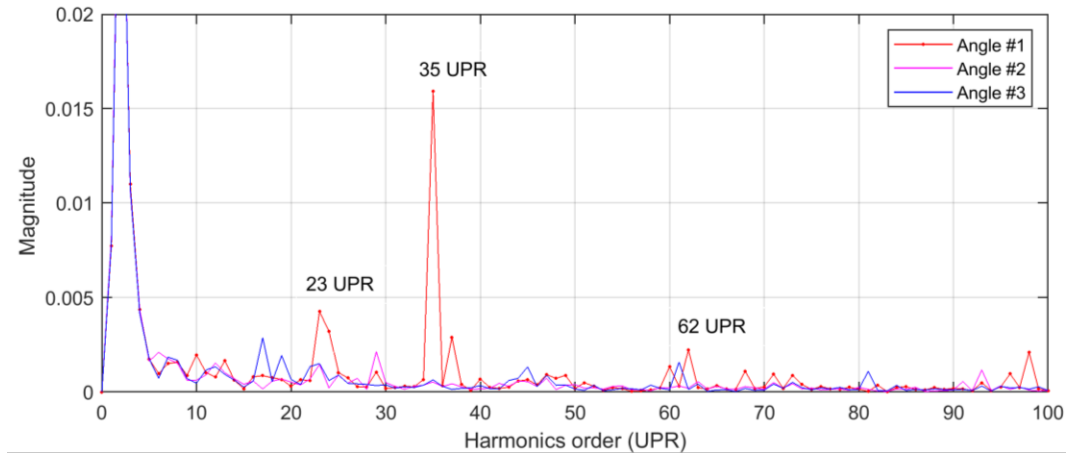
profiles are shown in Figure D-7 c). It can be seen that the artefact profile for the first angles set shows obvious peaks at the 35 UPR and 62 UPR, which agrees with the low values of the weighting function.

A frequency-domain modification method is applied to each curve to address this problem. For each angle set, the magnitude of the artefact profile spectrum is scaled to be the smallest of the three, while the phase of each harmonic order is kept unchanged for this angle set. Then they are converted back into waveforms by inverse FFT. The modified artefact profile is shown in Figure D-7 b) and the results show that the maximum differences between the three measurements is reduced from 24.1 nm to 7.3 nm, thus the harmonic problem is effectively reduced by 70% in this case. The modified results possess much improved agreement between the three measurements. The peak-to-peak synchronous X radial error is measured to be 108.1 nm, 112.1 nm and 101.1 nm respectively.



(a) Separated artefact profile without modification

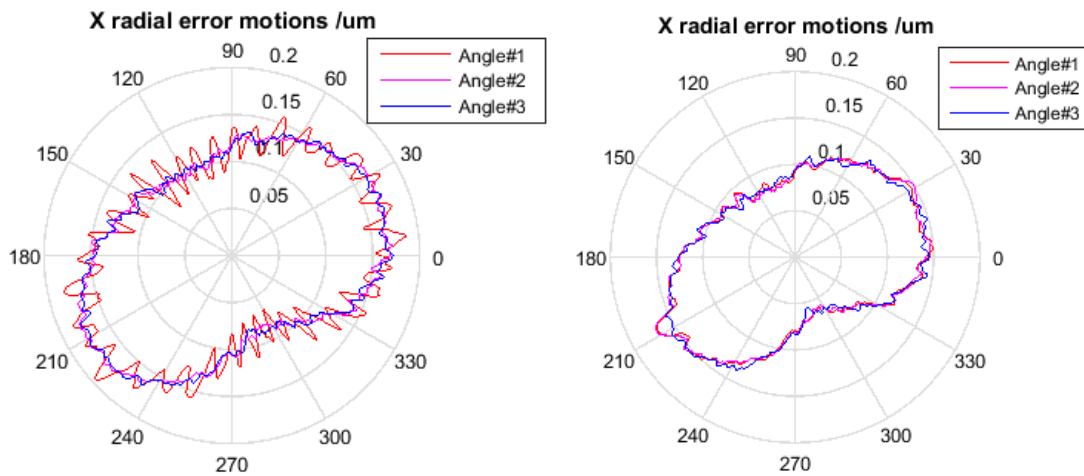
(b) Modified artefact profile



c) FFT of separated artefact profile from the three angle setups without modification

Figure D-7: Harmonic suppression problem and modified results

Figure D-8 a) and b) shows the synchronous X radial error motions before and after frequency domain modification. Significant improvement of result repeatability is achieved. The radial error motions at the seven axial locations are then used to calculate the tilt error of the spindle by linear fitting.



(a) Errors before modification

(b) Results with modification

Figure D-8: X radial error measured with three angle sets

# Bibliography

- [1] A. Nicolaus, R. Meeß, and G. Bartl, “New Avogadro spheres for the redefinition of the kilogram,” *Key Eng. Mater.*, vol. 613, pp. 17–25, 2014.
- [2] K. P. Thompson and J. P. Rolland, “Freeform optical surfaces: a revolution in imaging optical design,” *Opt. Photonics News*, vol. 23, no. 6, p. 30, Jun. 2012.
- [3] A. M. Herkommer, “Advances in the design of freeform systems for imaging and illumination applications,” *J. Opt.*, vol. 43, no. 4, pp. 261–268, Dec. 2014.
- [4] J. Reimers, A. Bauer, K. P. Thompson, and J. P. Rolland, “Freeform spectrometer enabling increased compactness,” *Nat. Publ. Gr.*, vol. 6, 2017.
- [5] H. J. Tiziani, R. Hentschel, and B. Braunecker, *Advanced optics using aspherical elements*. SPIE Press, 2008.
- [6] Y. Furukawa and N. Moronuki, “Effect of material properties on ultra precise cutting processes,” *CIRP Ann.*, vol. 37, no. 1, pp. 113–116, Jan. 1988.
- [7] K. S. Chon and Y. Namba, “Single-point diamond turning of electroless nickel for flat X-ray mirror,” *J. Mech. Sci. Technol.*, vol. 24, no. 8, pp. 1603–1609, Aug. 2010.
- [8] S. Goel, X. Luo, A. Agrawal, and R. L. Reuben, “Diamond machining of silicon: A review of advances in molecular dynamics simulation,” *Int. J. Mach. Tools Manuf.*, vol. 88, pp. 131–164, Jan. 2015.
- [9] N. Taniguchi, “Current status in, and future trends of, ultraprecision machining and ultrafine materials processing,” *CIRP Ann.*, vol. 32, no. 2, pp. 573–582, Jan. 1983.
- [10] F. Fang and V. C. Venkatesh, “Diamond cutting of silicon with nanometric finish,” *CIRP Ann.*, vol. 47, no. 1, pp. 45–49, Jan. 1998.
- [11] F. Fang, X. Zhang, A. Weckenmann, G. X. Zhang, and C. J. Evans, “Manufacturing and measurement of freeform optics,” *CIRP Ann. - Manuf. Technol.*, vol. 62, no. 2, pp. 823–846, Jan. 2013.
- [12] X. Liu, X. Zhang, F. Fang, Z. Zeng, H. Gao, and X. Hu, “Influence of machining errors on form errors of microlens arrays in ultra-precision turning,” *Int. J. Mach. Tools Manuf.*, vol. 96, pp. 80–93, Sep. 2015.
- [13] D. W. Hoepfner and V. Chandrasekaran, “Fretting in orthopaedic implants: A review,” *Wear*, vol. 173, no. 1–2, pp. 189–197, Apr. 1994.
- [14] “Data on File at Depuy Orthopaedics. Inc. WR#010120.”
- [15] C. J. Evans and J. B. Bryan, “‘Structured’, ‘textured’ or ‘engineered’ surfaces,” *CIRP Ann.*, vol. 48, no. 2, pp. 541–556, Jan. 1999.

- [16] A. A. G. Bruzzone, H. L. Costa, P. M. Lonardo, and D. A. Lucca, "Advances in engineered surfaces for functional performance," *CIRP Ann.*, vol. 57, no. 2, pp. 750–769, Jan. 2008.
- [17] S. Zhang, Y. Zhou, H. Zhang, Z. Xiong, and S. To, "Advances in ultra-precision machining of micro-structured functional surfaces and their typical applications," *Int. J. Mach. Tools Manuf.*, vol. 142, pp. 16–41, Jul. 2019.
- [18] J. Geng, "Three-dimensional display technologies," *Adv. Opt. Photonics*, vol. 5, no. 4, p. 456, 2013.
- [19] M. Zhang, Z. Geng, R. Pei, X. Cao, and Z. Zhang, "Three-dimensional light field microscope based on a lenslet array," *Opt. Commun.*, vol. 403, pp. 133–142, Nov. 2017.
- [20] L. Li and A. Y. Yi, "Design and fabrication of a freeform prism array for 3D microscopy," *J. Opt. Soc. Am. A*, vol. 27, no. 12, p. 2613, 2010.
- [21] Brian Wowk, "Phased Array Optics." 1991.
- [22] P. Wang, N. Mohammad, and R. Menon, "Chromatic-aberration-corrected diffractive lenses for ultra-broadband focusing," *Sci. Rep.*, vol. 6, no. 1, p. 21545, Aug. 2016.
- [23] M. M. Marekškereň, J. Svoboda, M. Květoň, J. Hopp, M. Possolt, and P. Fiala, "Diffractive elements for correction of chromatic aberrations of illumination systems," *EPJ Web Conf.*, vol. 48, p. 25, 2013.
- [24] E. R. Dufresne and D. G. Grier, "Optical tweezer arrays and optical substrates created with diffractive optics," *Rev. Sci. Instrum.*, vol. 69, no. 5, pp. 1974–1977, May 1998.
- [25] P. Gorenstein, "Focusing X-ray optics for astronomy," *X-Ray Opt. Instrum.*, vol. 2010, pp. 1–19, Dec. 2010.
- [26] F. Xue, W. Zhao, Y. Chen, and Z. Wang, "Research on error averaging effect of hydrostatic guideways," *Precis. Eng.*, vol. 36, no. 1, pp. 84–90, Jan. 2012.
- [27] C. F. Cheung, L. B. Kong, L. T. Ho, and S. To, "Modelling and simulation of structure surface generation using computer controlled ultra-precision polishing," *Precis. Eng.*, vol. 35, no. 4, pp. 574–590, Oct. 2011.
- [28] E. Brinksmeier, Y. Mutlugünes, F. Klocke, J. C. Aurich, P. Shore, and H. Ohmori, "Ultra-precision grinding," *CIRP Ann.*, vol. 59, no. 2, pp. 652–671, Jan. 2010.
- [29] D. J. Stephenson, D. Veselovac, S. Manley, and J. Corbett, "Ultra-precision grinding of hard steels," *Precis. Eng.*, vol. 25, no. 4, pp. 336–345, Oct. 2001.
- [30] D. Golini, W. I. Kordonski, P. Dumas, and S. J. Hogan, "Magnetorheological finishing (MRF) in commercial precision optics manufacturing," 1999, vol. 3782, pp. 80–91.

- [31] Y. Namba *et al.*, “Ultra-precision polishing of electroless nickel molding dies for shorter wavelength applications,” *CIRP Ann.*, vol. 57, no. 1, pp. 337–340, Jan. 2008.
- [32] Y. Namba, H. Tsuwa, R. Wada, and N. Ikawa, “Ultra-precision float polishing machine,” *CIRP Ann.*, vol. 36, no. 1, pp. 211–214, Jan. 1987.
- [33] C.-C. Chen, Y.-C. Cheng, W.-Y. Hsu, H.-Y. Chou, P.-J. Wang, and D. P. Tsai, “Slow tool servo diamond turning of optical freeform surface for astigmatic contact lens,” in *Proc. SPIE 8126, Optical Manufacturing and Testing IX*, 2011, vol. 8126, p. 812617.
- [34] T. A. Dow, M. H. Miller, and P. J. Falter, “Application of a fast tool servo for diamond turning of nonrotationally symmetric surfaces,” *Precis. Eng.*, vol. 13, no. 4, pp. 243–250, Oct. 1991.
- [35] Z. Zhu, S. To, and S. Zhang, “Theoretical and experimental investigation on the novel end-fly-cutting-servo diamond machining of hierarchical micro-nanostructures,” *Int. J. Mach. Tools Manuf.*, vol. 94, pp. 15–25, Jul. 2015.
- [36] M. Mukaida and J. Yan, “Ductile machining of single-crystal silicon for microlens arrays by ultraprecision diamond turning using a slow tool servo,” *Int. J. Mach. Tools Manuf.*, vol. 115, pp. 2–14, Apr. 2017.
- [37] D. Li *et al.*, “Theoretical and experimental investigation of surface topography generation in slow tool servo ultra-precision machining of freeform surfaces,” *Materials (Basel)*, vol. 11, no. 12, p. 2566, Dec. 2018.
- [38] Z. Q. Yin, Y. F. Dai, S. Y. Li, C. L. Guan, and G. P. Tie, “Fabrication of off-axis aspheric surfaces using a slow tool servo,” *Int. J. Mach. Tools Manuf.*, vol. 51, no. 5, pp. 404–410, May 2011.
- [39] X. Lu and D. L. Trumper, “Ultrafast tool servos for diamond turning,” *CIRP Ann.*, vol. 54, no. 1, pp. 383–388, Jan. 2005.
- [40] X. Lu, “Electromagnetically-driven ultra-fast tool servos for diamond turning,” Massachusetts Institute of Technology, 2005.
- [41] F. Tian, Z. Yin, and S. Li, “A novel long range fast tool servo for diamond turning,” *Int. J. Adv. Manuf. Technol.*, vol. 86, no. 5–8, pp. 1227–1234, 2016.
- [42] X. Zhang, K. Liu, X. Shan, and Y. Liu, “Roll-to-roll embossing of optical linear Fresnel lens polymer film for solar concentration,” *Opt. Express*, vol. 22, no. S7, p. A1835, Dec. 2014.
- [43] R. Huang, X. Zhang, M. Rahaman, A. S. Kumar, and K. Liu, “Ultra-precision machining of radial Fresnel lens on roller moulds,” *CIRP Ann.*, vol. 64, no. 1, pp. 121–124, Jan. 2015.
- [44] K. Garrard, A. Sohn, and T. Dow, “Design, fabrication and testing of kinoform lenses,” 2008.

- [45] C. J. Li, Y. Li, X. Gao, and C. V Duong, "Ultra-precision machining of Fresnel lens mould by single-point diamond turning based on axis B rotation," *Int. J. Adv. Manuf. Technol.*, vol. 77, no. 5–8, pp. 907–913, Mar. 2015.
- [46] Y. Takeuchi, S. Maeda, T. Kawai, and K. Sawada, "Manufacture of multiple-focus micro fresnel lenses by means of nonrotational diamond grooving," *CIRP Ann.*, vol. 51, no. 1, pp. 343–346, Jan. 2002.
- [47] E. Brinksmeier, R. Gläbe, and L. Schönemann, "Diamond micro chiseling of large-scale retroreflective arrays," *Precis. Eng.*, vol. 36, no. 4, pp. 650–657, Oct. 2012.
- [48] E. Brinksmeier, R. Gläbe, and L. Schönemann, "Review on diamond-machining processes for the generation of functional surface structures," *CIRP J. Manuf. Sci. Technol.*, vol. 5, no. 1, pp. 1–7, Jan. 2012.
- [49] E. Brinksmeier and L. Schönemann, "Generation of discontinuous microstructures by Diamond Micro Chiseling," *CIRP Ann.*, vol. 63, no. 1, pp. 49–52, Jan. 2014.
- [50] E. Brinksmeier *et al.*, "Submicron functional surfaces generated by diamond machining," *CIRP Ann.*, vol. 59, no. 1, pp. 535–538, Jan. 2010.
- [51] E. Brinksmeier, R. Gläbe, and C. Flucke, "Manufacturing of molds for replication of micro cube corner retroreflectors," *Prod. Eng.*, vol. 2, no. 1, pp. 33–38, 2008.
- [52] R. Huang, X. Zhang, W. K. Neo, A. S. Kumar, and K. Liu, "Ultra-precision machining of grayscale pixelated micro images on metal surface," *Precis. Eng.*, vol. 52, pp. 211–220, Apr. 2018.
- [53] S. To, Z. Zhu, and H. Wang, "Virtual spindle based tool servo diamond turning of discontinuously structured microoptics arrays," *CIRP Ann.*, vol. 65, no. 1, pp. 475–478, Jan. 2016.
- [54] O Riemer, "Advances in ultra precision manufacturing," in *Proc. Jpn. Soc. Precis. Eng.*, 2011.
- [55] J. B. Bryan, "Design and construction of an ultraprecision 84 inch diamond turning machine," *Precis. Eng.*, vol. 1, no. 1, pp. 13–17, Jan. 1979.
- [56] C.-C. Chen, Y.-C. Cheng, W.-Y. Hsu, H.-Y. Chou, P.-J. Wang, and D. P. Tsai, "Slow tool servo diamond turning of optical freeform surface for astigmatic contact lens," in *Proc. SPIE 8126, Optical Manufacturing and Testing IX*, 2011, vol. 8126, p. 812617.
- [57] S. J. Ludwick, D. A. Chargin, J. A. Calzaretta, and D. L. Trumper, "Design of a rotary fast tool servo for ophthalmic lens fabrication," *Precis. Eng.*, vol. 23, no. 4, pp. 253–259, Oct. 1999.
- [58] S. Rakuff and J. F. Cuttino, "Design and testing of a long-range, precision fast tool servo system for diamond turning," *Precis. Eng.*, vol. 33, no. 1, pp. 18–25,

Jan. 2009.

- [59] S. Scheiding *et al.*, “Diamond milling or turning for the fabrication of micro lens arrays: comparing different diamond machining technologies,” *Opt. Express*, vol. 19, no. 24, pp. 23938–23951, 2011.
- [60] S. Zhang, S. To, Z. Zhu, and G. X. Zhang, “A review of fly cutting applied to surface generation in ultra-precision machining,” *Int. J. Mach. Tools Manuf.*, vol. 103, pp. 13–27, 2016.
- [61] P. Comley, P. Morantz, P. Shore, and X. Tonnellier, “Grinding metre scale mirror segments for the E-ELT ground based telescope,” *CIRP Ann.*, vol. 60, no. 1, pp. 379–382, Jan. 2011.
- [62] R. Neugebauer, B. Denkena, and K. Wegener, “Mechatronic systems for machine tools,” *CIRP Ann. - Manuf. Technol.*, vol. 56, no. 2, pp. 657–686, Jan. 2007.
- [63] D. Laro, R. Boshuisen, J. Dams, and J. van Eijk, “Linear hybrid actuator for active force cancellation,” in *International Symposium on Linear Drives for Industry Applications*, 2011, vol. 8, pp. 244–248.
- [64] S. Ito, S. Troppmair, F. Cigarini, and G. Schitter, “High-speed scanner with nanometer resolution using a hybrid reluctance force actuator,” *IEEJ J. Ind. Appl.*, vol. 8, no. 2, pp. 170–176, 2019.
- [65] E. Csencsics, J. Schlarp, and G. Schitter, “High-performance hybrid-reluctance-force-based tip/tilt system: design, control, and evaluation,” *IEEE/ASME Trans. Mechatronics*, vol. 23, no. 5, pp. 2494–2502, Oct. 2018.
- [66] G. Sze-Wei, L. Han-Seok, M. Rahaman, and F. Watt, “A fine tool servo system for global position error compensation for a miniature ultra-precision lathe,” *Int. J. Mach. Tools Manuf.*, vol. 47, no. 7–8, pp. 1302–1310, 2007.
- [67] K.-M. Chang, W.-T. Cheng, and Y.-T. Liu, “Development of non-axisymmetric aspheric ultraprecision machining using FPGA-based piezoelectric FTS,” *Sensors Actuators A Phys.*, vol. 291, pp. 99–106, 2019.
- [68] E. Kouno and P. A. McKeown, “A fast response piezoelectric actuator for servo correction of systematic errors in precision machining,” *CIRP Ann.*, vol. 33, no. 1, pp. 369–372, 1984.
- [69] S. R. Patterson and E. B. Magrab, “Design and testing of a fast tool servo for diamond turning,” *Precis. Eng.*, vol. 7, no. 3, pp. 123–128, 1985.
- [70] Y. Hara, S. Motonishi, K. Yoshida, and N. Ikawa, “A new micro-cutting device with high stiffness and resolution,” *CIRP Ann.*, vol. 39, no. 1, pp. 375–378, 1990.
- [71] B. H. Jared, T. A. Dow, and K. P. Garrard, “Fabrication of surface perturbations on inertial confinement fusion targets.” 1996.



- [72] D. L. Trumper and X. Lu, "Fast tool servos: advances in precision, acceleration, and bandwidth," in *Towards Synthesis of Micro-/Nano-systems*, Springer, 2007, pp. 11–19.
- [73] H. K. McCue, "The motion control system for the large optics diamond turning machine (LODTM)," in *Contemporary Methods of Optical Manufacturing and Testing*, 1983, vol. 433, pp. 68–75.
- [74] P. B. Leadbeater, M. Clarke, W. J. Wills-More, and T. J. Wilson, "A unique machine for grinding large, off-axis optical components: the OAGM 2500," *Precis. Eng.*, vol. 11, no. 4, pp. 191–196, Oct. 1989.
- [75] T. Raparelli, V. Viktorov, F. Colombo, and L. Lentini, "Aerostatic thrust bearings active compensation: Critical review," *Precis. Eng.*, vol. 44, pp. 1–12, Apr. 2016.
- [76] A. Shimokohbe and H. Aoyama, "An active air bearing: A controlled-type bearing with ultra-precision, infinite static stiffness, high damping capability and new functions," *Nanotechnology*, vol. 2, no. 1, pp. 64–71, 1991.
- [77] A. Shimokohbe, O. Horikawa, K. Sato, and H. Sato, "An active air journal bearing with ultraprecision, infinite static stiffness, high damping capability and new functions," *CIRP Ann.*, vol. 40, no. 1, pp. 563–566, Jan. 1991.
- [78] O. Horikawa, K. Sato, and A. Shimokohbe, "An active air journal bearing," *Nanotechnology*, vol. 3, no. 2, pp. 84–90, Apr. 1992.
- [79] J. C. Lee, K. Il Lee, and S.-H. Yang, "Development of compact three-degrees-of-freedom compensation system for geometric errors of an ultra-precision linear axis," *Mech. Mach. Theory*, vol. 99, pp. 72–82, May 2016.
- [80] G. Aguirre, F. Al-Bender, and H. Van Brussel, "A multiphysics model for optimizing the design of active aerostatic thrust bearings," *Precis. Eng.*, vol. 34, no. 3, pp. 507–515, 2010.
- [81] F. Al-Bender, "On the modelling of the dynamic characteristics of aerostatic bearing films: From stability analysis to active compensation," *Precis. Eng.*, vol. 33, no. 2, pp. 117–126, 2009.
- [82] H. Mizumoto, S. Arii, Y. Kami, K. Goto, T. Yamamoto, and M. Kawamoto, "Active inherent restrictor for air-bearing spindles," *Precis. Eng.*, vol. 19, no. 2–3, pp. 141–147, Oct. 1996.
- [83] S.-K. Ro, S. Kim, Y. Kwak, and C. H. Park, "A linear air bearing stage with active magnetic preloads for ultraprecise straight motion," *Precis. Eng.*, vol. 34, no. 1, pp. 186–194, Jan. 2010.
- [84] N. R. Kane, J. Sihler, and A. H. Slocum, "A hydrostatic rotary bearing with angled surface self-compensation," *Precis. Eng.*, vol. 27, no. 2, pp. 125–139, Apr. 2003.
- [85] A. H. Slocum, P. A. Scagnetti, N. R. Kane, and C. Brunner, "Design of self-

- compensated, water-hydrostatic bearings,” *Precis. Eng.*, vol. 17, no. 3, pp. 173–185, Jul. 1995.
- [86] H. Zhang, B. Kou, Y. Jin, L. Zhang, H. Zhang, and L. Li, “Modeling and analysis of a novel planar eddy current damper,” *J. Appl. Phys.*, vol. 115, no. 17, p. 17E709, May 2014.
- [87] S. K. Sze Kwan Cheah and H. A. Sodano, “Novel eddy current damping mechanism for passive magnetic bearings,” *J. Vib. Control*, vol. 14, no. 11, pp. 1749–1766, Nov. 2008.
- [88] K. K. Tan, S. Huang, C. S. Teo, and R. Yang, “Controller design of eddy current braking in an air bearing system,” *Automatica*, vol. 48, no. 11, pp. 2831–2836, Nov. 2012.
- [89] Yongdae Kim, Byounguk Sohn, Woosub Youm, Jongkyu Jung, Jonghyun Lee, and K. Park, “Voice coil motor nano stage with an eddy current damper,” in *2008 10th International Conference on Control, Automation, Robotics and Vision*, 2008, pp. 1714–1717.
- [90] Chih-Hsien Lin, S.-K. Hung, M.-Y. Chen, Shan-Tsung Li, and L.-C. Fu, “A novel high precision electromagnetic flexure-suspended positioning stage with an eddy current damper,” in *2008 International Conference on Control, Automation and Systems*, 2008, pp. 771–776.
- [91] M. F. Zaeh and M. Hennauer, “Prediction of the dynamic behaviour of machine tools during the design process using mechatronic simulation models based on finite element analysis,” *Prod. Eng.*, vol. 5, no. 3, pp. 315–320, Jun. 2011.
- [92] E. V. Bordatchev, P. E. Orban, and A. Rehorn, “Experimental analysis and modeling of the dynamic performance of machine tool spindle-bearing systems,” in *Sensors and Controls for Intelligent Manufacturing*, 2001, vol. 4191, pp. 92–103.
- [93] G. B. Arfken and H. J. Weber, *Mathematical methods for physicists*. San Diego, CA: AAPT, 1999.
- [94] L. Jabben, “Mechatronic design of a magnetically suspended rotating platform,” Delft University of Technology, 2007.
- [95] Y. Sun, W. Chen, Y. Liang, C. An, G. Chen, and H. Su, “Dynamic error budget analysis of an ultraprecision flycutting machine tool,” *Int. J. Adv. Manuf. Technol.*, vol. 76, no. 5–8, pp. 1215–1224, Feb. 2015.
- [96] L. Andolfatto, S. Lavernhe, and J. R. R. Mayer, “Evaluation of servo, geometric and dynamic error sources on five-axis high-speed machine tool,” *Int. J. Mach. Tools Manuf.*, vol. 51, no. 10–11, pp. 787–796, Oct. 2011.
- [97] P. M. Ferreira and C. R. Liu, “A method for estimating and compensating quasistatic errors of machine tools,” *J. Manuf. Sci. Eng.*, vol. 115, no. 1, pp. 149–159, Feb. 1993.

- [98] D. Kono, S. Weikert, A. Matsubara, and K. Yamazaki, "Estimation of dynamic mechanical error for evaluation of machine tool structures," *Int. J. Autom. Technol.*, vol. 6, no. 2, pp. 147–153, 2012.
- [99] M. Iwasaki, K. Seki, and Y. Maeda, "High-precision motion control techniques: A promising approach to improving motion performance," *IEEE Ind. Electron. Mag.*, vol. 6, no. 1, pp. 32–40, 2012.
- [100] Y. Koren and C. C. Lo, "Advanced controllers for feed drives," *CIRP Ann.*, vol. 41, no. 2, pp. 689–698, Jan. 1992.
- [101] D. Dahlmann, N. Sassi, and B. Denkena, "Approaches for detailed modelling of ultra-precision positioning systems," *Mod. Mech. Eng.*, vol. 6, pp. 44–50, 2016.
- [102] Y. Hori, "Disturbance suppression on an acceleration control type DC servo system," in *19th Annual IEEE Power Electronics Specialists Conference*, 1988, pp. 222–229.
- [103] R. D. Lorenz, "Design principles and implementation of acceleration feedback to improve performance of dc drives," *IEEE Trans. Ind. Appl.*, vol. 28, no. 3, pp. 594–599, 1992.
- [104] G. Ellis and R. D. Lorenz, "Comparison of motion control loops for industrial applications," in *Conference Record of the 1999 IEEE Industry Applications Conference. Thirty-Forth IAS Annual Meeting (Cat. No.99CH36370)*, 1999, vol. 4, pp. 2599–2605.
- [105] R. J. E. Merry, M. J. G. van de Molengraft, and M. Steinbuch, "Velocity and acceleration estimation for optical incremental encoders," *Mechatronics*, vol. 20, no. 1, pp. 20–26, Feb. 2010.
- [106] H. Shim, M. Kochem, and M. Tomizuka, "Use of accelerometer for precision motion control of linear motor driven positioning system," in *Proceedings of the 24th Annual Conference of the IEEE Industrial Electronics Society*, 1998, vol. 4, pp. 2409–2414.
- [107] J. Wittmann, R. Hagl, and R. Kennel, "Hybrid current and acceleration control of servo drives," *Int. Exhib. Conf. Power Electron. Intell. Motion, Renew. Energy Energy Manag.*, no. May, pp. 16–18, 2017.
- [108] F. Tian, K. Craig, and M. Nagurka, "Disturbance attenuation in a magnetic levitation system with acceleration feedback," *Proc. IEEE Int. Conf. Ind. Technol.*, pp. 59–64, 2011.
- [109] M. Griese and J. Maas, "Acceleration estimation and feedback for two-mass servo systems," *IEEE/ASME Int. Conf. Adv. Intell. Mechatronics, AIM*, pp. 370–375, 2017.
- [110] A. Dumanli and B. Sencer, "Optimal high-bandwidth control of ball-screw drives with acceleration and jerk feedback," *Precis. Eng.*, vol. 54, pp. 254–268,

Oct. 2018.

- [111] S. Katsura, K. Irie, and K. Ohishi, "Wideband force control by position-acceleration integrated disturbance observer," *IEEE Trans. Ind. Electron.*, vol. 55, no. 4, pp. 1699–1706, 2008.
- [112] H. Butler, "Acceleration feedback in a lithographic tool," *Control Eng. Pract.*, vol. 20, no. 4, pp. 453–464, 2012.
- [113] F. Chen, X. Lu, and Y. Altintas, "A novel magnetic actuator design for active damping of machining tools," *Int. J. Mach. Tools Manuf.*, vol. 85, pp. 58–69, 2014.
- [114] J. Munoa, X. Beudaert, K. Erkorkmaz, A. Iglesias, A. Barrios, and M. Zatarain, "Active suppression of structural chatter vibrations using machine drives and accelerometers," *CIRP Ann.*, vol. 64, no. 1, pp. 385–388, Jan. 2015.
- [115] J. Abir, P. Morantz, S. Longo, and P. Shore, "A novel accelerometer based feedback concept for improving machine dynamic performance," in *International Federation of Automatic Control*, 2016, vol. 49, no. 21, pp. 553–558.
- [116] J. Abir, S. Longo, P. Morantz, and P. Shore, "Optimized estimator for real-time dynamic displacement measurement using accelerometers," *Mechatronics*, vol. 39, pp. 1–11, 2016.
- [117] G. Pritschow, C. Eppler, and W.-D. Lehner, "Ferraris sensor – the key for advanced dynamic drives," *CIRP Ann.*, vol. 52, no. 1, pp. 289–292, Jan. 2003.
- [118] W. J. Zong, Z. Q. Li, T. Sun, K. Cheng, D. Li, and S. Dong, "The basic issues in design and fabrication of diamond-cutting tools for ultra-precision and nanometric machining," *Int. J. Mach. Tools Manuf.*, vol. 50, no. 4, pp. 411–419, Apr. 2010.
- [119] W. J. Zong, D. Li, K. Cheng, T. Sun, H. X. Wang, and Y. C. Liang, "The material removal mechanism in mechanical lapping of diamond cutting tools," *Int. J. Mach. Tools Manuf.*, vol. 45, no. 7–8, pp. 783–788, Jun. 2005.
- [120] W. J. Zong, T. Sun, D. Li, K. Cheng, and Z. Q. Li, "Nano-precision diamond cutting tools achieved by mechanical lapping versus thermo-mechanical lapping," *Diam. Relat. Mater.*, vol. 17, no. 6, pp. 954–961, Jun. 2008.
- [121] W. J. Zong, T. Sun, D. Li, and K. Cheng, "Design criterion for crystal orientation of diamond cutting tool," *Diam. Relat. Mater.*, vol. 18, no. 4, pp. 642–650, Apr. 2009.
- [122] Y. Furukawa and N. Moronuki, "Effect of material properties on ultra precise cutting processes," *CIRP Ann.*, vol. 37, no. 1, pp. 113–116, Jan. 1988.
- [123] S. To, C. F. Cheung, and W. B. Lee, "Influence of material swelling on surface roughness in diamond turning of single crystals," *Mater. Sci. Technol.*, vol. 17, no. 1, pp. 102–108, Jan. 2001.

- [124] K. Liu and S. N. Melkote, "Effect of plastic side flow on surface roughness in micro-turning process," *Int. J. Mach. Tools Manuf.*, vol. 46, no. 14, pp. 1778–1785, Nov. 2006.
- [125] M. Tauhiduzzaman and S. C. Veldhuis, "Effect of material microstructure and tool geometry on surface generation in single point diamond turning," *Precis. Eng.*, vol. 38, no. 3, pp. 481–491, Jul. 2014.
- [126] M. C. Kong, W. B. Lee, C. F. Cheung, and S. To, "A study of materials swelling and recovery in single-point diamond turning of ductile materials," *J. Mater. Process. Technol.*, vol. 180, no. 1–3, pp. 210–215, Dec. 2006.
- [127] B. Zhang, "An investigation of the effect of machine loop stiffness on grinding of ceramics," *CIRP Ann.*, vol. 50, no. 1, pp. 209–212, Jan. 2001.
- [128] B. Zhang, J. Wang, F. Yang, and Z. Zhu, "The effect of machine stiffness on grinding of silicon nitride," *Int. J. Mach. Tools Manuf.*, vol. 39, no. 8, pp. 1263–1283, Aug. 1999.
- [129] D. Huo, K. Cheng, and F. Wardle, "Design of a five-axis ultra-precision micro-milling machine—UltraMill. Part 2: integrated dynamic modelling, design optimisation and analysis," *Int. J. Adv. Manuf. Technol.*, vol. 47, no. 9, pp. 879–890, 2010.
- [130] G. Boothroyd, *Fundamentals of metal machining and machine tools*, vol. 28. Crc Press, 1988.
- [131] P. McKeown and J. Corbett, "Ultra precision machine tools," in *Autonome produktion*, Springer, 2004, pp. 313–327.
- [132] L. C. Hale, R. R. Donaldson, C. Castro, C. A. Chung, and D. J. Hopkins, "Development of a hydrostatic journal bearing with slit-step compensation," Lawrence Livermore National Lab.(LLNL), Livermore, CA (United States), 2006.
- [133] R. Ramesh, M. A. Mannan, and A. N. Poo, "Error compensation in machine tools — a review: Part I: geometric, cutting-force induced and fixture-dependent errors," *Int. J. Mach. Tools Manuf.*, vol. 40, no. 9, pp. 1235–1256, Jul. 2000.
- [134] R. Ramesh, M. A. Mannan, and A. N. Poo, "Error compensation in machine tools- a review. Part II: Thermal errors," *Int. J. Mach. Tools Manuf.*, vol. 40, no. 9, pp. 1257–1284, Jul. 2000.
- [135] P. Münch, S. Liu, and M. Dommaschk, "Modeling and current control of modular multilevel converters considering actuator and sensor delays," in *2009 35th Annual Conference of IEEE Industrial Electronics*, 2009, pp. 1633–1638.
- [136] C. Brecher, D. Lindemann, and C. Wenzel, "Influences of closed loop control components on the performance of ultra-precision machines," *Key Eng. Mater.*, vol. 625, pp. 207–212, 2014.

- [137] D. Renton and M. A. Elbestawi, "Motion control for linear motor feed drives in advanced machine tools," *Int. J. Mach. Tools Manuf.*, vol. 41, no. 4, pp. 479–507, Mar. 2001.
- [138] R. M. Schmidt, G. Schitter, and A. Rankers, *The design of high performance mechatronics-: High-tech functionality by multidisciplinary system integration*. IOS Press, 2014.
- [139] J. F. Cox, *Fundamentals of linear electronics: integrated and discrete*. Cengage Learning, 2002.
- [140] S. Ziegler, R. C. Woodward, H. H.-C. Iu, and L. J. Borle, "Current sensing techniques: A review," *IEEE Sens. J.*, vol. 9, no. 4, pp. 354–376, 2009.
- [141] M. H.-M. Cheng, A. Mitra, and C.-Y. Chen, "Synchronization controller synthesis of multi-axis motion system," in *2009 Fourth International Conference on Innovative Computing, Information and Control (ICICIC)*, 2009, pp. 918–921.
- [142] P. Avitabile, "Modal space - in our own little world," *Exp. Tech.*, vol. 37, no. 6, pp. 5–7, Nov. 2013.
- [143] R. W. Schafer and A. V Oppenheim, *Discrete-time signal processing*. Prentice Hall Englewood Cliffs, NJ, 1989.
- [144] L. Ljung, *System identification*. Hoboken, NJ, USA: John Wiley & Sons, Inc., 1999.
- [145] D. L. Brown and R. J. Allemang, "Review of spatial domain modal parameter estimation procedures and testing methods," in *International Modal Analysis Conference (IMAC) XXVII*, 2009, p. 23.
- [146] P. Gahinet, R. Chen, B. Eryilmaz, and B. Singh, "Automated PID controller design, using parameters that satisfy a merit function." U.S. Patent 9,886,008, 2018.
- [147] S. M. Ross *et al.*, *Stochastic processes*, vol. 2. Wiley New York, 1996.
- [148] Z. Zhu, S. To, W.-L. Zhu, P. Huang, and X. Zhou, "Cutting forces in fast-/slow tool servo diamond turning of micro-structured surfaces," *Int. J. Mach. Tools Manuf.*, vol. 136, pp. 62–75, Jan. 2019.
- [149] K. Zhou and J. C. Doyle, *Essentials of robust control*, vol. 104. Prentice hall Upper Saddle River, NJ, 1998.
- [150] J. O. Krah, "Bode plot based auto-tuning – Enhanced solution for high performance servo drives," pp. 382–387, 2004.
- [151] R. D. Hampton and M. S. Whorton, "Frequency-weighting filter selection, for H/sub 2/control of microgravity isolation systems: a consideration of the" implicit frequency weighting" problem," in *IMTC/99. Proceedings of the 16th IEEE Instrumentation and Measurement Technology Conference (Cat. No.*

99CH36309), 1999, vol. 1, pp. 268–273.

- [152] A. H. Sayed and T. Kailath, “A survey of spectral factorization methods,” *Numer. Linear Algebr. with Appl.*, vol. 8, no. 6–7, pp. 467–496, Sep. 2001.
- [153] K. K. Tan, S. Y. Lim, T. H. Lee, and H. Dou, “High-precision control of linear actuators incorporating acceleration sensing,” *Robot. Comput. Integr. Manuf.*, vol. 16, no. 5, pp. 295–305, Oct. 2000.
- [154] M. Griese and J. Maas, “Control concepts with acceleration feedback for servo systems,” *IEEE/ASME Int. Conf. Adv. Intell. Mechatronics, AIM*, vol. 2016-Septe, pp. 816–821, 2016.
- [155] J. Deur and N. Peric, “A comparative study of servosystems with acceleration feedback,” in *Record of the 2000 IEEE Industry Applications Conference. Thirty-Fifth IAS Annual Meeting and World Conference on Industrial Applications of Electrical Energy*, 2000, pp. 1533–1540.
- [156] J. Yang, C. Hu, Y. Zhu, Z. Wang, and M. Zhang, “Experimental investigation of shaping disturbance observer design for motion control of precision mechatronic stages with resonances,” *Mech. Syst. Signal Process.*, vol. 92, pp. 334–348, 2017.
- [157] S. Zhang, S. To, G. X. Zhang, and Z. Zhu, “A review of machine-tool vibration and its influence upon surface generation in ultra-precision machining,” *Int. J. Mach. Tools Manuf.*, vol. 91, pp. 34–42, Apr. 2015.
- [158] S. Zhang, S. To, S. J. Wang, and Z. Zhu, “A review of surface roughness generation in ultra-precision machining,” *Int. J. Mach. Tools Manuf.*, vol. 91, pp. 76–95, Apr. 2015.
- [159] W. Chang, W. Zhong, F. Ding, F. Wardie, and X. Luo, “Development of a compact ultra-precision six-axis hybrid micro-machine,” in *2017 World Congress on Micro and Nano Manufacturing: A Joint Conference of ICOMM/4M/IFMM*, 2017.
- [160] D. J. Whitehouse, “Some theoretical aspects of error separation techniques in surface metrology,” *J. Phys. E.*, vol. 9, no. 7, pp. 531–536, 1976.
- [161] D. Moore, “Design considerations in multiprobe roundness measurement,” *J. Phys. E.*, vol. 22, no. 6, pp. 339–343, 1989.
- [162] G. X. Zhang, Y. H. Zhang, S. M. Yang, and Z. Li, “A multipoint method for spindle error motion measurement,” *CIRP Ann.*, vol. 46, no. 1, pp. 441–445, Jan. 1997.
- [163] P. Huang, S. To, and Z. Zhu, “Diamond turning of micro-lens array on the roller featuring high aspect ratio,” *Int. J. Adv. Manuf. Technol.*, pp. 1–7, 2018.
- [164] Y. Liu *et al.*, “Experimental investigation on form error for slow tool servo diamond turning of micro lens arrays on the roller mold,” *Materials (Basel)*, vol. 11, no. 10, p. 1816, Sep. 2018.

- [165] M. Boerlage, M. Steinbuch, P. Lambrechts, and M. van de Wal, "Model-based feedforward for motion systems," *Proc. 2003 IEEE Conf. Control Appl. 2003 (CCA 2003)*, vol. 2, no. 1, pp. 1158–1163, 2003.
- [166] W. Zhong, X. Luo, W. Chang, F. Ding, and Y. Cai, "A real-time interpolator for parametric curves," *Int. J. Mach. Tools Manuf.*, vol. 125, pp. 133–145, Feb. 2018.
- [167] Y. Sun, Y. Zhao, Y. Bao, and D. Guo, "A novel adaptive-feedrate interpolation method for NURBS tool path with drive constraints," *Int. J. Mach. Tools Manuf.*, vol. 77, pp. 74–81, Feb. 2014.
- [168] X. Beudaert, S. Lavernhe, and C. Tournier, "Feedrate interpolation with axis jerk constraints on 5-axis NURBS and G1 tool path," *Int. J. Mach. Tools Manuf.*, vol. 57, pp. 73–82, Jun. 2012.
- [169] J. A. Butterworth, L. Y. Pao, and D. Y. Abramovitch, "The effect of nonminimum-phase zero locations on the performance of feedforward model-inverse control techniques in discrete-time systems," in *Proceedings of the American Control Conference*, 2008, pp. 2696–2702.
- [170] J. A. Butterworth, L. Y. Pao, and D. Y. Abramovitch, "Architectures for tracking control in atomic force microscopes," in *IFAC Proceedings*, 2008, vol. 41, no. 2, pp. 8236–8250.
- [171] D. M. Alter and T.-C. Tsao, "Control of linear motors for machine tool feed drives: experimental investigation of optimal feedforward tracking control," *J. Dyn. Syst. Meas. Control*, vol. 120, no. 1, p. 137, Mar. 1998.
- [172] Y. Luo, A. Serrani, S. Yurkovich, D. B. Doman, and M. W. Oppenheimer, "Model predictive dynamic control allocation with actuator dynamics," in *Proceedings of the 2004 American Control Conference*, 2004, vol. 2, pp. 1695–1700 vol.2.
- [173] Y. Altıntaş, "Direct adaptive control of end milling process," *Int. J. Mach. Tools Manuf.*, vol. 34, no. 4, pp. 461–472, 1994.
- [174] S. Cappa, D. Reynaerts, and F. Al-Bender, "A sub-nanometre spindle error motion separation technique," *Precis. Eng.*, vol. 38, no. 3, pp. 458–471, 2014.
- [175] R. Grejda, E. R. Marsh, and R. R. Vallance, "Techniques for calibrating spindles with nanometer error motion," *Precis. Eng.*, vol. 29, no. 1, pp. 113–123, 2005.
- [176] E. R. Marsh, J. Couey, and R. R. Vallance, "Nanometer-level comparison of three spindle error motion separation techniques," *J. Manuf. Sci. Eng.*, vol. 128, no. 1, p. 180, 2006.
- [177] G. X. Zhang and R. K. Wang, "Four-point method of roundness and spindle error measurements," *CIRP Ann.*, vol. 42, no. 1, pp. 593–596, Jan. 1993.
- [178] J. F. Tu, B. Bossmanns, and S. C. C. Hung, "Modeling and error analysis for assessing spindle radial error motions," *Precis. Eng.*, vol. 21, no. 2–3, pp. 90–



101, Sep. 1997.